UNIVERSITAT POLITÈCNICA
DE CATALUNYA
BARCELONATECH

Aerodynamic analysis of complex geometries using CFD

David Eduardo Aljure Osorio

ADVERTIMENT La consulta d'aquesta tesi queda condicionada a l'acceptació de les següents condicions d'ús: La difusió d'aquesta tesi per mitjà del repositori institucional UPCommons (http://upcommons.upc.edu/tesis) i el repositori cooperatiu TDX (http://www.tdx.cat/) ha estat autoritzada pels titulars dels drets de propietat intel·lectual **únicament per a usos privats** emmarcats en activitats d'investigació i docència. No s'autoritza la seva reproducció amb finalitats de lucre ni la seva difusió i posada a disposició des d'un lloc aliè al servei UPCommons o TDX.No s'autoritza la presentació del seu contingut en una finestra o marc aliè a UPCommons (*framing*). Aquesta reserva de drets afecta tant al resum de presentació de la tesi com als seus continguts. En la utilització o cita de parts de la tesi és obligat indicar el nom de la persona autora.

ADVERTENCIA La consulta de esta tesis queda condicionada a la aceptación de las siguientes condiciones de uso: La difusión de esta tesis por medio del repositorio institucional UPCommons (http://upcommons.upc.edu/tesis) y el repositorio cooperativo TDR (http://www.tdx.cat/?locale-attribute=es) ha sido autorizada por los titulares de los derechos de propiedad intelectual **únicamente para usos privados enmarcados** en actividades de investigación y docencia. No se autoriza su reproducción con finalidades de lucro ni su difusión y puesta a disposición desde un sitio ajeno al servicio UPCommons No se autoriza la presentación de su contenido en una ventana o marco ajeno a UPCommons (*framing)*. Esta reserva de derechos afecta tanto al resumen de presentación de la tesis como a sus contenidos. En la utilización o cita de partes de la tesis es obligado indicar el nombre de la persona autora.

WARNING On having consulted this thesis you're accepting the following use conditions: Spreading this thesis by the institutional repository UPCommons (http://upcommons.upc.edu/tesis) and the cooperative repository TDX (http://www.tdx.cat/?locale-attribute=en) has been authorized by the titular of the intellectual property rights **only for private uses** placed in investigation and teaching activities. Reproduction with lucrative aims is not authorized neither its spreading nor availability from a site foreign to the UPCommons service. Introducing its content in a window or frame foreign to the UPCommons service is not authorized (framing). These rights affect to the presentation summary of the thesis as well as to its contents. In the using or citation of parts of the thesis it's obliged to indicate the name of the author.

UPC CTTC

Aerodynamic analysis of complex geometries using CFD

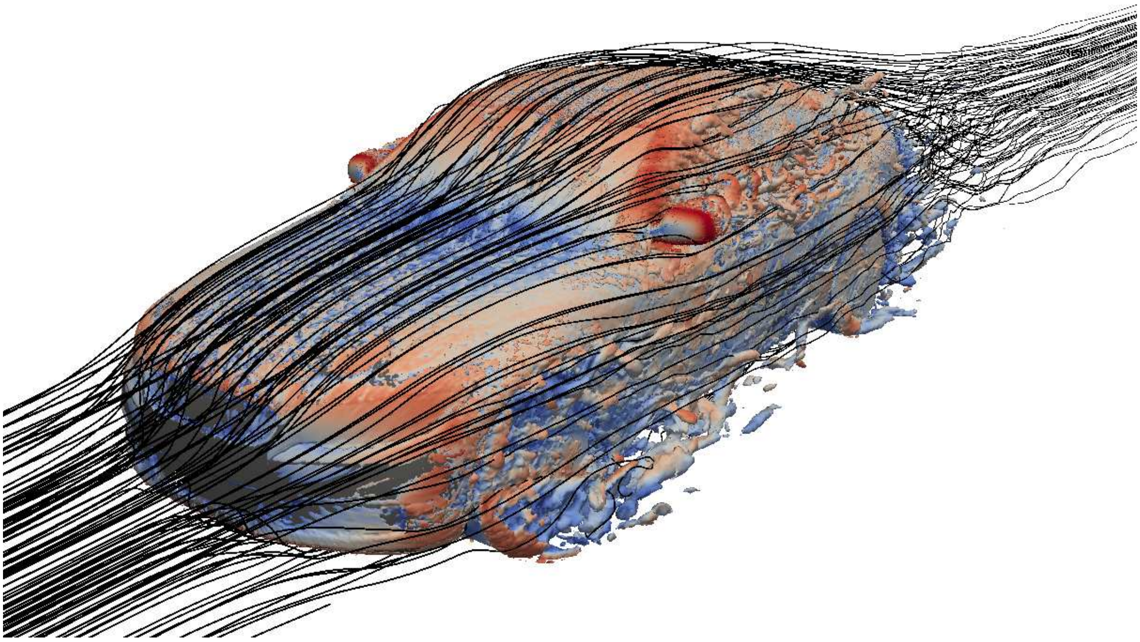

Centre Tecnològic de Transferència de Calor
Departament de Màquines i Motors Tèrmics
Universitat Politècnica de Catalunya

David Eduardo Aljure Osorio
Doctoral Thesis

Aerodynamic analysis of complex geometries using CFD

David Eduardo Aljure Osorio

TESI DOCTORAL

presentada al

Departament de Màquines i Motors Tèrmics
E.S.E.I.A.A.T.
Universitat Politècnica de Catalunya

per a l'obtenció del grau

Doctor per la Universitat Politècnica de Catalunya

Terrassa, April, 2017

Aerodynamic analysis of complex geometries using CFD

David Eduardo Aljure Osorio

Director de la Tesi

Dr. Assensi Oliva Llena

Tribunal Qualificador

Dr.
University of
Dr.
University of
Dr.
University of

Mientras el extranjero enigmático de un poema de Baudelaire amaba por encima de todo «las nubes que pasan... allá lejos... las maravillosas nubes»; más de un siglo y medio después el joven ingeniero también escrudiñaba los cielos pero buscando lo previsible en lo imprevisible. No le importaba saber si iba a llover, sólo lo fascinaba el movimiento impredecible de los aires y los fluidos. Alguna noche, su mirada se perdía en el movimiento del humo expirado de un cigarro. Los domingos señalados, atisbaba las ruedas de Fórmula 1, embriagado por su celeridad.

Quería entender las turbulencias de las nubes, del humo, de las ruedas. Quería descifrar la dinámica del aire. Pero, ¿cómo analizar el caos? Con tubos, soplos, ordenadores, con simulaciones y ecuaciones. . .

Sabía, pero, que las ecuaciones llegarían hasta donde podían llegar y que le dejarían espacio para imaginar.

Sabı'a que nunca dejaría de ver, como Baudelaire, «las nubes que pasan... allá lejos... las maravillosas nubes».
Myriam Mallart

Acknowledgements

I would like to use this space to acknowledge the contribution of a number of people that made possible the completion of this thesis work. From start to finish, this work has been a long endeavor, spanning from my undergraduate thesis, master and finally this Phd. A journey that has taken me over 7 years to complete and in which a vast number of people have contributed, in one way or another.

In particular, I want to show my gratitude to:

Prof. Assensi Oliva, head of the Heat and Mass Transfer Technological Center (CTTC), he has trusted me to find my own way during this thesis project, allowing me freedom to pursue my goals. Additionally, I would like to express my gratitude to all the staff within the CTTC that has aided in my research by providing documentation, technical equipment and, most important of all, support. Within the CTTC I would like to acknowledge Joaquim Rigola, for his assistance in the development of chapter 4, Federico Favre and Daniel Martinez for the collaboration in chapter 6, Aleix Baez and Joan Calafell for their help in chapter 7 and Carles-David Pérez for reviewing this dissertation.

Oriol Lehmkuhl and Ivette Rodriguez, for their guidance and insight in most of the work I carried out. Their help and expertise have greatly enriched this thesis project.

Finally, I would also like to thank all my family and friends. Being sane outside the lab kept me sane inside.

This work has been funded by:

The “Ministerio de Economía y Competitividad, Secretaría de Estado de Investigación, Desarrollo e Innovación”, Spain (Projects:ENE2010-17801 and ENE2014-60577-R“).

By the collaboration project between “Universitat Politècnica de Catalunya” and Termo Fluids S.L.

And, most importantly, by The “Departamento Administrativo de Ciencia, Tecnología e Innovación - Colciencias” through their doctoral training program “Francisco Jose de Caldas”.

I also would like to knowledge Sinisa Krajnović, Eric Serre and Matthieu Minguez for providing results to permit comparison in the Ahmed car and the access to MareNostrum SuperComputer III and FinisTerrae II granted by the “Red Española de Supercomputación”

Abstract

Aerodynamic analysis has become one of the most important tools in many engineering applications. In this sense, this thesis work is aimed at performing aerodynamic analysis of different geometries, expanding the available knowledge and obtaining valuable insight from the obtained results. Aerodynamic analysis can be carried out, principally, in two ways: Experimental research and Computational Fluid Dynamics (CFD). The former makes use of prototypes, wind tunnels and test tracks, making it a very expensive option. On the other hand, CFD makes use of numerical tools to solve the Navier-Stokes equations within a computational discretized domain. This latter approach is essentially limited by the available computational power and by the aerodynamicist's experience.

This work comprises eight chapters. The first one is an introduction to the type of flows and geometries considered, as well as, the general methodology followed in the posterior studies. The following six chapters are the core of this dissertation, and encompass the numerical resolution of the Navier-Stokes equations in selected geometries, ordered by complexity level. In particular, the contents of these seven chapters have been submitted or published in international journals and conferences. For this reason, they are self contained and few changes have been made. The reader might find that some concepts are repeated along them. The last chapter contains concluding remarks. Finally, appendix 1 descrives some applications of aerodynamic studies to some related projects and appendix 2 comprises a list of publications done during the PhD.

Contents

1 INTRODUCTION 25
1.1 Prologue . . . 25
1.1.1 RANS . . . 26
1.1.2 LES . . . 26
1.1.3 DNS . . . 26
1.2 Objectives of this thesis . . . 27
1.3 Outline of the thesis . . . 27

2 Three dimensionality in the wake of the flow around a circular cylinder 29
2.1 Introduction . . . 29
2.2 Mathematical and numerical model . . . 31
2.2.1 Governing equations and numerical method . . . 31
2.2.2 Definition of the case and boundary conditions . . . 32
2.2.3 Computational domain and spatial discretization . . . 32
2.2.4 Time integration study . . . 33
2.2.5 Mesh sensitivity study . . . 34
2.3 Results . . . 39
2.3.1 Wake three-dimensionality . . . 39
2.3.2 Frequency analysis . . . 48
2.3.3 Shear layers and instability mechanisms . . . 51
2.4 Conclusions . . . 56

3 Influence of rotation on the flow over a cylinder at Re=5000 61
3.1 Introduction . . . 61
3.2 Definition of the case . . . 63
3.2.1 Mathematical and numerical models . . . 63
3.2.2 Boundary conditions . . . 64
3.2.3 Spatial discretization . . . 64
3.2.4 Validation of the numerical approach . . . 66
3.3 Results . . . 66
3.3.1 Instantaneous flow . . . 66
3.3.2 Mean flow characteristics . . . 74
3.3.3 Force coefficients . . . 77
3.3.4 Periodic behavior . . . 79
3.4 Conclusions . . . 80

4 Numerical analysis of the turbulent fluid flow through valve geometries. 85
4.1 Introduction 85
4.2 Definition of the case 86
4.3 Mathematical formulation 87
  4.3.1 Governing equations and numerical method 87
  4.3.2 Large eddy simulation turbulence models 87
4.4 Numerical results 87
  4.4.1 Mesh and time integration analysis 87
  4.4.2 Turbulence model analysis 91
  4.4.3 Geometrical analysis 92
4.5 Conclusions 94

5 Flow and Turbulent Structures Around Simplified Car Models 97
5.1 Introduction 97
5.2 Definition of the Case 99
  5.2.1 Geometries and Computational Domain 99
  5.2.2 Mathematical and Numerical Model 99
  5.2.3 Numerical Method 102
5.3 Results 104
  5.3.1 Numerical Analysis 104
  5.3.2 CLES analysis 105
  5.3.3 Flow Structures 111
5.4 Conclusions 117

6 On the IBM approximation for the wheel aerodynamic simulation 119
6.1 Introduction 119
6.2 Definition of the case 120
6.3 Mathematical and numerical model 121
  6.3.1 Boundary conditions 122
  6.3.2 Spatial discretization 123
6.4 Results and discussion 124
  6.4.1 Fabianic model 124
  6.4.2 Ahmed model 127
6.5 Conclusions 129

7 Flow over a realistic car model: Wall modeled large eddy simulations assessment and unsteady effects 131
7.1 Introduction 131
7.2 Mathematical and Numerical Model 134
  7.2.1 Governing equations 134
  7.2.2 Wall model 134
  7.2.3 Numerical method 135
  7.2.4 Case definition 135
  7.2.5 Mesh description 136
  7.2.6 Time integration study 137
  7.2.7 Mesh sensitivity study 139
7.3 RESULTS 143
  7.3.1 WMLES analysis 143
  7.3.2 SGS model effect 147
  7.3.3 Time step and CPU time 149

7.3.4 Flow Structures 150
7.4 CONCLUSIONS 155

8 Conclusions and future work **157**

List of Figures

2.1 Geometry and computational domain. 32

2.2 Location of the computational probes, P1 [$x/D = 2$ $y/D = 0$], P2 [$x/D = 0.75$ $y/D = 0.65$] and P3 [$x/D = 3.5$ $y/D = 0$]. 33

2.3 (a): Time evolution of the averaged stream-wise velocity. (b): Time evolution of the stream-wise velocity fluctuations. Solid line: P1 [2D,0], Dashed line: P2: [0.75D,0.65D]. 34

2.4 Mean pressure distribution around the circular cylinder for the different meshes. Solid line mesh M1, dashed line mesh M2, dash-dash line mesh M3, dotted line mesh M4, dash-dot line mesh M5, dash-dot-dot Lehmkuhl et al. [67] ($Re = 3900$), crosses Norberg [89] ($Re = 3000$), circles Norberg [89] ($Re = 8000$). 36

2.5 Mean (a) stream-wise and (b) RMS stream-wise velocities in the wake center line. Solid line mesh M1, dashed line mesh M2, dash-dash line mesh M3, dotted line mesh M4, dash-dot line mesh M5, squares Norberg [89] ($Re = 5000$), triangles Lam et al. [59] ($Re = 6000$), crosses Prasad and Williamson [106] ($Re = 5427$). 37

2.6 Span wise averaged energy spectra of the cross-stream wise velocity fluctuations at two locations (a) P1 (b) P2. 38

2.7 Coherent structures represented by means of Q iso contours $Q^* = 3$. (a)$2\pi D$ span-wise length, (b) $3\pi D$ span-wise length. 40

2.8 Two point correlations in the span-wise direction for the velocity components. (a)Stream wise. (b) Cross-stream-wise. (c) Span wise. Solid line: $2\pi D$ span-wise length, Dashed line: $3\pi D$ span-wise length. 41

2.9 Vortex dislocations, span-wise view. (a) Velocity field at the wake centerline plane. (b) Span wise flow visualization by Norberg at Re=5500 [87]. 42

2.9 Cont: Vortex detachment time evolution. $p^* = -0.4$ $\omega_z \pm 15$ and $Q^* = 50$ iso surfaces. 44

2.10 (a) $p^* = -0.7$ iso surface and (b) Cross stream velocity in the mid plane showing the loss of coherence in a vortex tube. 45

2.11 (a) Cross stream velocity and (b) pressure time history for P1 showing the passage of a vortex distortion. 46

2.12 Cross-stream velocity on the (t,z) plane, illustrating the local perturbations on the coherence of the signal at P1 (a) and the recovery of coherence downstream at P3 (b). 47

2.13 Span wise variations of the energy spectra for the cross flow velocity for P1. 48

2.14 Fourier spectrogram for the cross flow velocity for P1 at plane $z/D = \pi$. (a) All integration time. (b) close up for $1920 \leq TU \leq 2180$. (c) close up for $2920 \leq TU \leq 3180$. 49

2.15 Empirical mode decomposition of the cross flow velocity for P1 (a) full time range, (b) close up to $1900 \leq TU \leq 2200$, (c) close up to $2900 \leq TU \leq 3200$. 50
2.16 Hilbert spectrum for the IMFs shown in Fig. 2.15. The energy levels increase as color darkens. 51
2.17 Span wise view at two locations showing the two different types of instabilities governing the flow, (a) $z/D = 5.89$ global instabilities and (b) $z/D = 0.2$ convective instabilities. Figure is colored by pressure. 52
2.18 Shear layer roll up for (a) $TU = 2500.6$, using span wise non-dimensional vorticity $\omega_z^*/\omega_{z-max}^* = 5.5\%$, and resulting vortex tubes (b) $TU = 2503.6$ using non-dimensional pressure $p^* = -0.7$. Both images are colored by span wise velocity. 53
2.19 Span wise velocity within the shear layer (P1) at two span wise locations, $z/D = 2.2$ and $z/D = 4.1$. 54
2.20 Pressure and Q* contours depicting the shear layer roll up at two span wise locations, left $z/D = 2.3$ and right $z/D = 4.1$. 55
2.21 Shear layer roll up for (a) $TU = 2513.1$, using span wise non-dimensional vorticity $\omega_z^*/\omega_{z-max}^* = 5.5\%$, and resulting vortex tubes (b) $TU = 2516.1$ using non-dimensional pressure $p^* = -0.7$. Both images are colored by span wise velocity. 56
2.22 Span wise velocity within the shear layer (P1) at two span wise locations, $z/D = 4.8$ and $z/D = 1.8$. 57
2.23 Pressure and Q* contours depicting the shear layer roll up at two span wise locations, left $z/D = 4.8$ and right $z/D = 1.8$. 58

3.1 Geometry and computational domain. 63
3.2 Detail of the unstructured meshes for the two dimensional plane. Cases (a) $\alpha = 0$, (b) $\alpha = 2$, (c) $\alpha = 5$. 65
3.3 Mean stream wise velocity (a) and its fluctuations (b) in the wake centerline. Comparison with results from the literature. Solid line present results, squares Norberg [89] ($Re = 5000$), triangles Lam et al. [59] ($Re = 6000$), crosses Prasad and Williamson [106] ($Re = 5427$). 67
3.4 Time evolution of the average (left) stream wise velocity $< u_1 > /U_{ref}$ and (right) stream wise Reynolds stresses $< u_1' u_1' > /U_{ref}^2$ at different stations. (a) $\alpha = 0$, (b) $\alpha = 2$, (c) $\alpha = 5$. 68
3.5 Coherent structures represented by means of $Q^* = 3$ iso contours colored by pressure. (a) $\alpha = 0$, (b) $\alpha = 1$, (c) $\alpha = 2$, (d) $\alpha = 3$, (e) $\alpha = 4$ and (f) $\alpha = 5$. 69
3.6 Coherent structures viewed from the top of the cylinder (surface velocity in the same direction as flow velocity) represented by $Q^* = 3$ isosurfaces. (a) $\alpha = 0$, (b) $\alpha = 1$, (c) $\alpha = 2$, (d) $\alpha = 3$, (e) $\alpha = 4$ and (f) $\alpha = 5$. 70
3.7 Top and bottom shear layers depicted through non-dimensional spanwise vorticity iso surfaces. (a) $\alpha = 1$ top $\omega_3^* = -2.46$, (b) $\alpha = 2$ top $\omega_3^* = -1.78$, (c) $\alpha = 1$ bottom $\omega_3^* = 3.79$ and (d) $\alpha = 2$ bottom $\omega_3^* = 4.30$. 71
3.8 Identification of Taylor-Görtler vortices at the cylinder surface for $\alpha = 5$ using non-dimensional stream wise vorticity ω_1^*, at the plane $x = 0$. 71
3.9 Span wise location for the build up of TG structures at $\alpha = 5$ at two different times. (a) 82.5 TU (b) 500.0 TU viewed using non-dimensional stream wise vorticity $\omega_1^* = \pm 15$, colored by velocity magnitude. 72
3.10 Shedding of structures in the stream wise direction for $\alpha = 5$. (a) 82.5 TU (b)83.0 TU (c) 83.5 TU. Non-dimensional Q iso contours $Q^* = 3$, colored by stream wise vorticity. 73

3.11 Streamlines and pressure field for the different rotation ratios. (a) $\alpha = 0$, (b) $\alpha = 1$, (c) $\alpha = 2$, (d) $\alpha = 3$, (e) $\alpha = 4$, (f) $\alpha = 5$. The location of the saddle point ‘S’ and stagnation point ‘SP’ are also marked in the figure. . . 75
3.12 Shear layer length viewed using threshold values of non-dimensional span wise vorticity $\omega_3^* = 5.5\%\omega_{max}^*$. (a) $\alpha = 0$, (b) $\alpha = 1$, (c) $\alpha = 2$ and (d) $\alpha = 3$. 76
3.13 Circumvolving layer viewed using threshold values of non-dimensional span wise vorticity $\omega_3^* = 5.5\%\omega_{max}^*$. (a) $\alpha = 4$, (b) $\alpha = 5$. 76
3.14 Effect of the rotation ratio on (a) local pressure coefficient and (b) local skin friction coefficient around the cylinder surface. 0° corresponds to the front of the cylinder and angles are measured in counter clock wise direction. . . . 77
3.15 (a) Drag coefficient and (b) lift coefficient behavior with respect to rotation ratio. Comparison with potential flow theory ($2\pi\alpha$), Prandtl’s limit (4π) and results from Mittal and Kumar [81] for $Re = 200$. 78
3.16 (a) Segment of the instantaneous lift coefficient; (b) Energy spectrum of a probe located in the near wake at different rotation ratios. For clearness, the y-axis in (b) is shifted. 80
3.17 Mean stream-wise and stream-wise root-mean-square (rms) velocity in three cross flow locations. (a) x/D=0.6 , (b) x/D=1, (c) x/D=2. Solid line present results and symbols Norberg [89] at $Re = 5000$. 82

4.1 (a) Outline and dimensions for the two valve geometries and (b) Outline of the computational domain. 86
4.2 Meshes along the xy cut plane, (a) straight geometry and (b) cone geometry. 88
4.3 Numerical probes’ location, (a) straight geometry, (b) cone geometry. 88
4.4 Stream wise velocity W time history for the different numerical probes in the (a) straight geometry and (b) cone geometry. 89
4.5 Z-component velocity autocorrelation function for the different numerical probes in the (a) straight geometry and (b) cone geometry. 90
4.6 Pressure distribution over the lower face of the valve disc and velocity profiles over the gap at $x = d/2$,$x = d/4 + D/4$ and $x = D/2$ for (a) straight geometry, (b) cone geometry. 91
4.7 LES results for the pressure profile along the plate on (a) straight geometry, (b) cone geometry. LES results for the velocity profiles in the gap. (c) straight geometry, (d) cone geometry. 92
4.8 pressure distribution over the plate for both geometries, (a): gap opening $s/d = 0.033$, (b): gap opening $s/d = 0.11$ and (c): gap opening $s/d = 0.022$. 93
4.9 Effective flow area for the different valve openings. 94
4.10 Instantaneous velocity field for both geometries, (a): gap opening $s/d = 0.033$, (b): gap opening $s/d = 0.11$ and (c): gap opening $s/d = 0.022$. 95

5.1 Model dimensions - Units in meters. 99
5.2 a)Computational domain - All dimensions in meters. 100
5.3 Visualization of the mesh in the channel. 103
5.4 Mesh study on both geometries. (a)Average stream-wise velocity and RMS velocity profiles over the slant wall in the mid plane. (b)Average pressure coefficient in the underbody and in the back. 105
5.5 Velocity profiles in the Ahmed car. 107
5.6 Velocity profiles in the Ahmed car. 108
5.7 Pressure coefficients in the Asmo car. 109
5.8 Pressure coefficients in the Asmo car. 110

5.9 Time-averaged stream wise vortices. 112
5.10 Time-averaged streamlines in the back of the car models. 113
5.11 Recirculation bubble behind the geometries. 114
5.12 Time-averaged non-dimensional pressure contours. 115
5.13 Instantaneous Q-iso surfaces in the front of the Ahmed car, $Q = 20$. 115
5.14 Instantaneous Q-iso surfaces in the front of the Asmo car, $Q = 20$. 116
5.15 Instantaneous Q-iso surfaces in the rear of the Ahmed car, $Q = 200$. 116
5.16 Instantaneous iso surfaces in the back of the Asmo car, $Q = 200$. 117

6.1 Fabianic model geometry and computational domain. 120
6.2 Ahmed car model geometry and computational domain. 121
6.3 IBM approximation - Fabianic model. 123
6.4 IBM approximation - Ahmed model. 124
6.5 Pressure distribution in the wheelhouse. 125
6.6 (a) Coherent structures on the front of the wheel, (b) coherent structures on the outside of the wheel and (c) coherent structures on the outside of the wheel. Left present results, right Krajnović S. and Basara [58]. 126
6.7 $Q = 10$ instantaneous iso-surfaces around the Ahmed body. 127
6.8 $Q = 50$ average iso-surfaces around the Ahmed body. 128

7.1 (a) Model dimensions. (b)Computational domain - Units in meters. 135
7.2 Visualization of cut planes of the mesh at different positions. 136
7.3 Force coefficients time evolution for Mesh 4 137
7.4 Numerical probes' location 137
7.5 Pressure coefficient vs time for the different probes 138
7.6 Caption on page 139 138
7.6 Autocorrelation function for the pressure time history at the monitored stations 139
7.7 y^+ distribution for the different meshes. From top to bottom: Mesh 1, Mesh 2, Mesh 3 and Mesh 4. 140
7.8 Caption on page 142 141
7.8 Average pressure coefficient profile over (a) the top of the car geometry in the mid plane, (b)the bottom of the car geometry in the mid plane and (c) the side of the car geometry in the horizontal y=$0.03L_{ref}$ plane 142
7.9 Distribution of the pressure coefficient at the rear window. Left: Heft et al. [34], right: present LES 143
7.10 Averaged pressure coefficient along the top of the car in the mid plane. . . . 144
7.11 Averaged pressure coefficient along the top of the car in the mid plane. . . . 145
7.12 Averaged pressure coefficient along the bottom of the car in the mid plane. . 146
7.13 Averaged pressure coefficient over the side of the car geometry in the horizontal y=$0.03L_{ref}$ plane 147
7.14 Average pressure coefficient profile over the rear window at different span wise locations and using different SGS models. (a) $z/L_{ref} = 0.00$, (b) $z/L_{ref} = 0.05$, (c) $z/L_{ref} = 0.1$, (d) $z/L_{ref} = 0.125$. Left SIGMA SGS model, right VMS SGS model. Comparison with Guilmineau [31] 148
7.15 span wise locations for the pressure profiles at the rear window 149
7.16 Instantaneous turbulent structures around the car viewed from the front, coloured by velocity magnitude. (a) $Q^* = 1$ iso surfaces. (b) non-dimensional stream wise vorticity $\omega^* \pm 50$. 150
7.17 Averaged pressure coefficient Cp over the surface of the car. 151

7.18 Energy spectra for the pressure fluctuations at stations P1 and P2. 152
7.19 Turbulent structures around the car, viewed from the back, coloured by velocity magnitude. (a) $Q^* = 1$ iso surfaces. (b) non-dimensional stream wise vorticity $\omega^* \pm 50$. 153
7.20 Averaged pressure coefficient Cp over the surface of the car. 154
7.21 Energy spectra for the pressure fluctuations at stations P3, P4, P6 and P8. 154
7.22 Frequency spectra on the drivAer model at the locations specified on Fig. 7.4.155

List of Tables

2.1 Mesh parameters. CV_{plane} is the number of control volumes in the plane, N_{planes} is the number of planes in the span-wise direction, L_Z the length of the span-wise directions, NCV the total number of control volumes in the domain. 33
2.2 Statistical flow parameters for the different meshes. Comparison with literature available results. Drag coefficient (C_D), Strouhal number (St), base pressure coefficient ($C_{p_{base}}$), fluctuating lift coefficient ($C_{L'}$), separation angle (ϕ_s) and recirculation length (L_{rec}/D). [a]: [87], [b]: [88], [c]: [90], [d]: [89]. . . 35
2.3 Relation between shear layer frequency St_{KH} and vortex shedding frequency St_{vs}. 39

3.1 Details of simulation parameters for the different rotation ratios. 65
3.2 Statistical flow parameters for $\alpha = 0$. Comparison with literature available results. [†][87], [‡][88], [††][89]. 66
3.3 Flow parameters. Recirculation length (L_{rec}/D), coordinates of the saddle point S and its angular position (θ_s), location of the stagnation point (θ_{sp}) and angular position of the separation points θ_{sep-D} (downstream moving wall) and θ_{sep-U} (upstream moving wall). *Point off the cylinder. Angles are measured in counter-clockwise direction. 74
3.4 Base pressure ($C_{p_{base}}$), minimum pressure (p_{min}), drag coefficient C_D, lift coefficient C_L, lift coefficient fluctuations C_{Lrms}, and lift to drag C_L/C_D ratio. **Pressure maximum in the cylinder surface. 77
3.5 Dominating non-dimensional frequencies (St). *Vortex shedding twin peak for $\alpha = 5$. 79
3.6 Mesh sensitivity parameters. 83

4.1 Mesh parameters. NCV the total number of control volumes in the domain, $y^+_{min}D$ and $y^+_{avg}D$ minimum and averaged y^+ on the valve disc, and $y^+_{min}O$ and $y^+_{avg}O$ minimum and averaged y^+ on the discharge orifice surface. . . . 88
4.2 Numerical probes' location. 89

5.1 Mesh parameters. 103
5.2 Pressure drag (Ahmed car=0.285 [1]) and drag (Asmo car=0.153 [4]) with different meshes and turbulence models. 106
5.3 Ahmed car drag coefficients. 106
5.4 Ahmed car lift coefficients. 107
5.5 Asmo car drag coefficients. 111
5.6 Asmo car lift coefficients. 111

6.1 Computational domain and geometry dimensions in mm. 122

6.2 force coefficients on the Fabianic geometry, comparison to results by Krajnović et. al. [58]. . . . 124
6.3 force coefficients on the Ahmed geometry. . . . 127

7.1 Force coefficients and comparison to selected numerical and experimental results. [1]: Heft et al. [34], [2]: Guilmineau [32], [3] Peters et al. [99], [4]: Shinde et al. [123], [5]: Strangfeld et al. [128], [6]: Guilmineau [31], [7]: Ashton et al. [5] 141
7.2 Force coefficients for the different numerical configurations and experimental results. [1]: Heft et al. [34] . . . 143
7.3 Average time step dt, iteration time t_{iter}, number of iterations and overall time t_{cpu} required for the different numerical configurations. . . . 149

Chapter 1

INTRODUCTION

It should be noted that the present work is a continuation of the undergraduate thesis “Simulación numérica de problemas de transferencia de calor y dinámica de fluidos” and the master thesis “Turbulent flow modeling and solution” performed by the author. Aerodynamic analysis by means of computational fluid dynamics (CFD) can be used as a very important tool in many practical applications in engineering, such as the prediction of force and moment coefficients on aerodynamic bodies, and pressure drop within piped flows, amongst many others. CFD results yield plenty of detailed information on the flow configurations that are studied. Historically, most of the aerodynamic studies performed have been carried out using experiments, however, wind tunnels, on-track testing and prototype building is a costly and complicated endeavor. The development of computers and the consequent increase of calculation power has shown CFD to be an exceptional tool to reduce cost and increase performance in plenty of cases.

1.1 Prologue

Aerodynamics is the branch of fluid dynamics that deals with the movement of air and its interaction with solids. As most fluid dynamic problems, aerodynamics is governed, by the Navier-Stokes equations (NSE). These equations are the result of applying the Newton's second law of motion to fluids. In the present dissertation the incompressibility hypothesis is assumed. Resulting equations can be expressed in the following way:

$$\frac{\partial u_i}{\partial x_i} = 0 \tag{1.1}$$

$$\frac{\partial u_i}{\partial t} + \frac{\partial (u_i u_j)}{\partial x_j} - \nu \frac{\partial^2 u_i}{\partial x_j \partial x_j} + \rho^{-1} \frac{\partial p}{\partial x_i} = 0 \tag{1.2}$$

where $\mathbf{u}$ is the three-dimensional velocity vector, p is the pressure scalar field, ν stands for kinematic viscosity and ρ for the density of the fluid.

Industrial level applications deal with turbulent flow, however, due to its unstable, irregular and chaotic nature (see, for instance Pope [102]), its solution is very complicated. Studies in the first half of the XX century have defined turbulence as the irregular motion observed in fluids in close proximity to solid surfaces or when different streams cross paths. Complexities arise due to the non-lineal interaction between the viscous and inertial effects present in the NSE. Numerical solution of fluid dynamics concerning turbulence is divided, basically, in three branches: Direct Numerical Simulation (DNS), Large Eddy Simulation (LES) and Reynolds Average Navier-Stokes (RANS).

1.1.1 RANS

The Reynolds Averaged Navier-Stokes (RANS) simulations are the simplest numerical methods used to study turbulent flow dynamics, however, they are the cheapest and most widely spread in the industry. In 1894 Reynolds introduced a velocity decomposition method:

$$\phi(X,t) =< \Phi(X,t) > +\phi(X,t) \tag{1.3}$$

where <> indicates a time averaged value. Two components are present in this decomposition, a temporal average and the fluctuation. Using this technique on the NSE (Eqs. 1.1 and 1.2) yield the RANS equations.

$$\frac{\partial < u_i >}{\partial t} + < u_j > \frac{\partial < u_i >}{\partial x_j} = \nu \nabla^2 < u_j > - \frac{\partial < u_j u_i >}{\partial x_j} - \frac{1}{\rho} \frac{\partial < p >}{\partial x_i} \tag{1.4}$$

Eqs. 1.4 are very similar to the complete NSE, however they solve for time-averaged quantities. Furthermore, a new term appears, the stress tensor $< u_j u_i >$. This tensor is the result of the random fluctuations in the fluid flow (turbulent transport). This tensor plays a major role in the solution of the equations and suitable models must be used to calculate it.

1.1.2 LES

Large Eddy Simulations (LES) do not solve for averaged quantities. In this type of simulations instantaneous data is obtained, to then be integrated over time. In this type of simulations large, three-dimensional unsteady scales are directly solved, whereas smaller scales are modeled. This type of simulations are much more computationally challenging than the RANS models, however, LES models yield more precise and complete results. Taking into account Kolmogorov's first similarity hypothesis [54], turbulent scales can be divided in 2: large or resolved scales (directly solved) and small or sub grid-scales (modeled)

Two steps are followed in LES simulations:

- Filtering: A filter operator is applied to the NSE, decomposing the variables $\phi(X,t)$ into a resolved part $\overline{\phi}(X,t)$ and a residual (sub grid-scale SGS) $\phi'(X,t)$. The filter applied to the NSE is a convolution of the velocity $U(X,t)$ with a filter function $G(r,X)$ [68]:

  $$\overline{\phi}_i(X) = \int G(r,X)\phi(X-r,t)dr \tag{1.5}$$

  Applying this to the NSE yields the LES equations:

  $$\frac{\partial \overline{u_i}}{\partial t} + \overline{u_j}\frac{\partial \overline{u_i}}{\partial x_j} = \nu \frac{\partial^2 \overline{u_i}}{\partial x_j \partial x_j} - \frac{1}{\rho}\frac{\partial \overline{p}}{\partial x_i} - \frac{\partial \tau_{ij}}{\partial x_j} \tag{1.6}$$

- Model closure: The model is closed, in a similar way as with the RANS models, by modeling the resulting tensor. For LES this is the SGS stress tensor.

1.1.3 DNS

For DNS, unlike in LES of RANS, all spatial and temporal scales are solved. Results from these simulations are very precise, however the computational costs associated with it are very high. From the Kolmogorov scales definition the smallest length and temporal scales depend on $Re^{-3/4}$ and $Re^{-1/2}$, respectively [102]. This means that, for a three-dimensional model, computational requirements scale, approximately, with Re^3. Incompressible Navier-Stokes equations for DNS are as follows:

$$\frac{\partial u_i}{\partial x_i} = 0 \tag{1.7}$$

$$\frac{\partial u_i}{\partial t} + \frac{\partial (u_i u_j)}{\partial x_j} - \nu \frac{\partial^2 u_i}{\partial x_j \partial x_j} + \rho^{-1} \frac{\partial p}{\partial x_i} = 0 \tag{1.8}$$

where $\mathbf{u}$ is the three-dimensional velocity vector, $\mathbf{p}$ is the pressure field, ν stands for the kinematic viscosity and ρ for the density of the fluid.

1.2 Objectives of this thesis

Recent advances in CFD and high performance computing (HPC) have made possible the study of a great number of flows related with industrial research. In this sense, CFD and aerodynamics have played a major role in the development of modern aircraft, wind turbines, large structures and road vehicles, amongst many others. Three main tools are used when dealing with aerodynamic studies, RANS, LES and DNS simulations. Of these three, only RANS is completely embedded within the industrial world. Large computational requirements and long run times are the major set backs in implementing LES and DNS. Considering the actual state-of-the-art in aerodynamic studies, the main objectives of this thesis are:

- Perform aerodynamic analyses on simplified geometries using novel approaches providing insight and new information useful for the scientific community.

- Use the experience gained on simplified geometries to perform aerodynamic analysis on complex, industrial related geometries to allow the advance in the understanding of the physics governing different flow phenomena.
- Perform aerodynamic analysis on real life applications.

To do so, the numerical formulation comprising of: symmetry preserving discretization [141], fractional step method [13] and diverse turbulence models have been used on unstructured collocated meshes partitioned using Metis software [50] and ran using HPC facilities.

1.3 Outline of the thesis

As has been aforementioned, this dissertation is aimed at performing aerodynamic analysis of diverse geometries of scientific and industrial relevance. The following two chapters present direct numerical simulations (DNS) of a cylinder in cross flow at $Re = 5000$ and with varying rotational speeds.

In Chapter 2, the cylinder with no rotation is studied, identifying the causes behind the three dimensional phenomena observed and analyzing in detail the vortex shedding and distortions caused by two instability mechanisms, global and convective type. Chapter 3 studies the changes brought upon the flow when the cylinder is rotating. Rotation velocities in the range $0 \leq \alpha = U_T/U_{ref} \leq 5$ are studied. Vortex shedding, flow distribution and points of interest greatly change as rotation increases. Furthermore, a secondary unsteady zone was found for $\alpha = 5$.

Chapter 4 contains the study of different aspects concerning valve geometries at an industrial level *Re* number. The effects of a straight geometry and a conical one are analyzed and their behavior with different opening ratios is studied. For this study, synthetic turbulence is used at the inlet, allowing the numerical simulations to be one step closer to practical applications. Pressure profiles over the valve disc greatly change with the change of geometry. Additionally, the conical geometry exhibits a 40% reduction in pressure rise, as well as significant reduction in the velocity gain within the valve gap. All in all, an important pressure drop reduction is expected when using the cone geometry.

Final chapters deal with automotive-type simulations. Chapter 5 contains a LES study of two simplified car geometries, the Ahmed car and the Asmo car. 4 turbulence models are used, where the better performing ones were found to be the VMS and SIGMA models. Furthermore, flow structures are analyzed in detail and reveal major differences in the flow configuration around both cars, where one exhibits a high drag coefficient (Ahmed car) and the other a very low one (Asmo car). Chapter 6 studies the effect of the rotating wheels and moving ground on simplified car bodies, this case the Fabianic body and the Ahmed body with wheels and wheel-wells. An innovative approach for the rotating wheels was used, the immersed boundary method (IMB), however, it was found that, although large scale phenomena is well captured, the errors introduced by the IMB taint the results. The final chapter of the core of this thesis deals with LES and WMLES simulations on a generic realistic car model, using moving ground and rotating simplified wheels. Results show using that the WMLES approach in conjunction with an algebraic wall model improve the results with very little computational cost. Furthermore, flow structures and the unsteady phenomena present in the car are analyzed in detail.

The final chapter, (Chapter 8) presents some concluding remarks, whereas appendix 1 presents two real cases where aerodynamic analysis has been performed and appendix 2 a list of publications done during the length of the pHd studies.

Chapter 2

Three dimensionality in the wake of the flow around a circular cylinder

Main contents of this chapter have been published in:

Aljure, D. E., Lehmkuhl, O., Rodriguez, I. and Oliva, A. Three dimensionality in the wake of the flow around a circular cylinder at Reynolds number 5000. o *Comput. Fluids* 147.

Abstract
The turbulent flow around a circular cylinder has been investigated at $Re = 5000$ using direct numerical simulations. Low frequency behavior, vortex undulation, vortex splitting, vortex dislocations and three dimensional flow within the wake were found to happen at this flow regime.

In order to successfully capture the wake three dimensionality, different span-wise lengths were considered. It was found that a length $L_Z = 2\pi D$ was enough to capture this behavior, correctly predicting different aspects of the flow such as drag coefficient, Strouhal number and pressure and velocity distributions when compared to experimental values. Two instability mechanisms were found to coexist in the present case study: a global type instability originating in the shear layer, which shows a characteristic frequency, and a convective type instability that seems to be constantly present in the near wake. Characteristics of both types of instabilities are identified and discussed in detail. As suggested by Norberg, a resonance-type effect takes place in the vortex formation region, as the coexistence of both instability mechanisms result in distorted vortex tubes. However, vortex coherence is never lost within the wake.

2.1 Introduction

Aerodynamic research has been going on for over 100 years where bluff body flow has been a very active research area and the flow around a circular cylinder a benchmark problem. Flow over this geometry has been extensively studied and the understanding of the dynamics and structures present has grown extensively in the past few decades. Geometrical simplicity and an abundance of relevant three dimensional results make this an exceptional case study. Experimental observations on this geometrical configuration date back to the late XIX – early XX century with the work of famous physics like Strouhal, Von Kármán and Prandtl; and hundreds of research papers have been written concerning the study of the present configuration (see for instance Williamson [148] and citations therein).

The laminar to turbulent transition in the present case is limited by the particular geometry and flow conditions, i.e. transition is not induced by the body geometry itself but rather by the interactions of different unstable regions in the flow. Three different zones can be found: the boundary layer in the cylinder, two shear layers on top and bottom of the body and, finally, the wake. Extensive work carried out by different authors such as Bloor [6], Gerrard [28], Roshko [115, 116] have made possible the description of the different regimes encountered and the particular phenomena associated with them.

A number of experimental and numerical studies [96, 131, 132, 151, amongst others] have been focused on the phenomenon of three-dimensional wake transition which occurs at Reynolds numbers between $Re = 190 - 260$ [148]. This regime has been associated with discontinuities in the Strouhal number and base pressure coefficient as the Reynolds number increases. Furthermore, the appearance of vortex pairs, vortex adhesion [151], upstream facing vortex loops [69] and low-frequency irregularities [6] have also been reported. This geometry and the three dimensional behavior present was further studied by Williamson [146], who observed an additional phenomenon: vortex dislocations. This phenomenon is related to the break down of turbulence and is considered as a mechanism of wake transition, as the vortex shedding shifts from wake mode A to wake mode B. Natural vortex dislocations have been also reported in different wake-type flows such as mixing layers [10], the flow over a flat plate [82], the flow over a cone [92] and the flow over a stepped cylinder [70]. Vortex dislocations might be seen as defects in the two dimensional vortex tubes whose continuity is broken as a consequence of the frequency difference between two span-wise cells [146] or between cells of similar frequency which are out-of-phase with each other [10]. Braza et al. [9] studied the natural vortex dislocation phenomenon that occurs in the three dimensional wake transition at $Re = 220$. They showed the existence of naturally occurring dislocations in the near wake, and the similarity of these structures to those obtained by Williamson [146] using a ring on the cylinder to force their appearance. Additionally, they analyzed the physical processes related to the introduction of stream and cross-stream-wise vorticity components and their impact on the span-wise variations of the Von Kármán vortex filaments and described the steps that lead to vortex dislocations.

At higher Reynolds numbers, vortex irregularities have been suggested to be related with fundamental changes in the three-dimensionality of the wake past a cylinder. Several authors have observed transitional behavior around $Re \approx 5000$. This behavior is evidenced by different changes in wake configuration. An increase in the fluctuations of drag and lift forces and a loss of coherence in the vortex shedding (observed as a wider bandwidth in the spectrum at the vortex shedding frequency) have been reported. Furthermore, several authors point to changes in the base pressure profile and the vortex formation length, as well as, variation in length and behavior of the shear layers.

Son and Hanratty [125] studied the velocity gradients around the cylinder observing an increase in the separation angle with Reynolds number. Additionally they found that a small zone of positive velocity gradient, which they named zone B, appeared after the separation point and could be explained by the existence of a small separation bubble that decreased in size with Reynolds number. Finally, observations for the region following region B, region C (back of the cylinder), showed that for $Re = 5000$ and $Re = 10000$ the gradient in this zone remains small with a slight increase towards the cylinder centerline, larger for $Re = 10000$. For Reynolds numbers $Re \geq 20000$ the trend in the profile seemed to change with a much larger increasing rate as it approaches the cylinder center. The authors stated that results in this section are open to question due to the small magnitude of this quantity and that it may be changing direction. Kourta et al. [55] observed, through hot-wire measurements and flow visualizations, two different types of interaction between the vortex shedding and the small scale structures in the transition process in the cylinder wake. For a lower Reynolds range, that they defined as $2000 < Re < 16000$, they found a strong interaction due to similar frequencies in both phenomena. For the larger Reynolds numbers, $16000 < Re < 60000$, the two phenomena are disconnected and the small vortices act as an eddy viscosity. Unal and Rockwell [138] found that the formation length decreased for Reynolds numbers $Re > 1900$, indicating an increase in the base pressure coefficient. Additionally for the higher Reynolds numbers they studied, $Re = 3400$ and $Re = 5040$, a distortion in the velocity fluctuation distribution with respect to the kinetic energy appeared, larger for $Re = 5040$. Finally, they performed an eigenfunction analysis on the velocity distribution along the shear layer and compared it with theoretical distributions finding that the data for Reynolds numbers between $1900 < Re < 3400$ follows the theory, however large deviations were observed for $Re = 5040$. Lin et al. [72] performed experimental observations on this geometry, observing for the Reynolds numbers $Re = 1000$ and $Re = 5000$ low levels of vorticity and low speed in the base region. They argued that the vortex formation is decoupled from the near-base region of the cylinder and this implied a predominant role of convective-type instabilities leading to large vortex formation. The authors wondered whether there is a shift in the vortex formation regime causing a change from the convective to a global instability mechanism for higher Re numbers and if this change in vortex formation mechanism is responsible for the large changes in the base pressure coefficient observed in the Reynolds number range $1000 < Re < 10000$.

Norberg, in several works [86, 87, 89, 90], showed the appearance of a transition in wake behavior for the flow at $Re \approx 5000$ including undulating vortex filaments and "vortex splitting". He suggested that these structures might be related to what he observed as a shift from high to low quality vortex shedding. Finally, Norberg suggested that for $Re < 5000$ transition to turbulence is triggered by vortices in the wake, whereas after that Re number turbulence is triggered by a Kelvin-Helmholtz (KH) instability within the shear layer. At the critical value ($Re = 5000$) the two mechanisms coincide causing a resonance like behavior. Prasad and Williamson [106] investigated the changes in the three-dimensional near-wake structures over the time for $190 < Re < 10000$ and the influence of the end conditions on the flow structure. The authors paid special attention to the wake transition regime and its relation with the flow parameters, including the vortex shedding frequency. They devoted especial attention to the flow around $Re \approx 5000$ where they stated the wake might be experiencing a fundamental change. They observed different phenomena such as a discontinuity in the value of the Strouhal number, a twin-peak spectrum near the vortex shedding frequency and vortex dislocations along the cylinder axis. The authors question whether these observations were introduced by the end plates used in their experiments, the finite length of the cylinder or if they were a real feature of the flow. Rajagopalan and Antonia [107] also studied the flow over a large range of Reynolds numbers in the sub critical range and focused on the shear layer instabilities. They found that the relation of the ratio between shear layer frequency and vortex shedding frequency with the Reynolds number changed around $Re = 5000$. This change supports the previous observations of a change in the flow organization at this Re number. Supporting the hypothesis proposed by Lin et al. [72], Rajagopalan and Antonia [107] suggested that a convective instability mechanism governs the flow for $Re > 5000$ rather than a global instability mechanism.

It is important to note that some scattering of results has been observed in this Reynolds number range, probably due to different experimental configurations (span-wise length, blocking ratio, time integration period, inflow conditions). However, the work done so far evidences the presence of a transition in wake behavior for the flow around $Re \approx 5000$. The present work aims to investigate this configuration using direct numerical simulations (DNS) in order to confirm the presence of the three dimensional behavior observed at $Re = 5000$ and to try to deepen the knowledge into the transitional behavior observed. Additionally, a detailed study into the instability mechanisms present in the flow is carried out. To the authors' knowledge no DNS studies have been performed at this Reynolds number.

2.2 Mathematical and numerical model

2.2.1 Governing equations and numerical method

In order to study the flow, the incompressible Navier-Stokes equations are solved:

$$\frac{\partial u_i}{\partial x_i} = 0 \tag{2.1}$$

$$\frac{\partial u_i}{\partial t} + \frac{\partial (u_i u_j)}{\partial x_j} - \nu \frac{\partial^2 u_i}{\partial x_j \partial x_j} + \rho^{-1} \frac{\partial p}{\partial x_i} = 0 \tag{2.2}$$

where u_i is the three-dimensional velocity field (u_1, u_2, and u_3 are also referred to as U, V and W), p is the pressure field, ν stands for the kinematic viscosity and ρ for the density of the fluid.

A collocated unstructured mesh is built and the spatial discretization is carried out by means of finite volume techniques. A second-order conservative scheme [141] for the continuous differential operators, an explicit second order self-adaptive scheme for the temporal discretization, a backward Euler scheme for the pressure gradient and a fractional step algorithm for the velocity-pressure coupling are used. A more in depth presentation of the numerical schemes used can be found in Aljure et al. [3], Jofre et al. [45], Trias et al. [135]. As the meshes are constructed using a constant-step extrusion in the span wise direction of a 2D unstructured grid, the Poisson equation can be solved by means of a direct Schur-Fourier decomposition solver [7].

All simulations are run with the TermoFluids high performance parallel unstructured code (www.termofluids.com) and are carried out on the in-house JFF cluster and on the Mare-nostrum III supercomputer, details on the computing characteristics are found in Aljure et al. [3]. METIS library [50] is used for domain partitioning and parallel communications are implemented following a pure distributed model by means of the Message Passing Interface (MPI) standard. Meshes reported in this work are partitioned from 160 to 512 CPUs, as meshes grow (see Table 2.1). The wall-clock time spent on each simulation is directly proportional to the number required of time-steps and their cost. For case M5, with a mesh of about 37×10^6 elements, the required iteration time is approximately 0.19 s on the Marenostrum supercomputer. For the whole simulation about 3.16×10^6 outer iterations are performed, which results in a simulation time of approximately 8.54×10^4 CPU hour. The code and numerical approach used in the present simulations have been proved to yield accurate solutions in flows with massive separations [3, 66, 67, 113, 114].

2.2.2 Definition of the case and boundary conditions

The geometry to be considered is a cylinder with diameter D shown in Fig. 2.1 submerged in an uniform fluid flow. Simulations are carried out at a Reynolds number $Re = U_{ref}D/\nu = 5000$ based on the cylinder diameter D and the free-stream velocity U_{ref}.

As this paper focuses on the three-dimensional effects that might appear in the near wake, three different span-wise sizes are considered: $Lz = n\pi D$, being $n = 1$, 2 and 3. Thus, the computational domain is $30D \times 20D \times Lz$ in the stream-, cross-stream and span-wise directions. The center of the cylinder is located at a distance of $10D$ downwind from the inlet boundary and at a distance of $20D$ from the outlet boundary (see Fig. 2.1).

A constant inlet velocity profile $u_i = (U_{ref}, 0, 0)$ is imposed. A pressure based condition is imposed for the outflow such that the mass conservation is fulfilled at each time step. In addition, in order to avoid any influence from non-physical waves reflected by the artificial outflow boundary, a buffer zone at $x > 14D$ is used [140]. Top and bottom surfaces are modeled as slip boundaries, periodic boundary conditions are set for the span-wise direction ones and the cylinder surface is modeled as a no-slip wall.

2.2.3 Computational domain and spatial discretization

In order to correctly solve all the phenomena present in the boundary layer a fine near wall mesh is necessary. Similarly, a fine mesh is also required for the full solution of the shear layers. Furthermore, the near wake zone must be refined to correctly predict the flow structures, i.e vortex

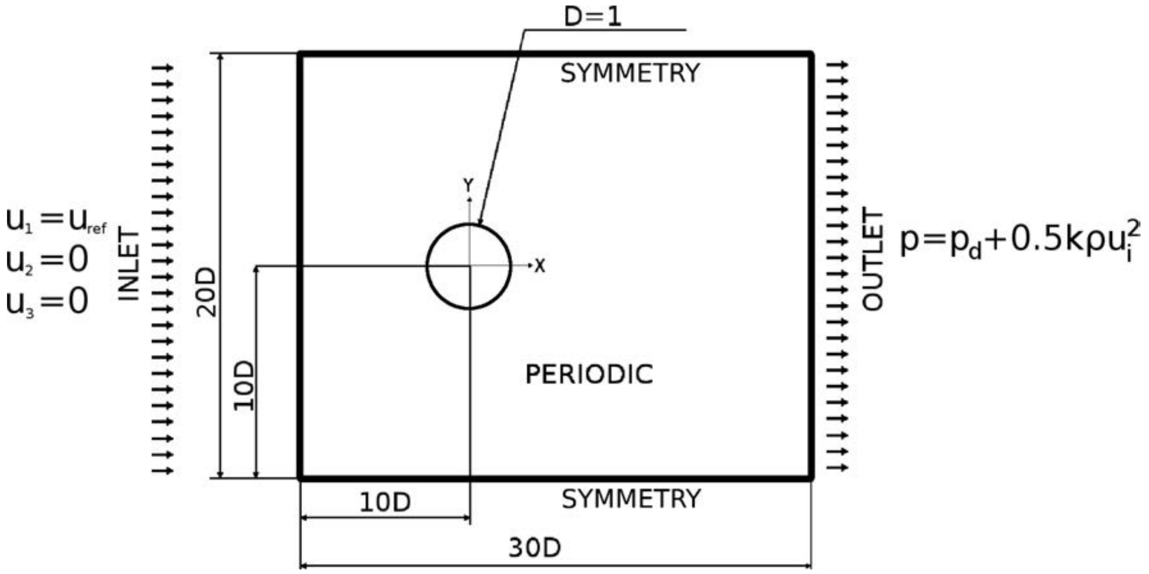

Figure 2.1: Geometry and computational domain.

Table 2.1: Mesh parameters. CV_{plane} is the number of control volumes in the plane, N_{planes} is the number of planes in the span-wise direction, L_Z the length of the span-wise directions, NCV the total number of control volumes in the domain.

	CV_{plane}	N_{planes}	Δz	L_Z	NCV
M1		128		πD	1.13×10^7
M2	88519	256	$0.0245D$	$2\pi D$	2.27×10^7
M3		384		$3\pi D$	3.40×10^7
M4	115709	160	$0.0196D$	πD	1.86×10^7
M5		320		$2\pi D$	3.70×10^7

shedding, Von-Kármán vortex street and three dimensionality. As the flow moves away from the cylinder the relative importance of flow structures in the force coefficients and velocity profiles diminish and so does the mesh resolution.

Details about the different meshes used are given in Table 2.1. The meshes used contain about 11, 23 and 34 million control volumes (CV) for πD, $2\pi D$ and $3\pi D$ span-wise lengths respectively for the 88519 plane mesh. For the 115709 plane mesh, they contain about 18.6 and 37 million CV for πD and $2\pi D$ span-wise lengths, respectively.

2.2.4 Time integration study

Simulations are started from homogeneous flow and are advanced in time, about 500 time units ($TU = tU_{ref}/D$), until the initial transient behavior is washed out. Afterwards, statistics have been collected and averaged by integrating the instantaneous data over a sufficiently long-time period: about 3500 TU, over 700 shedding cycles. This time integration span results in a long simulation time and should ensure converged statistics and a large time span to analyze the three dimensional phenomena present. First and second order statistics are averaged in time and space (in the span wise direction). Flow magnitudes are also studied by means of probes in several locations (see Fig. 2.2).

Fig. 2.3 shows the time history averaging for the first and second order statistics registered at different locations in the wake for mesh M5. Point 1 (P1) is located at the cylinder centerline, whereas Point 2 (P2) is located well within the shear layer (see Fig. 2.2). It can be seen in the figure that these quantities stabilize around $TU = 2000$ after being integrated for 1500 TU. A longer time integration span was chosen to fully guarantee well converged statistics along the whole domain.

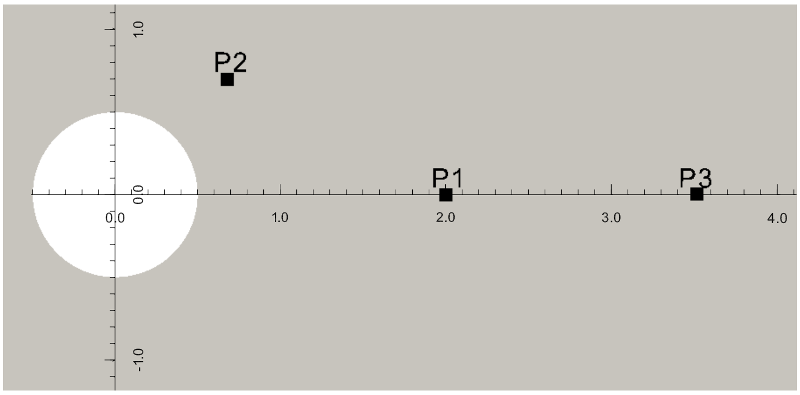

Figure 2.2: Location of the computational probes, P1 [$x/D = 2$ $y/D = 0$], P2 [$x/D = 0.75$ $y/D = 0.65$] and P3 [$x/D = 3.5$ $y/D = 0$].

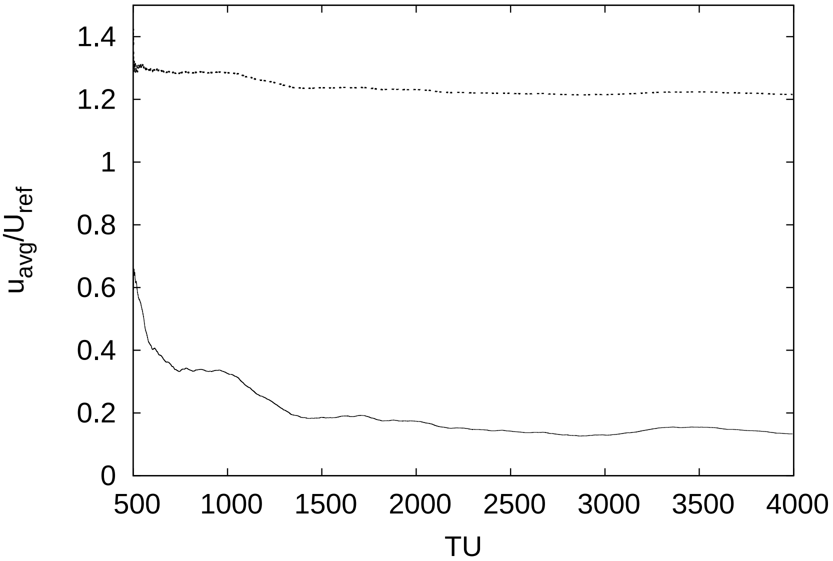

(a)

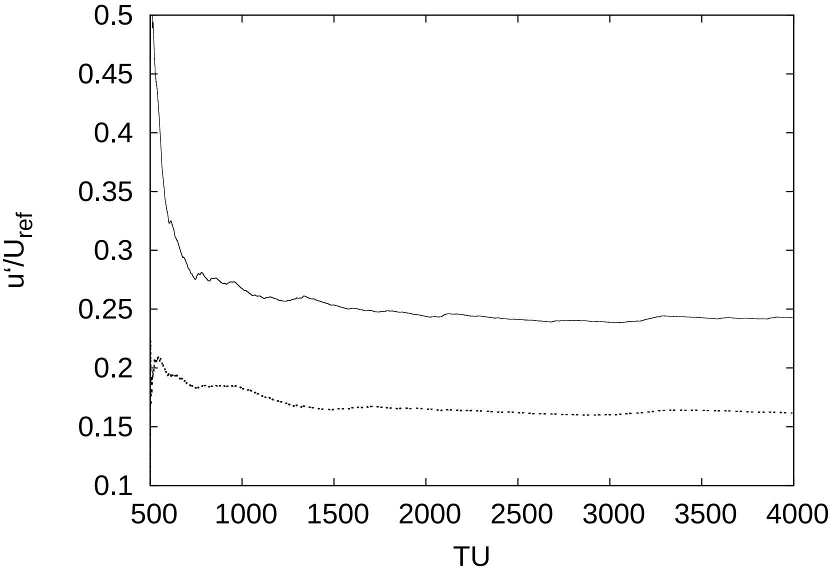

(b)

Figure 2.3: (a): Time evolution of the averaged stream-wise velocity. (b): Time evolution of the stream-wise velocity fluctuations. Solid line: P1 [2D,0], Dashed line: P2: [0.75D,0.65D].

2.2.5 Mesh sensitivity study

Although many meshes were used for computations, for the sake of brevity, results in this section are only presented for the meshes summarized in section 2.2.3. In order to ensure that the smallest scales of the flow have been solved, a-posteriori analysis has been done by evaluating the ratio between the mesh size and the Kolmogorov scales. The latter are calculated using $\eta = (\nu^3/\epsilon)^{1/4}$, where ν corresponds to kinematic viscosity and $\epsilon = \nu S_{ij} S_{ij}$ the energy dissipation rate. Present simulations reach, for the finer meshes, a mesh ratio (h/η, being $h = \sqrt[3]{Vol_{cell}}$) under 3. The highest values found ($h/\eta > 3$) correspond to the shear and boundary layers, which are laminar and the Kolmogorov hypotheses do not apply. This parameter is especially important in the near wake area, that is $0.5 < x/D < 3$ and $-1 < y/D < 1$. Mesh M5 has, in this area, a volume-

Table 2.2: Statistical flow parameters for the different meshes. Comparison with literature available results. Drag coefficient (C_D), Strouhal number (St), base pressure coefficient ($C_{p_{base}}$), fluctuating lift coefficient ($C_{L'}$), separation angle (ϕ_s) and recirculation length (L_{rec}/D). ^{a}: [87], ^{b}: [88], ^{c}: [90], ^{d}: [89].

Case	C_D	St	-$C_{p_{base}}$	$C_{L'}$	ϕ_s[°]	L_{rec}/D
mesh M1	1.12	0.210	1.020	0.248	87.4	1.144
mesh M2	1.09	0.209	0.970	0.199	87.0	1.272
mesh M3	1.10	0.210	0.985	0.212	87.1	1.237
mesh M4	1.06	0.210	0.945	0.173	86.7	1.365
mesh M5	1.05	0.210	0.957	0.156	86.9	1.357
Norberg ($Re = 5000$ - EXP)	1.02^a	0.209^a	0.932^b	0.146^c	-	1.40^d
Son and Hanratty [125] ($Re = 5000$ - EXP)	-	-	-	-	86	-
Lin et al. [72] ($Re = 5000$ - EXP)	-	-	0.84	-	-	-
Unal and Rockwell [137] ($Re = 5040$ - EXP)	-	-	0.84	-	-	-
Kourta et al. [55]($Re = 4800$ -EXP)	-	-	-	-	-	1.6
Jordan and Ragab [46] ($Re = 5600$ - LES)	1.01	0.206	1.02	-	87	-
Dong et al. [22] ($Re = 4000$ - EXP)	-	-	-	-	-	1.47
Lam et al. [59] ($Re = 6000$ - EXP)	0.96	-	-	-	-	1.62
Lehmkuhl et al. [67] ($Re = 3900$ - DNS)	1.015	0.215	0.935	-	88	1.36
Ma et al. [75] ($Re = 3900$ - DNS Case I)	0.96	0.203	0.96	-	-	1.12

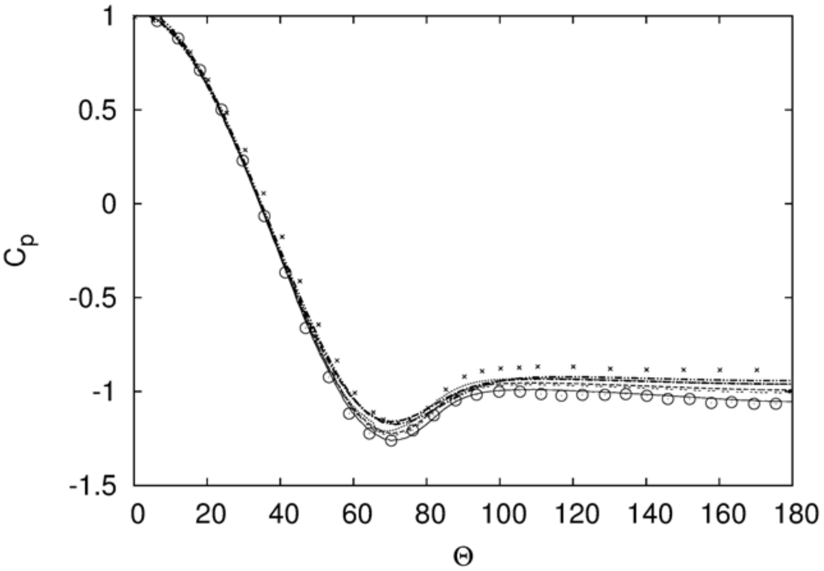

Figure 2.4: Mean pressure distribution around the circular cylinder for the different meshes. Solid line mesh M1, dashed line mesh M2, dash-dash line mesh M3, dotted line mesh M4, dash-dot line mesh M5, dash-dot-dot Lehmkuhl et al. [67] ($Re = 3900$), crosses Norberg [89] ($Re = 3000$), circles Norberg [89] ($Re = 8000$).

averaged ratio of resolved scales to Kolmogorov scales of $h/\eta = 1.1$. A second aspect to assess the meshes is the viscous boundary layer near the solid walls and its requirements to be well solved. In the case under study, the boundary layer is laminar, as transition to turbulence in the attached boundary layers occurs beyond $Re = 2\times10^5$ [116]. This fact allows the boundary layer thickness to be readily be estimated. The meshes used in this work are constructed so as to guarantee that at least 3 control volumes are located well within the boundary layer. Finally, the shear layers require a full resolution by having enough grid points within. Saad et al. [118] performed experiments to evaluate the behavior of the shear layer and the near wake of the circular cylinders. Their measurements in the unforced cylinder gave the approximate size of the shear layer for $Re = 5000$, $1.7478/D$ long and $0.2134/D$ wide. Considering this, over 5000 mesh points (for each plane) are located within this area to ensure its complete resolution.

In order to check the mesh discretization and grid parameters used in the present computations, results are compared to literature available results. In this sense, time-averaged flow parameters are summarized in Table 2.2. Studied magnitudes include the mean drag coefficient (C_D), the non-dimensional vortex shedding frequency (Strouhal number $St = f_{vs}D/U_{ref}$), base pressure coefficient ($-C_{p_{base}}$), fluctuating lift coefficient ($C_{L'}$), separation angle (ϕ_s) and recirculation length (L_{rec}/D). For comparison sake, values for these parameters are presented from diverse published works (experimental and numerical) for the Reynolds number range $3900 \leq Re \leq 6000$. In general, computed parameters are in quite good agreement with published works, falling within the expected scattering reported at this Reynolds number. In particular present DNS results show minimal differences with the long-term solution by Lehmkuhl et al. [67].

Fig. 2.4 shows the mean pressure distribution around the cylinder. Results are compared to those measured by Norberg [87] for $Re = 3000$ and $Re = 8000$ and the long term averaged solution DNS results by Lehmkuhl et al. [67] for $Re = 3900$. All results converge to the same curve for the laminar region of the boundary layer up to approximately 60°. After this position, solutions show small differences. Solution for mesh M5 and the long-term averaged solution for $Re = 3900$, again, show a similar behavior, however, pressure values are slightly lower for $Re = 5000$.

In Fig. 2.5, the stream wise velocity and its fluctuations in the wake centerline are plotted against results from the literature by Norberg [89] ($Re = 5000$), Lam et al. [59] ($Re = 6000$) and Prasad and Williamson [106] ($Re = 5427$). Results compare rather well, although main differ-

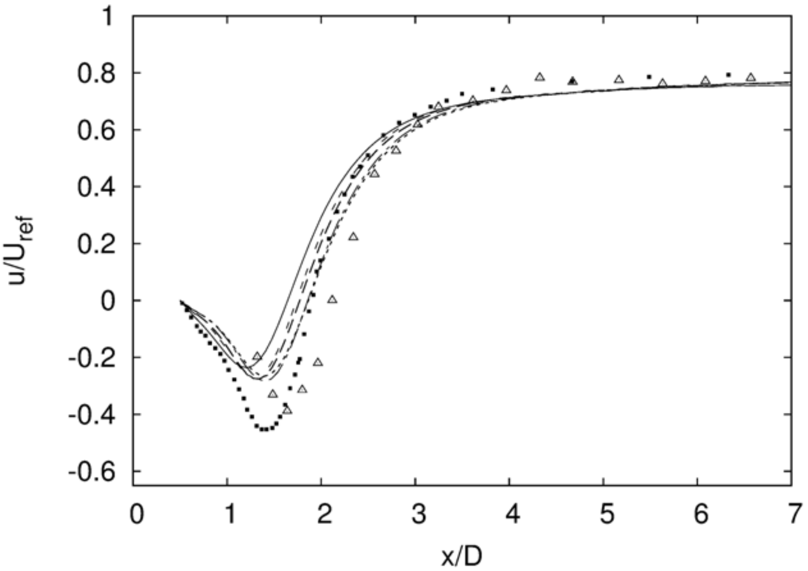

(a)

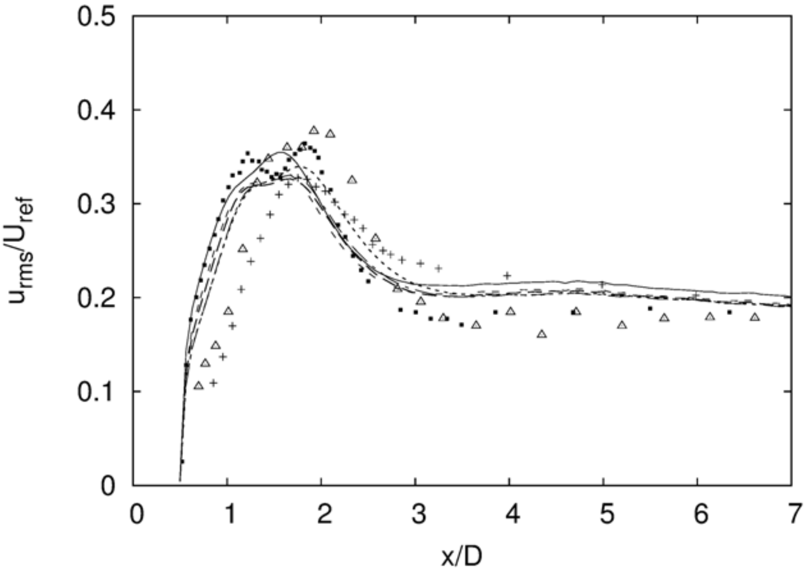

(b)

Figure 2.5: Mean (a) stream-wise and (b) RMS stream-wise velocities in the wake center line. Solid line mesh M1, dashed line mesh M2, dash-dash line mesh M3, dotted line mesh M4, dash-dot line mesh M5, squares Norberg [89] ($Re = 5000$), triangles Lam et al. [59] ($Re = 6000$), crosses Prasad and Williamson [106] ($Re = 5427$).

ences are present in the magnitude of the minimum velocity in the wake. As commented before, fundamental changes in the wake around this Reynolds number have been reported, affecting the wake topology and, thus, some scattering is expected. This is more evident in the stream wise velocity fluctuations, where different profiles around the maximum peak are observed. Norberg's averaged profiles resemble the low-energy mode (mode L) observed at $Re = 3900$ [67] with a two-lobed stream-wise velocity fluctuation profile and a lower stream-wise velocity minimum. Solutions obtained with all meshes showed a similar profile to that obtained for the long term solution at $Re = 3900$ by Lehmkuhl et al. [67]. In fact, the stream-wise fluctuation profile follows the same trend to that obtained by Prasad and Williamson [106] for $Re = 5427$. More results are presented in Aljure et al. [3].

Fig. 2.6 shows the energy spectrum of the cross-stream wise velocity fluctuations, and for comparison the $-5/3$ Kolmogorov law is also represented. Also, readily visible on Fig. 2.6a and Fig. 2.6b is the energy peak corresponding to the vortex shedding frequency, $St_{vs} = 0.21$, in agreement with literature reported results (see Table 2.2). In addition to the energy peak corresponding to the non-dimensional vortex shedding frequency, the KH shear layer instabilities non-dimensional frequency St_{KH} can also be seen on Fig. 2.6b as a broad-band peak around $St_{KH} = 1.65$. This broad-band peak energy peak is the result of an unstable shear layer that unevenly transports energy to the near wake. Flow in this geometry and with $Re = 5000$ shows a

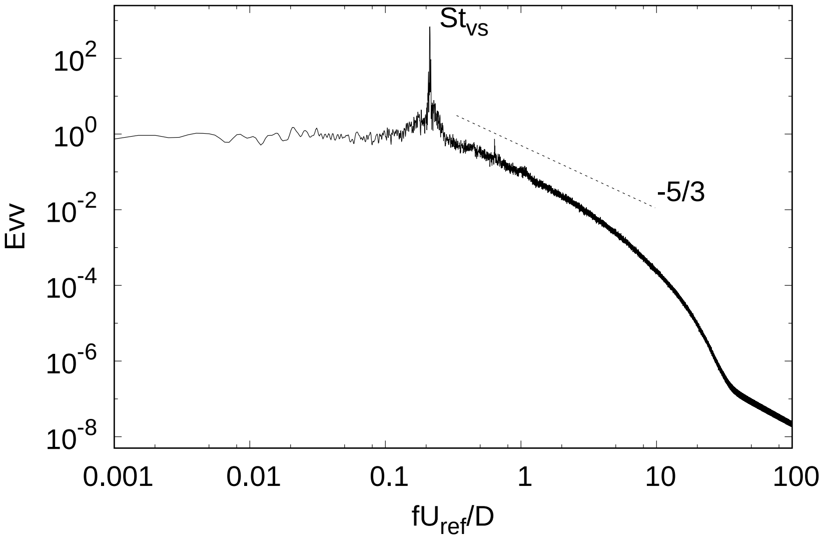

(a)

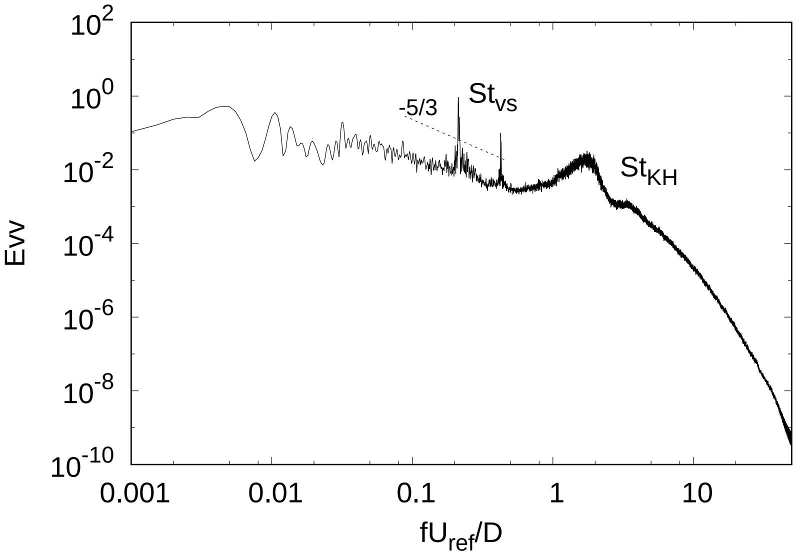

(b)

Figure 2.6: Span wise averaged energy spectra of the cross-stream wise velocity fluctuations at two locations (a) P1 (b) P2.

Table 2.3: Relation between shear layer frequency St_{KH} and vortex shedding frequency St_{vs}.

Author	St_{KH}/St_{vs}
Bloor [6]	7.95
Unal and Rockwell [137]	8.0
Chyu et al. [15]	6.7
Prasad and Williamson [105]	7.1
Present	7.86

rather large vortex shedding peak evidencing a very energetic vortex shedding phenomenon. This large peak indicates a strong coherence in the flow and affects the rest of the spectrum showing harmonic peaks at higher wave numbers ($St \approx 0.42$ and $St \approx 0.63$). A harmonic peak is also present for the shear layer frequency around around $St = 3.5$, although not as notorious as with the vortex shedding frequency. The frequency of these instabilities, which are closely related to the formation of vortices, has been measured experimentally by different researchers and its value expressed as a ratio of the vortex shedding frequency (St_{KH}/St_{vs}). Table 2.3 shows the present results compared to different results from the literature. The value of f_{KH}/f_{vs} found in the present work is within the range of these studies, where the ratio between these two frequencies varies from 6 to 8 for $Re \approx 5000$.

2.3 Results

2.3.1 Wake three-dimensionality

Proper identification of the vortical structures are a means for understanding the flow dynamics. In this work coherent structures are identified and analyzed by means of non-dimensional pressure iso contours $p^* = p/(0.5\rho U_{ref}^2)$, non-dimensional vorticity $\omega^* = \omega D/U_{ref}$ and non-dimensional Q-criterion $Q^* = QD^2/U_{ref}^2$ [40]. Fig. 2.7 shows, using the Q-criterion, the coherent structures using $2\pi D$ and $3\pi D$ span-wise lengths. It is important to point out that three dimensional behavior is seen in both domain lengths, having curved vortex cores and inclined vortex ribs. As the flow moves downstream, the span wise irregularities remain: vortex tubes show distortion and the span wise velocity component cause their shape to shift constantly. However, the span wise coherence of the vortex street is not lost.

As three dimensional behavior is observed in the wake, two point correlations are calculated to evaluate the span wise lengths simulated. Fig. 2.8 shows this parameter for the different velocity components at the location P1, also evidencing the footprint of span wise structures present in the near wake. Figs. 2.8a and 2.8c show that a span-wise length of $2\pi D$ captures correctly the three dimensional phenomena for the respective velocity components. Fig. 2.8b, which depicts the correlation for the cross-stream velocity, shows that the $3\pi D$ span-wise length is enough to correctly solve and capture the large scale span-wise behavior. The $2\pi D$ span-wise length captures this behavior, however it is cut short from returning to the zero value. As seen in Fig. 2.7, mesh M5 is able to capture the phenomena present, even though the span-wise length is $2\pi D$. Finally, it is important to point out that increasing the span-wise length from $2\pi D$ to $3\pi D$ carries with it a considerable increase in computational effort.

Evidence of the three-dimensionality present in this configuration was presented by Norberg [87] for the flow at $Re = 5500$, and is shown in Fig. 2.9b. In the figure, a span-wise view of the flow obtained is presented (Fig. 2.9a) and compared to the flow visualizations made by Norberg [87]. The figure shows the undulating vortex filaments mentioned by Norberg [86, 87] and Prasad and Williamson [106]. Also seen in Fig. 2.9 is the vortex-splitting phenomenon, similar to a “Y” like shape in the near wake and marked in Fig. 2.9 for clarity. It is important to note the large length scale of the span-wise structures. A detailed study into three dimensional behavior in the wake is carried out in this section.

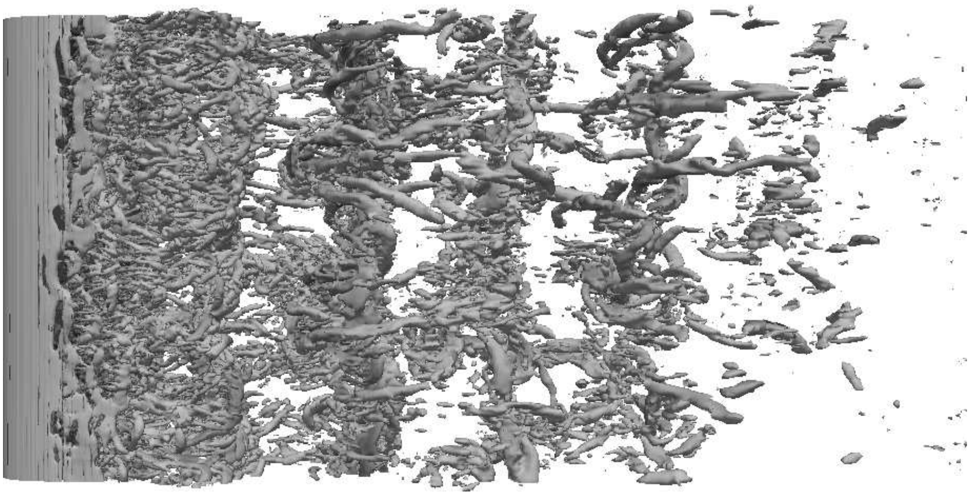

(a)

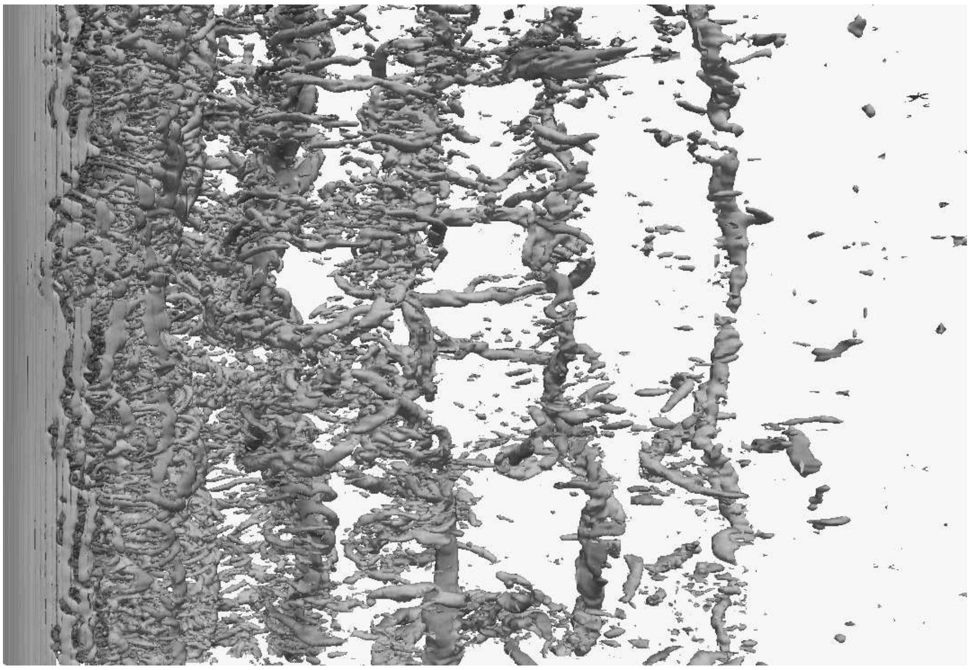

(b)

Figure 2.7: Coherent structures represented by means of Q iso contours $Q^* = 3$. (a)$2\pi D$ span-wise length, (b) $3\pi D$ span-wise length.

To obtain an overall view of the vortex formation and the irregularities present Fig. 2.9 shows, using p^*, Q^* and ω^* iso surfaces, the events leading to the detachment of vortex tubes. At $1/8T$, the top shear layer is starting to roll up creating a vortex core, named here Vt1. Additionally, marked in the image for clarity, flow structures from the bottom shear layer are seen to interact with the Vt1 vortex forming on top. As explained by Gerrard [28], entrainment flow is absorbed partially by the top shear layer and by the growing vortex, influencing the vortex formation. Entrainment flow towards the growing vortex does not vary significantly with Reynolds number, however, entrainment flow towards the opposing shear layer increases with increasing Reynolds number [28]. At the present flow regime, entrainment flow seems to affect the shear layer generating unstable behavior.

At $1/4T$, the vortex Vt1 continues forming, however, irregularities that appear during the shear layer roll up create stream and cross-stream-wise structures that interact with the vortex

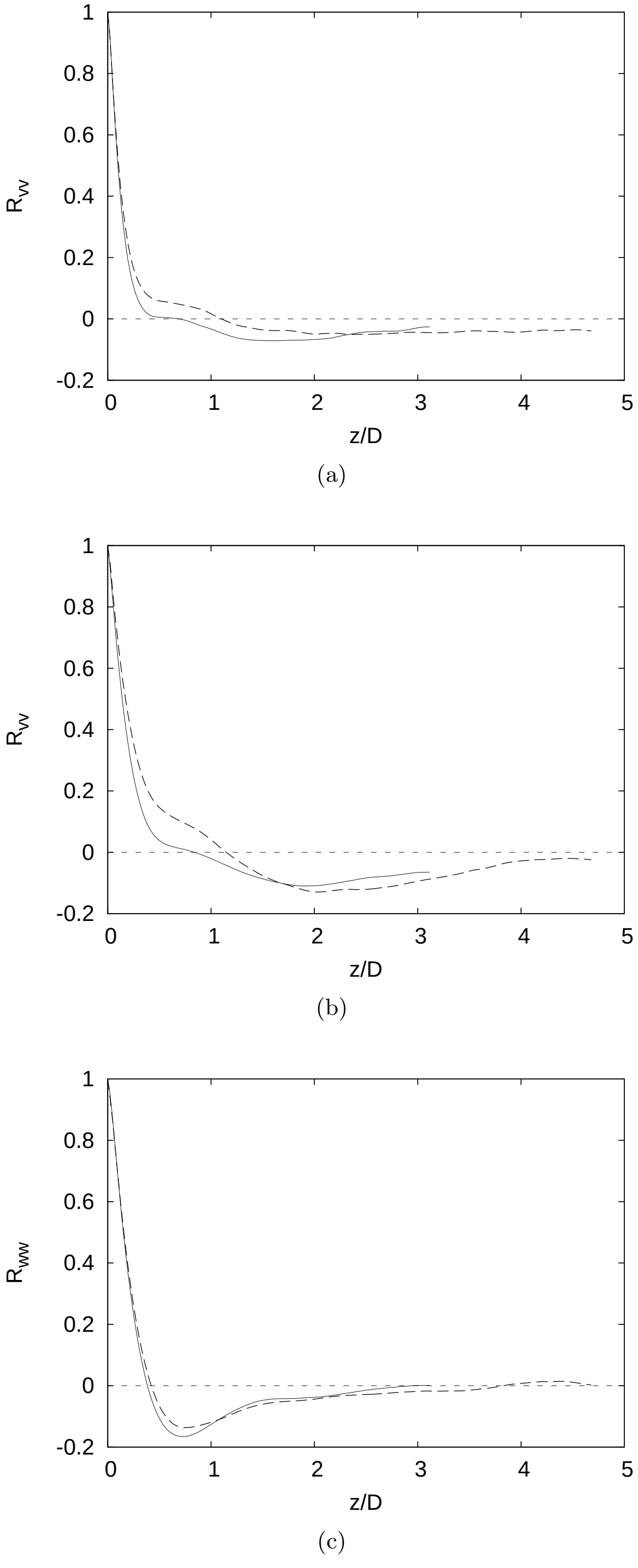

Figure 2.8: Two point correlations in the span-wise direction for the velocity components. (a)Stream wise. (b) Cross-stream-wise. (c) Span wise. Solid line: $2\pi D$ span-wise length, Dashed line: $3\pi D$ span-wise length.

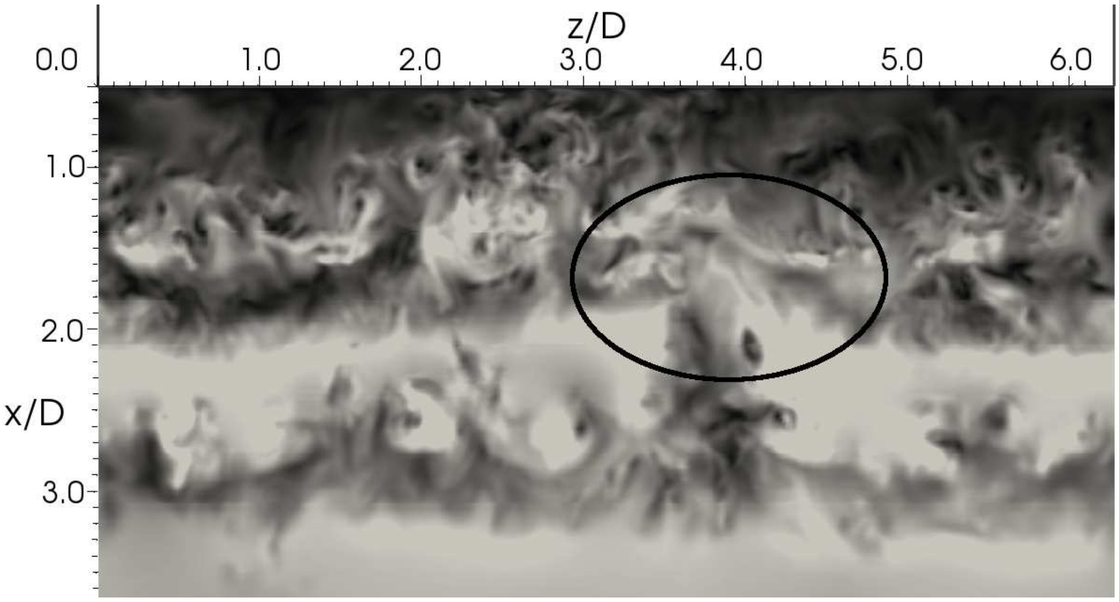

(a) Present work Mesh M5

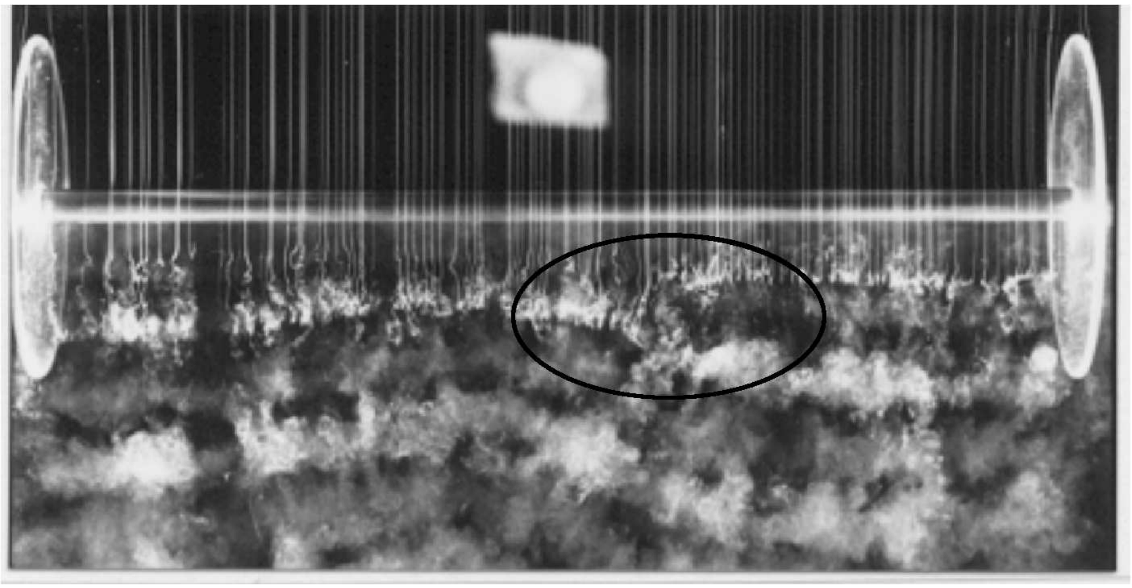

(b) Norberg [87] Re=5500

Figure 2.9: Vortex dislocations, span-wise view. (a) Velocity field at the wake centerline plane. (b) Span wise flow visualization by Norberg at Re=5500 [87].

core. These interactions modify their shape and the way they detach from the cylinder. Marked in the image are three locations that have been affected by these interactions.

At $3/8T$, the uneven shear layer roll up ends up breaking the continuity in the structure of the vortex core. As the main vortex core starts to move downstream the locations marked in the image (same locations as in $1/4T$) fall behind and remain attached to the vortex formation region.

At $1/2T$, vortex Vt1 starts to detach from the formation region. As it does, it remains broken and the stream-wise structures interacting with it continue to deform the vortex core, see Fig. 2.9d. At this stage, parts of the vortex tube have already detached from the formation region, whereas some parts fall behind and remain attached.

At $5/8T$, the detaching process is finished for all the span of the tube. As a result of the delayed locations identified in previous frames, several vortex distortions are visible and marked

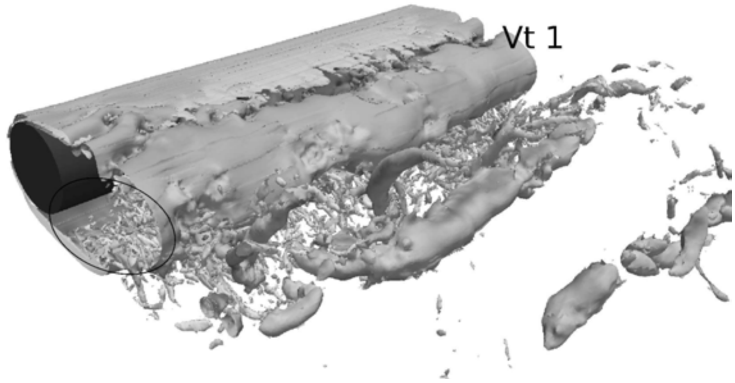

(a) 1/8T

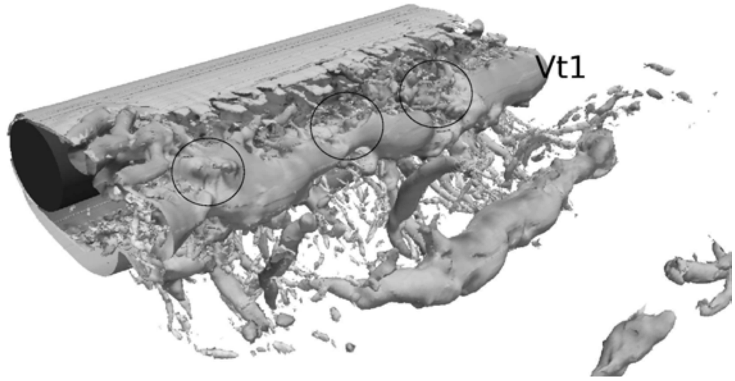

(b) 1/4T

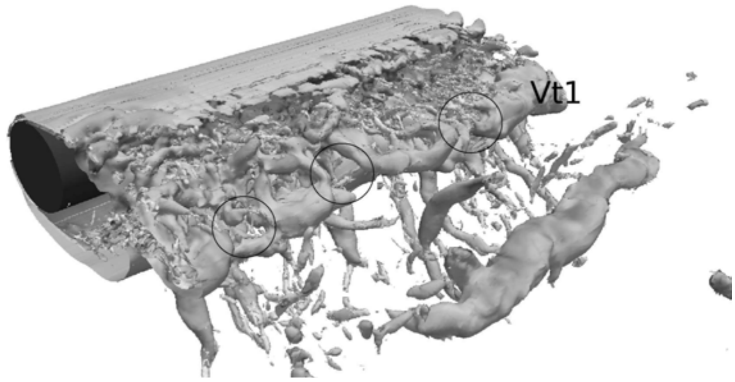

(c) 3/8T

Caption on page 44.

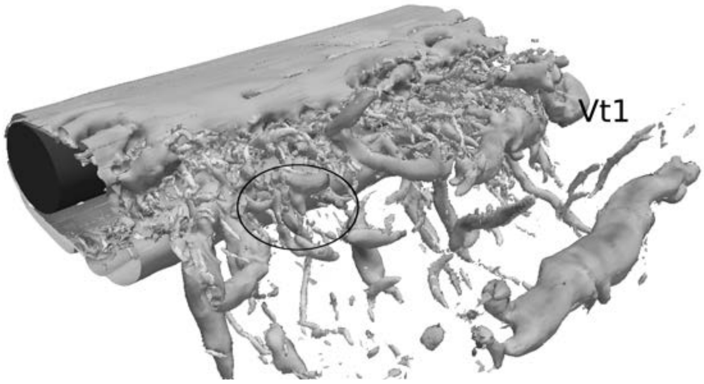

(d) $1/2T$

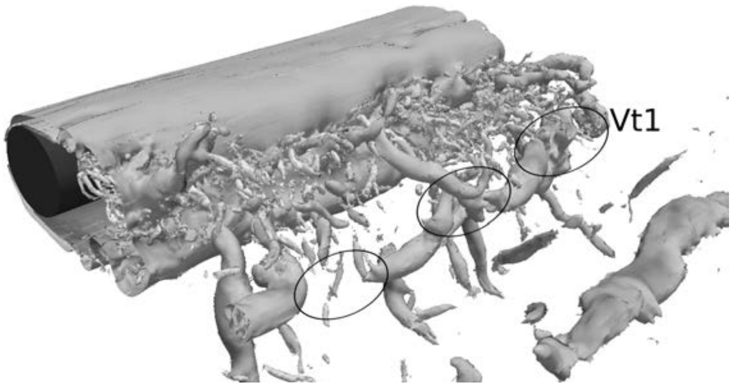

(e) $5/8T$

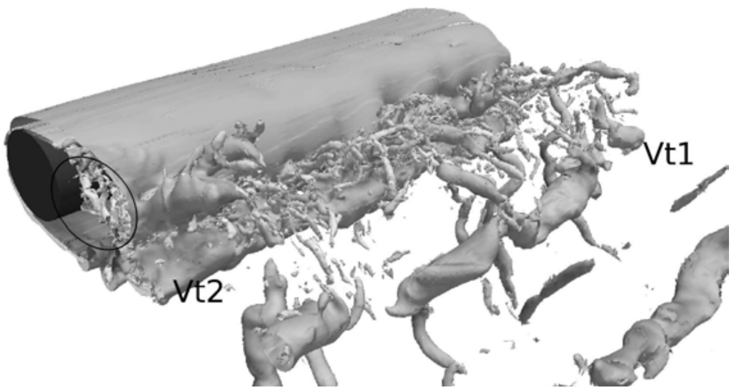

(f) $3/4T$

Figure 2.9: Cont: Vortex detachment time evolution. $p^* = -0.4$ $\omega_z \pm 15$ and $Q^* = 50$ iso surfaces.

in Fig. 2.9e. Finally, at $3/4T$, a second vortex tube (Vt2) starts to detach from the lower part of the cylinder. Entrainment flow is again visible leaving the top shear layer and entering the bottom shear layer and the vortex forming, so that the process is repeated. Additionally, vortex Vt1 is seen as it travels downstream taking part in the span wise coherent vortex street.

Direct effects of the three dimensional behavior can be seen on the vortex cores as they travel downstream. Fig. 2.10 shows the non-dimensional pressure p^* iso surfaces in the wake of the cylinder and the cross-stream velocity in the mid plane. The vortex cores are visible from the top of the cylinder (x-z plane) and show a higher grade of three dimensional behavior not seen in flows with lower Re [67]. Flow at the present regime show span-wise distortions of the vortex tubes after they detach from the formation region due to the irregularities present within the shear layers. These irregular vortex tubes are then shed, and as they travel downstream their geometry continues to shift due to three dimensional phenomena present. It is interesting to note the appearance of a local break in the vortex tubes, similar to what has been described as vortex dislocations [9].

Vortex dislocations can be seen as a local break of the vortex tubes and have been considered

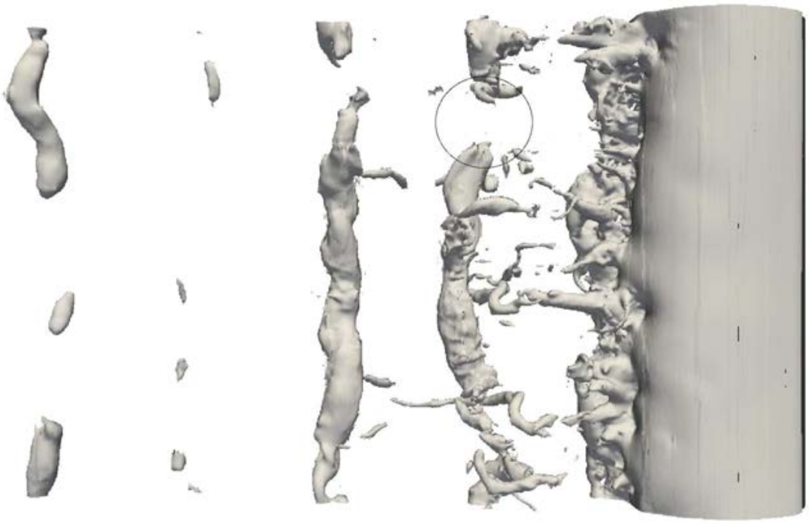

(a)

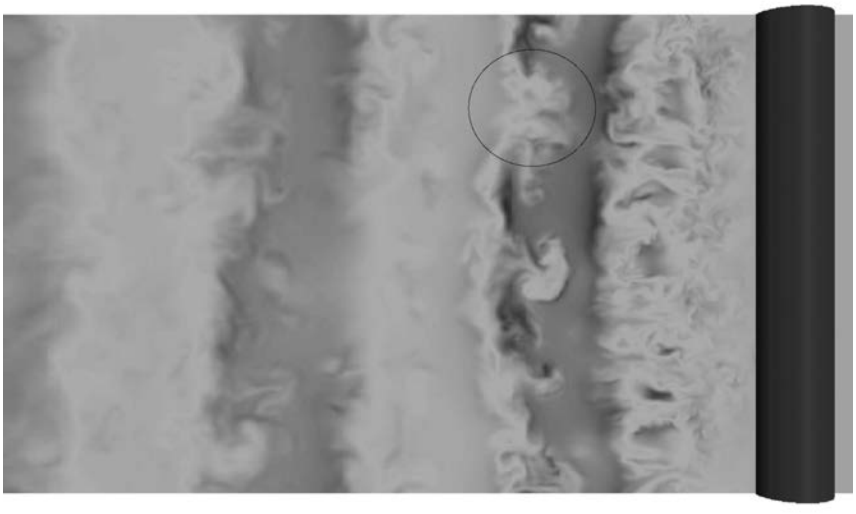

(b)

Figure 2.10: (a) $p^* = -0.7$ iso surface and (b) Cross stream velocity in the mid plane showing the loss of coherence in a vortex tube.

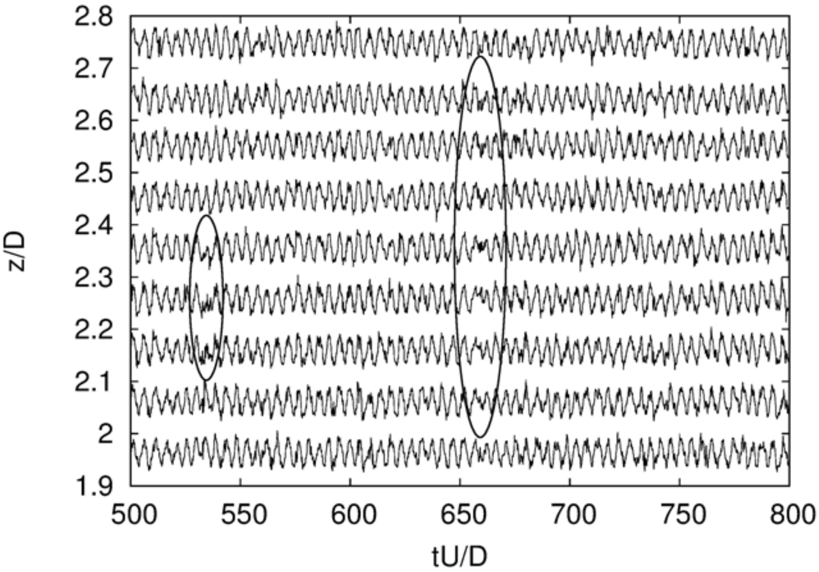

(a)

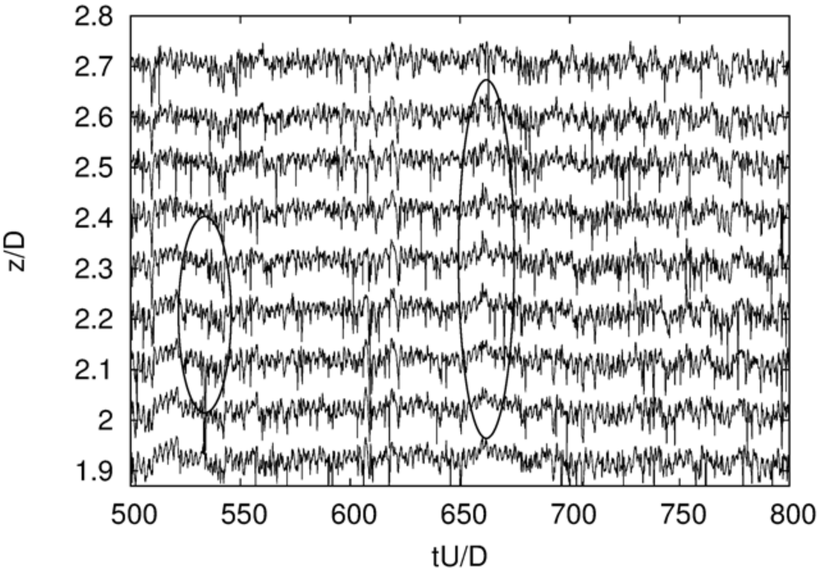

(b)

Figure 2.11: (a) Cross stream velocity and (b) pressure time history for P1 showing the passage of a vortex distortion.

a characteristic of the instability mode-A occurring at $Re \approx 200$ [147, 148]. Furthermore, dislocations have been confirmed numerically by the DNS of Braza et al. [9], where they found that vortex dislocations in the transition regime were accompanied by a shift in phase of the mode A undulations. Their existence at $Re \approx 5000$ has also been experimentally observed by Prasad and Williamson [106], who documented the occurrence of dislocations along the span of the cylinder and raised the possibility that this phenomenon is a fundamental feature of the cylinder wake flow in the "upper-sub-critical regime ($5000 < Re < 2 \times 10^5$). To confirm the presence of this phenomenon, time histories of velocity and pressure were analyzed. Fig. 2.11 shows, by means of the cross-stream velocity and pressure time history, the presence of what might be vortex dislocations. The velocity signal shows modulation, whereas the pressure signal shows a local maximum,

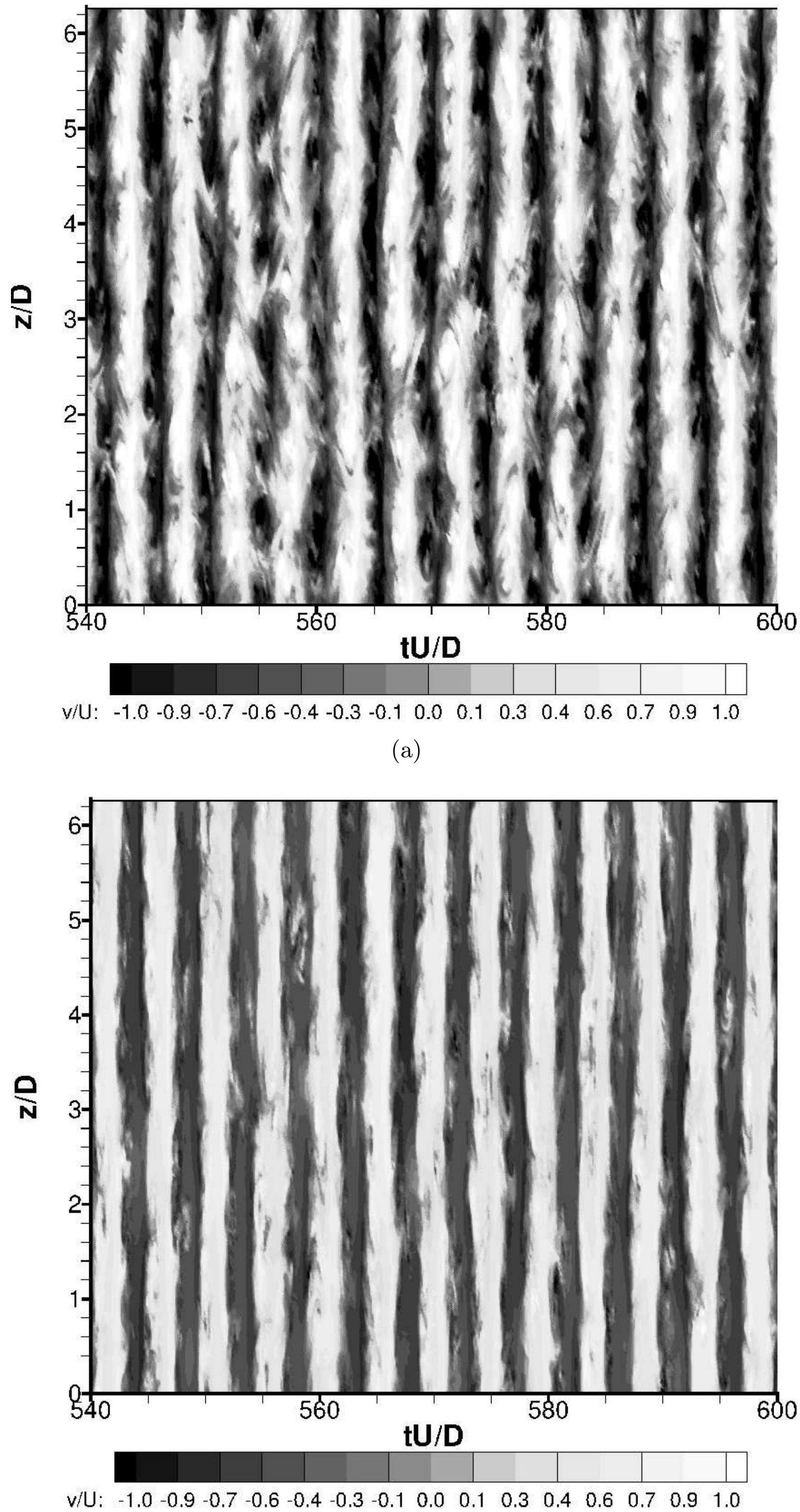

(a)

(b)

Figure 2.12: Cross-stream velocity on the (t,z) plane, illustrating the local perturbations on the coherence of the signal at P1 (a) and the recovery of coherence downstream at P3 (b).

followed by a rapid drop. Both features suggests a dislocation is passing through (both events are marked in the images for clarity).

It is interesting to provide an overall view on the effect of vortex distortions observed on the wake flow. Fig. 2.12 shows the passage of different vortex tubes by means of the cross-stream (V/U_{ref}) velocity time history. First, and most notorious, at location P1 a large number of distortions are visible (Fig. 2.12a). Moreover, the local breaks in the vortex tube continuity throughout the span seem to show a random distribution with time. As has been shown in Fig 2.6, the shear layer instability shows a broad-band characteristic frequency, whereas no characteristic frequency has been found for the convective-type instability. This behavior suggests the convective instability is constantly present within the near wake, whereas the shear layer instability occurs at different moments in time and span wise location. The appearance of the shear layer instabilities might be causing, as suggested by Norberg, a resonance type effect that distorts the shear layer roll-up. A detailed analysis showing the steps leading to vortex distortions is carried out in Section 2.3.3. Local discontinuities are visible on almost all vortex tubes shown in Fig. 2.12a, and no direct relation can be observed between the dislocations in adjacent vortex cores. Fig. 2.12b shows the cross-stream velocity at a location further downstream, P3. At this location barely any distortions are seen on the vortex tubes. The DNS study by Braza et al. [9] concluded that the appearance of stream wise vorticity in the cylinder wake, led to the appearance of vortex dislocations which affected the coherence of the whole wake. However, this is not the case for the present flow regime.

2.3.2 Frequency analysis

In order to further study the behavior of the vortex shedding and KH instabilities in the near wake, a fast Fourier transform was performed on the cross flow velocity for each plane on P1 (see Fig. 2.2). The results are presented in Fig 2.13. The vortex shedding frequency is seen as the dominant one in the flow for all z positions and, even though there are some variations in the spectral energy along the span, no large reduction of these energy peaks is observed at any span wise location. According to Braza et al. [9] spectral energy reduces in the regions where vortex dislocations occur, however, as observed in Fig 2.13, spectral energy does not vary much along the span. This behavior suggests that the distortions do not affect the vortex shedding as their occurrence do not greatly change the energy associated with this phenomenon.

To perform a more in depth study of the vortex shedding phenomenon present, a Fourier spectrogram for the cross flow velocity for the span wise mid plane is presented in Fig. 2.14.

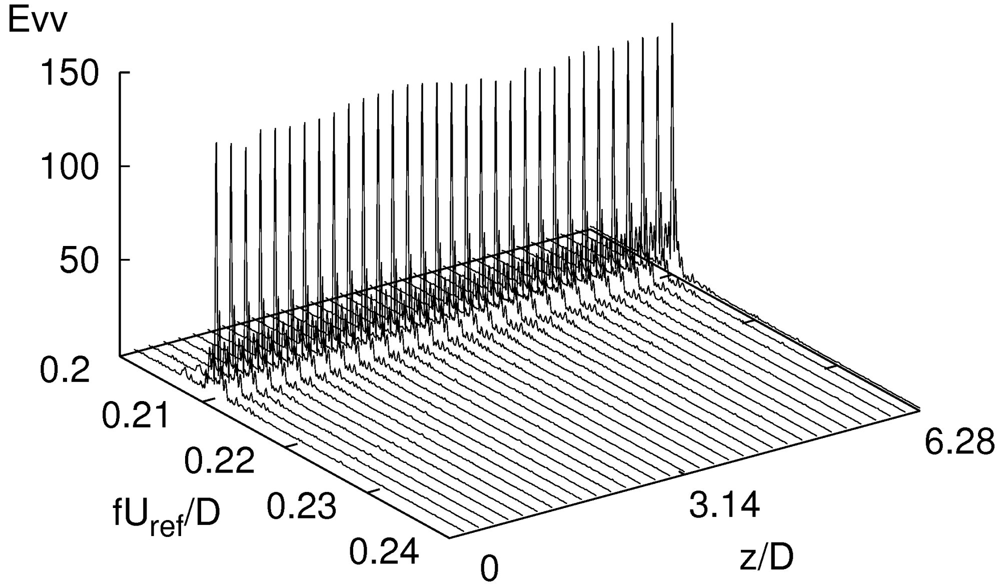

(a)

Figure 2.13: Span wise variations of the energy spectra for the cross flow velocity for P1.

A spectrogram is a visual representation of the spectrum of frequencies in a signal as they vary with time. Results for this spectrogram are approximate due to the fact that present results are not evenly spaced in time. As expected, there is a high energy area around the non-dimensional frequency $St = 0.2$, coinciding with the vortex shedding frequency. Notice that even though the largest energy content occurs around the vortex shedding frequency, small variations in both frequency and energy are observed along the whole time span. These variations might be associated with irregularities in the vortex formation at that location. Close-ups of these variations are depicted in Figs. 2.14b-c for $1920 \leq TU \leq 2180$ and $2920 \leq TU \leq 3180$, where variations of the energy content and in the value of the vortex shedding frequency are shown.

As our data is unevenly spaced in time, and as seen from the spectrogram, several frequency components seem to be acting in the flow, the empirical mode decomposition (EMD) method proposed by Huang et al. [37] is here used. This method breaks down a signal into different function components, known as intrinsic mode functions (IMFs), and a monotone residue. This process is carried out by means of an iterative algorithm. The advantage of this method over others, such as the Fourier transform or wavelet analysis, is that data can be unevenly spaced, have non-linear behavior and be non-stationary. Thus, it renders the possibility of characterization and parametrization of multi-scale patterns.

This technique has been applied to analyze the signal of the cross-stream velocity of probe P1. As the probes used are sampled for all planes in the span wise direction, resulting in a N plane signal, the signal corresponding to the mid-plane has been used. For the analysis, the initial time-series has been decomposed into eight IMFs plus a residual. Fig. 2.15 shows the resulting decomposition. Observing the different IMFs it can be seen that the behavior in the present case is composed, as expected, of different frequency components. As can be observed from Fig. 2.15, each IMF component shows a lower frequency than the previous one. IMF 1 depicts the turbulent fluctuations inherent of all turbulent flows, whereas IMF 2 shows the vortex shedding component

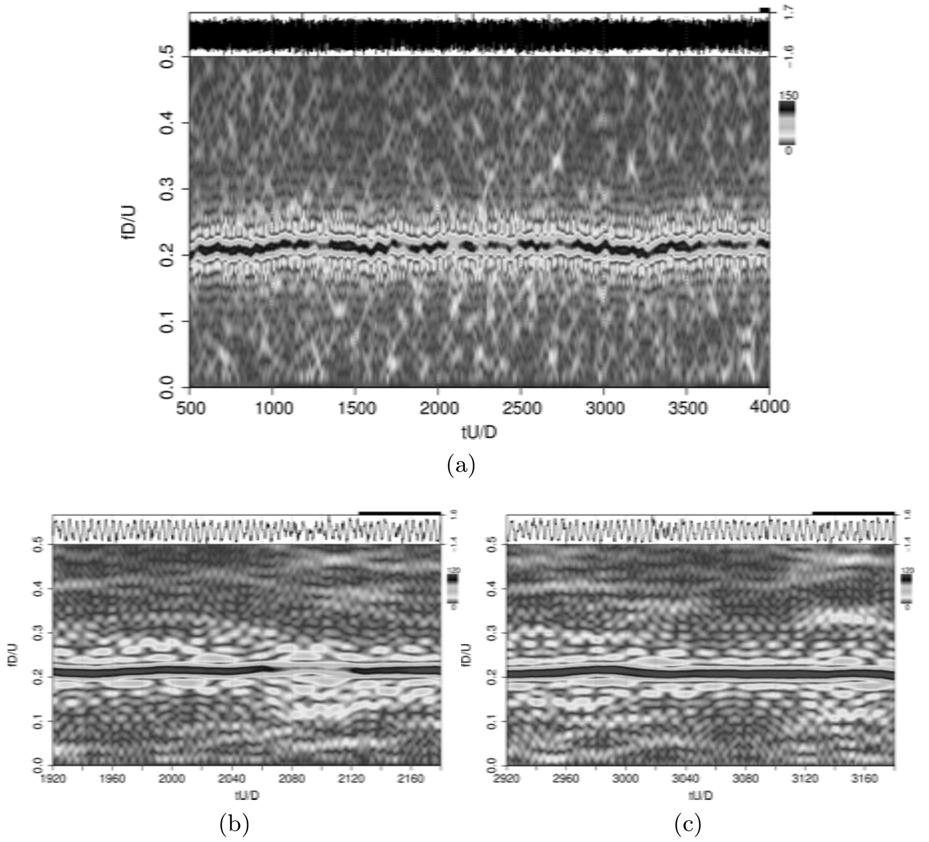

(a)

(b)

(c)

Figure 2.14: Fourier spectrogram for the cross flow velocity for P1 at plane $z/D = \pi$. (a) All integration time. (b) close up for $1920 \leq TU \leq 2180$. (c) close up for $2920 \leq TU \leq 3180$.

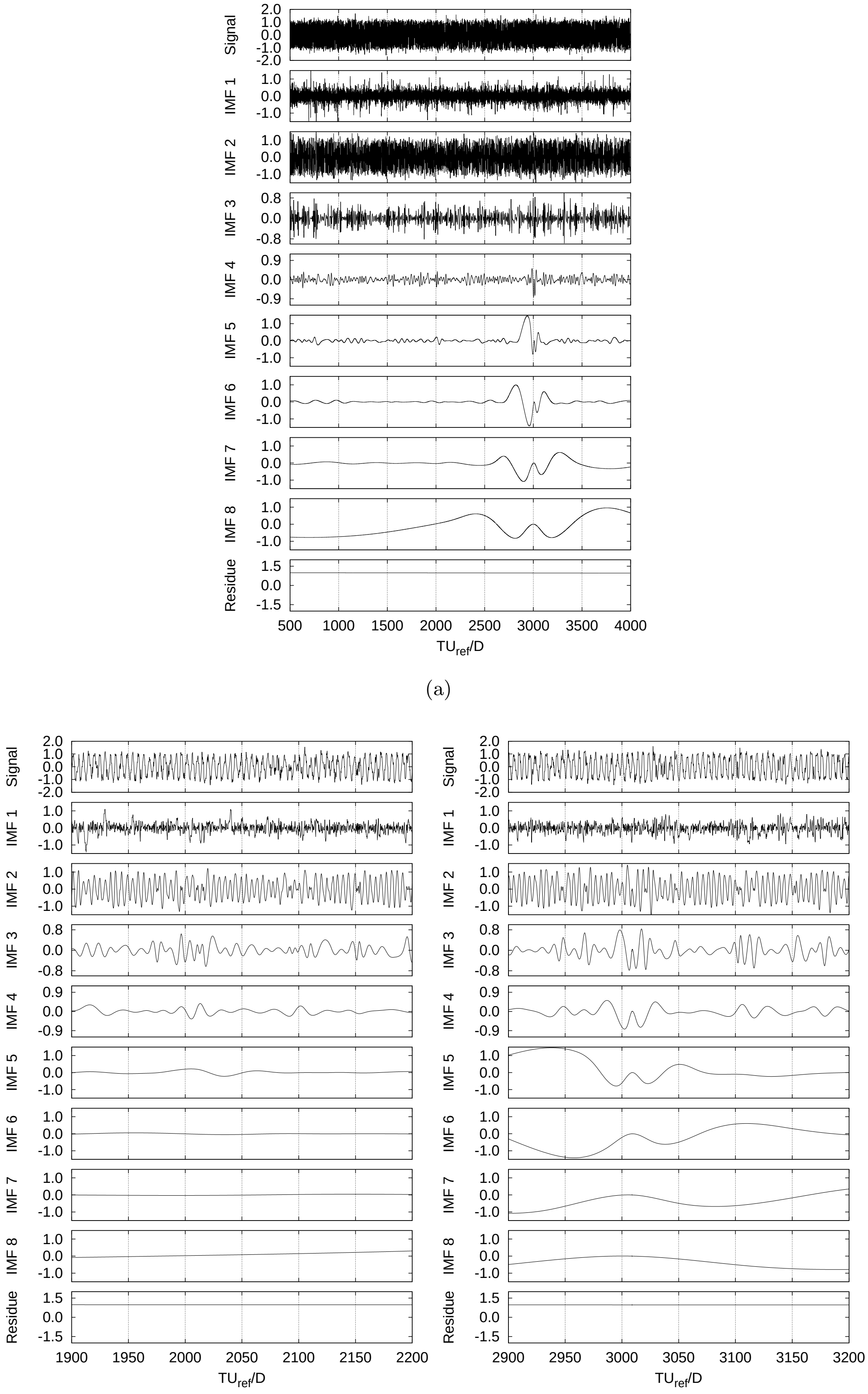

(a)

(b)

(c)

Figure 2.15: Empirical mode decomposition of the cross flow velocity for P1 (a) full time range, (b) close up to $1900 \leq TU \leq 2200$, (c) close up to $2900 \leq TU \leq 3200$.

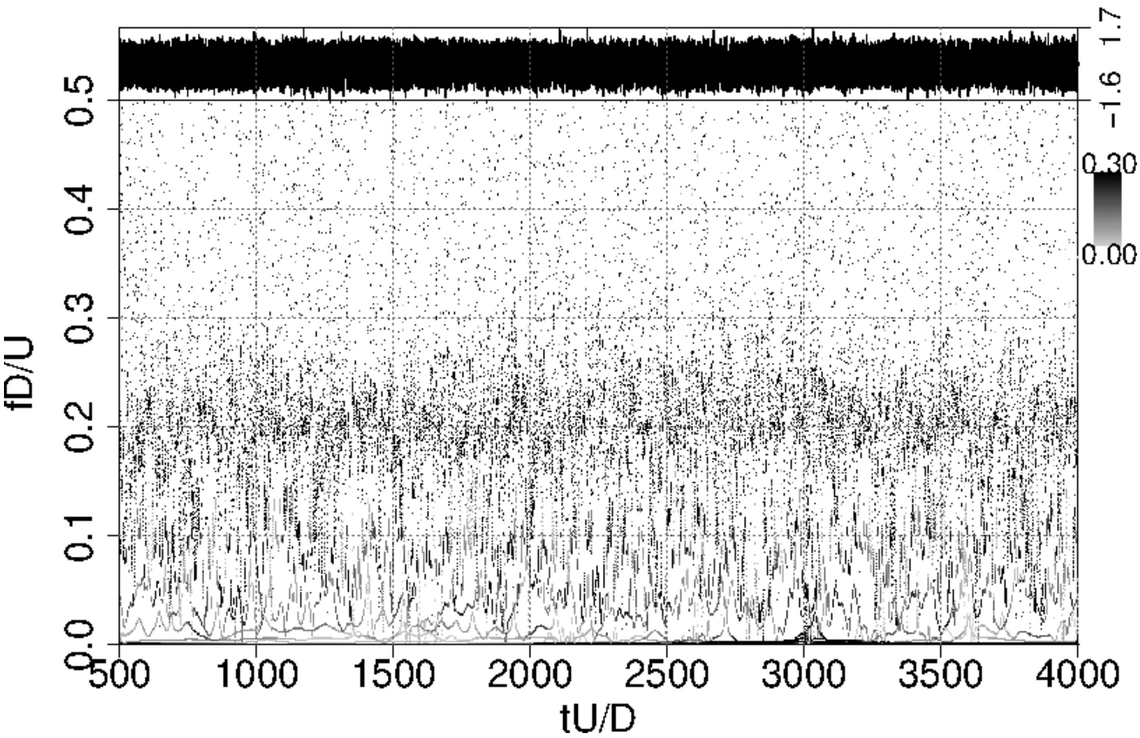

Figure 2.16: Hilbert spectrum for the IMFs shown in Fig. 2.15. The energy levels increase as color darkens.

of the signal. As can be seen from this IMF component, vortex shedding shows irregularities in its frequency and amplitude with regards to time. The rest of the IMFs then represent the lower frequency components acting on the wake flow and introducing irregularities into the vortex shedding.

The Hilbert transform is then applied to each IMF to compose the Hilbert spectrum (Fig. 2.16), which presents a quantification of the energy and frequency variations in time. Observing the Hilbert spectrum in Fig. 2.16, the vortex shedding (high energy) phenomena is readily seen around the non-dimensional frequency $St = 0.2$. Additionally, the lower frequency components represented by the higher order IMFs are also seen, presenting an energy level comparable to that of the vortex shedding. Interactions between these different frequencies disturb the local structure of the vortex street creating the 3D behavior observed.

2.3.3 Shear layers and instability mechanisms

Lin et al. [72], Norberg [89] and Rajagopalan and Antonia [107] all have suggested the existence of two instability mechanism in the wake of cylinders. Lin et al. [72] and Rajagopalan and Antonia [107] both have suggested the flow at the present Reynolds number is governed by a convective instability mechanism, i.e. instabilities stemming from the near wake, rather than by a global instability, i.e. instabilities in the shear layer. On the other hand, Norberg [89] suggests that the two instability mechanisms coincide for $Re = 5000$ causing a resonance like behavior.

Fig. 2.17 shows, for the same time instant, a span wise view at two different planes where the vortex formation structure varies as the flow is governed by the different instabilities. As the shear layer instability occurs transition to turbulence takes place in this region. On the contrary, when the flow is governed by the convective type instabilities transition is done within the recirculation zone, resulting in a larger vortex formation region. The co-existence of these two types of instabilities result in the un-even shear layer roll up observed in Fig. 2.18.

The shear layer roll up defines how the vortex tubes are formed. Fig. 2.18a shows the shear layer roll up at $TU = 2500.6$. Shear layers are visualized using non-dimensional span wise vorticity at a level 5.5% of the maximum span wise vorticity on the cylinder surface (defined in a similar fashion as in Dong et al. [22]). Marked in the image are locations where the shear layer roll-up evidences the span wise irregularities in its length. Fig. 2.18b shows the resulting vortex tube at $TU = 2503.6$. Marked in the image are the locations where the 2D continuity of the tubes is disrupted. Also, note there exists more than one location where the continuity is lost along the span.

To further study this behavior, span wise velocity is plotted over time at two different span wise locations, $z/D = 2.2$ and $z/D = 4.1$. As can be seen in Fig. 2.19, the shear layer shows the KH instability for $z/D = 4.1$, whereas it is not present in span wise location $z/D = 2.2$.

To further understand the vortex irregularities generated, Fig. 2.20 shows, using non-dimensional Q ($0 \leq Q* \leq 50$) and pressure ($-0.3 < p^* < -2$) contours, the vortex detachment process on two different span-wise planes for a vortex shedding cycle around $TU = 2500$. Fig. 2.20a shows the first step in this process where, as the shear layer finish their roll up phase, the vortex tube starts to move downstream. Notice in the left of Fig. 2.20a, the large amount of small structures (shown as the darker contour) in the vortex formation region compared to those present in the right. It is

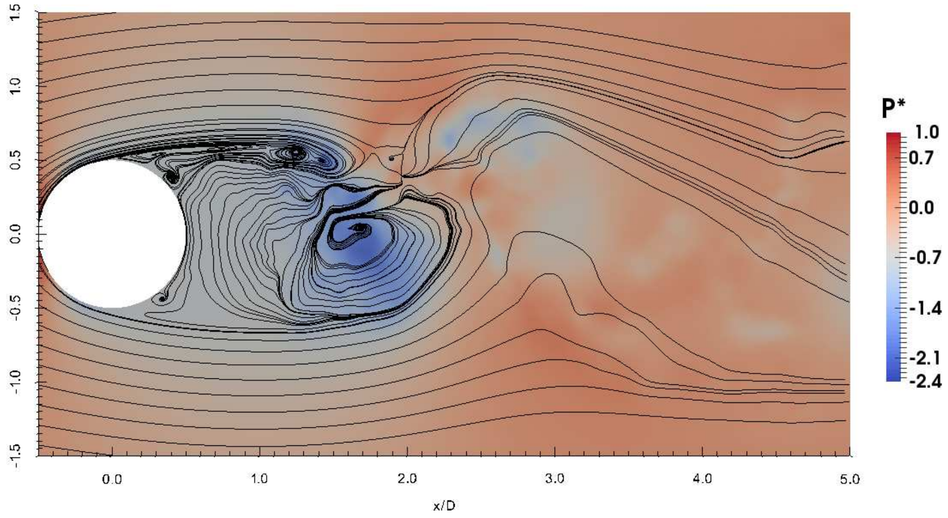

(a)

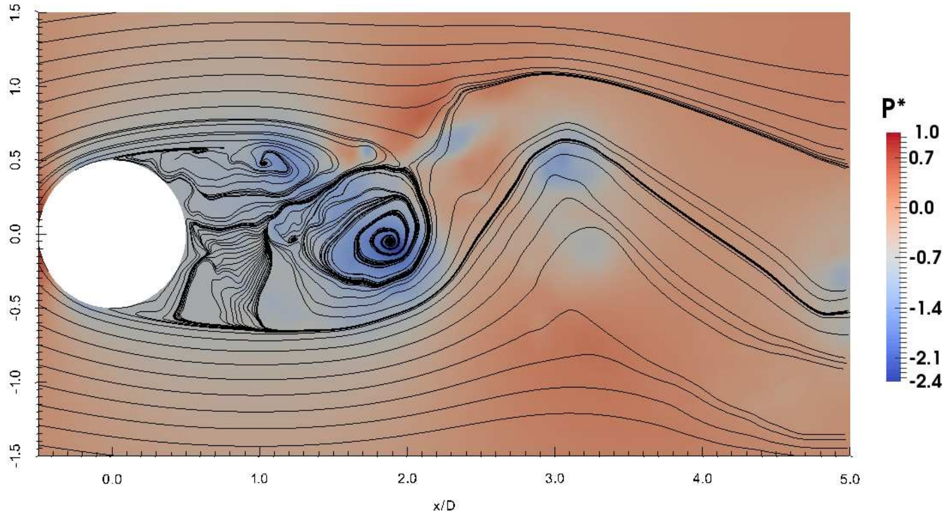

(b)

Figure 2.17: Span wise view at two locations showing the two different types of instabilities governing the flow, (a) $z/D = 5.89$ global instabilities and (b) $z/D = 0.2$ convective instabilities. Figure is colored by pressure.

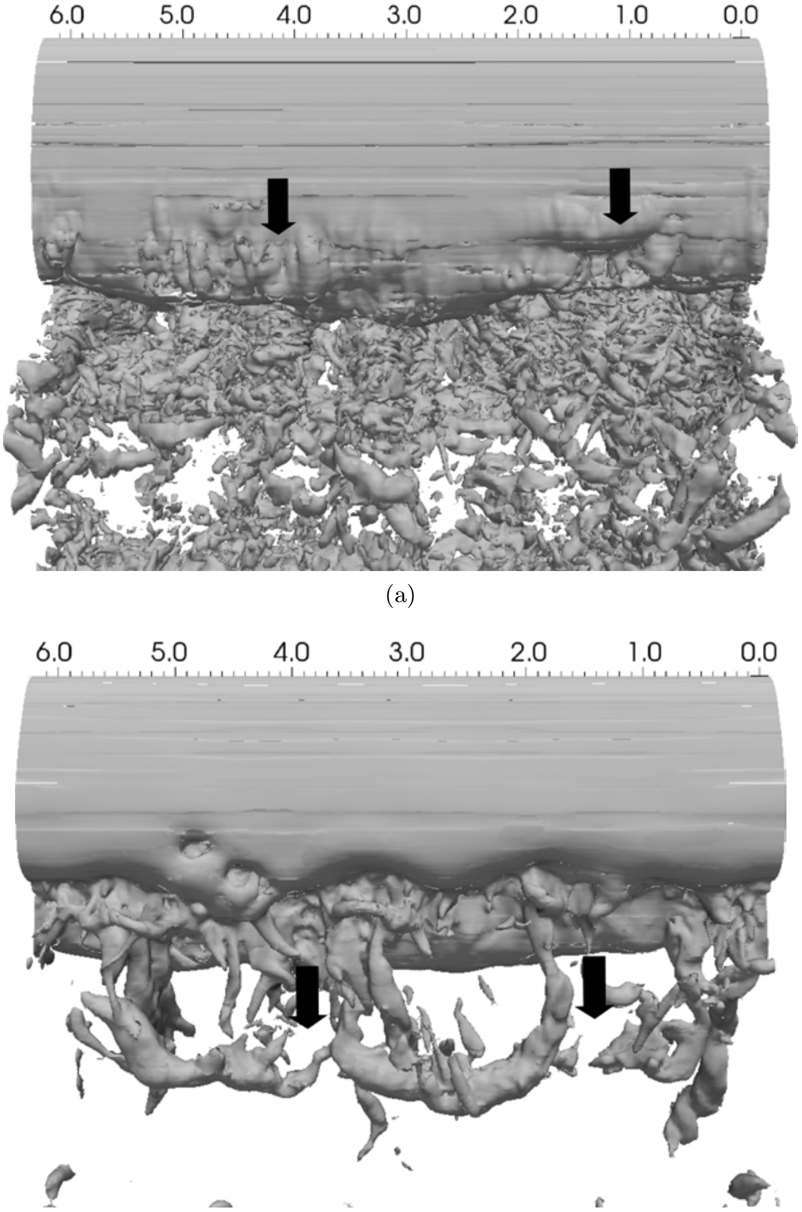

(a)

(b)

Figure 2.18: Shear layer roll up for (a) $TU = 2500.6$, using span wise non-dimensional vorticity $\omega_z^*/\omega_{z-max}^* = 5.5\%$, and resulting vortex tubes (b) $TU = 2503.6$ using non-dimensional pressure $p^* = -0.7$. Both images are colored by span wise velocity.

also important to notice the slightly larger formation length present in the left.

As time advances, the vortex core starts to detach (Fig. 2.20b), however, the influence of the different mechanisms present cause vortex detachment to be done in a different fashion. In the left of Fig. 2.20b, the vortex core moves downstream as it detaches from the recirculation area. However, in the right of the image, the vortex core starts to deform as the shear layer delays the vortex detachment, as seen in the right of Fig. 2.20b.

In the later stages of vortex detachment (Fig. 2.20c), the vortex tube (on the left side) successfully detaches and starts to travel downstream maintaining its circle-like shape. In the right, pressure contours deform greatly as the vortex core detaches. In this plane the structural integrity of the span-wise structure is lost, however, the span wise coherence is recovered downstream, as seen in Fig. 2.20d.

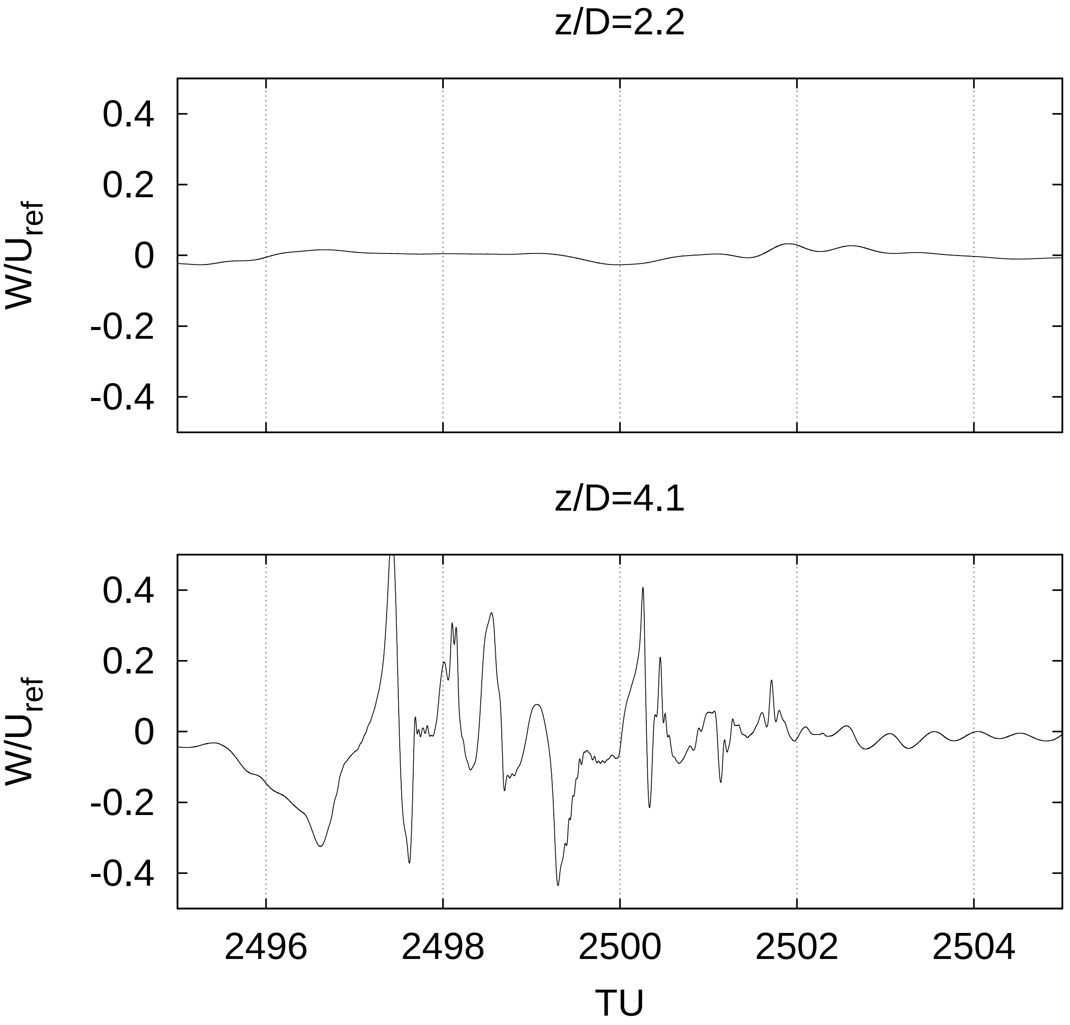

Figure 2.19: Span wise velocity within the shear layer (P1) at two span wise locations, $z/D = 2.2$ and $z/D = 4.1$.

At a vortex shedding cycle around $TU = 2513$, the vortex tubes do not show the large deformations visible in Fig.2.18b (see Fig. 2.21b). As the shear layer rolls up to create this vortex tube, it does so without the large span wise irregularities in its length (see Fig. 2.21a). In a similar fashion as before, the span wise velocity is plotted for the two span wise locations $z/D = 4.8$ and $z/D = 1.8$ in Fig. 2.22. A quick examination reveals that no shear layer instabilities are present in these planes, suggesting this vortex tube is completely governed by the recirculation instability mechanism.

Fig. 2.23 shows, similarly as Fig. 2.20, the vortex detachment process at the two span wise locations shown in Fig. 2.22. The beginning of this process is similar to what was observed before. Fig. 2.23a, shows the small structures within the recirculation area. Note that the vortex formation length is slightly different, however, the vortex in the right is larger.

As the shear layer roll up finishes, the vortex tube starts to move downstream, and it does so in a more uniform fashion than that observed in Fig. 2.20 (see Fig. 2.23b). It is important to note that the cross-flow location of the vortex center varies along the span. Finally, Figs. 2.23c-d show the vortex tube as it finishes the detachment process and travels downstream. The structural integrity of this tube is conserved throughout the whole process and the resulting vortex tube has

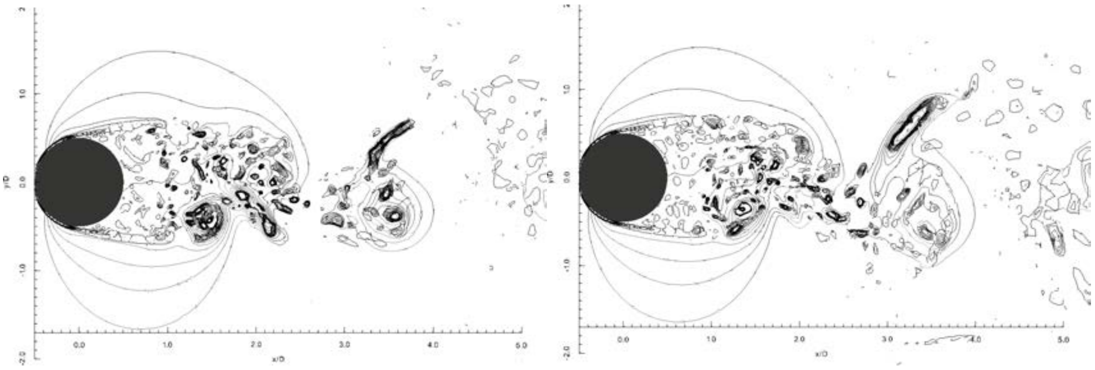

(a) $1/4T$

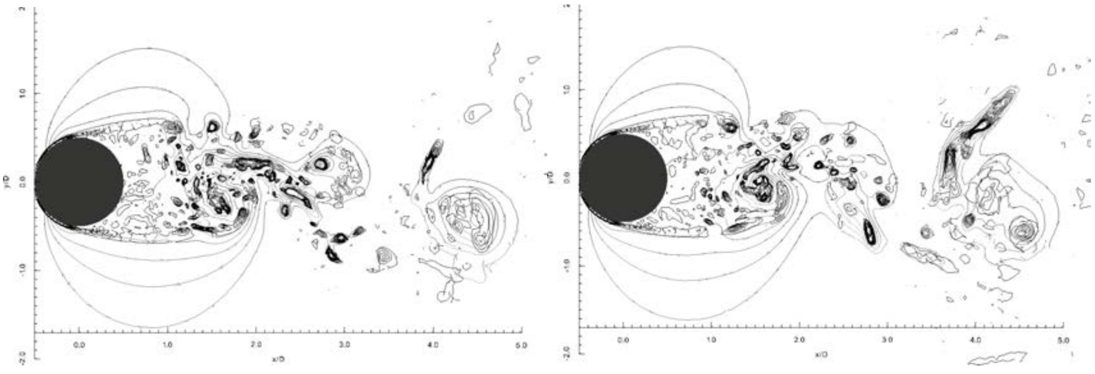

(b) $1/2T$

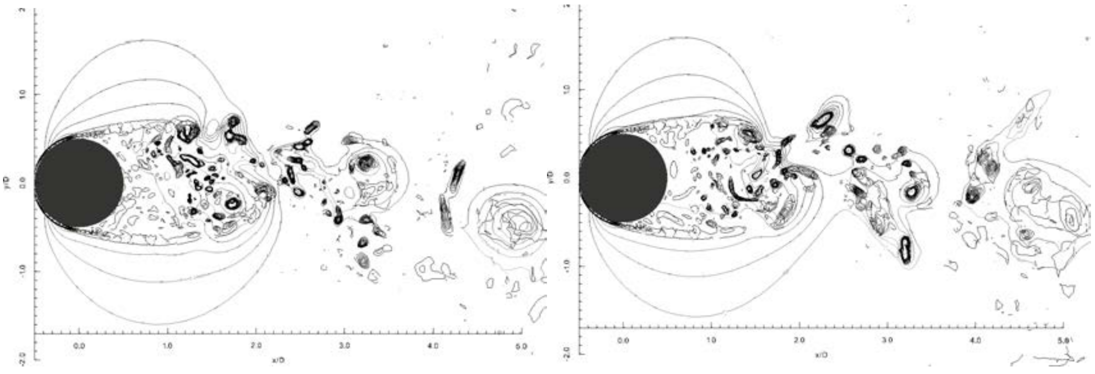

(c) $5/8T$

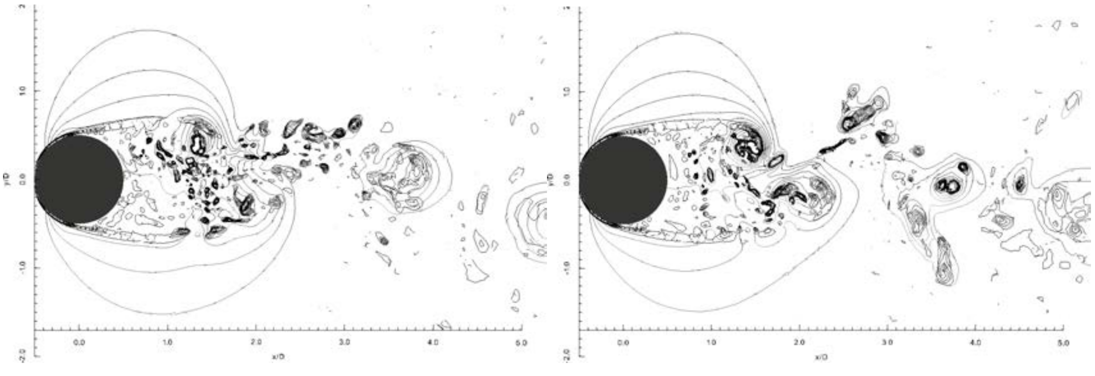

(d) $3/4T$

Figure 2.20: Pressure and Q* contours depicting the shear layer roll up at two span wise locations, left $z/D = 2.3$ and right $z/D = 4.1$.

a quasi-2D structure (Fig. 2.21b).

2.4 Conclusions

DNS computations were carried out to study the flow around a circular cylinder at $Re = 5000$. Different authors point to this flow regime as a transition point in the flow behavior. In order to correctly capture the three dimensional behavior found in this flow regime, a larger span-wise size than that used for previous DNS with lower Re had to be used. In the present investigation a span-wise size of $2\pi D$ was found to be enough to capture the three dimensional phenomena. In general, results from the present simulations agree quite well with published works, falling within

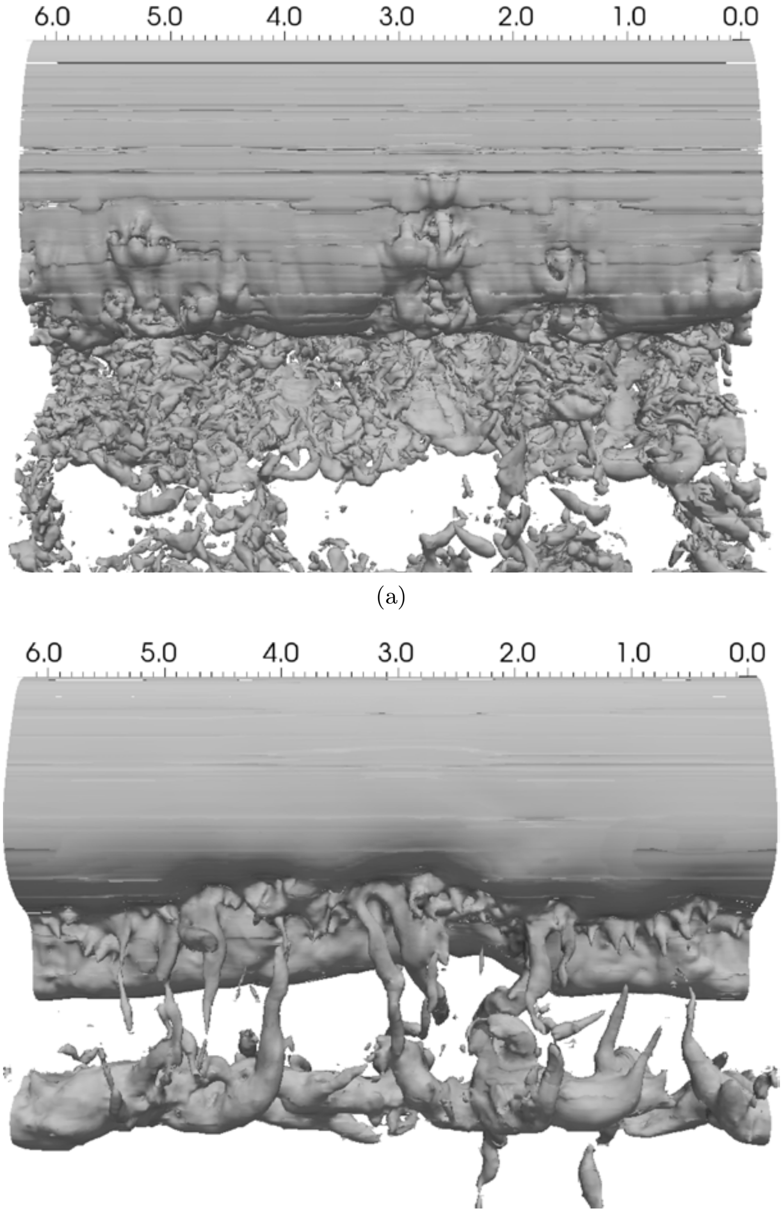

(a)

(b)

Figure 2.21: Shear layer roll up for (a) $TU = 2513.1$, using span wise non-dimensional vorticity $\omega_z^*/\omega_{z-max}^* = 5.5\%$, and resulting vortex tubes (b) $TU = 2516.1$ using non-dimensional pressure $p^* = -0.7$. Both images are colored by span wise velocity.

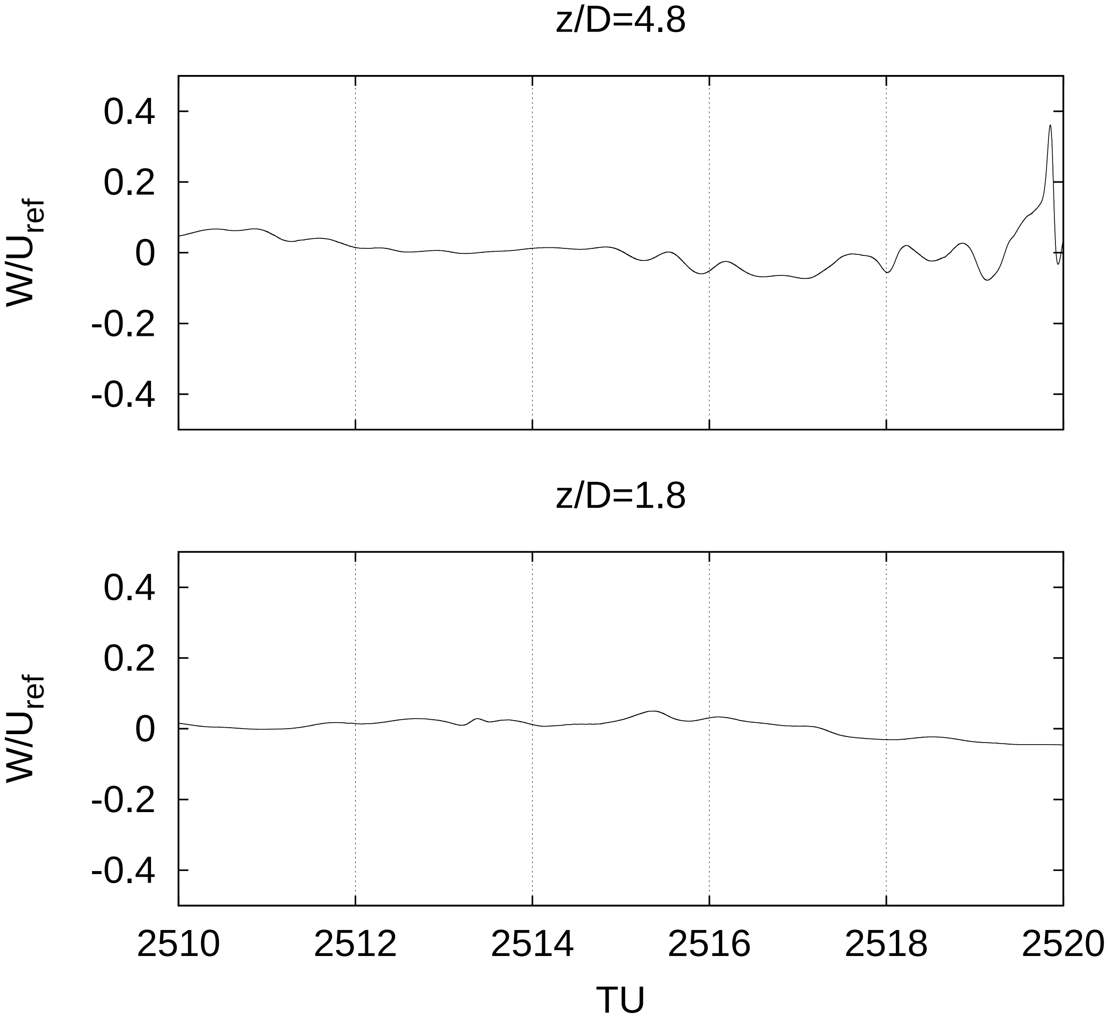

Figure 2.22: Span wise velocity within the shear layer (P1) at two span wise locations, $z/D = 4.8$ and $z/D = 1.8$.

the expected scattering present at this Reynolds number. The long-term solutions performed along $3500TU$ show a similar profile to that observed for $Re = 3900$ [67]. As expected, vortex shedding and KH instabilities are observed and large energy peaks are obtained in the energy spectra indicating a very coherent vortex shedding and a strong influence of the KH instabilities in the rest of the flow.

For this flow regime, the shear layers and the near wake exhibit a three-dimensional behavior not observed at lower Re numbers, which points out to a fundamental change in the flow. The three-dimensionality of the wake is seen as vortex distortions and variation in the vortex formation length. The latter, was already reported at a lower Reynolds number of $Re = 3900$ [67]. However, at $Re = 5000$, the three-dimensional behavior is extended to the whole near wake region exhibiting vortex splitting, vortex undulation and local vortex dislocations. In contrast to the vortex dislocation reported by Braza et al. [9], all these phenomena are found to be limited to the vortex formation region, as the coherence of the vortex street is not lost downstream.

As previously suggested by Norberg, it has been found evidence that the three-dimensional behavior appears to be the result of the coexistence of two instability mechanisms: a global and a convective-type instability. Actually, Norberg suggested that wake three-dimensionality is caused

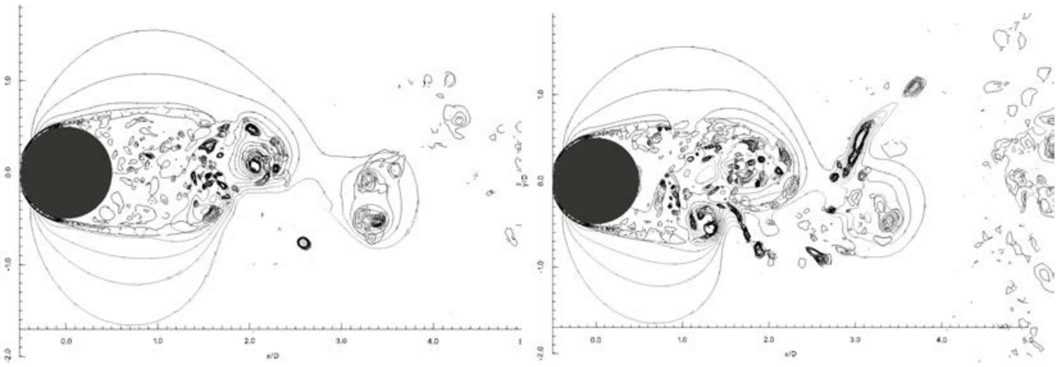

(a) $1/4T$

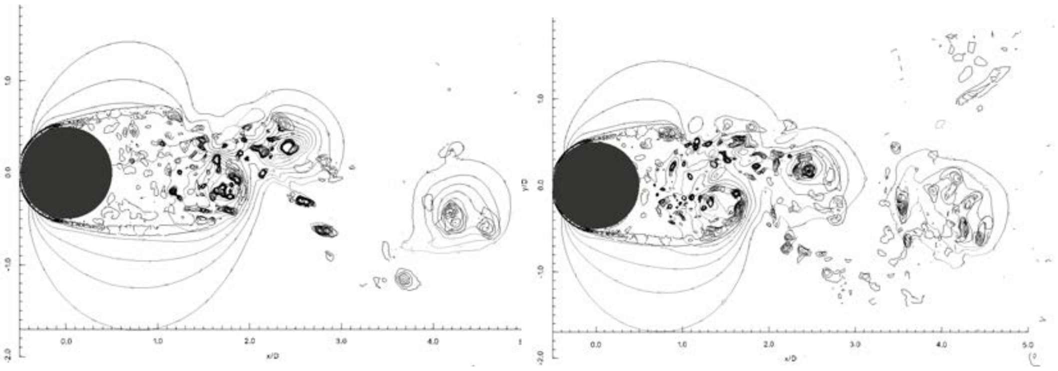

(b) $1/2T$

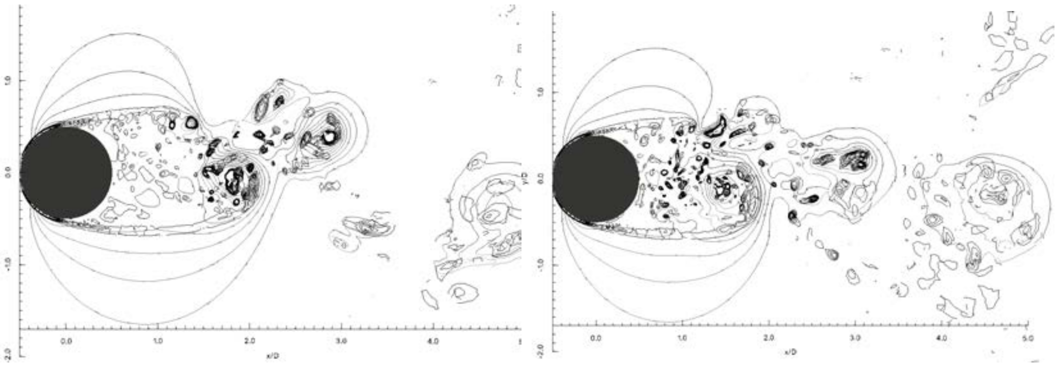

(c) $5/8T$

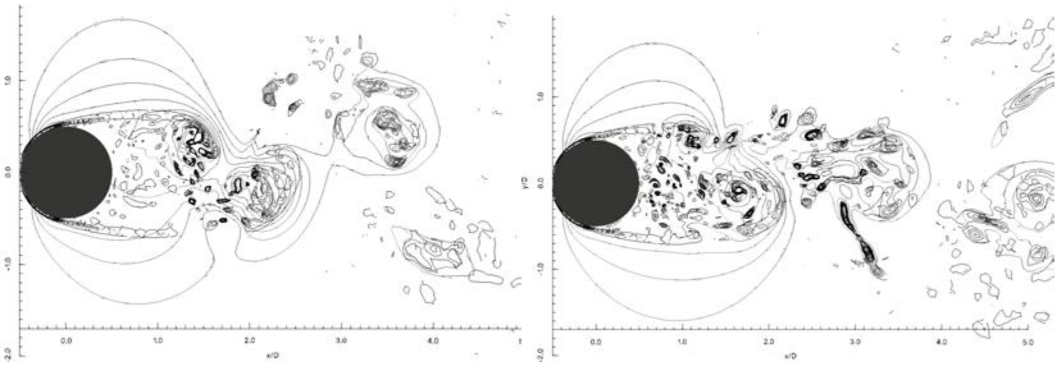

(d) $3/4T$

Figure 2.23: Pressure and Q* contours depicting the shear layer roll up at two span wise locations, left $z/D = 4.8$ and right $z/D = 1.8$.

by a resonance-like behavior within the near wake. Present results show evidence that the resonance effects does exist, and the three dimensional behavior is triggered by the occurrence of both global and convective, instabilities within the same vortex tube. These two instabilities at a same span wise location result in a different formation length and a distorted shear layer. As the shear layer roll up happens, vortex formation length variations in the span wise direction produce distorted vortex tubes. Nonetheless, the span wise distribution of the local breaks in the vortex tubes shows a random behavior, and is related to the appearance of the shear layer instability.

Chapter 3

Influence of rotation on the flow over a cylinder at Re=5000

Main contents of this chapter have been published in:

Aljure, D. E., Rodriguez, I., Lehmkuhl, O., Pérez-Segarra, C.-D. and Oliva, A. Influence of rotation on the flow over a cylinder at Re=5000 *Int. J. Heat Fluid Fl.* 55.
Aljure, D. E., Rodriguez, I., Lehmkuhl, O., Pérez-Segarra, C.-D. and Oliva, Aerodynamic fluctuating forces on a rotating cylinder *11th world congress on Computational Mechanics, 6th European conference on computational fluid dynamics., At Barcelona*, July 2014.
Aljure, D. E., Rodriguez, I., Lehmkuhl, O., Pérez-Segarra, C.-D. and Oliva, Influence of rotation on the flow over a cylinder at Re=5000 *10th International ERCOFTAC Symposium on Engineering Turbulence Modelling and Measurements, At Marbella, Spain*, September 2014.

Abstract

The influence of the rotation ratio on the forces acting on a circular cylinder at $Re = 5000$ has been investigated by means of direct numerical simulations (DNS). Spin ratios in the range $0 \leq \alpha = U_T/U_{ref} \leq 5$ have been considered. The results showed that rotation causes vortex shedding to cease for spin ratios $\alpha \geq 2$, in very good agreement with previous numerical and experimental research. Furthermore, as a consequence of the increased angular velocity of the cylinder the onset of Taylor-Görtler structures is also observed. Symmetry in the flow is broken as rotation ratio increases. This is specially evident in the shear layers as they start to curve towards the side with the lower pressure gradient causing the shrinkage of the vortex formation region. As these changes occur, both the stagnation point and the saddle point, formed in the closure of the recirculation region, shift in location coming closer to each other as the rotation ratio increases. For larger rotational speeds, the recirculation area behind the cylinder disappears and shear layers roll over the cylinder creating a "circumvolving" layer that greatly changes the wake topology. For $\alpha \geq 4$, the circumvolving layer forces the stagnation point off the cylinder surface, whereas for $\alpha = 5$, the accumulation of vorticity close to the stagnation point makes vortices to be shed on one side of the cylinder. Moreover, the changes that rotation cause on the aerodynamic forces on the cylinder are analyzed and discussed in detail.

3.1 Introduction

The flow around a rotating cylinder at $Re = 5000$ with rotation relation ranging $0 \leq \alpha \leq 5$ is simulated using direct numerical simulations (DNS). Viscous forces cause the flow attached to the cylinder to rotate about, strengthening the flow on one side of the cylinder and acting against it on the opposite side. According to the Bernoulli equation, this effect implies a rise in the pressure on one side of the cylinder and lowering it on the other creating a lift force, also referred to as the Magnus effect. This geometry has previously been studied, especially for the laminar regime using both experimental techniques and two dimensional (2D) simulations.

Prandtl (1925, 1926) performed experiments using a cylinder with end plates placed between two parallel walls up to a ratio of $\alpha = 4$, and observed how the wake deflects as rotation ratio increased, together with the appearance of a lift force. The theoretical analysis performed in his paper suggested a limit for the lift coefficient, $C_L = 4\pi$. However, his experimental results yielded a lift coefficient lower than the theoretical limit. Glauert [30] studied the 2D flow on this geometry at rotation rates where flow separation is suppressed. He theorized that there would be no limit whatsoever, however, his evidence was inconclusive. More recently, Chew et al. [11], via 2D numerical simulations for the flow at $Re = 1000$ and $0 < \alpha < 6$, stated that for spin ratios $\alpha < 2$ the lift force increases linearly, but for larger values it presents an asymptotic behavior and does not surpass Prandtl's limit, in agreement with the statement of a limit in the lift coefficient. On the other hand, numerical results by Mittal and Kumar [81] at $Re = 200$ reported a lift coefficient beyond Prandtl's limit for high rotation rates.

Regarding the flow topology, Thom [129] performed experiments at a rotation ratio $\alpha = 2$ and measured the velocity field and surface pressure. Further experiments [130] allowed to deepen the understanding on the flow topology for higher spin ratios and the behavior of the lift and drag coefficient with respect to rotation ratio. Ludwig [73] carried out experiments for low rotation rates ($\alpha \leq 0.3$). Using hot-wire anemometers, he identified the flow separation points and predicted a linear relation of the location of the separation point on the downstream-moving wall with the rotation ratio α. Chou [14] also studied the changes in flow topology for the cases with $Re = 1000$ and $\alpha < 3$, and $Re = 10000$ and $\alpha \leq 2$ using 2D numerical simulations. The author found that the locations for the stagnation points were in good agreement with previous references. More recently, Karabelas [49], using large-eddy simulation (LES) for the flow at $Re = 1.4 \times 10^5$ and spin ratio range $0 < \alpha < 2$, showed that flow patterns are strongly affected by the latter. Furthermore, his results confirmed the shift of the stagnation point and observed that the location of turbulence transition shifted upstream. In general, studies on the flow topology [41, 81, 91] have shown that, as a result of the rotation of the cylinder the wake is deflected and the symmetry in the flow broken. It is also observed that the formation of coherent vortices is diminished on the side where the peripheral velocity goes against the free stream velocity.

One of the key characteristics of the flow past bluff bodies is the regular shedding of vortices forming the von-Kármán vortex street. The cylinder rotation affects the way vortices are shed and for large rotation ratios it has been reported that vortex shedding ceases to occur [11, 14, 21, 81]. The value of the critical rotation ratio was reported to be about $\alpha_{crit} = 2$ [14, 21]. Later, Mittal and Kumar [81] by means of numerical simulations found a critical value slightly lower $\alpha_{crit} = 1.9$ at $Re = 200$. Nonetheless, for low rotation ratios the overall dynamics of the vortex formation does not largely change, but rotation affects the vorticity strength and the vortex formation length [17, 60, 108]. Furthermore, vortex shedding frequency increases with rotation ratio, whereas wake meandering decreases [17, 52].

At large rotation ratios ($\alpha > \alpha_{crit}$), the dynamics of the shear layer and the wake changes owing to the vortex shedding suppression. Matsui [78], via experimental measurements for $59 \leq Re \leq 1600$ and a spin ratio $\alpha > 2$, reported the existence of a fluid layer rotating about the cylinder and a second fluid layer separating from the former at a point away from the cylinder surface. The inner circulating layer exhibited a Taylor-like instability, whereas vortices generated near the stagnation point, through a Görtler-like instability, separate from the inner layer to feed the wake. A similar phenomenon was also reported by Mittal and Kumar [81] by means of numerical simulations at $Re = 200$. They observed that for high rotation ratios ($4.35 < \alpha < 4.7$) the pile-up of vorticity near the stagnation point caused the shedding of vortices only in the sense of rotation.

Most of the experimental research work performed so far has been focused on the observation of the flow characteristics at different Reynolds numbers and rotation ratios. On the other hand, numerical investigations carried out have mostly been done in the laminar regime or for 2D domains. Little numerical investigation work has been done in the turbulent regime. In this sense, the present work aims at shedding some light on the effect of the rotation ratio in the vortex shedding and forces acting on the cylinder at $Re = 5000$ and for a large range of spin ratios $0 \leq \alpha \leq 5$. The changes in the flow topology as the rotation ratio increases are studied by means of the analysis of the instantaneous coherent structures, as well as by the inspection of the different near wake parameters such as the shear layer length, vortex formation region size, stagnation and saddle points location, amongst others. These issues are of major importance in many practical applications e.g. marine structures, civil engineering, aerodynamic design, etc.

3.2 Definition of the case

The geometry to be considered is a cylinder with diameter D submerged in a uniform fluid flow (see Fig. 3.1). The cylinder rotates about its axis with angular velocity Ψ. Simulations are carried out using a Reynolds number $Re = 5000$, based on the cylinder diameter D and the free-stream velocity U_{ref}, and for rotation ratios in the range $0 \leq \alpha \leq 5$.

The computational domain is $30D \times 30D \times 2\pi D$ in the stream, cross-stream and span wise directions. The center of the cylinder is located at a distance of $10D$ downwind from the inlet boundary and at a distance of $20D$ from the bottom boundary.

3.2.1 Mathematical and numerical models

In order to study the flow, the incompressible Navier-Stokes equations are solved:

$$\frac{\partial u_i}{\partial x_i} = 0 \tag{3.1}$$

$$\frac{\partial u_i}{\partial t} + \frac{\partial (u_i u_j)}{\partial x_j} - \nu \frac{\partial^2 u_i}{\partial x_j \partial x_j} + \rho^{-1} \frac{\partial p}{\partial x_i} = 0 \tag{3.2}$$

The governing equations are discretized on a collocated unstructured mesh by means of finite volume techniques. Spatial discretization is done using a second-order conservative scheme [141] that preserves the symmetry properties of the continuous differential operators and ensure both stability and conservation of the kinetic-energy balance. An explicit second order self-adaptive scheme that ensures stability for the temporal discretization of the convective, diffusive and derivative parts of the Navier-Stokes equations is implemented. This temporal integration scheme, presented by Trias and Lehmkuhl [134], chooses a Δt via a maximization problem based on a stability region created through the eigenvalues of the convective and diffusive matrix operators of the governing equations. A back-ward Euler scheme for the pressure gradient is used, whereas the velocity-pressure coupling is solved by means of a fractional step algorithm. For ensuring mass conservation a special definition for the projected velocity face flux is used based on the method proposed by Felten and Lund [27]. This approach results in a kinetic energy conservation error of

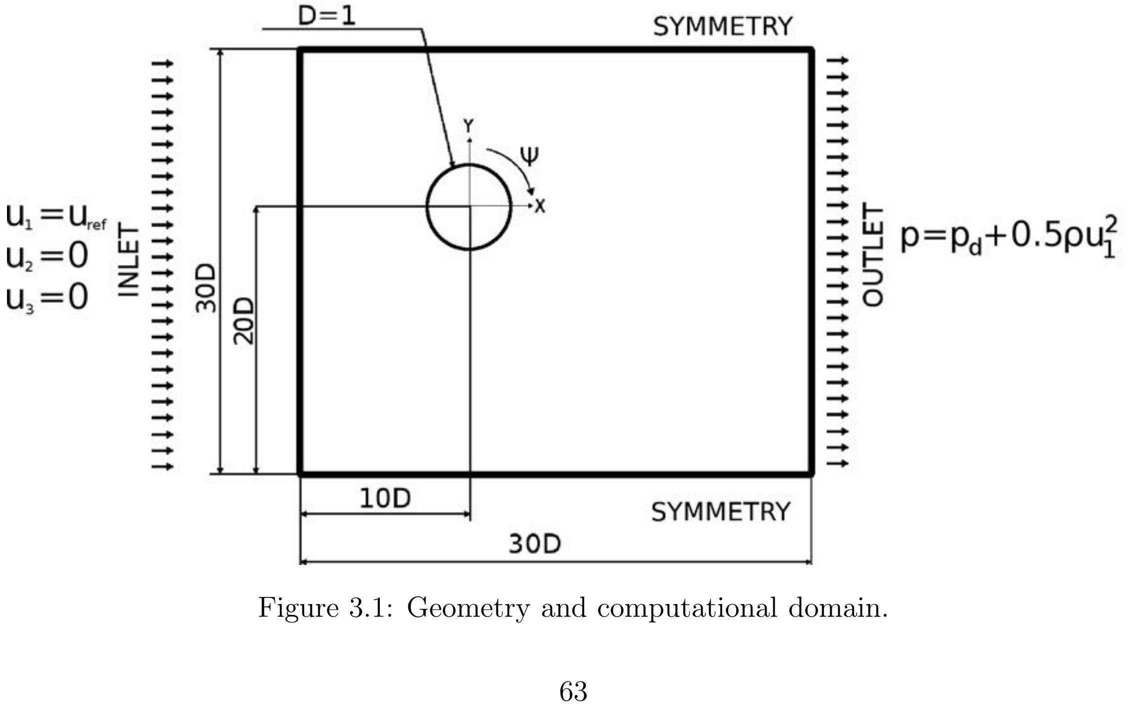

Figure 3.1: Geometry and computational domain.

order $\phi(\Delta t^m, \Delta h^2)$ which do not have a significant impact for the grid resolutions and the time steps used in DNS [67, 113]. For more details on the discretization the reader is referred to Jofre et al. [45] and Trias et al. [135].

For solving the Poisson equation, a direct Schur-Fourier decomposition method is chosen. As the three-dimensional meshes are constructed by means of a constant-step extrusion in the span wise direction of a 2D unstructured grid, a Fast Fourier Transform (FFT) method can be applied. This method decouples the initial system of equations into a set of two dimensional sub-systems, which are then solved by means of a direct Schur-complement decomposition solver [7].

Simulations are carried out on the in-house JFF cluster and on the Marenostrum III supercomputer. The JFF cluster is composed of 128 nodes with 2 AMD Opteron 2350 Quad Core processor linked with an infiniband DDR network and 40 nodes with 2 AMD 6172 CPUs (16 cores by CPU) linked with a QDR infiniband network and 2GB RAM per core, whereas the Marenostrum is based on Intel SandyBridge processors working at 2.6 GHz and coupled by means of an Infiniband network. For the computational meshes reported in this work, partitions of 512 CPUs are considered. Mesh partitions are performed in the present work using the METIS library [50], and parallel communications are implemented following a pure distributed model by means of the Message Passing Interface (MPI) standard. In terms of wall-clock time, the cost of each simulation depends on the number of time-steps required for completing the whole simulation and the cost per time-step. Since in the current computations a direct Poisson solver is used, the latter is constant for a given mesh and number of CPUs. For instance, for the $\alpha = 0$ case, the mesh size is about 37×10^6 control volumes and the cost per iteration is of approximately 0.19 s on the Marenostrum supercomputer. Considering that a large time span is necessary for obtaining converged statistics, about 3.16×10^6 outer iterations are required. Thus, the cost for this simulation is of approximately 8.54×10^4 CPU hours, that is approximately 7 days. For the higher rotation ratios considered in this work, this time is reduced as the time integration span is considerably shortened. The code and numerical approach used in the present simulations have been proved to yield accurate solutions in flows with massive separations [66, 67, 113, 114].

3.2.2 Boundary conditions

Boundary conditions are shown in Fig. 3.1. A constant inlet velocity profile $u_i = (U_{ref}, 0, 0)$ is imposed. A pressure based condition is imposed for the outflow such that the mass conservation is fulfilled at each time step. In addition, in order to avoid any influence from non-physical waves reflected by the artificial outflow boundary, a buffer zone at $x > 14D$ is used [140]. Top and bottom boundaries are modeled as symmetry ones, whereas for the span wise direction periodic boundary conditions are set. A surface velocity vector $u_i^s = \psi_i \times r_i$ is imposed in the cylinder, where the angular velocity magnitude is defined as $|\psi_i| = 2\alpha U_{ref}/D$.

3.2.3 Spatial discretization

A fine near-wall mesh, to correctly solve the boundary layer and the physical phenomena associated with this zone, is necessary. Similarly, a fine mesh for the full resolution of the shear layers is also required. Furthermore, the near wake zone must be refined to correctly resolve all relevant scales of motion. As the flow moves away from the cylinder the relative importance of flow structures in the force coefficients and near wake velocity profiles diminish and so does the mesh resolution. With these criteria, meshes presented in Table 3.1 are constructed. Details of the meshes used for different rotation ratios are presented in Fig. 3.2. Notice that control volumes (CV) are clustered not only around the cylinder but also close to the zone marked in the figure as x'. It is expected that as the rotation ratio increases, the wake bends towards the zone with the lower pressure gradient. Preliminary simulations using coarse meshes were performed to determine the overall wake behavior. Using this information, the fine meshes are constructed in order to follow the shape of the near wake, as depicted in Fig. 3.2.

Turbulent motion, as described by Kolmogorov, has a universal form for the smallest characteristic lengths, which are only dependent on viscosity and dissipation rate [54]. DNS must resolve all relevant scales of motion, i.e. in the turbulent zones the grid characteristic length must be of the same order of magnitude than the Kolmogorov scale. Present simulations reach, on average, a ratio

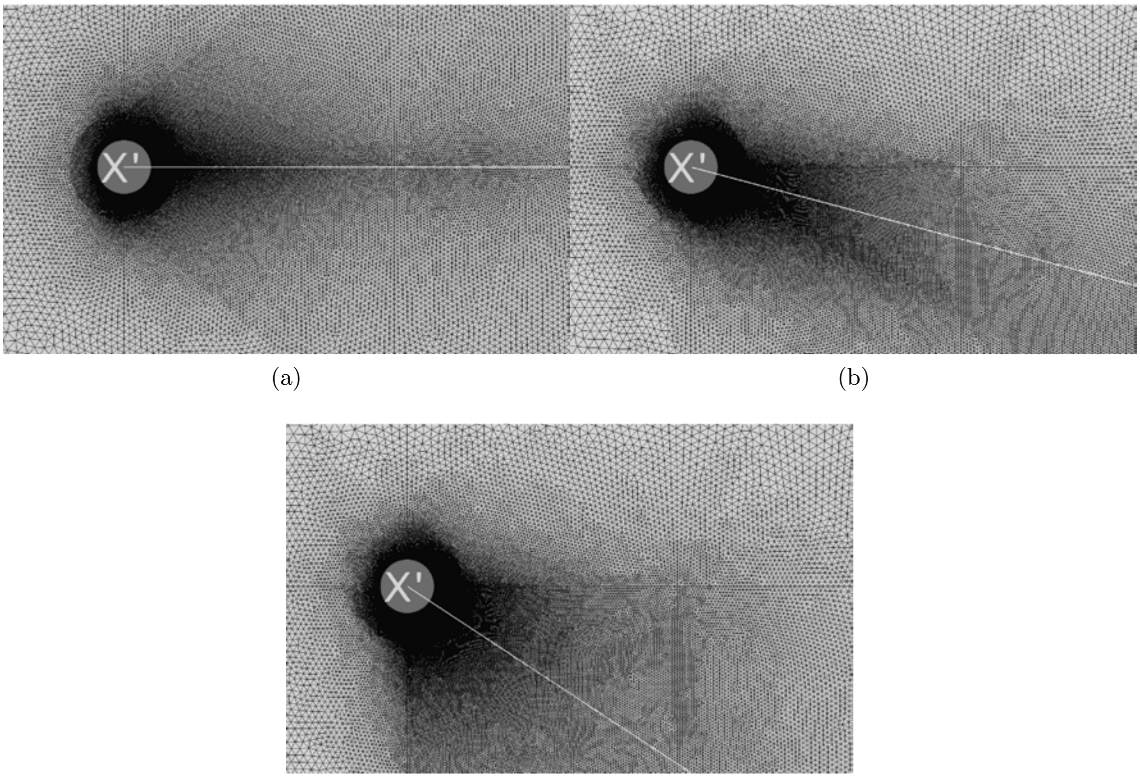

(a) (b)

(c)

Figure 3.2: Detail of the unstructured meshes for the two dimensional plane. Cases (a) $\alpha = 0$, (b) $\alpha = 2$, (c) $\alpha = 5$.

of the grid size to Kolmogorov scales under 2.5. This parameter for the near wake, $0 < x'/D < 3$, $-1 < y'/D < 1$, is also given in Table 3.1.

Furthermore, the boundary layer at the cylinder surface has to be well resolved. The non-dimensional wall normal distance can be evaluated as $y^+ = u_\tau y/\nu$, where u_τ is the friction velocity defined as $u_\tau = \sqrt{|\tau_w|/\rho}$ and τ_w is the wall shear stress. In Table 3.1, the non-dimensional wall normal distance for the first CV is also given. It should be borne in mind that within the viscous sub-layer, defined for $y^+ \leq 5$, viscous stresses are the dominating force in the flow. Thus, meshes used in the present investigation are built so, at least, the first two nodes in the boundary layer fall well within the viscous sub-layer to ensure its correct resolution.

Table 3.1: Details of simulation parameters for the different rotation ratios.

α	CV_{plane}	N_{planes}	NCV	h/η	y^+_{1min}	y^+_{1avg}	t_{int} $[TU]$
0	115709	320	3.70×10^7	1.05	0.12	0.95	3500
1	123145	320	3.94×10^7	0.98	0.05	1.50	2600
2	130020	320	4.16×10^7	0.74	0.04	1.28	900
3	133145	320	4.26×10^7	0.67	0.05	1.41	730
4	138461	320	4.43×10^7	0.56	0.04	1.47	450
5	147591	320	4.72×10^7	0.57	0.05	1.85	450

Table 3.2: Statistical flow parameters for $\alpha = 0$. Comparison with literature available results. †[87], ‡[88], ††[89].

Case	C_p	St_{vs}	$-C_{p_{base}}$	L_{rec}/D
present results, $\alpha = 0$	1.05	0.210	0.957	1.357
Norberg ($Re = 5000$ - EXP)	$1.02^{\dagger}$	$0.209^{\dagger}$	$0.932^{\ddagger}$	$1.40^{\dagger\dagger}$
Jordan and Ragab [46] ($Re = 5600$ - LES)	1.01	0.206	1.02	-
Lam et al. [59] ($Re = 6000$ - EXP)	0.96	-	-	1.62
Lehmkuhl et al. [67] ($Re = 3900$ - DNS)	1.015	0.215	0.935	1.36
Ma et al. [75] ($Re = 3900$ - DNS Case I)	0.96	0.203	0.96	1.12

3.2.4 Validation of the numerical approach

Numerical results in the literature for the rotating cylinder are scarce, however, in order to check the mesh discretization and grid parameters used in the present computations, results for the non-rotating cylinder ($\alpha = 0$) are compared to literature available results. In this sense, time-averaged flow parameters are summarized in Table 3.2. In the table, the mean pressure drag coefficient (C_p), the non-dimensional vortex shedding frequency St_{vs}, the base pressure coefficient ($C_{p_{base}}$) and the recirculation length (L_{rec}/D) are given. For comparison sake, values for these parameters from diverse published works are also presented. In general, computed parameters are in quite good agreement with published works, falling within the expected scattering reported at this Reynolds number. For this flow regime, the wake seems to be experiencing a fundamental change [see for instance 67, 87, 107]. These changes might be accompanied by vortex dislocations [147] and variation of the vortex formation length [67], amongst others.

In Fig. 3.3, the mean stream wise velocity ($< \cdot >$ stands for time and homogeneous direction average) and its fluctuations in the wake centerline are plotted against results from the literature. Results compare rather well, although main differences are present in the magnitude of the minimum velocity in the wake. As commented before, fundamental changes in the wake around this Reynolds number have been reported, affecting the wake three dimensionality and, thus, some scattering is expected. This is more evident in the stream wise velocity fluctuations where different profiles around the maximum peak are observed. A more detailed comparison of the stream wise velocity and its fluctuations for different meshes considered are given in 3.4.

3.3 Results

Simulations are started from homogeneous flow and advanced in time until the initial transient behavior is washed out and a statistical stationary flow is reached. After that, first and second order statistics are averaged in time and space (in the span wise direction) up until well converged statistics are obtained. For rotation ratios from $\alpha = 0$ to $\alpha = 5$, averaged variables stabilize after a certain integration time, as it is illustrated in Fig. 3.4. In the figure, the time history for the first and second order statistics registered by numerical probes at selected near wake locations, and for three different rotation ratios is shown. For cases with $\alpha \leq 2$, point 1 is located at the wake centerline and point 2 in the top shear layer. For cases with $\alpha \geq 3$, points are located within the near wake in two different locations. It can be seen that after an initial transient, stream wise velocity and its fluctuations stabilize. Thus, in all cases the integration time selected fully guarantee the averaged converged statistics (see Table 3.1 for time integration details).

3.3.1 Instantaneous flow

Unsteady flow is analyzed by extracting the coherent structures present in the wake. To do this, the Q-criterion which identifies a vortex in a region where the second invariant of the velocity gradient tensor is positive ($Q > 0$) is used. This criterion is defined as $Q = 0.5(||\Omega||^2 - ||S||^2)$,

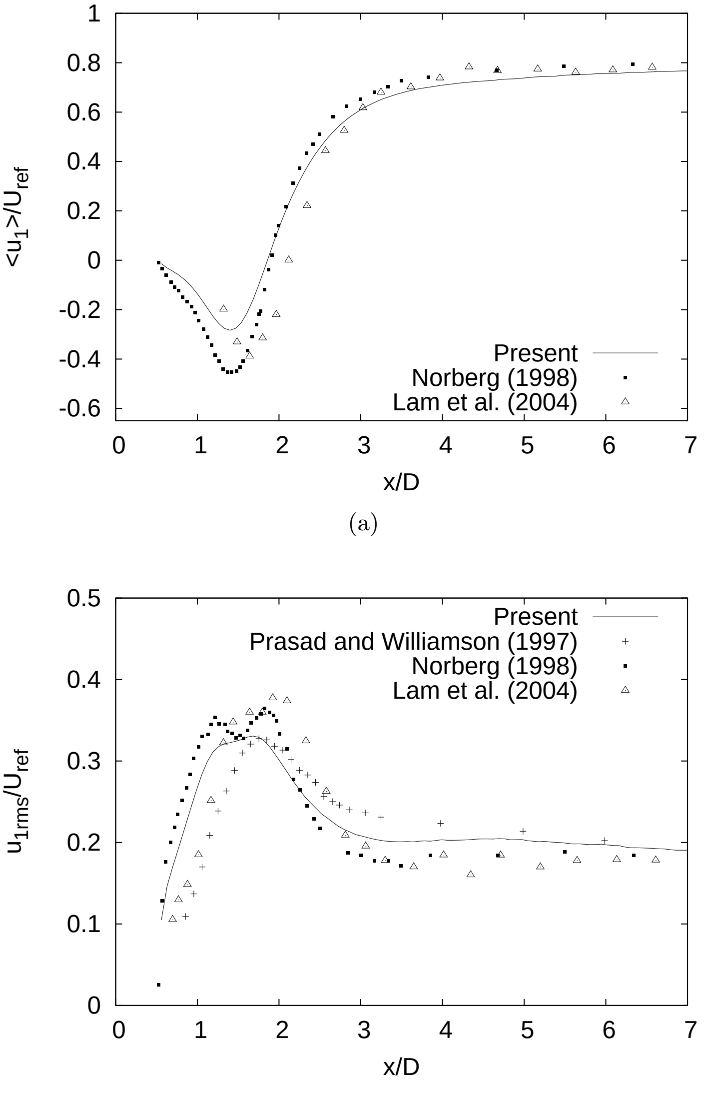

(a)

(b)

Figure 3.3: Mean stream wise velocity (a) and its fluctuations (b) in the wake centerline. Comparison with results from the literature. Solid line present results, squares Norberg [89] ($Re = 5000$), triangles Lam et al. [59] ($Re = 6000$), crosses Prasad and Williamson [106] ($Re = 5427$).

with $||\Omega||$ and $||S||$ the trace of the skew-symmetric and symmetric components of ∇u_i. Positive values of Q correspond to an area where rotation is greater than strain (Hunt et. al. 1988).

Figs. 3.5 and 3.6 depict the side and top views, respectively, of $Q^* = 3$ iso contours-contours. In general, the wake and its changes with respect to rotation ratio, as well as the structures captured are quite similar to those observed via experiments by Inoue et al. [41] at a lower Reynolds number $Re = 800$. It should be borne in mind that turbulence intensity is greatly affected by rotation speed, hence, when it comes to turbulent structures there is no a fair comparison between the different studied cases. As the spin ratio increases from $\alpha = 0$ to $\alpha = 1$, symmetry in the flow is broken and the wake slightly deflects in the direction of the tangential velocity (Figs. 3.5a and 3.5b). However, in agreement with reported observations at low rotating ratios [60] the wake structure does not change dramatically, i.e. the wake preserves its main structure with alternating vortices being shed from top and bottom shear layers. Visible in Figs. 3.6a and 3.6b are vortex tubes (marked VT for clarity) and ribs typical for these type of flows. As the spin ratio increases,

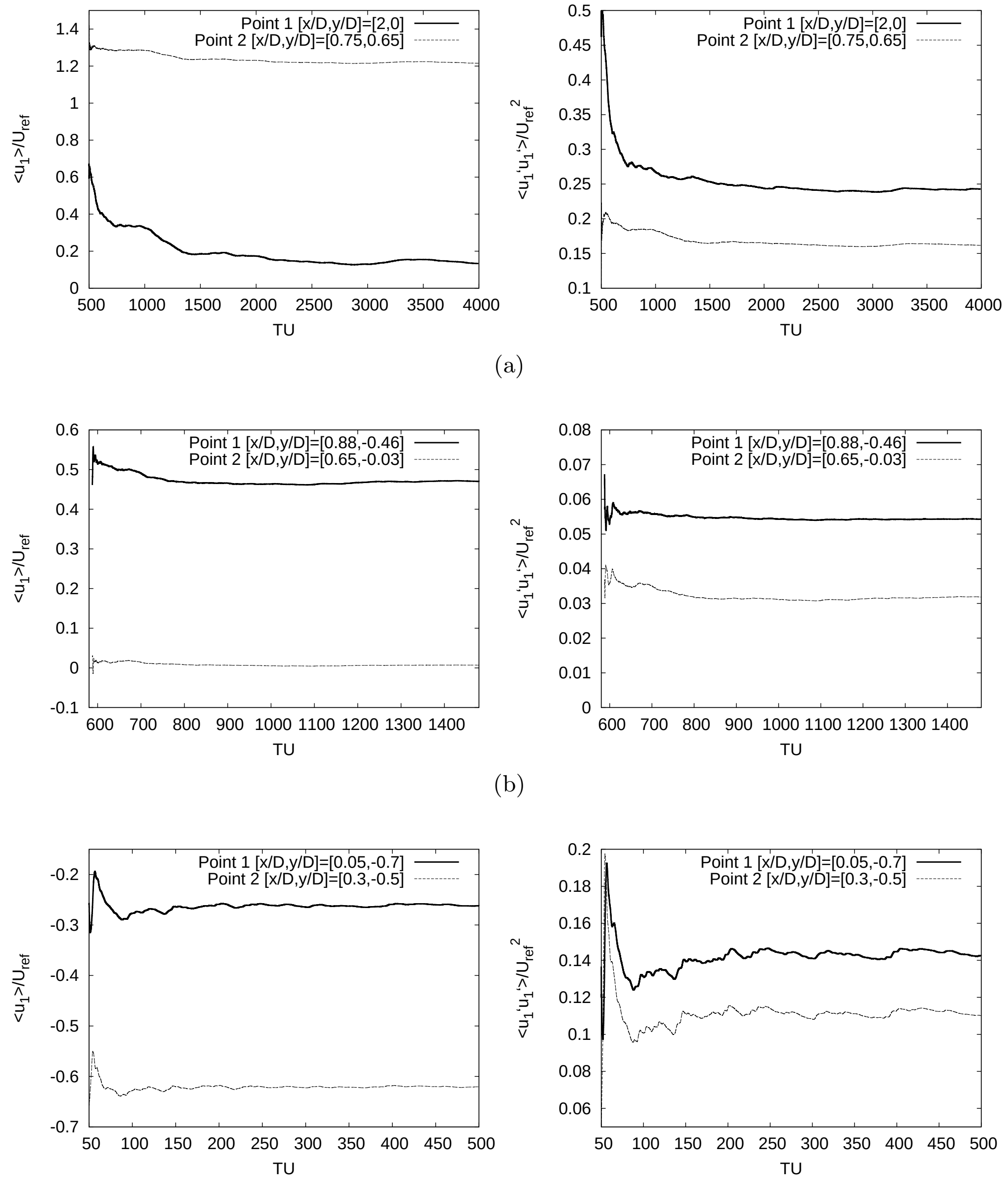

(a)

(b)

(c)

Figure 3.4: Time evolution of the average (left) stream wise velocity $< u_1 > /U_{ref}$ and (right) stream wise Reynolds stresses $< u_1' u_1' > /U_{ref}^2$ at different stations. (a) $\alpha = 0$, (b) $\alpha = 2$, (c) $\alpha = 5$.

rotation affects the shear layers and the way they interact with each other. At $\alpha = 2$, both shear layers cease their interaction and thus, the formation of the span wise coherent alternating vortices is inhibited (see Fig. 3.6c). We will discuss the effect of rotation on the shear layer topology in detail in the next section. The vortex shedding suppression causes the wake structure to change. At this rotation ratio the wake seems to be influenced mainly by the flow coming from the bottom of the cylinder. Furthermore, the coherent span wise vortex tubes are no longer visible. The wake is now composed of small scale vortices that detach in an un-organized fashion from the geometry, showing a fully turbulent wake with no coherence on the span wise direction, as evidenced by Fig. 3.6c.

It is worth noting the differences in the shear layers on the top and bottom sides, shown in Fig. 3.7 using non-dimensional span wise vorticity ω_3^* at values corresponding to 5.5% of the maximum vorticity level at the cylinder surface (see next section for more details). For both $\alpha = 1$ and $\alpha = 2$, the top shear layer separates laminarly from the cylinder and transitions to turbulence downwind. This transition occurs dominated by Kelvin-Helmholtz-like instabilities similar to what is observed on the non-rotating cylinder [55]. As the instabilities grow, crescent-shaped structures are formed in the zone where the shear layer rolls-up (see figs 3.7a, b). On the other hand, the bottom shear layer due to the influence of the moving surface (in the opposite direction to that of the main flow) does not show this shape, rather it transitions quite fast to a turbulent flow with the point of transition moving windward. Notice also the shear layer instabilities which have moved upwards close to the cylinder. Furthermore, the top shear layer bends in the direction of tangential velocity which, with the increase in the spin ratio, eventually wraps around the cylinder surface creating a vortical layer encompassing the whole circumference (more details in Section 3.3.2). For $\alpha = 3$ and $\alpha = 4$, the wake in the cross flow direction is thinner than for the other rotation ratios, as observed in Fig. 3.5. This reduction in wake width coincides with the rotation ratios where the drag coefficient is at its lowest (see Section 3.3.3). As rotation ratio increases to $\alpha = 5$ the wake is wider than for $\alpha = 3$ and $\alpha = 4$; this is a consequence of the increase in rotational velocity. As was

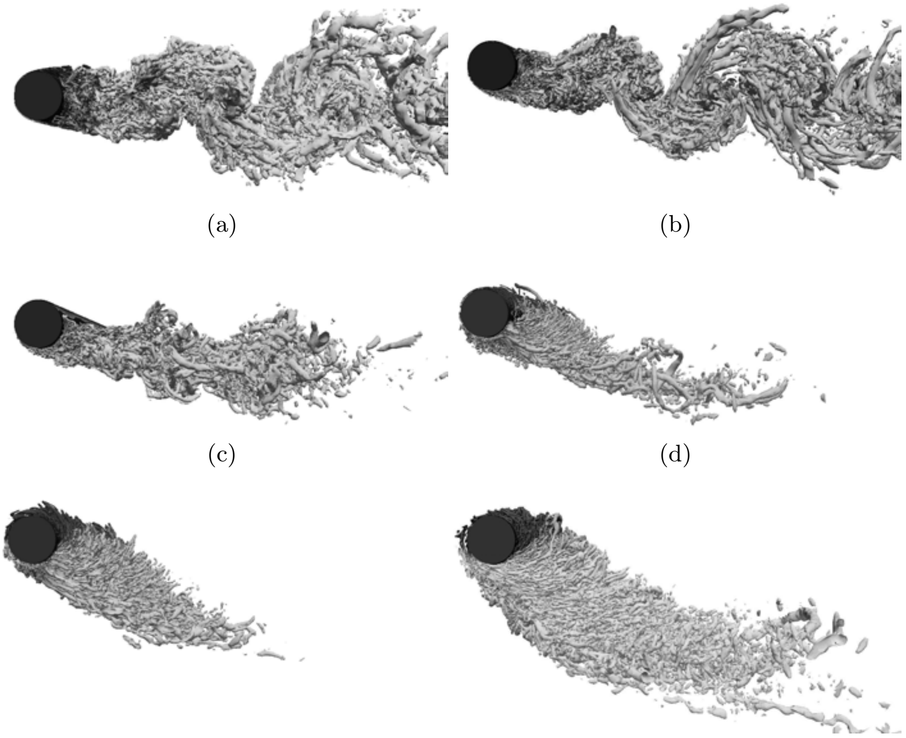
(a) (b) (c) (d) (e) (f)

Figure 3.5: Coherent structures represented by means of $Q^* = 3$ iso contours colored by pressure. (a) $\alpha = 0$, (b) $\alpha = 1$, (c) $\alpha = 2$, (d) $\alpha = 3$, (e) $\alpha = 4$ and (f) $\alpha = 5$.

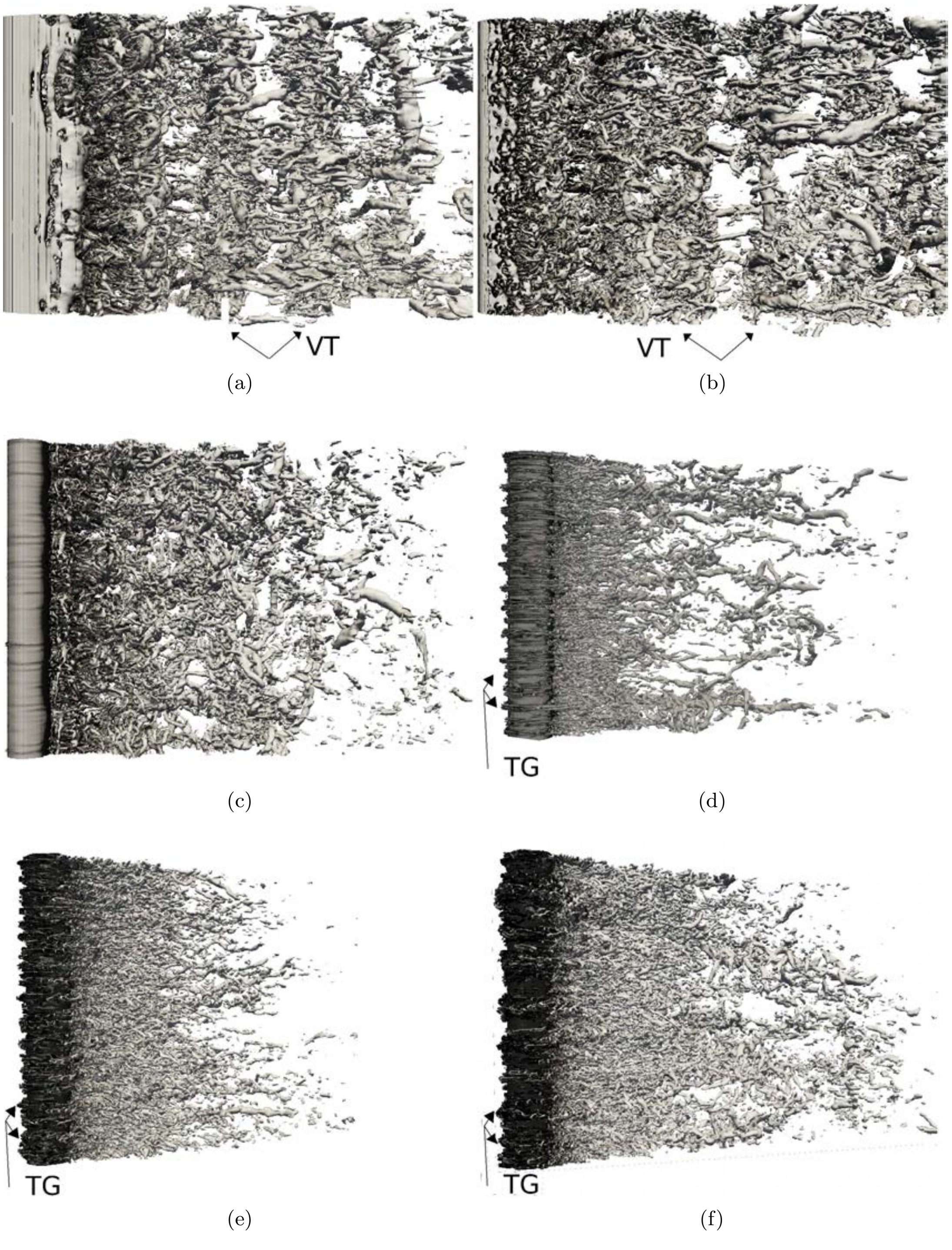

(a) (b)

(c) (d)

(e) (f)

Figure 3.6: Coherent structures viewed from the top of the cylinder (surface velocity in the same direction as flow velocity) represented by $Q^* = 3$ isosurfaces. (a) $\alpha = 0$, (b) $\alpha = 1$, (c) $\alpha = 2$, (d) $\alpha = 3$, (e) $\alpha = 4$ and (f) $\alpha = 5$.

observed by Matsui [78] and later by Mittal and Kumar [81], vorticity builds-up in the zone near the stagnation point (which has moved off of the cylinder) and allows the formation and shedding of vortices in the sense of rotation, feeding the wake and increasing its width. This phenomenon is also associated with the formation and growth of Taylor-Görtler vortices (TG) on the cylinder surface. The onset of TG vortices can be observed at $\alpha = 2$ (see 3.6c) and are fully developed for $\alpha = 3$ (see Fig. 3.6d). These vortices appear over the span of the cylinder and as spin ratio increases they increase in size.

For $\alpha = 5$, the TG vortices present are much larger and both the span wise distribution

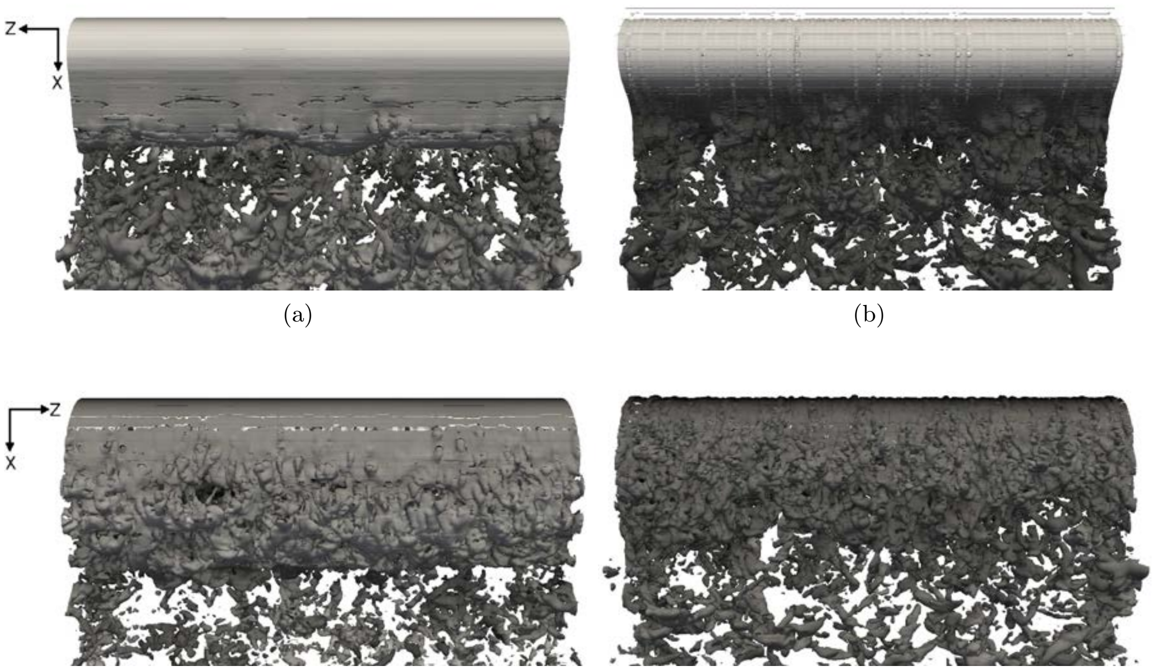

(a) (b)

(c) (d)

Figure 3.7: Top and bottom shear layers depicted through non-dimensional spanwise vorticity iso surfaces. (a) $\alpha = 1$ top $\omega_3^* = -2.46$, (b) $\alpha = 2$ top $\omega_3^* = -1.78$, (c) $\alpha = 1$ bottom $\omega_3^* = 3.79$ and (d) $\alpha = 2$ bottom $\omega_3^* = 4.30$.

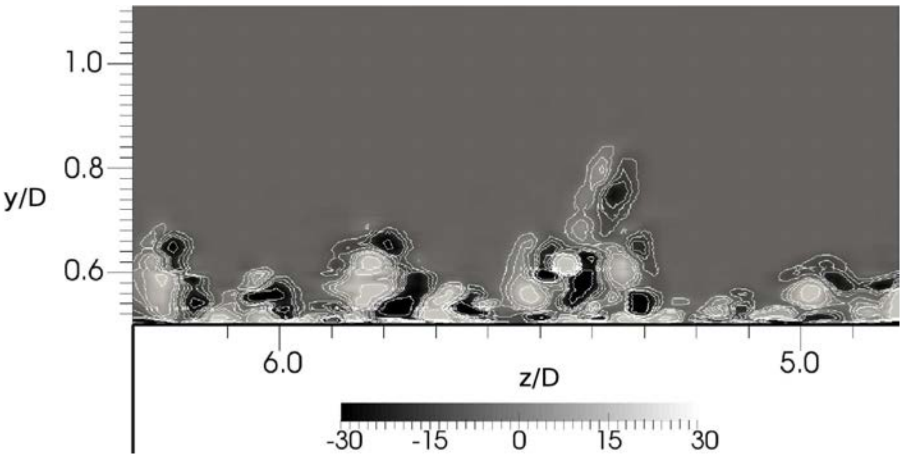

Figure 3.8: Identification of Taylor-Görtler vortices at the cylinder surface for $\alpha = 5$ using non-dimensional stream wise vorticity ω_1^*, at the plane $x = 0$.

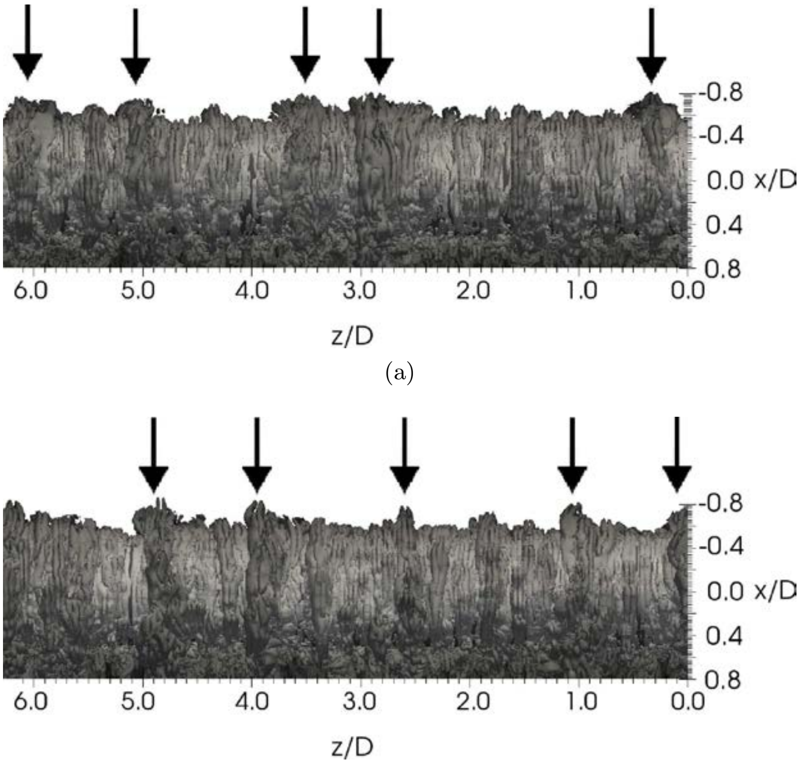

(a)

(b)

Figure 3.9: Span wise location for the build up of TG structures at $\alpha = 5$ at two different times. (a) 82.5 TU (b) 500.0 TU viewed using non-dimensional stream wise vorticity $\omega_1^* = \pm 15$, colored by velocity magnitude.

and time-dependent behavior change. At $\alpha = 5$, these vortex rings seem to cluster up along the span, building in size and posteriorly being shed off the top of the cylinder. The changes in flow configuration, particularly the location of the stagnation point and the large vortical layer wrapping around the surface (see Section 3.3.2), allow the TG vortices to increase their size. The TG structures present for $\alpha = 5$, that form and detach from the rotating boundary layer, are shown in more detail in Fig. 3.8. These structures are composed of pairs of counter rotating stream wise vortices that cluster around in groups throughout the span. By observing the mechanism of their formation it seems that the span wise location where these structures form and grow up varies in time in a random-like manner (see Fig. 3.9). The shedding of these structures is illustrated for three consecutive time instants in Fig. 3.10. In the figure, the process of detachment of the structure from the rotating boundary layer be observed. For clarity, a TG structure detaching from the top of the cylinder is marked. This vortex shedding is accompanied by an unsteady behavior in the near wake flow with a clear footprint in the velocity fluctuation spectrum (see Section 3.3.3).

The TG structure build-up is carried out by the interaction between the main flow and the rotating surface. Furthermore, stagnation point, now off of the cylinder, is located further away from the surface for $\alpha = 5$ than for $\alpha = 4$ resulting in a larger region within the vortical layer wrapped around the cylinder (see Section 3.3.2). This bigger region allows the vorticity pile-up to be larger before being shed to the near wake.

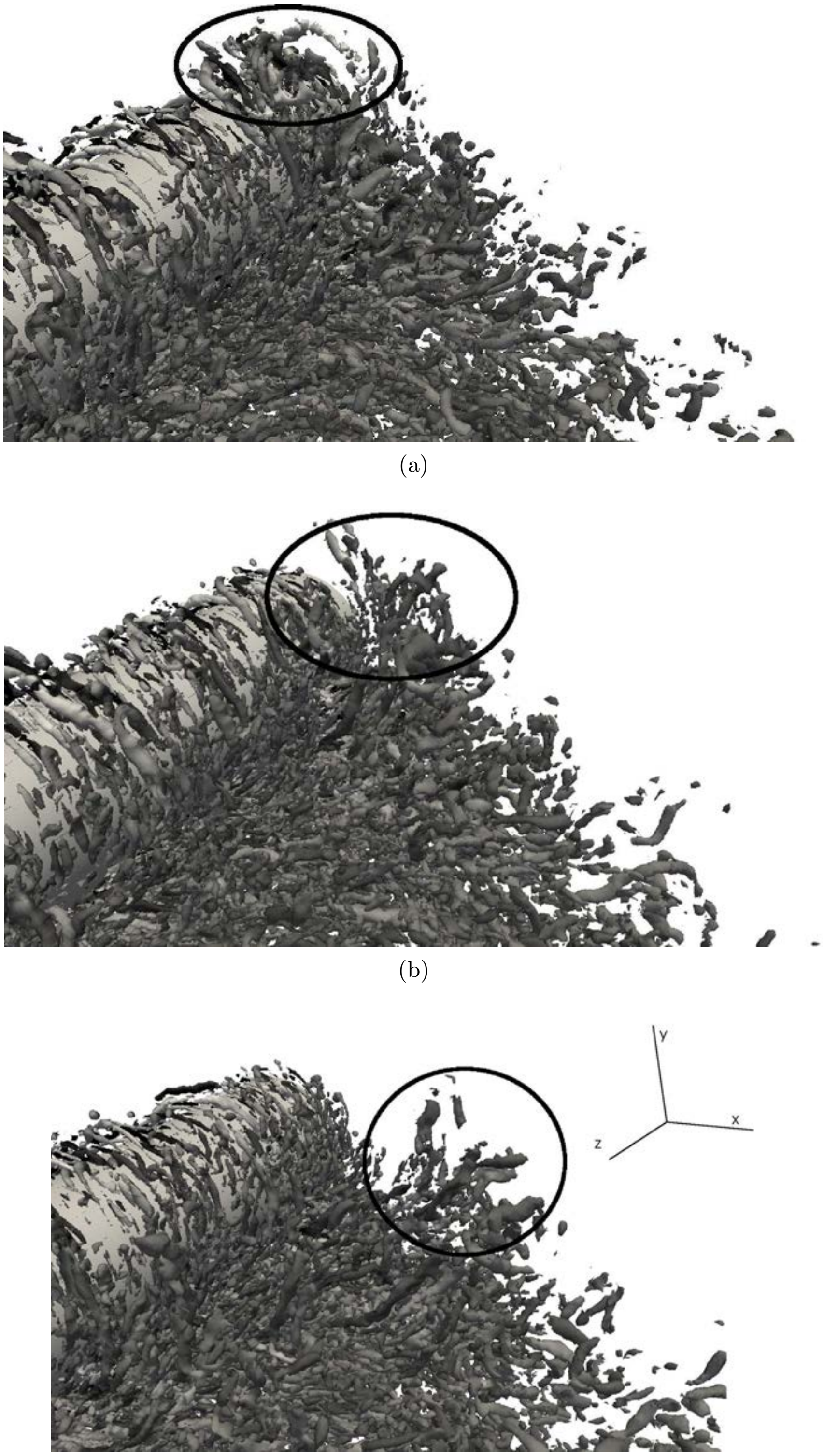

(a)

(b)

(c)

Figure 3.10: Shedding of structures in the stream wise direction for $\alpha = 5$. (a) 82.5 TU (b)83.0 TU (c) 83.5 TU. Non-dimensional Q iso contours $Q^* = 3$, colored by stream wise vorticity.

3.3.2 Mean flow characteristics

In the previous section the effects of rotation in the instantaneous flow and coherent structures have been discussed. These changes are also reflected in the mean flow. Fig. 3.11 shows the averaged streamlines colored by average pressure in the x-y plane. In the figure, the changes brought upon by the rotation of the cylinder can be observed. For $\alpha = 0$ the flow adopts the symmetrical configuration characteristic of this kind of flow at sub-critical Re numbers, i.e. shear layers are of the same length and the average flow adopts the typical two vortex configuration. Other characteristics for this flow are also observed: flow separation occurs symmetrically at the cylinder apex, and both stagnation and saddle points fall within the symmetry plane. As commented before, rotation breaks the symmetry in the flow. For $\alpha = 1$, as the wake is deflected in the direction of tangential velocity, the top vortex is smaller than the bottom one (see Fig. 3.11b). Furthermore, rotation affects the vortex formation zone provoking its shrinkage. In Table 3.3, average flow parameters are given. Notice that the recirculation zone shrinks around 42% respect to $\alpha = 0$, whereas saddle and stagnation points move closer to each other. Furthermore, flow separation on the downstream moving wall (top) is delayed, in agreement with the observations of Ludwig [73]. However, for $\alpha = 5$, the large vortical layer wrapped around the cylinder inhibits flow attachment to the downstream moving wall. For the upstream moving wall incoming flow does not attach to the wall for any rotation case, although a boundary-layer flow exists between the main flow and the moving surface and flow detaches from this fluid layer.

The length and shape of the shear layers also changes as a consequence of rotation. The top shear layers curve towards the side with the lower pressure gradient, whereas the bottom shear layer, influenced by the oncoming flow and the rotatory surface diffuses quite faster than the top one. Thus, both shear layers become asymmetric and with different lengths, as depicted in Fig. 3.12. To perform a quantitative analysis of the differences in the shear layers between the rotation ratios the shear-layer length, l_{SL}, is evaluated. This length, defined in a similar fashion as in Dong et al. [22], is here evaluated as the distance from the tip of a span wise contour line at a level 5.5% of the maximum vorticity level over the cylinder surface such that $\omega_3^* = 0.055\omega_{max}^*$. Using this criterion, the shear layers are identified in Fig. 3.12. In the figure, the length of both top and bottom shear layers is given. As can be seen, the shear layer length reduces as α increases. For $\alpha = 0$, both layers have the same length $l_{SL} = 1.57D$, which reduces to $l_{SL} = 1.25D$ in the top and $l_{SL} = 0.98D$ in the bottom for $\alpha = 1$, about 20.4% and 37.6%, respectively. This reduction is even more pronounced for $\alpha = 2$ (see Fig. 3.12). As the rotation ratio increases the changes observed at $\alpha = 1$ are magnified, i.e. the top recirculation vortex moves downward and recirculation region shrinks further (see Figs. 3.11c-d). At $\alpha = 3$ the top vortex does not form and the bottom one is barely visible, being the recirculation zone confined to a reduced region which is less than 10% of that at $\alpha = 0$. These effects are brought upon by the shear layers wrapping around the cylinder. In fact, at $\alpha = 3$ the bottom shear layer does not form and the top shear layer has almost rolled over the cylinder (see Fig. 3.12).

Table 3.3: Flow parameters. Recirculation length (L_{rec}/D), coordinates of the saddle point S and its angular position (θ_s), location of the stagnation point (θ_{sp}) and angular position of the separation points θ_{sep-D} (downstream moving wall) and θ_{sep-U} (upstream moving wall). *Point off the cylinder. Angles are measured in counter-clockwise direction.

α	L_{rec}/D	S $(x/D, y/D)$	θ_s	θ_{sp}	θ_{sep-D}	θ_{sep-U}
0	1.36	(1.86,0)	180°	0°	274.8°	82.2°
1	0.79	(1.27,-0.27)	168°	10°	257.7°	39.4°*
2	0.42	(0.86,-0.38)	156.2°	30°	248.5°	44.2°*
3	0.10	(0.41,-0.47)	131.1°	45°	247.7°	67.1°*
4	-	(0.13,-0.64)	101.5°	101.5°*	253.4°	-
5	-	(0.01,-0.97)	89.4°	89.4°*	-	-

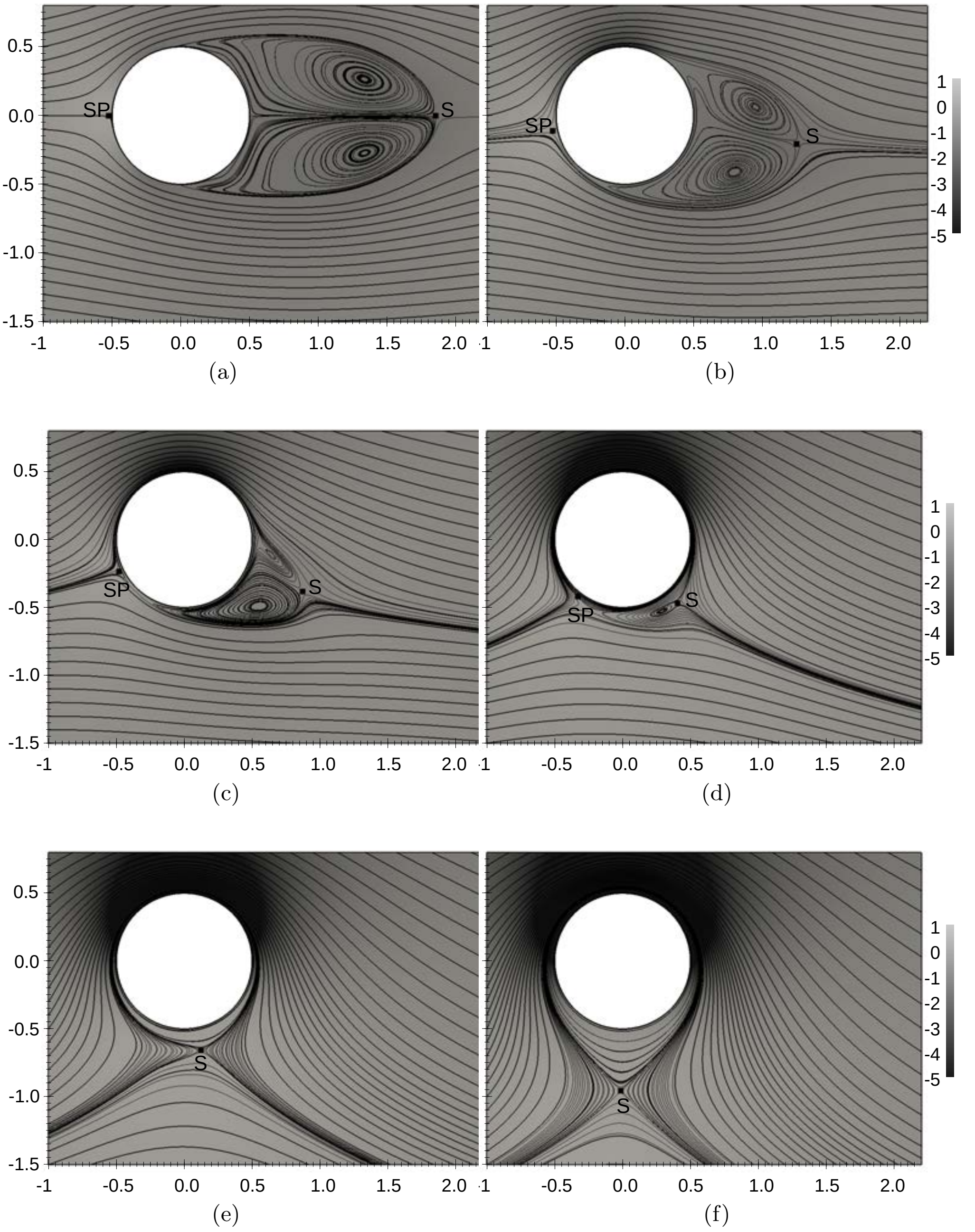

Figure 3.11: Streamlines and pressure field for the different rotation ratios. (a) $\alpha = 0$, (b) $\alpha = 1$, (c) $\alpha = 2$, (d) $\alpha = 3$, (e) $\alpha = 4$, (f) $\alpha = 5$. The location of the saddle point 'S' and stagnation point 'SP' are also marked in the figure.

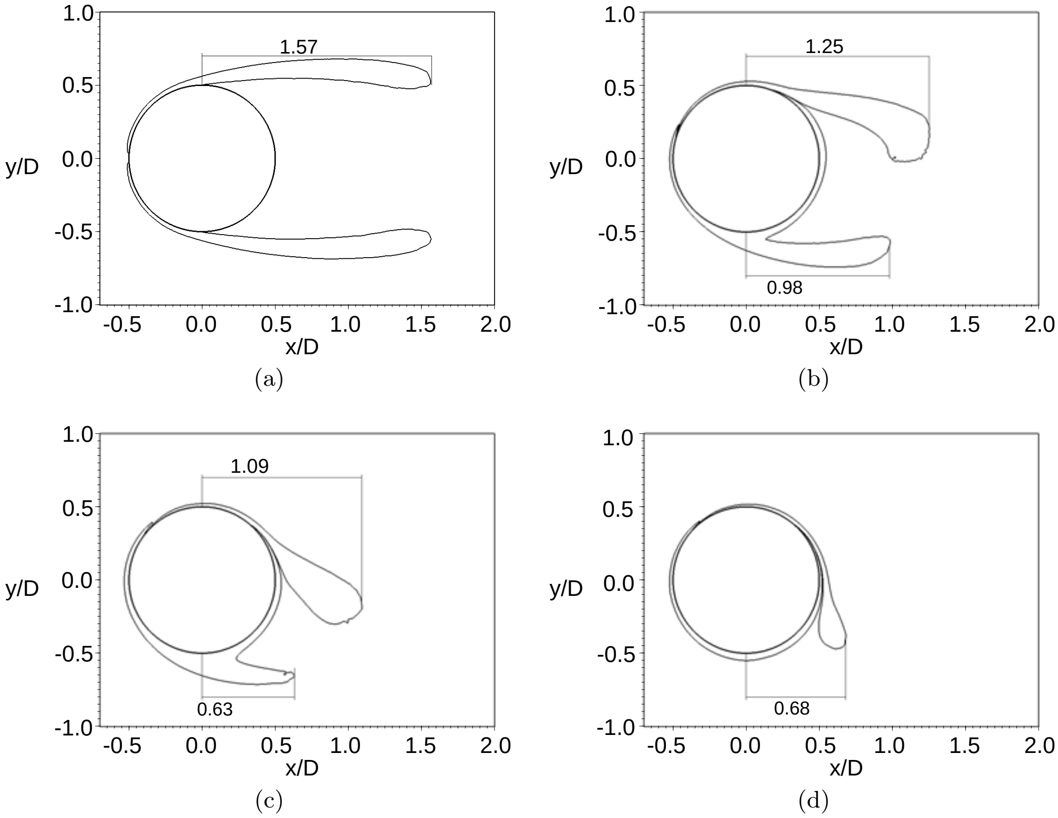

(a) (b) (c) (d)

Figure 3.12: Shear layer length viewed using threshold values of non-dimensional span wise vorticity $\omega_3^* = 5.5\%\omega_{max}^*$. (a) $\alpha = 0$, (b) $\alpha = 1$, (c) $\alpha = 2$ and (d) $\alpha = 3$.

At higher rotation ratios, $\alpha \geq 4$, a second change in the wake structure occurs. The stagnation point and the saddle point both have come closer together and now coincide in their location, off the cylinder surface (see Table 3.3). As a consequence of the high rotational speed, a region of high vorticity wrapped around the cylinder is formed. This region, hereafter referred to as circumvolving layer, is depicted in Fig. 3.13. In the figure, the same criterion for identifying the shear layers has been used. This circumvolving layer, enclosed between the cylinder surface and the outer edge of the vortical region is characterized by a non-constant thickness which also increases with rotation

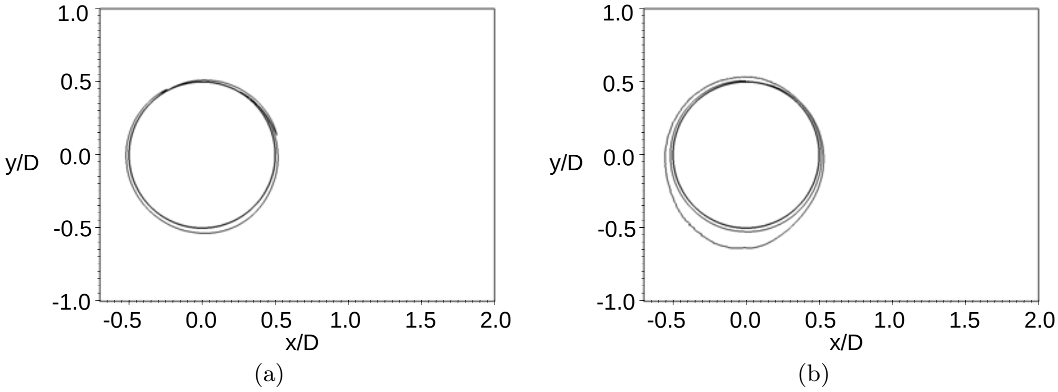

(a) (b)

Figure 3.13: Circumvolving layer viewed using threshold values of non-dimensional span wise vorticity $\omega_3^* = 5.5\%\omega_{max}^*$. (a) $\alpha = 4$, (b) $\alpha = 5$.

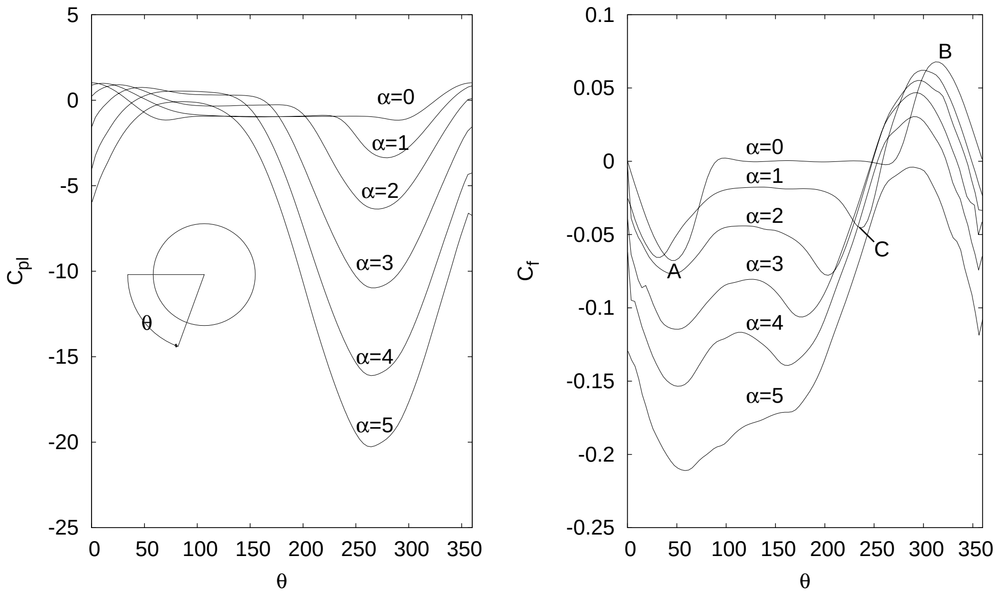

(a) (b)

Figure 3.14: Effect of the rotation ratio on (a) local pressure coefficient and (b) local skin friction coefficient around the cylinder surface. 0° corresponds to the front of the cylinder and angles are measured in counter clock wise direction.

ratio. As can be seen in the figure, the circumvolving layer is thicker near the stagnation zone $\theta \approx 90°$. As a result of the increase in vorticity, this layer strengthens with increasing spin ratio, and pushes the stagnation point off the cylinder. For these spin ratios recirculation area in the mean flow is not visible (see Figs. 3.11e and 3.11f).

3.3.3 Force coefficients

As the cylinder rotates, the fluid velocity on the top of the cylinder increases inducing a drop in the pressure. This low pressure zone on the top of the cylinder increases in size and lowers in magnitude as rotation ratio increases, and in turn affects the force coefficients acting on the cylinder surface (see Table 3.4). The local pressure coefficient and skin friction distributions along the cylinder circumference are plotted in Fig. 3.14. For the non-rotating case, as expected, the pressure distribution is symmetric corresponding with the symmetric wake configuration described

Table 3.4: Base pressure ($C_{p_{base}}$), minimum pressure (p_{min}), drag coefficient C_D, lift coefficient C_L, lift coefficient fluctuations C_{Lrms}, and lift to drag C_L/C_D ratio. **Pressure maximum in the cylinder surface.

α	0	1	2	3	4	5
p_{min}	-1.2	-3.3	-6.4	-10.9	-16.2	-20.6
$C_{p_{base}}$	-0.94	-0.99	-0.32	0.32	0.54**	0.05**
C_D	1.05	0.90	0.36	0.18	0.25	0.64
C_L	0.00	1.40	4.47	8.93	13.21	16.01
C_{Lrms}	0.19	0.40	0.08	0.06	0.04	0.68
C_L/C_D	0.00	1.56	12.42	49.61	52.84	25.02

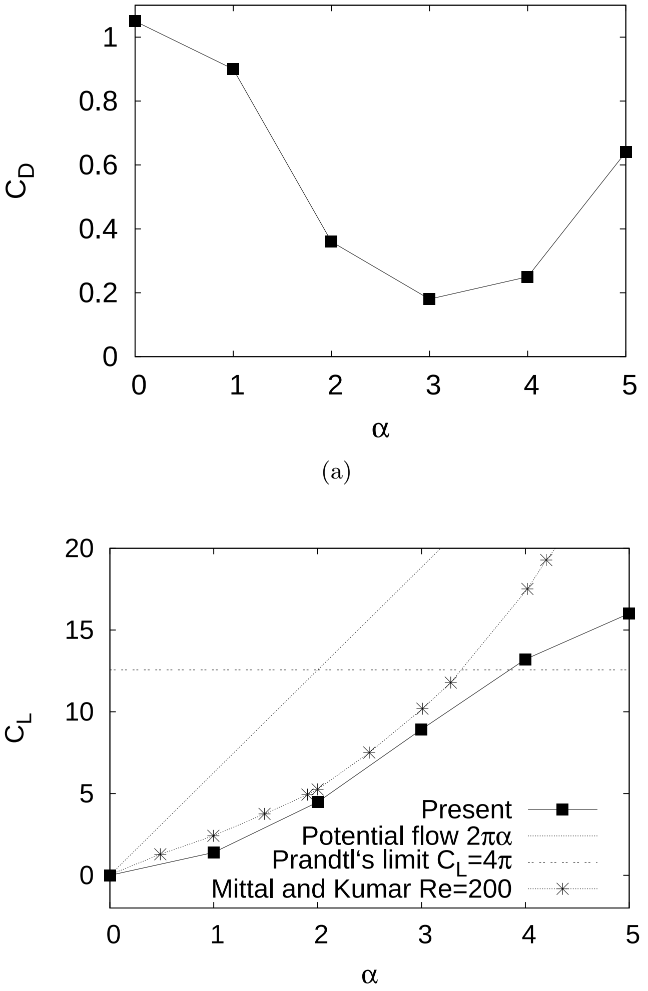

(a)

(b)

Figure 3.15: (a) Drag coefficient and (b) lift coefficient behavior with respect to rotation ratio. Comparison with potential flow theory ($2\pi\alpha$), Prandtl's limit (4π) and results from Mittal and Kumar [81] for $Re = 200$.

in the previous section. With the increase in angular velocity, as the recirculation region not only shrinks but also decreases in width, the cylinder base region reduces its angular span while increases its value (see Fig. 3.14a for $\alpha \leq 3$). At these low rotation ratios, there is a significant reduction of the drag coefficient and the magnitude of the lift force increases (see also Fig. 3.15).

Prandtl [103] stated that the maximum lift in such configuration is limited to 4π, however, the theory presented by Glauert [30] stated that lift should increase indefinitely with rotational speed. In general, quite different solutions are reported. Present results, although larger than the theoretical limit proposed by Prandtl [103], are lower than those presented by Mittal and Kumar [81] from 2D simulations for a lower Reynolds number ($Re = 200$). Nonetheless, the behavior for the lower rotation ratios is quite similar. The larger departures from the values obtained by Mittal and Kumar [81] are produced for the higher rotation ratios, at $\alpha > 3$, where the rate of increase of the lift coefficient with respect to spin ratio decreases, as can be observed in Fig. 3.15b. These differences might be attributed to the three-dimensional effects induced by the turbulent flow at the present Reynolds number $Re = 5000$.

For the higher rotation rates, $\alpha \geq 4$, the pressure distribution shows a very different trend respect to the other cases (see Fig. 3.14a). For these rotation ratios there is no base pressure, as is to be expected with the changes in flow configuration and the disappearance of the recirculation region; in its place, a high pressure zone is found near the location of the stagnation point, now off the cylinder surface. Furthermore, the low pressure zone on top of the cylinder now spans for much of the circumference (see Fig. 3.14a). It is worth noting that both pressure and flow distributions for high rotation rates resemble those of potential flow. Mittal and Kumar [81] did also observe the same behavior at a lower Reynolds number of $Re = 200$, where for the higher spin rates the pressure distribution is qualitatively similar to that resulting from inviscid flow.

The behavior of the drag coefficient follows a different trend than the lift coefficient. For the low rotation configuration ($\alpha \leq 3$), where there is a recirculation zone behind the cylinder, the drag coefficient decreases to increase again for the higher rotation ratios, $\alpha \geq 4$. This is due to the aforementioned changes in the pressure distribution and wake configuration brought upon by rotation.

In addition, it is interesting to analyze the effect of rotation on the skin friction (see Fig. 3.14b). Three peaks are shown in the figure. A bottom peak, located at $\theta \approx 45°$ for $\alpha = 0$ (thereafter referred to as A), a second peak, located at $\theta \approx 315°$ for $\alpha = 0$ (thereafter referred to as B), and a rotation-induced peak near the back (thereafter referred to as C), seen at $\theta \approx 240°$ for $\alpha = 1$. Chew et al. [11], from 2D simulations at $Re = 1000$, observed a limiting value for peak A, he did not see the appearance of peak C and reported that skin friction and local pressure distributions veered towards self-similarity. They further argued that self-similarity led to an asymptotic behavior in the force coefficients. The behavior resulting from the present simulations is quite different, as no self-similarity nor a limiting value for peak A are observed whatsoever, and force coefficients do not behave asymptotically. For $\alpha = 0$, the typical antisymmetric distribution is observed and peaks A and B have the same magnitude, although opposite sign. As spin ratio increases, this distribution greatly changes. For spin ratios $\alpha < \alpha_{crit}$, peak A, although moving upstream, does not exhibit a magnitude increase. Furthermore, peak B moves slightly downstream, consistent with the delay in flow separation. As angular velocity increases, the velocity gradient near the wall around peaks A and C increases as well, contributing in the creation of the vortical layer observed in this zone (see Fig. 3.12b-d) prior to the full wrap-around of the shear layers. Moreover, peak B continues to move downstream as its maximum value decreases for all spin ratios until, for $\alpha = 5$, where the velocity gradient on top of the cylinder is always negative.

3.3.4 Periodic behavior

As commented before, rotation affects the wake and the vortex shedding. These changes can readily be seen if the instantaneous lift is inspected. In Fig. 3.16a, a segment of the time history of the lift coefficient for the different rotation ratios is presented. As the shear layers have moved closer as a consequence of the rotation (from $\alpha = 0$ to $\alpha = 1$), and rotation seems to suppress some three-dimensional effects reported at $Re = 5000$ for $\alpha = 0$ [87, 106, amongst others], the coherence in the span wise direction is enforced and thus an increase in the magnitude in the fluctuations is observed. However, once the rotation ratio surpasses the critical value $\alpha_{crit} = 2$, the asymmetry in the shear layers is magnified (see Fig. 3.12 where the length of the bottom shear layer is too small at $\alpha = 2$). As a result, shear layers can not interact between each other and vortex shedding ceases. This is reflected in the amplitude of the fluctuations of the lift which reduces fivefold (see Fig. 3.16a and Table 3.4). Yet, as discussed in Section 3.3.1, for $\alpha = 5$ the formation and shedding into the wake of TG structures on one side of the cylinder was observed to happen accompanied by the appearance of an unsteady behavior in the lift force. As can be seen in Fig 3.16a, the amplitude of the lift fluctuations greatly increases for this spin ratio. This can also be observed

Table 3.5: Dominating non-dimensional frequencies (St). *Vortex shedding twin peak for $\alpha = 5$.

α	0	1	2	3	4	5*
St_{vs}	0.209	0.223	-	-	-	0.046 - 0.067
St_{KH}	1.83	1.80	-	-	-	-

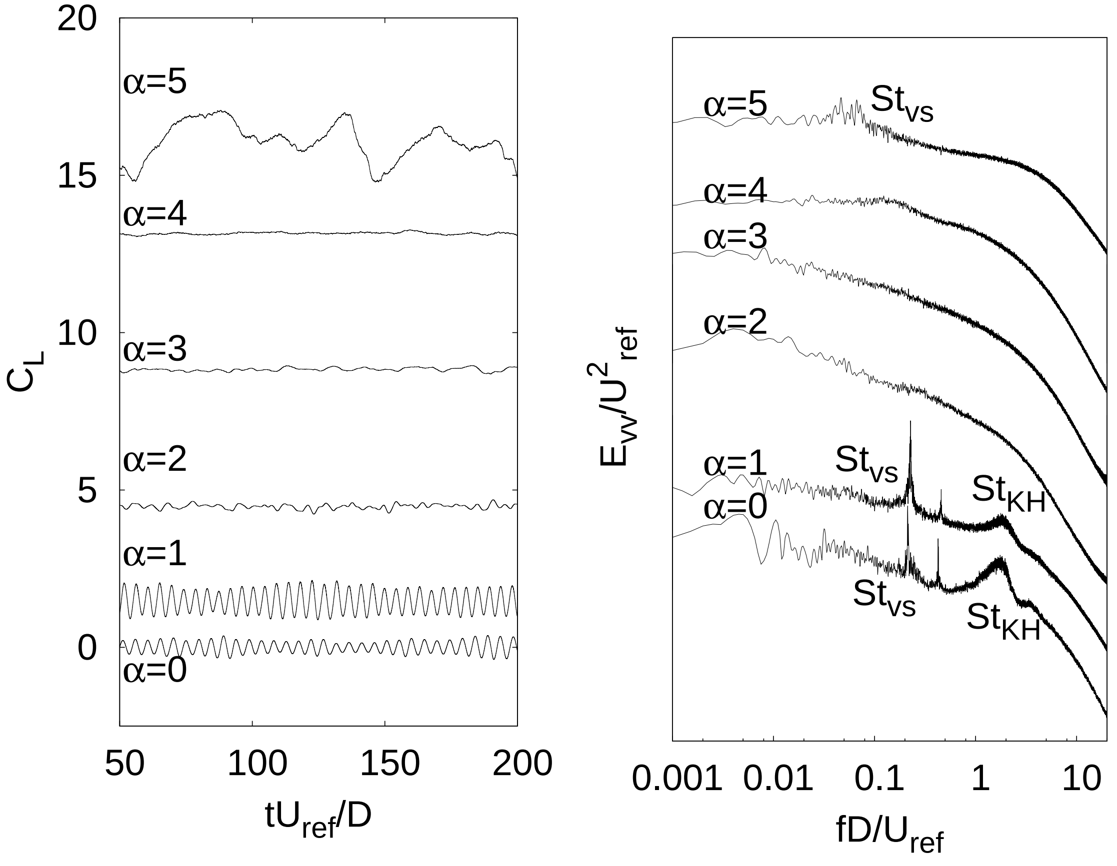

(a) (b)

Figure 3.16: (a) Segment of the instantaneous lift coefficient; (b) Energy spectrum of a probe located in the near wake at different rotation ratios. For clearness, the y-axis in (b) is shifted.

by the inspection of the non-dimensional energy spectrum of the cross-stream velocity fluctuations E_{vv}/U^2_{ref} of a probe located in the near wake (see Fig. 3.16b). In the figure, an energetic peak at the vortex shedding frequency can be observed at $\alpha < \alpha_{crit}$. Notice also a secondary broad-band peak at a larger frequency. This peak is related to the shear layer instabilities which are registered at these low rotation ratios. At larger rotation ratios, no vortex shedding peak is observed in the spectrum, although at $\alpha = 5$, the spectrum well captures a double peak at non-dimensional frequencies $St = 0.046$ and $St = 0.067$ which seem to be the footprint of the TG vortices shed from one side of the boundary layer. Similar peaks were also observed at this rotation ratio for lower Reynolds numbers [127]. A summary of these frequencies is also given in Table 3.5.

3.4 Conclusions

In this work, direct numerical simulations of the flow around a circular cylinder at $Re = 5000$ and rotation ratios $0 \leq \alpha \leq 5$ have been carried out. For the low rotation ratios $\alpha < \alpha_{crit}$, the wake dynamics does not change drastically; shear layers interact with each other and vortex shedding takes place. However, rotation causes the wake to be deflected in the direction of tangential velocity and shear layers to shrink. In addition, as the symmetry is broken by rotation, shear layers have different lengths on each side of the cylinder. For $\alpha = 1$ top shear layer length reduces by 20.4%, whereas the bottom one does so by 37.6%. As a consequence of the reduction in the shear layers' length other aspects are also affected; vortex formation region shrinks by 41.9% for $\alpha = 1$ and vortex shedding frequency increases slightly. Moreover, the changes in the flow structure are also evident in the location of several points of interest such as the stagnation point, shifting from 0° at $\alpha = 0$ to 10° for $\alpha = 1$, or the saddle point moving in accordance with the formation region shrinkage and the wake deflection. Furthermore, flow separation is delayed in the downstream moving wall, whereas the separation point in the upstream moving wall moves windward. The changes in the flow field are accompanied by changes in the force coefficients. At $\alpha = 1$ the lift coefficient is $C_L = 1.40$, while the drag coefficient reduces by 14.3% with respect to $\alpha = 0$. Moreover, as the shear layers come closer together some three-dimensional phenomena present for the non-rotating case are vanished, enforcing the coherence of the vortex tubes behind and resulting in higher lift fluctuations, $C_{Lrms} = 0.4$ for $\alpha = 1$, vs. $C_{Lrms} = 0.19$ for $\alpha = 0$.

The effects of rotation as spin ratio reaches α_{crit} are magnified . In agreement with previous works, a critical rotation ratio at $\alpha_{crit} = 2$ has been observed in the present work. At this critical rotation ratio, shear layers continue to shrink and deflect in the direction of the tangential velocity. Additionally, vortex formation region shrinks notably as the shear layers cease their interaction, the recirculation length being around 30% of the length obtained for the non-rotating cylinder. Furthermore, both the span wise coherence of the von-Kármán vortex street and periodic shedding of vortices disappear. As a consequence of the loss of the periodic behavior, lift fluctuations are greatly reduced, $C_{Lrms} = 0.08$, while the lift force continues to increase and the drag is further decreased. Moreover, as the shear layers roll over the cylinder the onset of TG vortices is observed.

With further increment of the spin ratio $\alpha > \alpha_{crit}$, both wake dynamics and flow configuration are greatly changed. For $\alpha = 3$ only the top shear layer is formed and it is almost completely wrapped around the cylinder. The vortex formation region length is less than 10% respect to that for $\alpha = 0$. For higher spin ratios the shear layers completely roll over the cylinder, changing the structure of the flow field around it. A circumvolving layer is formed and TG structures form around the cylinder surface. At $\alpha = 4$, the circumvolving layer forces the stagnation point off the cylinder surface, merging the saddle point with the stagnation point into the same physical location. Furthermore, the recirculation region is no longer present. Due to these changes in the flow configuration, the decreasing trend of the drag coefficient observed for lower rotation ratios changes. Drag coefficient reduces from $C_D = 1.05$ for $\alpha = 0$ to $C_D = 0.18$ for $\alpha = 3$ to then increase for the two higher rotation ratios, $C_D = 0.25$ for $\alpha = 4$ and $C_D = 0.64$ for $\alpha = 5$. The lift continues to increase beyond Prandtl's limit of $C_L = 4\pi$, $C_L \approx 5.1\pi$ for $\alpha = 5$; however, for $\alpha > 3$ this rate of increase is lower than for lower spinning ratios. For the larger spin ratio, the growth of the region within the circumvolving layer is observed. In addition, TG structures are clustered in groups along the span in a random-like manner to posteriorly shed from the top side. The footprint of this shedding is observed in the cross-stream wise velocity fluctuation spectrum as a twin peak around $St = 0.046$ and $St = 0.067$. The shedding of these structures is accompanied by large lift force fluctuations, $C_{Lrms} = 0.68$ for $\alpha = 5$, a nearly 260% rise with respect to the non-rotating case. Finally, neither self-similarity nor asymptotic behavior of the forces acting on the cylinder was observed for the rotation relations simulated in the present work.

Appendix: Mesh sensitivity studies for $\alpha = 0$

In order to analyze the influence of some mesh parameters, different resolutions in both the 2D plane and the span wise direction were considered. In Table 3.6, a summary of the meshes and some statistical flow parameters obtained are given.

Furthermore, in Fig. 3.17 a comparison between all the meshes and experiments by Norberg [89] for the velocity and its fluctuations at different locations in the near wake is depicted. All meshes in general perform quite good, however, as commented in Section 3.2.4, some scattering in the results is observed. Norberg's averaged profiles resemble the low-energy mode (mode L) observed at $Re = 3900$ [67] with a two-lobed stream-wise velocity fluctuation profile and a lower stream-wise velocity minimum. Present solutions shows a similar profile to that obtained for the long term solution at $Re = 3900$ in Lehmkuhl et al. [67]

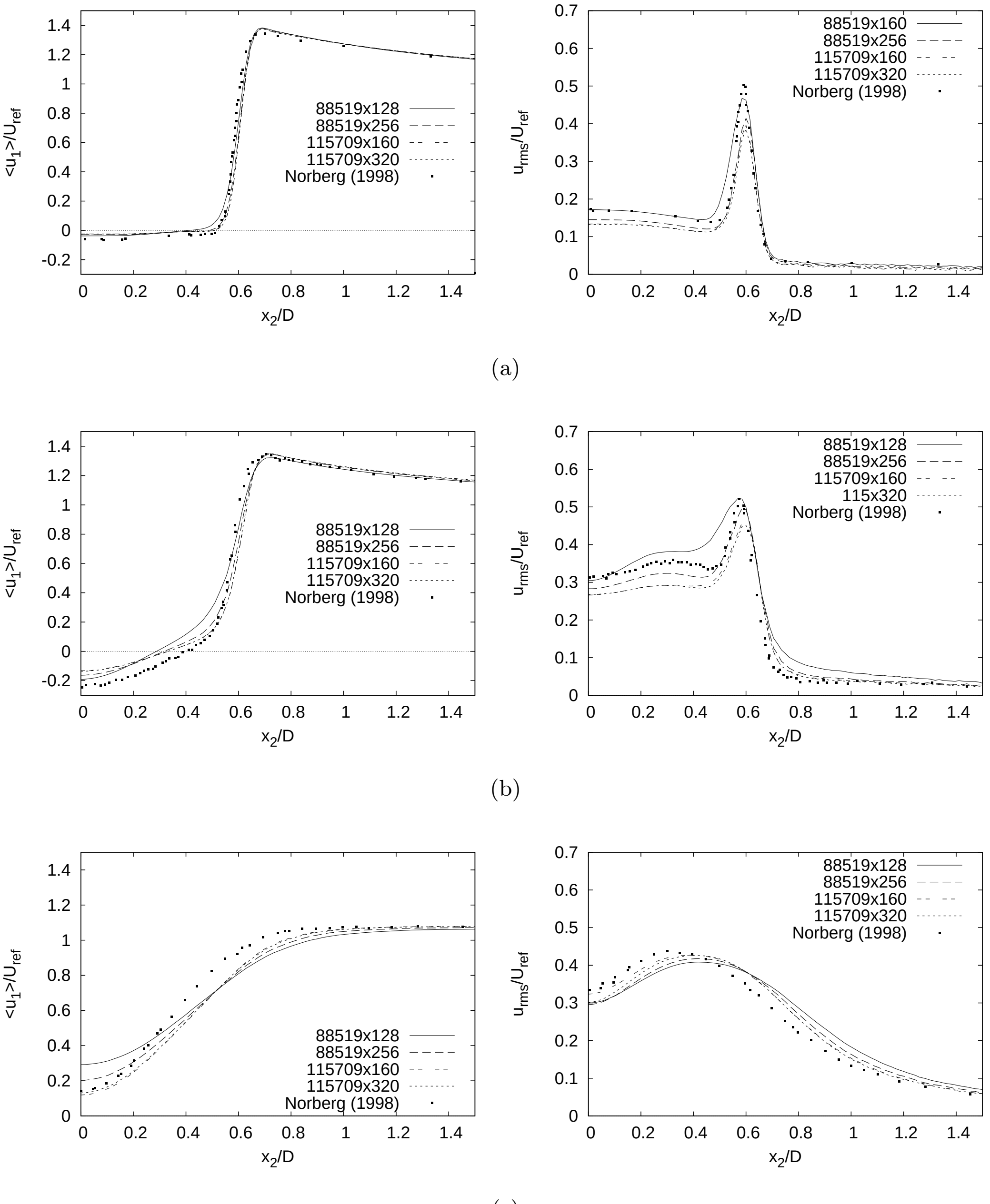

(a)

(b)

(c)

Figure 3.17: Mean stream-wise and stream-wise root-mean-square (rms) velocity in three cross flow locations. (a) x/D=0.6 , (b) x/D=1, (c) x/D=2. Solid line present results and symbols Norberg [89] at $Re = 5000$.

Table 3.6: Mesh sensitivity parameters.

Case	L_z	h/η	C_p	St_{vs}	-$C_{p_{base}}$	L_{rec}/D
88519×128	πD	1.27	1.12	0.210	1.020	1.144
88519×256	$2\pi D$	1.27	1.09	0.209	0.970	1.272
115709×160	πD	1.05	1.06	0.210	0.945	1.365
115709×320	$2\pi D$	1.05	1.10	0.210	0.985	1.237

Chapter 4

Numerical analysis of the turbulent fluid flow through valve geometries.

Main contents of this chapter have been published in:

Rigola, J., Aljure, D. E., Lehmkuhl, O., Pérez-Segarra, C.-D. and Oliva, A. Numerical analysis of the turbulent fluid flow through valves. Geometrical aspects influence at different positions *IOP Conference Series Materials Science and Engineering*90(1):012026

Abstract

The aim of this paper is to carry out a group of numerical experiments over the fluid flow through a valve reed, using the CFD&HT code TermoFluids, an unstructured and parallel object-oriented CFD code for accurate and reliable solving of industrial flows. Turbulent flow and its solution is a very complex problem due to there is a non-lineal interaction between viscous and inertial effects further complicated by their rotational nature, together with the three-dimensionality inherent in these types of flow and the non-steady state solutions. In this work, different meshes, geometrical conditions and LES turbulence models (WALE, VMS, QR and SIGMA) are tested and results compared. On the other hand, the fluid flow boundary conditions are obtained by means of the numerical simulation model of hermetic reciprocating compressors tool, NEST-compressor code. The numerical results presented are based on a specific geometry, where the valve gap opening percentage is 11% of hole diameter and Reynolds numbers given by the one-dimensional model is 4.22×10^5, with density meshes of approximately 8 million CVs. Geometrical aspects related with the orifice's shape and its influence on fluid flow behavior and pressure drop are analyzed in detail, furthermore, flow results for different valve openings are also studied.

4.1 Introduction

The radial outflow between two coaxial disks is technologically important for different applications (radial diffusers, air bearings, valve reeds, etc.). In all these cases the flow is quite complex, presenting a pressure gradient that may be either positive or negative depending on radial location. Furthermore, turbulent flow is often encountered, thus, turbulence models are critical on the numerical resolution of this technological relevant application.

The numerical results are obtained using the three dimensional, parallel, unstructured and object oriented code TermoFluids [64] using LES models, a high Reynolds number (close to real working conditions) and turbulent inlet flow. In fact, the present paper is an updated version of previous works [112] and [110] that used extruded meshes, low Reynolds numbers and did not use low Mach models[111]. agged/redes+sociales/page/10 Experimental ([143] and [24]) and numerical ([119] and [74]) have been performed setting a basis to understand the physics underlying in the flow. First attempts of numerical simulation of turbulent flows by means of RANS $k-\epsilon$ and $k-\omega$ models were carried out under low Re numbers ([95] and [77]). More recently, some papers presents numerical results based on LES turbulent models for low Reynolds number 2.5×10^4 [117], or RANS turbulent models for higher Reynolds numbers 1.6×10^6 [16]. Finally, two-dimensional numerical cases that were experimental validated under specific experimental apparatus, although for very low Reynolds numbers, were presented in [76].

From a compressor study viewpoint the fluid flow is composed by two different physics (entrance flow through a channel and a free jet through a surface)(see fig 4.1a). In that sense, the present paper is focused on the numerical simulation model of the fluid flow through the valve reeds, considering a simplified geometry of an axial hole plus a radial diffuser. The methodology proposed by [121], [8] and [124] is based on two parameters: i) effective flow area $(KA)_e$ that relates the actual mass flow rate with an ideal mass flow rate per unit flow area (assuming isentropic contraction process) defined as $m = (KA)_e(\rho\nu)_{id} = (KA)_e Y \sqrt{2\rho_u(p_u - p_d)}$; and ii) the effective force area A_f defined as ratio of the actual net force on the valve and the force obtained assuming a constant pressure drop distribution, defined as $F = (p_u - p_d)A_f$, the most usual method for valve analysis and compressor design [19]

4.2 Definition of the case

The geometries to be considered are: geometry A (straight) where the hole is cylindrically shaped with constant diameter, and geometry B (cone) where the hole is drawn in a conical way linearly enlarging the diameter. Both cases are fitted with a top plate acting as the valve disc.

Fig. 4.1 shows the geometrical features and computational domain to be studied, where $D = 1.5d$, $s = 0.11d$, $h = 0.24d$, $\alpha = 20°$ and $l = 15d$. Flow inlet is done through the bottom boundary such that $Re = \rho W_{ref} d/\mu = 4.22 \times 10^5$, result obtained from NEST-compressor simulations. NEST analyses thermal, fluid-dynamic and aerodynamic behavior in this type. Synthetic turbulence ([53], [20]) is used to create a turbulent inlet flow, using the Reynolds stresses values for a channel with a $Re_\tau = 6000$ ([120]. Flow outlet is the outer semi-sphere (see Fig. 4.1b). The pressure based outflow condition uses a constant p chosen to fulfill the mass conservation condition at each time step, i.e. the mass inflow equals the mass outflow. In addition, a buffer zone at $r > 14d$ is used where the Reynolds number is decreased from 4.22×10^5 to 4.22×10^3 in order to avoid any influence from non-physical waves reflected by the artificial outflow boundary [140]. The orifice walls, the plate and bottom wall surfaces are modeled using a no-slip condition.

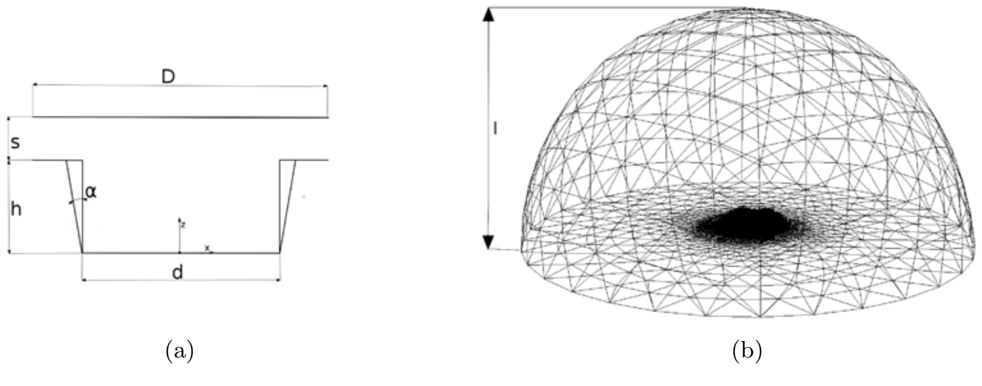

(a) (b)

Figure 4.1: (a) Outline and dimensions for the two valve geometries and (b) Outline of the computational domain.

4.3 Mathematical formulation

4.3.1 Governing equations and numerical method

In order to study the flow, the filtered incompressible Navier-Stokes equations are solved:

$$\frac{\partial \overline{u_i}}{\partial x_i} = 0 \tag{4.1}$$

$$\frac{\partial \overline{u_i}}{\partial t} + \frac{\partial (\overline{u_i u_j})}{\partial x_j} - \nu \frac{\partial^2 \overline{u_i}}{\partial x_j \partial x_j} + \rho^{-1} \frac{\partial \overline{p}}{\partial x_i} = -\frac{\partial \tau_{ij}}{\partial x_j} \tag{4.2}$$

where $\overline{u_i}$ is the three-dimensional filtered velocity, $\overline{p}$ is the filtered pressure field, ν stands for the kinematic viscosity, ρ for the density of the fluid and τ_{ij} is the SGS stress tensor defined as $-2\nu_s \overline{S_{ij}} + 1/3\tau_{ij}\delta_{ij}$.

Governing equations are discretized on a collocated unstructured mesh by means of finite volume techniques. A second-order conservative scheme is used for the spatial discretization [141]. Such schemes preserve the symmetry properties of the continuous differential operators and ensure both, stability and conservation of the kinetic-energy balance. The velocity-pressure coupling is solved by means of a fractional-step algorithm. The temporal discretization for the convective, diffusive and derivative parts of equation (4.2) was made using a second order self-adaptive scheme [134]; whereas a back-ward Euler scheme was used for the pressure gradient. For more details about the discretization the reader is referred to [45] and [135].

4.3.2 Large eddy simulation turbulence models

In LES the spatial filter applied to the Navier Stokes equations separates large and small scales. This operation introduces new variables into the system of equations, the sub grid stresses (SGS). In order to solve the equations this term must be properly modeled. Four closure models are used in the present paper, WALE, VMS, SIGMA and QR, presented in [2]. The WALE model was proposed by [84] based on the square of the velocity gradient tensor. This SGS model accounts for the effects of the strain and rotation rates, as well as, a y^3 near wall scaling for the eddy viscosity. The variational multi scale method was formulated for the Smagorinsky model on a spectral domain by [38]. Later, this method was extended to the classical filtering approach in LES. The VMS method consists on applying a spatial test filter to the already filtered scales to divide the resolved scales of motion into large and small. The later are used to model the turbulent viscosity. QR model was proposed by [139] responding to the question of damping sub filter scales properly. It is a SGS model based on the invariants of the rate-of-strain tensor. Finally, SIGMA model, proposed by [85], is a sub grid-scale model derived from the analysis of the singular values of the resolved velocity gradient tensor.

4.4 Numerical results

4.4.1 Mesh and time integration analysis

Hybrid tetra-prism unstructured meshes are constructed to discretize the equations. A fine near wall mesh is necessary to correctly solve the boundary layer and the physical phenomena associated with this zone. A prism layer is appropriate in this area due to the relative simplicity to place these control volumes (CV) close to the surface and the log-law grow ratio that can be applied. This elements are placed in the present case on the valve disc and discharge orifice geometry. Furthermore, the gap zone must be refined to correctly predict the flow discharge from the valve. As the flow moves away from the gap outlet the relative importance of the flow on the valve operation diminishes and so does the mesh resolution (see Fig. 4.2). Three meshes are used with each valve model, see table 4.1 for details. Results in the present section have been obtained using the VMS turbulence model.

The fluid flows axially through the lower disk inlet orifice d and thickness h, after that, impacts on the upper solid disk of diameter D and finally, radially outflows through the gap between both coaxial disks. Present simulations use a turbulent inflow, which causes an unsteady turbulent

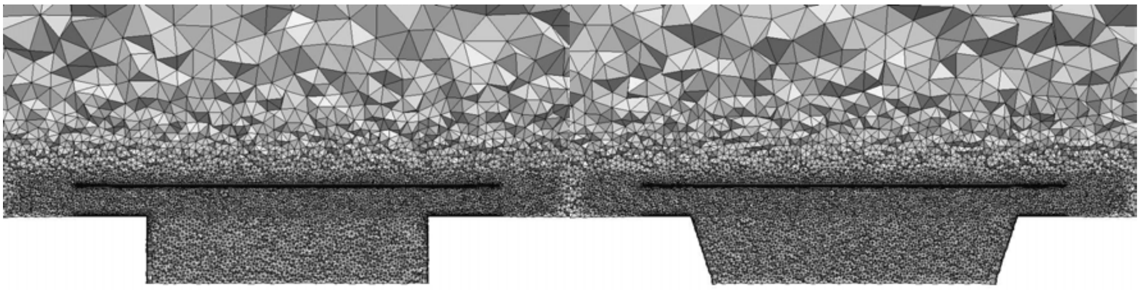
(a) (b)

Figure 4.2: Meshes along the xy cut plane, (a) straight geometry and (b) cone geometry.

behavior characterized by random-like velocity behavior and large fluctuations. In order to perform a time integration analysis several numerical probes were placed within the valve domain. For the straight geometry points P1, P2 and P3 are located near the upper disc along the gap length, P4 in the center, both axially and radially, of the gap and points P5, P6, P7 and P8 are placed near the lower wall alongside the gap. For the cone geometry locations are: P1, P2 and P3 are placed near the top wall and along the gap in similar position as for the straight geometry. P4 is placed at the center of the gap near the exit, P5, P6 and P7 are located along the slanted wall, P8 in the lower wall, near the exit of the gap and P9 near the center of the gap. Locations are detailed in table 4.2 and Fig. 4.3.

Simulations are started from a solution obtained using a laminar inflow flow and are advanced

Table 4.1: Mesh parameters. NCV the total number of control volumes in the domain, $y^+_{min}D$ and $y^+_{avg}D$ minimum and averaged y^+ on the valve disc, and $y^+_{min}O$ and $y^+_{avg}O$ minimum and averaged y^+ on the discharge orifice surface.

Geometry	Mesh	NCV	$y^+_{min}D$	$y^+_{avg}D$	$y^+_{min}O$	$y^+_{avg}O$
Straight	Mesh 1	2.13×10^5	2.98	111.97	9.24	106.28
	Mesh 2	1.11×10^6	0.13	18.44	2.27	18.66
	Mesh 3	7.83×10^6	0.04	8.51	0.34	9.63
Cone	Mesh 1	2.20×10^5	2.37	98.52	12.31	98.89
	Mesh 2	1.10×10^6	0.18	15.50	1.56	13.99
	Mesh 3	8.00×10^6	0.04	6.90	0.48	7.33

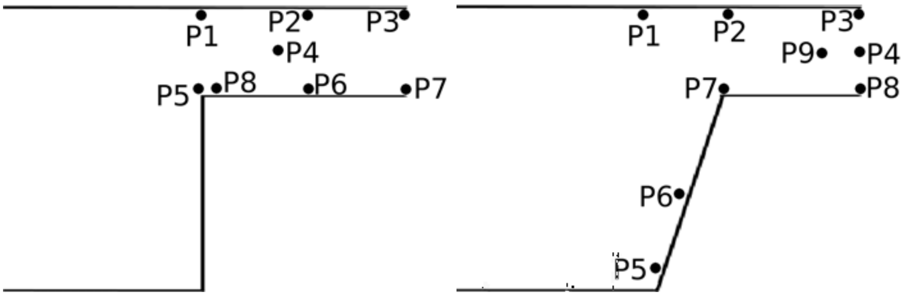

(a) (b)

Figure 4.3: Numerical probes' location, (a) straight geometry, (b) cone geometry.

Table 4.2: Numerical probes' location.

Geometry	Straight	Cone
P1	$[0.5, 0.32]$	$[0.5, 0.32]$
P2	$[0.625, 0.32]$	$[0.625, 0.32]$
P3	$[0.75, 0.32]$	$[0.75, 0.32]$
P4	$[0.625, 0.28]$	$[0.75, 0.28]$
P5	$[0.5, 0.24]$	$[0.52, 0.1]$
P6	$[0.625, 0.24]$	$[0.56, 0.19]$
P7	$[0.75, 0.24]$	$[0.625, 0.24]$
P8	$[0.51, 0.24]$	$[0.75, 0.24]$
P9	-	$[0.68, 0.28]$

in time until the initial transient behavior is washed out at around $0.5TU$ ($TU = tUref/d$). Afterwards statistics have been collected and averaged by integrating the instantaneous data. Stream wise velocity time history and autocorrelation functions for the z-component of velocity (W) at the different locations are shown in figs. 4.4 and 4.5. It is interesting to observe the behavior for the straight case, where probes P5 and P8, although being very close to each other

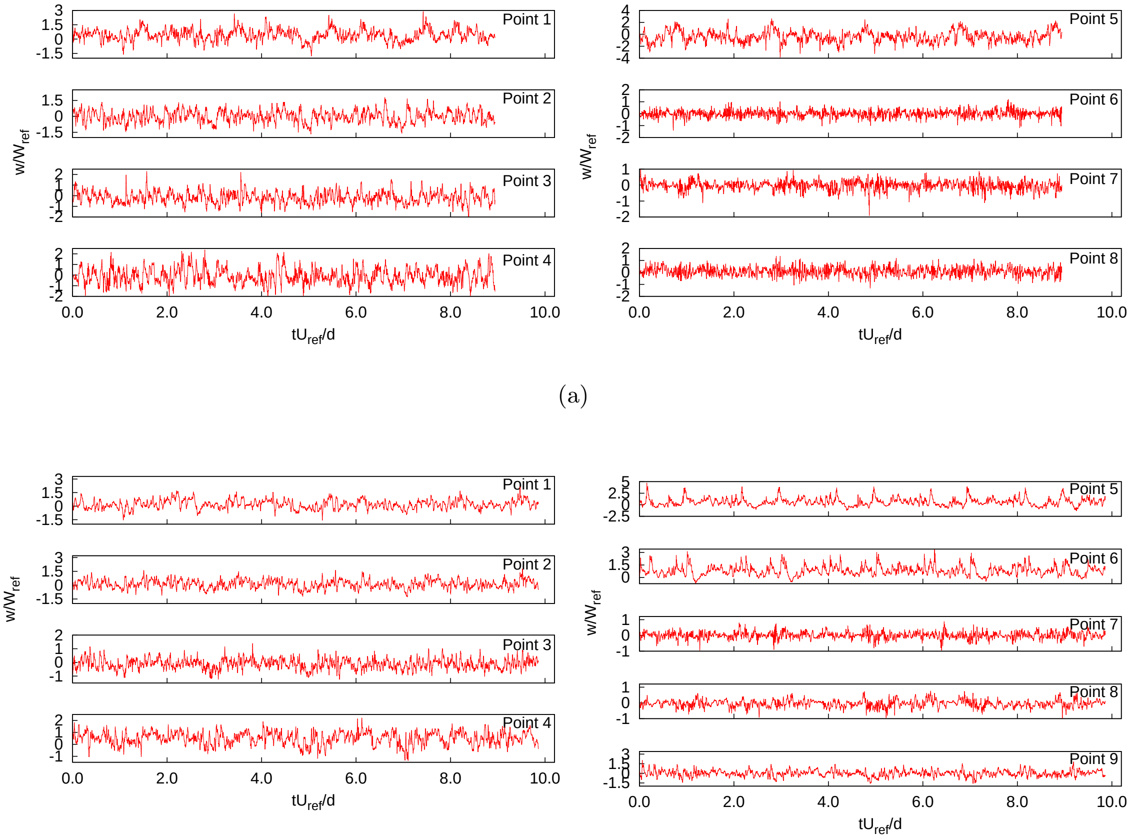

(a)

(b)

Figure 4.4: Stream wise velocity W time history for the different numerical probes in the (a) straight geometry and (b) cone geometry.

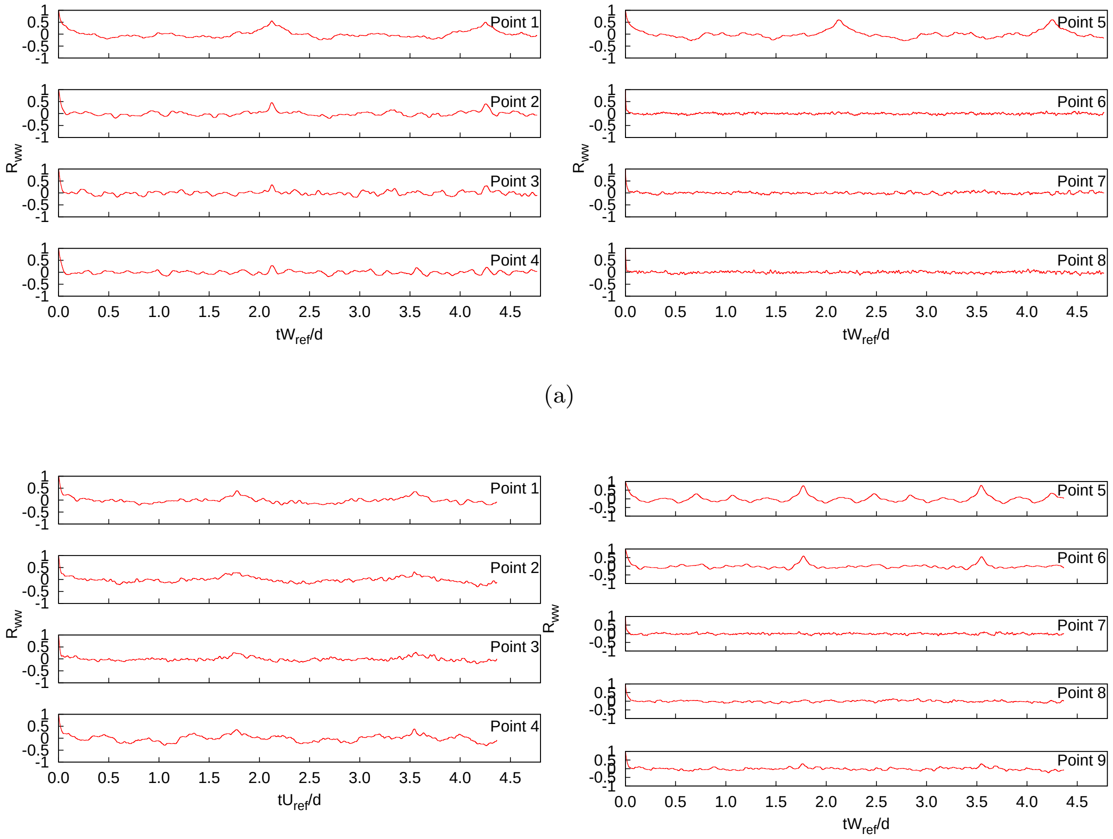

(a)

(b)

Figure 4.5: Z-component velocity autocorrelation function for the different numerical probes in the (a) straight geometry and (b) cone geometry.

show quite a different behavior. P5 is located near the valve seat corner and exhibits large velocity fluctuations. P8, located slightly downwind is located at the beginning of the recirculation region and, although fluctuation magnitude is less, its frequency is considerably higher P7 for the cone geometry is placed in a comparable location (just after the valve seat) and its turbulent behavior is lower, i.e. lower fluctuation amplitude and frequency. This difference in flow behavior is enhanced when observing probes P4 for the straight geometry and P9 for the cone geometry, both near the center of the gap. Flow for both geometries show some periodic like behavior towards the valve outlet (see Fig. 4.5a and 4.5b), however, as stated before, frequencies for the straight geometry seem higher than for the cone one.

Two important variables are shown in the numerical results presented. The first one is the fluid pressure distribution in the lower face of the upper disk, while the second one is the velocity magnitude (V) distribution along the gap between coaxial disks at different radial positions of $x = d/2$ (gap position 1), $x = d/4 + D/4$ (gap position 2) and $x = D/2$ (gap position 3) corresponding to the entrance, middle and exit of the gap, all shown in Fig. 4.6. Mesh independence is achieved for the 8×10^6 CV meshes as both pressure and velocity profiles show almost no change for a further mesh refinement. Stagnation pressure is significantly higher for the straight geometry than for the cone one, this is due to the higher velocity the flow reaches when passing through the straight valve. In the cone geometry this shape acts as a diffuser lowering the velocity of the impinging jet and easing into the direction change, thus, the flow carries less energy when crashing onto the top plate. Effects of these flow modifications are also visible through the gap. For the straight geometry flow reaches a higher velocity, additionally, the recirculation zone created by the valve seat corner is larger for the straight geometry than for the cone geometry (see figs. 4.6a and

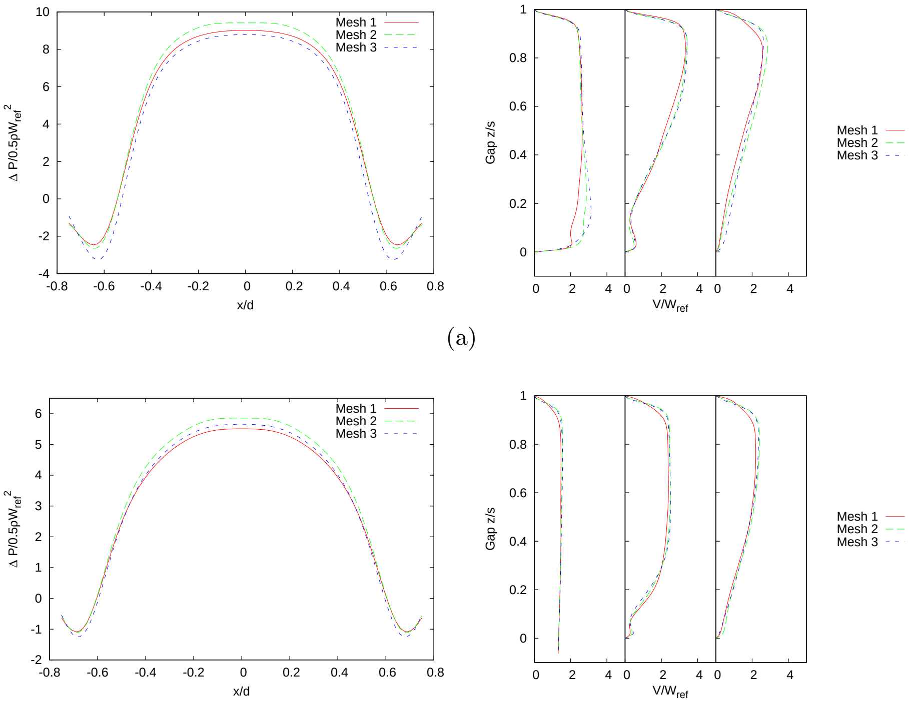

(a)

(b)

Figure 4.6: Pressure distribution over the lower face of the valve disc and velocity profiles over the gap at $x = d/2$,$x = d/4 + D/4$ and $x = D/2$ for (a) straight geometry, (b) cone geometry.

4.6b).

4.4.2 Turbulence model analysis

As exposed in section 4.3.2, four turbulence models were used to evaluate the results in the flow through the valves, VMS, WALE, QR and SIGMA. Results show great consistency when changing LES models, however, this is more evident in the cone geometry than in the conical one. Sudden direction change and the more pronounced valve seat corner create a more complex flow that poses a higher difficulty to solve.

WALE and QR models predict a slightly larger pressure distribution than the rest of the models for the straight geometry, whereas VMS and WALE do the same in the cone geometry. For the velocity profiles results take a different trend. In this zone velocities for the straight geometry are larger than for the conical one due to the sudden change of direction and area reduction. For the conical geometry this acceleration is more gradual resulting in lower final velocities. All models results are quite similar for the entrance of the gap, however the other location analyzed show results difference. SIGMA and VMS models show almost identical result in the remaining gap locations. For the straight geometry large differences are seen in gap positions 2 and 3. QR and WALE models both show larger velocities in the recirculation region for both geometries. For the cone geometry these differences reduce for gap position 3, whereas for the straight geometry the differences become larger. VMS model shows results that fall in between the other models, much more evident for the velocity results than for the pressure ones. Previous experiences with turbulent flow suggest VMS results could be the best LES model to use for more detailed simulations.

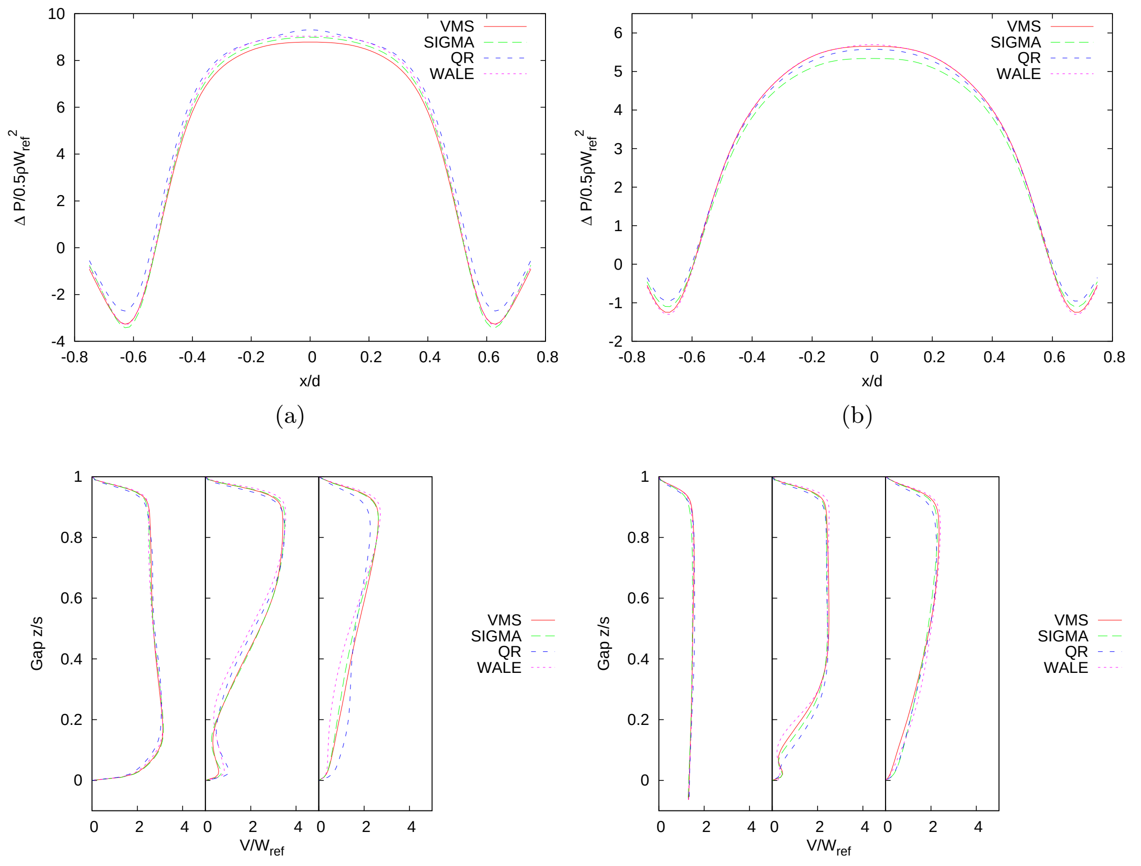

(a) (b)

(c) (d)

Figure 4.7: LES results for the pressure profile along the plate on (a) straight geometry, (b) cone geometry. LES results for the velocity profiles in the gap. (c) straight geometry, (d) cone geometry.

4.4.3 Geometrical analysis

Changing the discharge orifice geometry greatly changes the velocity and pressure behavior in the valve, as has been observed in the previous sections. To verify this behavior different gap openings were studied as well, $s/d = 0.033$ and $s/d = 0.22$, using the same mesh size parameters than for the base case. Gradual expansion allows the flow to change its direction sooner and reduce the energy carried when it impinges into the valve disc. This results in a considerably lower pressure rise in this element, as observed in Fig. 4.8. This lower pressure rise over the valve disc for the cone geometry results in a considerably higher effective flow area (see Fig.4.9), where for the straight geometry increases from 0.124 to 0.89 as the valve opens and for the cone geometry from 0.152 to 1.35. Effective force area also increases for both geometries, from 0.569 to 1.52 for the straight geometry and from 0.74 to 2.45 in the cone one.

Furthermore, the recirculation region in the valve seat is much smaller for the conical geometry. The sudden right angle change in the flow's direction causes heavy flow separation. When the inlet channel geometry is changed to the cone the sudden direction change now possesses a smaller angle, thus, creating a smaller recirculation region. A second factor affecting this region is the velocity magnitude. As the flow is incompressible a reduction in flow area is accompanied by an increase in its velocity. Although, geometrically, the inlet and gap outlet areas are the same, effective flow areas are different due to the different velocity field and pressure drops present en each geometry (see Fig.4.9). Observing Fig. 4.10 there is a much larger velocity increment for

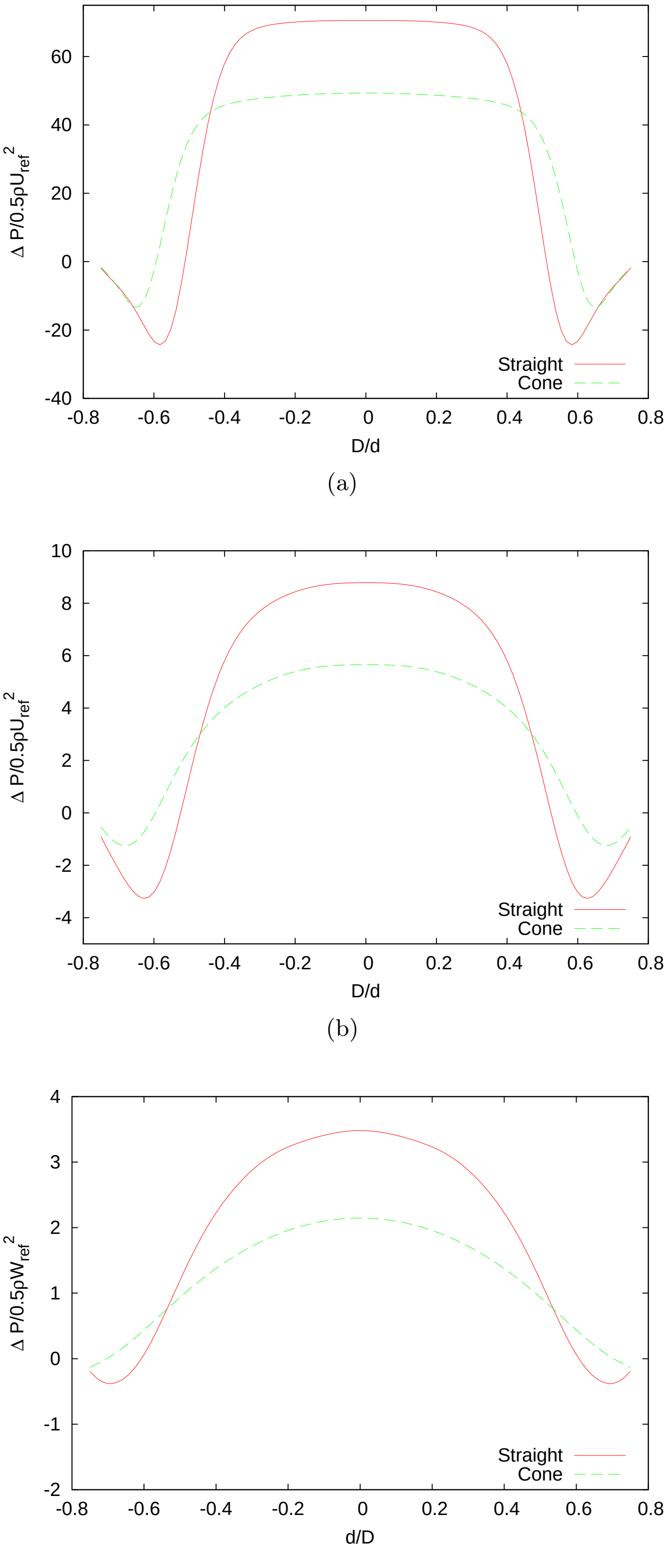

(a)

(b)

(c)

Figure 4.8: pressure distribution over the plate for both geometries, (a): gap opening $s/d = 0.033$, (b): gap opening $s/d = 0.11$ and (c): gap opening $s/d = 0.022$.

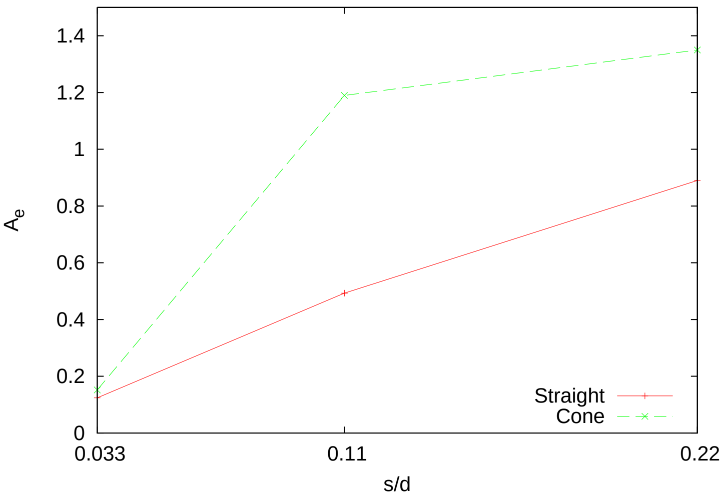

(a)

Figure 4.9: Effective flow area for the different valve openings.

the straight geometry than the conical one. As the valve opening increases from $s/d = 0.033$ to $s/d = 0.11$ both effective flow and force areas increase as well, however, as the gap opening further opens to $s/d = 0.22$ this trend changes. Effective flow area for the cone geometry reduces its rate of increase, whereas the effective force area decreases. In the straight geometry, although both effective areas increases, its rate of increment diminishes.

Finally non-dimensional pressure drop ($C_P = \Delta P/(0.5\rho W_{ref}^2)$) in the valve for the straight geometry and gap opening $s = 0.11d$ is $C_P = 4.11$, whereas for the cone geometry it is $C_P = 0.71$. This same behavior remains when the valve opening is greater ($s/d = 0.22$) and smaller ($s/d = 0.033$), non-dimensional pressure drop for these valve openings and the straight geometry are $C_P = 1.26$ and $C_P = 65.32$ respectively, and for the cone geometry $C_P = 0.53$ and $C_P = 43.52$ respectively. Non-dimensional pressure drop reduces as the valve opens and is also significantly lower for the cone geometry, 57.9% for $s/d = 0.033$, 82.7% for $s = 0.11d$ and 76.4% for $s = 0.22d$.

4.5 Conclusions

Turbulent flow simulations through different valve geometries at an industrial type Re flow regime were carried out and their result compared to each other. Two mayor aspects were analyzed and found to drastically change in shape and magnitude. Pressure profiles over the valve disc change from a nearly top-hat distribution to a smoother bell-shaped profile with the change of geometry. Additionally maximum pressure rise in this area is reduced nearly 40%. Velocity profiles in the gap show that for the straight geometry both, velocity magnitude and recirculation area, are larger then for the cone geometry. These effects greatly affect the valve operation, achieving a significant pressure drop reduction when using the cone geometry. Finally, it is important to note that the Mach number in some parts of the geometry surpass $Ma = 0.3$. In order to obtain better results compressible flow simulations are required.

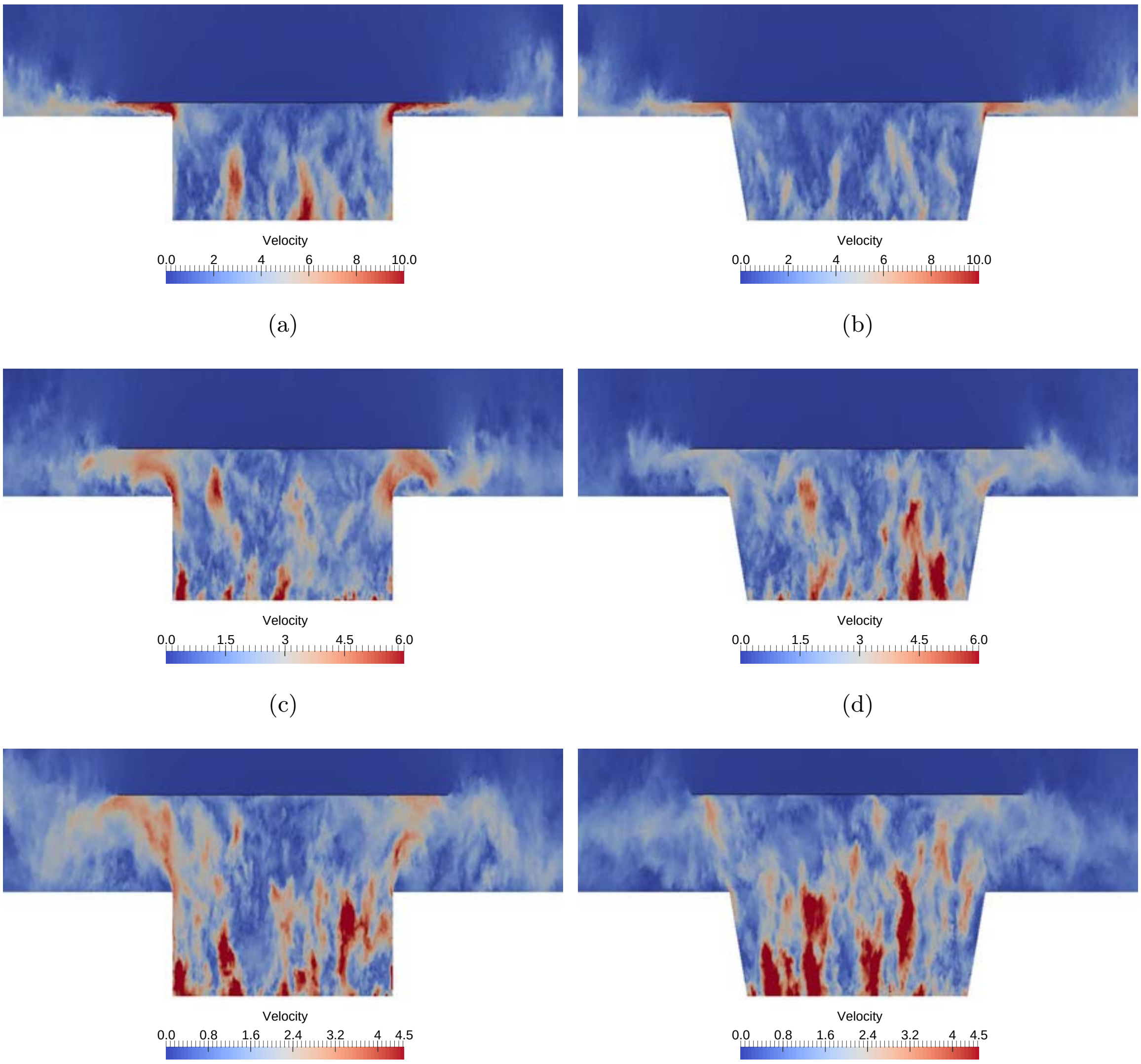

(a) (b)

(c) (d)

(e) (f)

Figure 4.10: Instantaneous velocity field for both geometries, (a): gap opening $s/d = 0.033$, (b): gap opening $s/d = 0.11$ and (c): gap opening $s/d = 0.022$.

Chapter 5

Flow and Turbulent Structures Around Simplified Car Models

Main contents of this chapter have been published in:

Aljure, D. E., Lehmkuhl, O., Rodríguez, I., and Oliva, A. Flow and Turbulent Structures Around Simplified Car Models *Comput. Fluids* 96
Aljure, D. E., Rodríguez, I.,Lehmkuhl, O.,Borrel, R. and Oliva, A. Flow and Turbulent Structures Around Simplified Car Models *Conference on Modelling Fluid Flow (CMFF'12)Conference on Modelling Fluid Flow (CMFF'12) at Budapest*January 2012.

Abstract

External car aerodynamic study has great importance in overall car efficiency and ride stability, making it a key element in successful automotive design. Flow over car geometries fully show three dimensional, unsteady turbulent characteristics. Additionally, vortex shedding, flow reattachment and recirculation bubbles can be found around the buff body. These phenomena greatly influence the key factors in aerodynamic study, the lift and drag coefficients, vital for ride stability and energy efficiency, respectively. The purpose of the present study is to compare and validate new generation LES models such as the VMS or SIGMA models and assess and compare the different large scale turbulent flow structures present in car aerodynamics using two basic car geometries and challenging LES.

In order to achieve the previously stated objectives flow around two model car geometries, the Ahmed and the Asmo car, is simulated. These generic buff bodies reproduce the basic fluid dynamics features of real cars using simplified geometries. Firstly, the flow over both geometries is studied and compared against experimental and other author's results to validate the numerical solution, afterward, various LES models are used to study the flow in detail and compare the structures found in both geometries.

5.1 Introduction

Computational fluid dynamics (CFD) has evolved greatly in the past two decades becoming a vital tool in industrial research, development and investigation. Due to the nature of fluid flows, most practical applications deal with turbulent motion. The modeling of this phenomenon is of importance within the CFD industry where vast resources are invested into its research. Within the different possible applications of the CFD technology come aerodynamics and automotive design. The automotive industry makes great advances every year; engine performance has increased greatly in the past decade, along with weight reduction and safety measures. These advances make aerodynamics more important to ensure high efficiency and vehicle drive stability.

The bodies to be studied in the present paper are the widely studied Ahmed car model with a 25° angle of the rear slanted surface (Krajnović and Davidson [56], Minguez et al. [79], Serre et al.

[122], Lehmkuhl et al. [63], among others), and the Asmo car model (Perzon and Davidson [97], Nakashima et al. [83], among others). The Ahmed body car is a semi-rectangular vehicle with a rounded front and a slanted back. The simplified topology of this model allows easy modeling, meshing and comparisons between experimental and numerical results. The second model, the Asmo car, has a square back rear, smooth surface, boat tailing and an under body diffuser. This model is characterized by no pressure induced boundary layer separation and low drag coefficient.

The Ahmed car was originally used in the experiments of Ahmed et al. [1]. They concluded that the flow structure in the wake was controlled, for a given Reynolds number, by the inclination of the slanted back. Lienhart et al. [71] performed further experiments with the 25° and 35° slant back geometries using a laser Doppler anemometer to make detailed measurements of the velocity profiles around the bodies. Numerous numerical studies have been carried out using the aforementioned geometry. The 25° and 35° geometries were used in the 9th ERCOFTAC workshop [42]. Results presented by different groups varied greatly, mainly by insufficient grid resolution and convergence. Hinterberger et al. [35] performed large eddy simulations (LES) for the 25° Ahmed geometry. The authors used two grids of 8.8M and 18.5M control volumes (CV). Flow comparison with the experiments performed by Lienhart et al. [71] revealed that the flow structures were well captured. Kapadia et al. [48] used a Spalart-Allmaras based Detached-Eddy Simulation (DES) to model the flow around the 25° and 35° Ahmed car using 2.3M CV, 3.1M CV and 4.6M CV meshes. The authors compared the Reynolds-Averaged Navier-Stokes (RANS) model, the DES and experimental results concluding that their simulations were not very satisfactory as the flow separations were not correctly predicted.

Krajnović and Davidson [56, 57], in two papers, performed large eddy simulations at a lower Reynolds number (2×10^5) to decrease the computational requirements. Three grids containing 3.5M, 9.6M, and 16.5M were used whereas a SIMPLEC algorithm solved the velocity-pressure coupling. The authors concluded that the influence of the Reynolds number in the wake, after the separations at sharp edges, is small. Furthermore, flow visualization results, including time averaged and instantaneous data, showed structures not observed in experimental set ups. Minguez et al. [79] performed high-order LES for the 25° slant back case using a mesh of 21M CV. They used a spectral vanishing viscosity technique to perform the LES around the geometry. The results, conducted at a Reynolds number $Re = 7.68 \times 10^5$, previously discarded by Krajnović and Davidson [56, 57], showed improvement in the overall flow resolution and allowed the visualization of all relevant structures. Serre et al. [122] compared four high order LES results computed over the Ahmed geometry using a Reynolds number $Re = 7.68 \times 10^5$. First, a Smagorinsky sub grid scale model with a wall-function and a mesh with 18.5M CV; second, a LES with near-wall resolution using a dynamic Smagorinsky model and a mesh with 40M CV; third, a LES based on spectral approximations with a 21M CV; and finally a Detached Eddy Simulation (DES) with a $k - \omega$ SST model and a mesh with 23.1M CV. Lehmkuhl et al. [63] used a coarser mesh to simulate the 25° slant back case with a 832K control volume mesh, and different LES models. Results from this paper showed the good stability and results a conservative formulation of the governing equations can achieve.

As for the Asmo car, it is a model created by Daimler-Benz in the 90's to investigate low drag bodies in automotive aerodynamics and testing of CFD codes with a geometry not related to the development of Mercedes cars. Wind tunnel experiments were made by both, Daimler-Benz and Volvo. Aronson et al. [4] studied the flow in the under body region of the car and the differences in drag different geometries (wheels and diffuser) achieved. Their analysis showed that the rear wheels contributed greatly to the drag coefficient. They also saw a significant reduction in drag when the model was equipped with a rear diffuser. Perzon and Davidson [97] performed stationary simulations using RANS models on a 380K CV mesh and transient simulations in a 760K CV mesh using the standard $k - \epsilon$ model and the SZL-model among others. Results of these simulations showed good agreement in pressure and high over prediction in the drag coefficient. Nakashima et al. [83] simulated the flow over the Asmo car using three tetrahedral meshes of 1.3M, 5.5M and 24M CV and both RANS and LES approaches. The LES simulations in this paper showed overall better results over the RANS models. Tsubokura et al. [136] performed LES and RANS simulations on the Asmo car using meshes with 5.5M and 24.3M. Their study on this geometry was aimed to validate the turbulence models for simulations on more complex geometries concluding at the end that LES is a powerful tool within vehicle aerodynamics. Simulations performed within the Xflow project in vehicle aerodynamics (2010) were carried out using a Reynolds number, based on body length, of $Re = 2.7 \times 10^6$. They used a LES with a wall-adapting local eddy diffusivity (WALE) model within a Lattice-Boltzman algorithm. The authors concluded that results for the drag coefficient are highly improved when using LES models.

Several difficulties arise when modeling turbulent flows. RANS models often fail to correctly reproduce flow dynamics, specially in detached flows. LES models demand high computational resources when dealing with industrial-type high Reynolds flows. In the present paper Challenging Large Eddy Simulations (CLES) are performed. In CLES coarse meshes are used in conjunction with conservative and symmetry preserving numerical schemes to reduce the computational requirements necessary to simulate CFD cases. This paper investigates the capabilities of CLES for reproducing the complex fluid flow phenomena present in automotive aerodynamics using simplified car models. Both geometries have been widely studied in the literature and flow structures around them are well known. Thus, by means of different SGS models, the flow structures obtained using different grids are compared to those identified in experimental and numerical works from the literature. In addition to the mean and instantaneous flows, aerodynamics coefficients are also compared. The performance of the different models for predicting these complex aerodynamics forces is discussed in detail.

5.2 Definition of the Case

5.2.1 Geometries and Computational Domain

The geometries to be considered are the 25° slant back Ahmed car shown in Fig. 5.1a and the Asmo car seen in Fig. 5.1b.

Both cases are solved in a rectangular computational domain of $9.1944 \times 1.87 \times 1.4m$ shown in Fig. 5.2. The front of the car is located at $2.1014m$ downwind from the inlet boundary. The outlet boundary is at a distance of $6.048m$ for the Ahmed car and of $6.282m$ for the Asmo car, measured from the rear end of the body. To simulate the same case conditions as those measured by Lienhart et al. [71] a 3/4 open wind tunnel is considered in both geometries.

5.2.2 Mathematical and Numerical Model

In order to study the flow, the filtered incompressible Navier-Stokes equations are solved:

$$\frac{\partial \overline{u_i}}{\partial x_i} = 0 \tag{5.1}$$

$$\frac{\partial \overline{u_i}}{\partial t} + \frac{\partial (\overline{u_i u_j})}{\partial x_j} - \nu \frac{\partial^2 \overline{u_i}}{\partial x_j \partial x_j} + \rho^{-1} \frac{\partial \overline{p}}{\partial x_i} = -\frac{\partial \tau_{ij}}{\partial x_j} \tag{5.2}$$

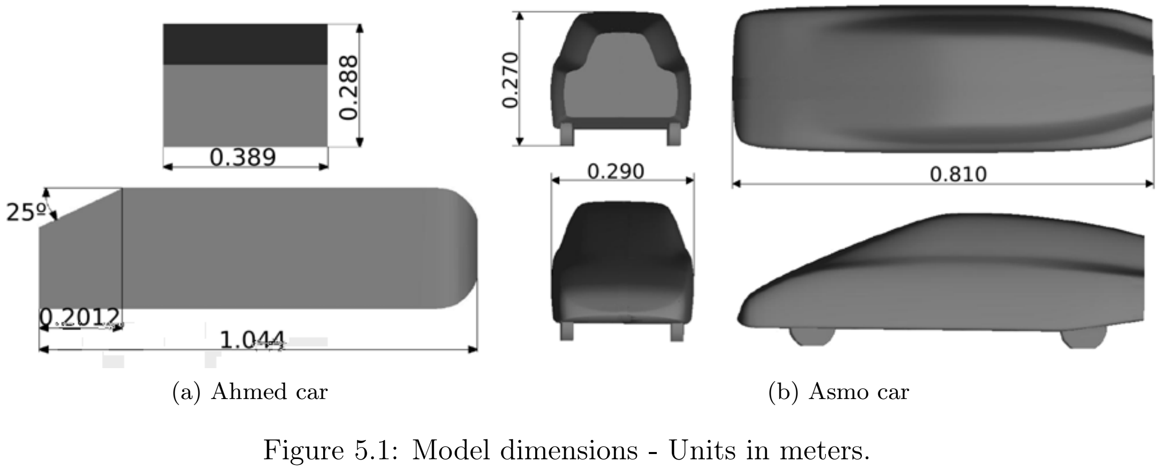

(a) Ahmed car

(b) Asmo car

Figure 5.1: Model dimensions - Units in meters.

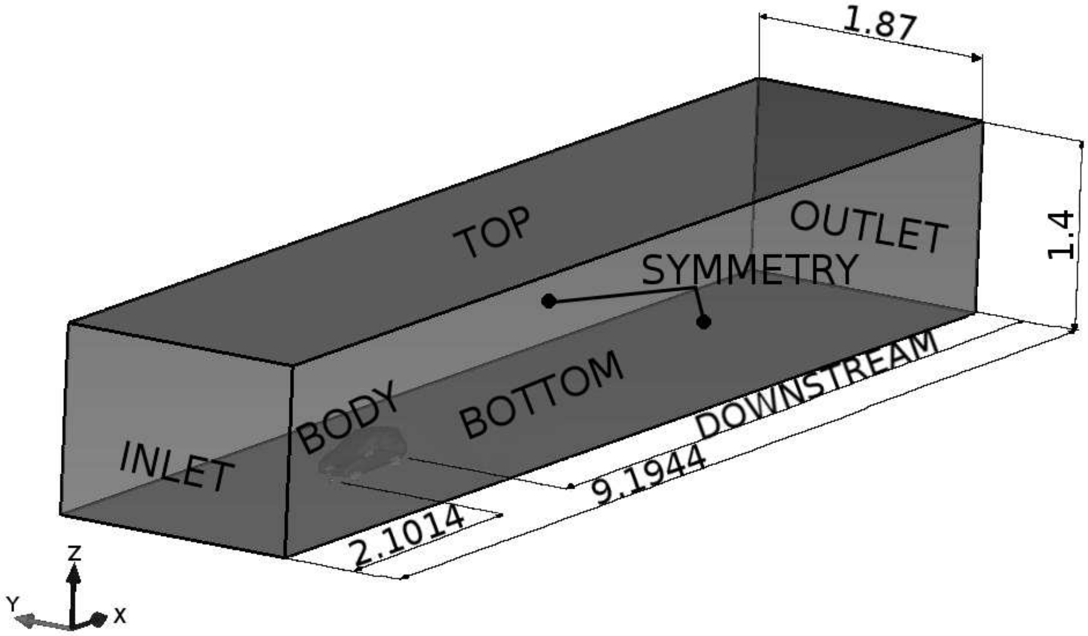

Figure 5.2: a)Computational domain - All dimensions in meters.

where $\overline{u_i}$ is the filtered three-dimensional velocity vector, $\overline{p}$ is the filtered pressure scalar field, ν stands for kinematic viscosity, ρ for the density of the fluid and τ corresponds to the SGS stress tensor:

$$\tau = -2\nu_{SGS}\overline{S} + (\tau : I)I/3 \tag{5.3}$$

where ν_{SGS} is the turbulent or sub grid viscosity and $\overline{S}$ is the filtered rate of strain tensor.

Turbulence modeling is carried out in the present paper by using different sub grid-scale (SGS) models: the wall-adapting local-eddy viscosity, WALE, [84], the WALE model within a variational multi scale framework, VMS, [38], the singular values sub grid model, SIGMA, [85], and the q-r model that uses invariants q and r of the filtered strain tensor to model eddy viscosity, QR, [139]. The default filter length chosen is twice the cubic root of the cell volume, $l = 2 \times \sqrt[3]{V}$. Hereafter a small description of each SGS model is given.

QR Model

This model was proposed by Verstappen [139] responding to the question of damping sub filter scales properly. It is a SGS model based on the invariants of the rate-of-strain tensor. This eddy viscosity model is fairly easy to implement as it does not involve explicit filtering and poses no greater difficulties than a standard Smagorinsky model.

$$
\begin{aligned}
\nu_{SGS} &= (c_{qr} l)^2 \frac{r^+}{q} \\
c_{qr} &= \frac{1}{\pi} + \frac{1}{24} \\
\overline{S} &= \frac{1}{2}\left(\frac{\partial(\overline{u_i})}{\partial x_j} + \frac{\partial(\overline{u_j})}{\partial x_i}^T\right) \\
|\overline{S}| &= (2\overline{S}\overline{S})^{1/2} \\
q &= \frac{1}{4}|\overline{S}|^2 \\
r = -det\overline{S} & \qquad\qquad r^+ = \begin{cases} r, \text{if } r > 0 \\ 0, \text{otherwise} \end{cases}
\end{aligned}
\tag{5.4}
$$

where c_{qr} is the model constant, q and r are invariants of $\overline{S}$.

SIGMA model

This model, proposed by Nicoud et al. [85], is a sub grid-scale model derived from the analysis of the singular values of the resolved velocity gradient tensor.

$$
\begin{aligned}
\nu_{SGS} &= (c_\sigma l)^2 \frac{\sigma_3(\sigma_1 - \sigma_2)(\sigma_2 - \sigma_3)}{\sigma_1^2} \\
\sigma_i &= \sqrt{\lambda_i} \\
c_\sigma &= 1.35 \\
Gu &= \frac{\partial(\overline{u_i})}{\partial x_j}^T + \frac{\partial(\overline{u_j})}{\partial x_i}
\end{aligned}
\tag{5.5}
$$

$$
I1 = tr(Gu), \qquad I2 = \frac{1}{2}\left(tr(Gu)^2\right) - \left(tr(Gu^2)\right), \qquad I3 = det(Gu)
$$

$$
I1 = \lambda_1 + \lambda_2 + \lambda_3, \qquad I2 = \lambda_1\lambda_2 + \lambda_1\lambda_3 + \lambda_2\lambda_3, \qquad I3 = \lambda_1\lambda_2\lambda_3
$$

where c_σ is the model constant, Gu is a symmetric semi-definite positive tensor derived form the velocity gradient tensor, λ_i are the eigenvalues of the Gu tensor, and σ_i are the singular values of the velocity gradient tensor.

WALE Model

The WALE model was proposed by Nicoud and Ducros [84] based on the square of the velocity gradient tensor. This SGS model accounts for the effects of the strain and rotation rates, as well as, a y^3 near wall scaling for the eddy viscosity.

$$
\begin{aligned}
\nu_{SGS} &= (c_{wale} l)^2 \frac{(\overline{\nu} : \overline{\Omega})^{3/2}}{(\overline{S} : \overline{S})^{5/2} + (\overline{\Omega} : \overline{\Omega})^{5/4}} \\
c_{wale}^2 &= 0.325 \\
\overline{S} &= \frac{1}{2}\left(\frac{\partial(\overline{u_i})}{\partial x_j} + \frac{\partial(\overline{u_j})}{\partial x_i}^T\right) \\
\overline{\Omega} &= \frac{1}{2}\left(\frac{\partial(\overline{u_i})}{\partial x_j} + \frac{\partial(\overline{u_j})}{\partial x_i}^T\right) - \frac{1}{3}\left(\frac{\partial(\overline{u_i})}{\partial x_i}^2\right)
\end{aligned}
\tag{5.6}
$$

where c_{wale} is the model constant, and $\overline{\Omega}$ is the filtered strain-of-rotation tensor.

VMS model

The variational multi scale method was originally formulated for the Smagorinsky model by Hughes T.J.R and J-B [39]. Later, Vreman [142] extended this method to the classical filtering approach in LES. The VMS method consists on applying a spatial test filter of length $\hat{l}$ to the already filtered scales $(\overline{f})$ to divide the resolved scales of motion into large $(\hat{f})$, and small (f') and using the later to model the turbulent viscosity.

$$f' = \overline{f} - \hat{f} \tag{5.7}$$

Having applied the filter, a governing equation for the large scale parts of $\overline{u_i}$ can be derived:

$$\frac{\partial \overline{u_i}}{\partial t} + \frac{\partial(\overline{u_i u_j})}{\partial x_j} - \nu \frac{\partial^2 \overline{u_i}}{\partial x_j \partial x_j} + \rho^{-1} \frac{\partial \overline{p}}{\partial x_i} = -\frac{\partial \hat{\tau}}{\partial x_i} - \nabla \cdot \tau' \tag{5.8}$$

where $\hat{\tau}$ is the large-sub grid scale tensor and τ' is the small-sub grid scale term. Neglecting the effect of the large scales of motion $(\hat{\tau} \approx 0)$ the turbulent viscosity is then calculated by using only the small-scales term τ'. Lehmkuhl et al. [62] used this small scales approach in conjunction with the WALE model:

$$\begin{aligned}
\tau' &= -2\nu_{SGS} S'_{ij} + \frac{1}{3}\tau' \delta_{ij} \\
\nu_{SGS} &= (c_{vms} l)^2 \frac{(\Omega' : \Omega')^{3/2}}{(S' : S')^{5/2} + (\Omega' : \Omega')^{5/4}} \\
c_{vms}^2 &= 0.325 \\
S' &= \frac{1}{2}\left(\frac{\partial(u_i')}{\partial x_j} + \frac{\partial(u_j')}{\partial x_i}^T\right) \\
\Omega' &= \frac{1}{2}\left(\frac{\partial(u_i')}{\partial x_j} + \frac{\partial(u_j')}{\partial x_i}^T\right) - \frac{1}{3}\left(\frac{\partial(u_i')}{\partial x_i}^2\right)
\end{aligned} \tag{5.9}$$

where c_{vms} is the model constant, equivalent to that used in the WALE model

5.2.3 Numerical Method

Numerical schemes

Governing equations are discretized on a collocated unstructured mesh by means of finite volume techniques. A second-order conservative scheme is used for the spatial discretization [141]. Such schemes preserve the symmetry properties of the continuous differential operators and ensure both, stability and conservation of the kinetic-energy balance. As was pointed out by [141] this methodology would be a good starting point for the formulation of SGS models. Thus, it might be expected to achieve good results even at high Reynolds numbers and with coarse grids. The velocity-pressure coupling is solved by means of a fractional-step algorithm; the temporal discretization for the convective, diffusive and derivative parts of equation (5.2) was made using a second order self-adaptive scheme [134]; whereas a back-ward Euler scheme was used for the pressure gradient.

Spatial Approximation

Different types of meshes are used to simulate the flow over the model cars. A fine near wall mesh is necessary to correctly solve the boundary layer and the physical phenomena associated with this zone. A prism layer is appropriate in this area due to the low non-orthogonal corrections required by this type of elements and the relative simplicity to place this CV close to the surface. Furthermore, the near wake zone must be refined to correctly predict the flow structures trailing the car. As the flow moves away the surface relative importance of flow structures in the force coefficients and velocity profiles diminish and so does the mesh resolution.

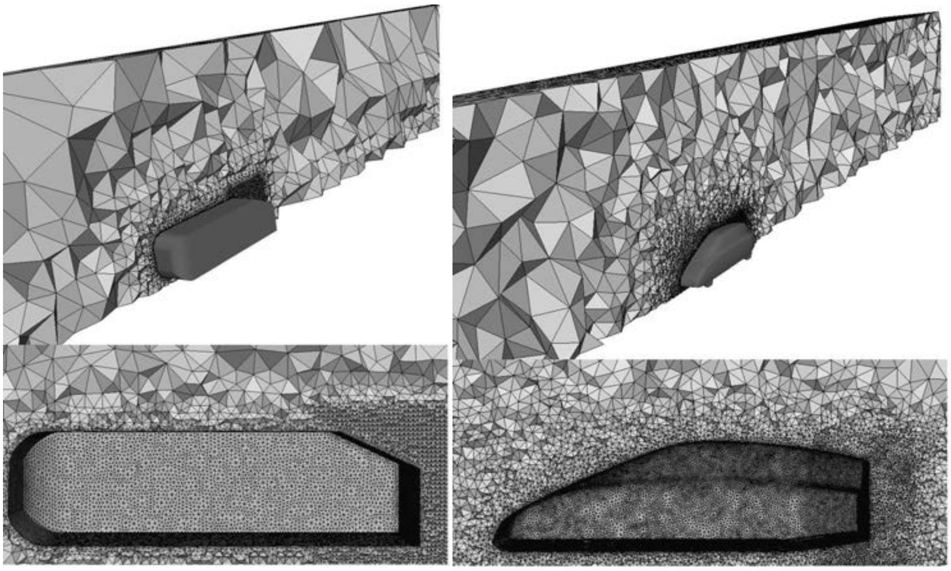

(a) Ahmed car.

(b) Asmo car.

Figure 5.3: Visualization of the mesh in the channel.

Table 5.1: Mesh parameters.

Model	Num nodes	min length scale (mm)	y^+ min	y^+ max	y^+ mean
Ahmed	486091	1.545	1.210	38.05	11.82
	1045294	1.243	0.524	36.27	11.67
	1561209	0.847	0.401	34.30	11.50
	4962087	0.720	0.283	26.39	6.51
Asmo	753974	1.547	1.569	34.24	14.10
	1988688	0.640	0.251	17.65	4.090
	2799723	0.591	0.1447	13.89	3.517
	5214958	0.093			

The present simulations are focused on the surroundings of the body and the near wake. Simulations resolving the full wake of the cars require different type of meshes clustering a great number of CV in the far wake to correctly resolve all scales of motion in that area. Three meshes are used with each car model, $500K$, $100K$ and $1600K$ CV for the Ahmed car and $800K$, $2000K$ and $2800K$ CV for the Asmo car.

Fig. 5.3a shows one of the meshes used for the Ahmed car. A hybrid tetra-prism mesh with a prismatic layer mesh to resolve the boundary layer is used. Furthermore, mesh refinement is done in the back of the car to resolve the near wake.

The mesh around the Asmo car has the same basic structure as that used for the Ahmed car (see Fig. 5.3b), a prismatic layer in the surface of the car and mesh refinement to solve the near wake are both considered.

Table 5.1 shows some relevant information on the meshes used. Min. length scale refers to the cube root of the smallest volume element in the mesh, y^+min, max and mean corresponds to the minimum, maximum and average location of the first control volume around the car, in wall units.

Boundary Conditions

As for the boundary conditions, a constant velocity inlet profile $u_i = (u_{ref}, 0, 0)$ is imposed. The outlet of the domain is modeled using a convective boundary condition. As the computational domain is a 3/4 open wind tunnel, in the top, front and back boundaries (see Fig. 5.2) symmetry conditions are imposed. No-slip conditions are set for the bottom and car surfaces. Both cases the Ahmed and Asmo car are simulated using the same boundary conditions and $Re = u_{ref} h_{ref}/\nu = 7.68 \times 10^5$ based on the body height.

All simulations are performed using the TermoFluids high performance parallel code [64]. Hybrid tetra-prism unstructured meshes are generated using the Ansys IcemCFD software. METIS [50] software is used for domain partitioning. All simulations are computed on the in-house JFF cluster, which is composed by 128 nodes with 2 AMD Opteron 2350 Quad Core processor linked with an infiniband DDR network and 40 nodes with 2 AMD 6172 CPUs (16 cores by CPU) linked with a QDR inifiniband network. Each core has 2GB RAM.

5.3 Results

5.3.1 Numerical Analysis

For obtaining the numerical results presented in this section, simulations are advanced in time until a statistical stationary flow is reached. Then, in order to ensure converged statistics, instantaneous data is integrated over a sufficiently long-time period. This integration time is about $TU = 76$ time units ($TU = tu_{ref}/h_{ref}$). VMS turbulence model is used in this section.

In Fig. 5.4a the results for the averaged stream-wise velocity profiles and the stream wise RMS profiles along the symmetry plane of the Ahmed car for different sections in the slant surface and the near wake are presented. These results are compared to the experimental results reported by Lienhart et al. [71]. Additionally, results from the 16.5M mesh from Krajnović and Davidson [56] and from the 21M mesh from Minguez et al. [79] are also plotted for comparison sake. As can be seen in the figure, the mesh of $1000K$ CV is capable of reproducing with quite good agreement the experimental results. A further refinement of the mesh ($1600K$ CV) does not improve substantially the results, but the computational cost increases. The flow resolution near the boundary layers from Krajnović and Davidson [56] show excellent agreement with experimental results. Results obtained in the present paper, although with much coarser meshes, are comparable in quality as those obtained by previous authors with finer meshes. When comparing results from Minguez et al. [79] with the ones obtained in the present work it is important to observe the recuperation region, i.e. the velocity profiles further away from the wall. In Minguez et al. [79] the velocity magnitudes are sub-predicted, in contrast to the flow evolution obtained in the present paper, by Krajnović and Davidson [56] and by Lienhart et al. [71]. The RMS velocity profiles show the same fact the velocity does, a $1000K$ CV mesh captures well the flow behavior, an excellent performance when compared to the larger meshes used by other authors.

Fig. 5.4b shows the average pressure coefficient ($c_p = (P - P_\infty)/(0.5\rho U_{ref}^2)$) profile alongside the symmetry plane of the underbody and in the back of the Asmo car. In this case, the three meshes studied (see table 5.1) are compared to the experimental results reported by both Volvo and Daimler-Benz (taken from Perzon and Davidson [97] and to the numerical results of Perzon and Davidson [97] and Tsubokura et al. [136]. As can be seen in the figure, the results obtained with the $1800K$ CV mesh and $2800K$ are quite close to the experimental data in the underbody, specially near the front, where the pressure spike is properly resolved. The rear pressure spike is under predicted. Furthermore, Perzon and Davidson [97] data from transient RANS simulation on $760K$ cells shows a larger error than present work data. Results by Tsubokura et al. [136] closely resemble the experimental ones, this profile comes from a LES simulation on 24.3M CV, which is much finer than the meshes used in the present work. Results in the back of the car by Tsubokura et al. [136] show a behavior very close to the experimental measurements, whereas some error is found for all meshes in the present investigation. Comparing those (Tsubokura et al. [136]) results from a 24.5M CV mesh with our $2800K$ CV mesh shows that, although coarse and showing error, the formulation and resolution of the governing equations within TermoFluids is done rather efficiently. When examining table 5.2 two facts stand out: First, the coarse meshes ($500K$ and $800K$) do not

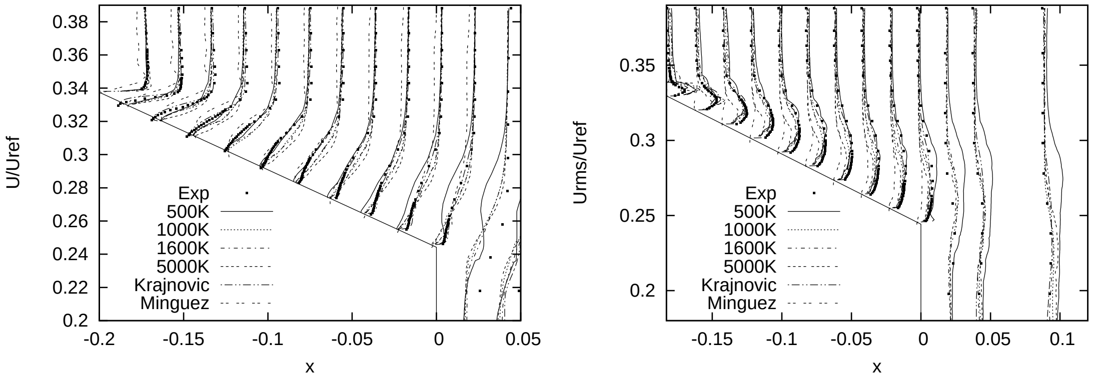

(a) Ahmed car.

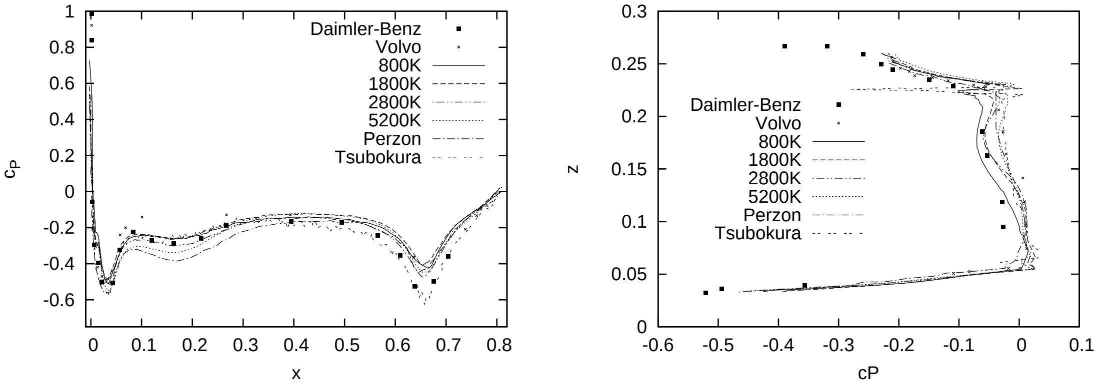

(b) Asmo car.

Figure 5.4: Mesh study on both geometries. (a)Average stream-wise velocity and RMS velocity profiles over the slant wall in the mid plane. (b)Average pressure coefficient in the underbody and in the back.

have enough resolution for a proper resolution of the flow. This fact is specially evident due to the large difference present between the drag values obtained with each SGS model. Second, it is seen that the finer meshes, ($1600K$ and $2800K$) show a consistent behavior, difference between experimental data and present work is under 10% for all models with these meshes, therefore, the behavior of the different turbulence models was evaluated using these meshes. It is important to note that using finer meshes increases the quality of the solution, keeping in mind that further increases in mesh resolution means larger computational resources are required.

5.3.2 CLES analysis

One of the main objectives of the present paper is too assess the validity of flow solutions using LES in coarse meshes and different SGS models. The performance of four different models is here analyzed. These models are: the QR, SIGMA, WALE and VMS, all presented in section 5.2. Hereafter the results for both geometries on the $1600K$ and $2800K$ CV meshes for the Ahmed and Asmo car respectively are presented.

Ahmed car

As mentioned before, for this geometry the experimental data obtained by Lienhart et al. [71] is available. In figure 6, the average stream-wise and RMS velocity in the mid plane of the slant wall and the near wake are presented. Stream-wise velocity profiles shown in Fig. 5.5a evidence that the WALE model and SIGMA model results for velocity are closer to the experimental data

Table 5.2: Pressure drag (Ahmed car=0.285 [1]) and drag (Asmo car=0.153 [4]) with different meshes and turbulence models.

Model	Mesh	QR (% dif)	VMS	SIGMA	WALE
Ahmed	500K	0.312 (9.47)	−0.137 (−148.1)	0.005 (−98.25)	0.279 (−2.11)
	1000K	0.301(5.61)	0.302 (5.96)	0.281 (−1.40)	0.310 (8.77)
	1600K	0.290(1.75)	0.292 (2.46)	0.284 (−0.35)	0.304 (6.67)
Krajnović and Davidson [56]					0.292 (2.46)
Asmo	800K	0.169 (10.38)	0.139 (−9.15)	0.160 (4.58)	0.143 (−6.54)
	2000K	0.165 (7.78)	0.164 (7.19)	0.187 (22.48)	0.171 (15.55)
	2800K	0.153 (0.13)	0.154 (0.65)	0.168 (9.80)	0.162 (5.88)
	XFLOW [15]				0.151(−1.31)

Table 5.3: Ahmed car drag coefficients.

Model	Pressure	Skin friction $(\times 10^3)$	Total	% difference
VMS	0.292	9.406	0.302	2.46%
QR	0.290	8.926	0.299	1.75%
WALE	0.304	12.33	0.315	6.67%
SIGMA	0.284	10.82	0.294	−0.35%
Exp [1]	0.285	–		

than the other two models. Moreover, it can be seen that the WALE, SIGMA and VMS models yield good results in the boundary layer of the slant wall, where the QR model fails to predict the flow behavior correctly. Results for all models in the near wake deviate from the measured values, further downstream, they recover the agreement with experimental data. This behavior can be attributed to insufficient grid resolution in this area.

Fig. 5.5b shows the stream-wise root mean square velocity profile, $urms$. In this case, the VMS model yielded the best results of all four models. Again the less accurate data is the one resulting from the QR model.

Fig. 5.6 shows the mean velocity and root mean square velocity profiles at the $y = 0.1$ plane. Results for the mean stream wise velocity do not vary much from one model to other, being the closest to the experimental results those obtained with the SIGMA model. This same trend can be observed in Fig. 5.6b, where even though the variations are larger, results are similar for all models. Again, the SIGMA model results are a tad closer to the experimental data.

Two of the most important aerodynamic parameters are the lift and drag forces. The drag coefficient quantifies the advancing resistance posed by the air (surrounding fluid) onto the vehicle. The lift coefficient quantifies the force exerted onto the vehicle in the direction perpendicular to the flow. Reducing the drag coefficient of a vehicle will reduce its overall fuel consumption. On the other hand, reducing the lift coefficient will improve ride stability and cornering performance.

Table 5.3 shows the drag coefficient obtained with the different SGS models. The SIGMA model performs well in predicting the drag, specially the pressure, whereas the WALE shows the worst results. Furthermore, the VMS and the QR models yield similar results. Indeed all four models perform in a similar fashion when resolving the viscous drag. Regarding lift forces, as can be seen in table 5.4, the Ahmed geometry has a high lift coefficient, being of the same magnitude as the drag coefficient. All models give close values of the lift coefficient except for the WALE model whose deviations are the largest.

In general, the SIGMA and VMS models outperform the QR and WALE models. SIGMA and

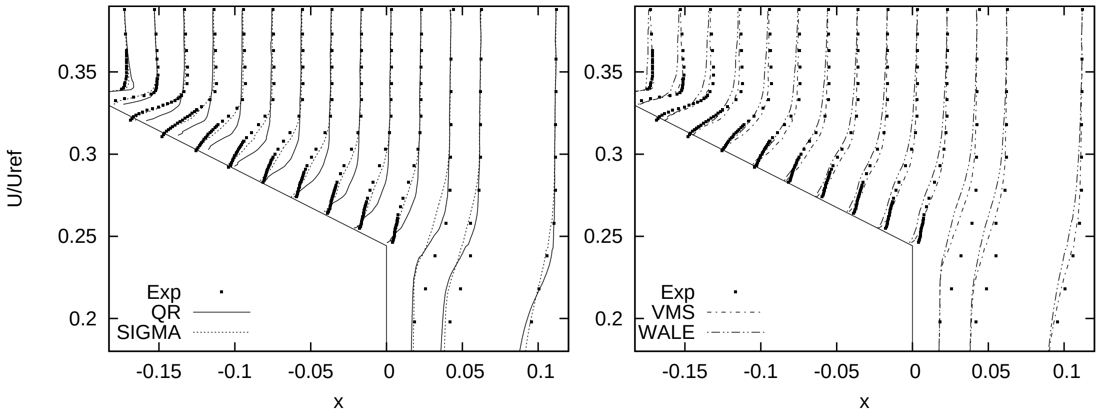

(a) Average stream-wise velocity profiles in the mid plane.

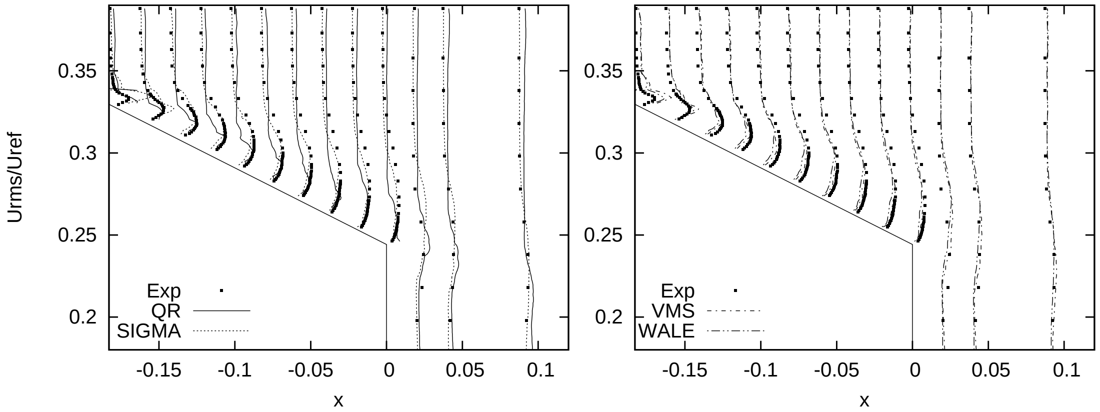

(b) RMS velocity profiles over the slant wall in the mid plane.

Figure 5.5: Velocity profiles in the Ahmed car.

Table 5.4: Ahmed car lift coefficients.

Model	Pressure	Skin friction ($\times 10^5$)	Total
VMS	0.331	12.88	0.331
QR	0.322	7.515	0.322
WALE	0.257	5.78	0.257
SIGMA	0.314	25.53	0.315

VMS results for mean velocity and RMS velocity are both very close to the experimental results. However, the VMS model over predicts the drag coefficient.

Asmo Car

The same models are used to solve the flow over the Asmo car. Fig. 5.7a shows the pressure distribution along the symmetry plane in the underbody. Results obtained with the QR model are the closest to the experimental results, showing very good agreement with the Daimler-Benz results. The SIGMA, VMS and WALE models show a good prediction of the front pressure spike. However, they fall short from the experimental results in the rear spike. WALE and SIGMA models under predict the pressure distribution in the frontal part of the car. The behavior of the VMS model is good; in the upwind section the results are close to the Daimler-Benz data whereas in the

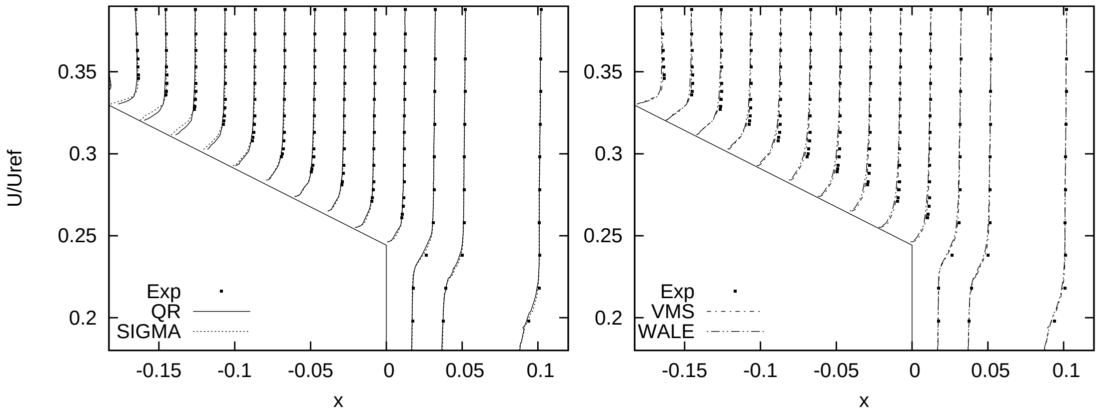

(a) Average stream-wise velocity profiles in the $y = 0.1$ plane.

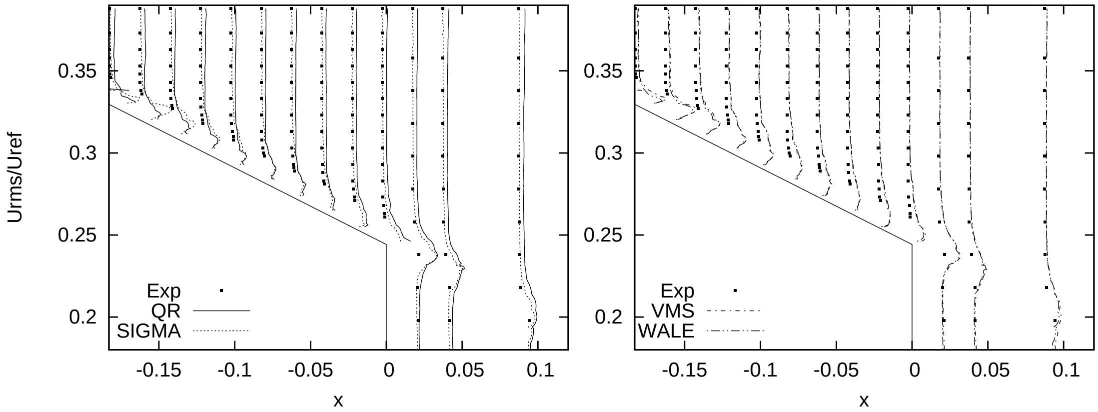

(b) RMS velocity profiles over the slant wall in the $y = 0.1$ plane.

Figure 5.6: Velocity profiles in the Ahmed car.

downwind section the results closely resemble those of the WALE and SIGMA models.

Fig. 5.7b shows the results over the rear of the car, where all of the models exhibit difficulties in the pressure profile resolution. The SIGMA model shows a good pressure distribution but it slightly under predicts it. VMS model under predicts the pressure coefficient near the roof. The QR models shows good agreement with experimental data in the top half of the car and and over predicts the pressure distribution near the bottom. Results obtained with the WALE model best resemble the experimental measurements. Fig. 5.7 shows that the QR model predicts a high negative pressure spike, probably associated with how spatial discretization influences the results within the model, specially where low quality meshes are encountered. This spike is also found by Tsubokura et al. [136].

Fig. 5.8a shows the results in the symmetry plane along the roof of the model. Results from all models are close to the experimental data. As will be shown in next section, there is a low pressure bubble wrapping around the car and centered in the middle of the roof. This produces a negative pressure spike in the figure, which all models reproduce in a similar fashion. Finally, Fig. 5.8b shows the pressure distribution in the frontal section. All models perform well on this area, with a correct prediction of the stagnation point. The SIGMA model predicts a higher stagnation pressure than the other three models, being closer to the Volvo measurements. In general, in both the roof and front part of the body, all models behave similarly.

Tables 5.5 and 5.6 show the force coefficients on the Asmo geometry. As it can be seen, the drag coefficient of the Ahmed car is nearly double the drag coefficient of the Asmo car. The drag coefficients calculated with the VMS and QR models are closer to the experimental value reported

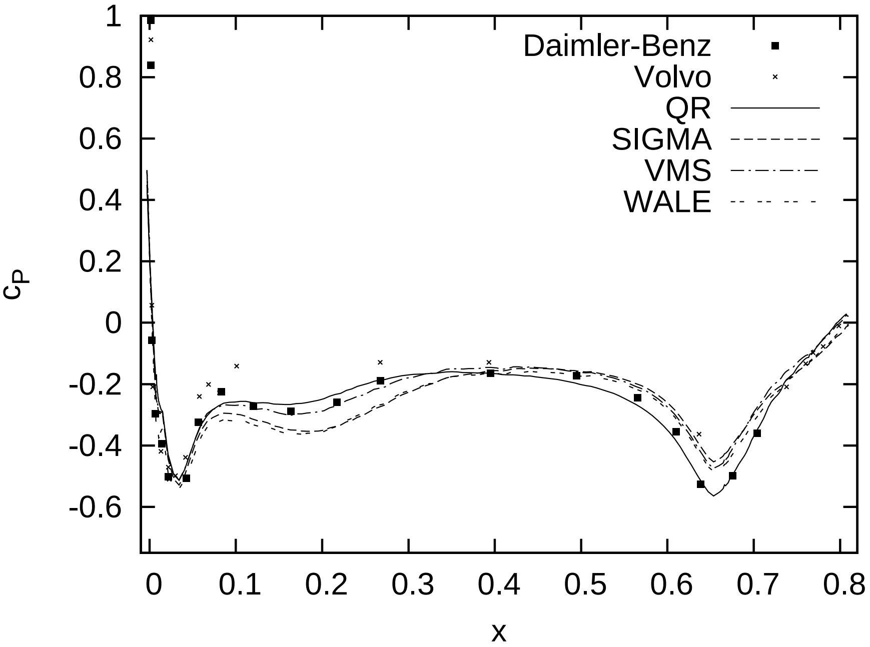

(a) Average pressure coefficient in the underbody

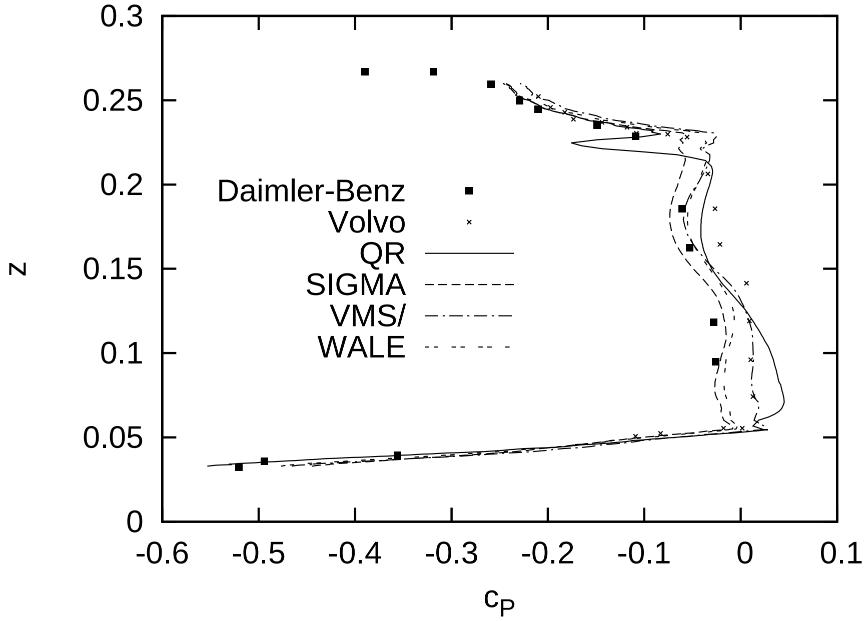

(b) Average pressure coefficient in the rear

Figure 5.7: Pressure coefficients in the Asmo car.

by Aronson et al. [4] than the other two models. With this mesh drag is over predicted in the WALE and the SIGMA models. All models predict a negative lift coefficient, the VMS, QR and SIGMA models report a very similar value. Comparing tables 5.4 and 5.6 it can be seen that the lift coefficient for the Asmo car is negative (down force) and its magnitude is smaller than the positive lift coefficient found for the Ahmed car.

The QR and WALE models showed better results for the pressure distribution for the Asmo

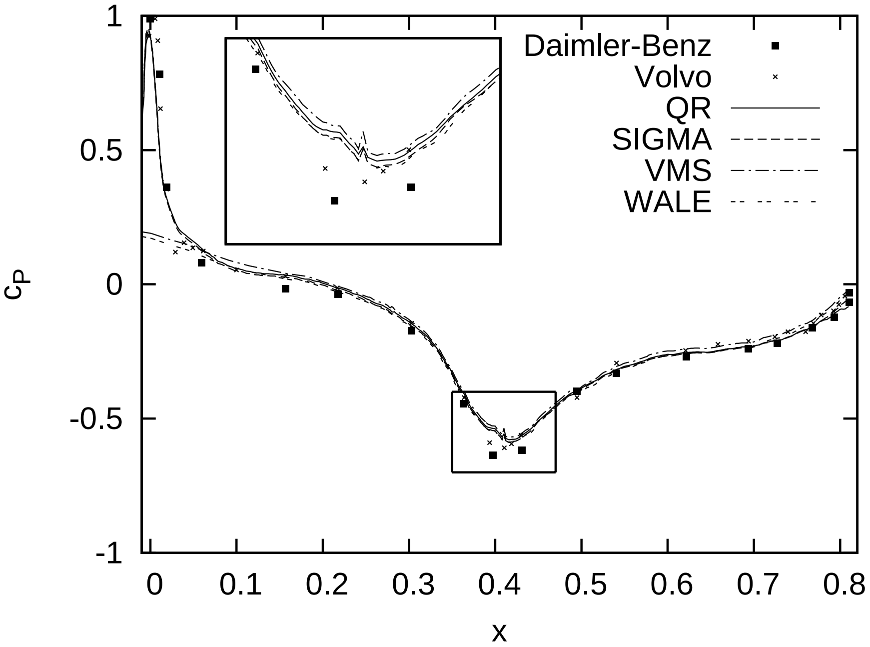

(a) Average pressure coefficient in the roof

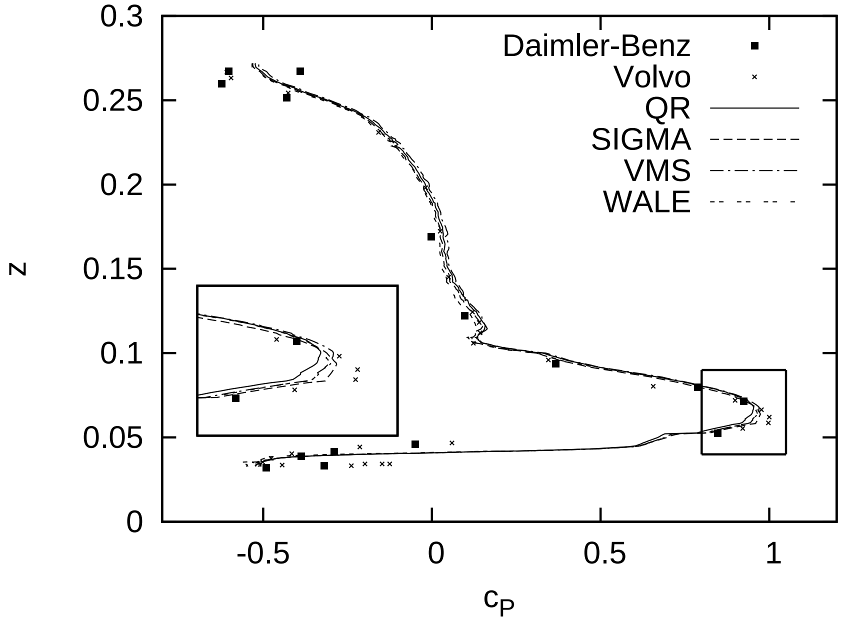

(b) Average pressure coefficient in the frontal section

Figure 5.8: Pressure coefficients in the Asmo car.

car. The drag coefficients were better predicted by the VMS and QR models.

Flow over the Ahmed car is better solved by the SIGMA and the VMS models. Flow in this geometry is characterized by heavy flow separation and a geometry influenced boundary layer. For the Asmo car, the QR and the VMS models show better results. The flow in this geometry is characterized by a laminarized flow structure and no pressure induced boundary layer separation. The QR model didn't perform well in the geometry-influenced boundary layer, however it had a

Table 5.5: Asmo car drag coefficients.

Model	Pressure	Skin friction	Total	% difference
VMS	0.143	0.011	0.154	0.65%
QR	0.140	0.013	0.153	0.13%
WALE	0.151	0.013	0.162	5.88%
SIGMA	0.154	0.014	0.168	9.80%
Exp [4]	–	–	0.153	

Table 5.6: Asmo car lift coefficients.

Model	Pressure	Skin friction ($\times 10^4$)	Total
VMS	-0.034	13.01	-0.023
QR	-0.039	16.60	-0.038
WALE	-0.069	8.95	-0.058
SIGMA	-0.030	18.69	-0.028

good performance when calculating force coefficients. The SIGMA model didn't perform well in the low pressure gradient flow. After the analysis of the results yielded by the LES models in both geometries it can be determined that the VMS shows a better overall behavior than the other three models, this SGS model is used for the results in the following sections.

5.3.3 Flow Structures

Average Flow Structures

According to Townsend's attached eddy hypothesis [133], the average large eddy motion consists of pairs of inviscid parallel roller vortices. These eddies extract energy from the mean flow through the vortex stretching mechanism. However, when the flow is bounded by a wall, the eddies are restricted and form double-cone eddies. Although Townsend's hypothesis holds for eddies spawning from a single point, these ideal flow structures hold great resemblance to the structures observed in the wake of both the Ahmed and Asmo car.

Several authors have proposed methods for identifying coherent structures of the flow (see for instance Hunt et al. [40], Jeong and Hussain [44], Chong et al. [12]). In the present work the Q-criterion proposed by Hunt et al. [40] is chosen for the identification of the coherent structures. The method is based on the second invariant of the velocity gradient tensor Q:

$$Q = \frac{1}{2}(||W^2|| - ||S^2||) \tag{5.10}$$

where $W = 1/2(\partial(\overline{u_i})/\partial x_i^T - \partial(\overline{u_i})/\partial x_i)$ is the strain-of-rotation tensor and $S = 1/2(\partial(\overline{u_i})/\partial x_i^T + \partial(\overline{u_i})/\partial x_i)$ is the rate of strain tensor.

The method identifies a vortical structure as a spatial region where $Q > 0$, i.e. where the rotation overcomes the strain. In Fig. 5.9, the time-averaged vortical structures for both the Ahmed and Asmo cars are presented.

Figures 5.9a and 5.9b show Q-iso contours of the vortices generated in the wake of the cars. These structures were obtained from the mean flow. As can be seen, two longitudinal vortices are generated in the back of the cars. The presence of these vortices can also be verified by means of a local pressure minimum, shown in figures 5.9c and 5.9d.

These turbulent structures are found on both the Ahmed and the Asmo geometries. However, when comparing the vortices in both geometries, the magnitude and strength of these structures in the Asmo car are lower, i.e. they are smaller in size than those present in the Ahmed car. This fact is specially evident in figures 5.9c and 5.9d, where compared to the pressure iso surface of

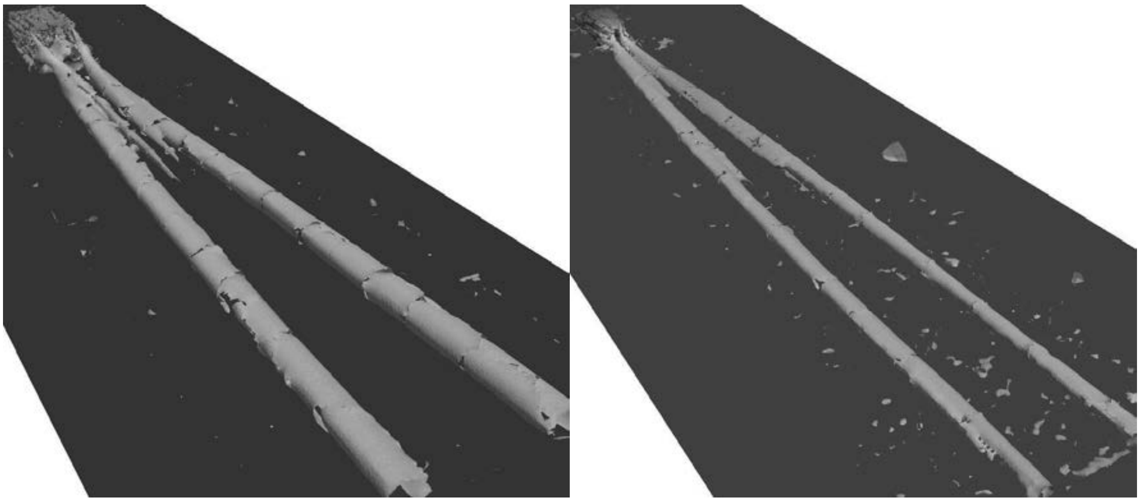

(a) Ahmed car Q=0.1

(b) Asmo car Q=0.1

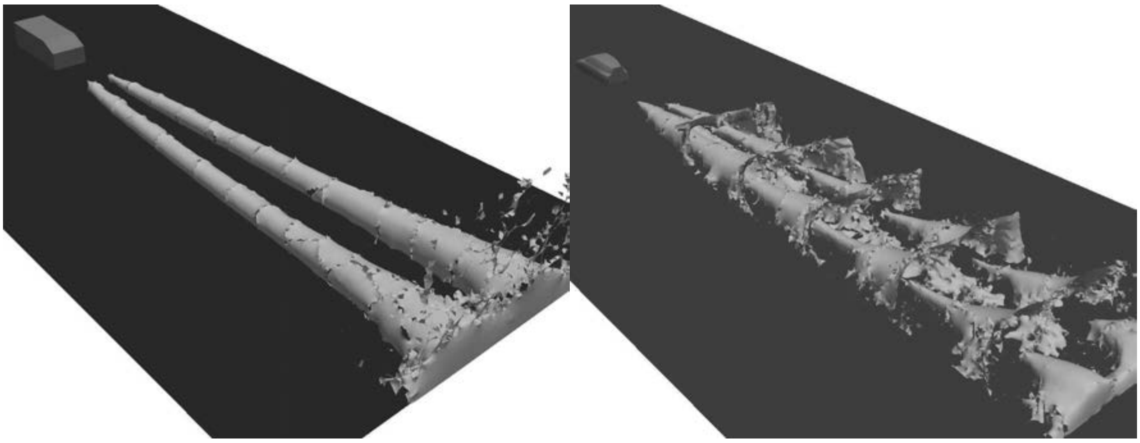

(c) Ahmed car P=0

(d) Asmo car P=(-0.01,0.01)

Figure 5.9: Time-averaged stream wise vortices.

the Ahmed car, the vortex structure in the Asmo car is fragmented into smaller, different valued pressure iso-surfaces making this eddy weaker in comparison to the one displayed by the Ahmed body flow. It can also be seen in Fig. 5.9 that the lower part of the vortices are bounded by the floor of the channel, which restricts the overall size of the eddy.[1] Fig. 5.10 shows the mean streamlines in the location where the main longitudinal vortices are generated. It is important to point out that even though the geometry in both cases is very different, i.e. the slant back in the Ahmed body and the curved profile of the Asmo car, the vortex generation mechanism seems to be the same. In both cases the following can be observed: i) a high speed stream moving along the side wall of the car; ii) a slow speed stream in the back of the car and, iii) the main flow traveling along the top of the body. In the Ahmed body the slow speed stream consists of fluid recirculating along the slant wall, whereas in the Asmo car it is the main recirculation bubble in the back. The vortex is generated by the interaction between these three streams, as the high speed stream passes the end of the side wall it flows towards the mid plane (pushed by the low pressure zone found in the back), crashing into the slow speed stream decelerating before colliding against the main flow present closer to the mid plane (where the pressure has a higher value). This second collision changes the mixed stream direction giving it a twirling motion, creating the longitudinal vortex.

---

[1] Fig. 5.9 was obtained using a mesh containing more CV in the wake area. All other mesh parameters remained the same

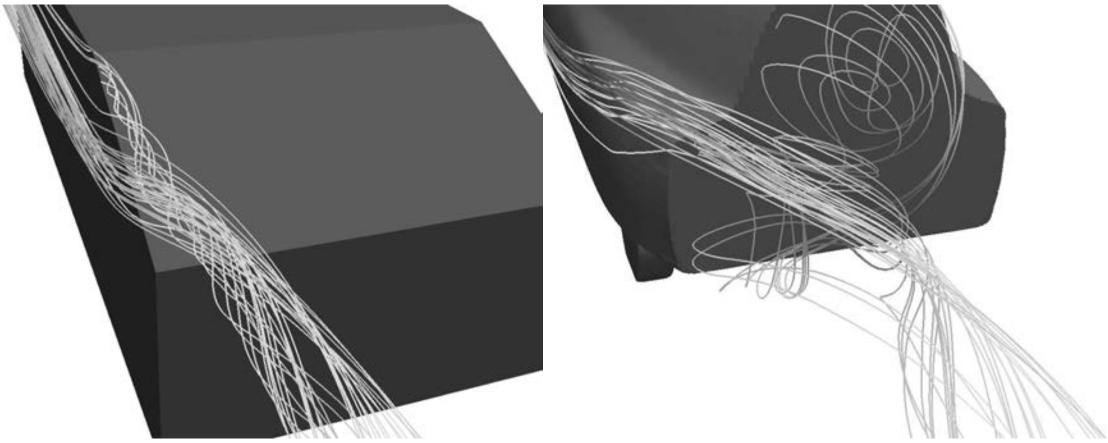

(a) Ahmed car (b) Asmo car

Figure 5.10: Time-averaged streamlines in the back of the car models.

Figures 5.11a and 5.11b show the recirculation bubbles behind the bodies. The recirculation non-dimensional length for the Ahmed body is around $0.69h_{ref}$ ($0.65h_{ref}$ in Krajnović and Davidson [56]), whereas for the Asmo body is around $0.48h_{ref}$. Besides from the size, the recirculation bubbles in both bodies differ in shape. In the Ahmed body it is composed of two straight span wise vortices generated by the flow coming down the slant back and the flow from the underbody. In the Asmo body, the vortex takes the shape of a horseshoe toroidal vortex bounded by the flow coming from the sides and the top of the body. The flow from the underbody, after passing through the diffuser, reduces its speed which decreases its influence in the recirculation bubble. This stream of fluid interacts with the toroidal vortex forming a smaller parallel vortex in the bottom of the recirculation bubble. Also shown in Fig. 5.11a is the flow detachment and recirculation areas that are formed in the slant back in the Ahmed car. The sudden geometry change causes the fluid to separate from the surface. This separation comes with a pressure drop that eventually pulls the fluid back towards the surface. The space between the detachment and reattachment point converts into a recirculation area. Flow detachment is generally identified by a low pressure zone. The places where fluid separation occurs are accompanied by steep pressure gradients that generate vortices and eddies, which in turn augment drag on the body. Other factors affecting the aerodynamic drag, and which are partially responsible for the pressure drag a body experiences, are the high pressure bubbles in the front of the geometry and low pressure bubbles in the back. Figures 5.12a and 5.12b depict the non-dimensional pressure coefficient (c_p) contours for the two bodies. These figures show that the pressure gradients in the Ahmed body are much greater than those of the Asmo body. Additionally, it can be seen that the Ahmed body has several zones of detachment. Furthermore, the pressure difference around the Ahmed car is larger than that of the Asmo car.

The mild pressure gradients in the Asmo body allow the flow to remain attached for most of the car length, producing a smaller wake as aforementioned. The steeper pressure gradients in the Ahmed body are strong enough to produce separated flow increasing the size of the recirculating bubble and pressure losses in the wake, and consequently increasing the pressure drag.

From Fig. 5.12, the high and low pressure bubbles around the bodies can be inferred. The low profile nose of the Asmo car allows the formation of a smoother flow pattern, diminishing the stagnation in the flow and reducing the size of the high pressure bubble. In the Ahmed car, the wider nose offers a larger resistance to the flow, increasing the size of the high pressure bubble. It is also important to notice that at the slant back the edges are in a low pressure zone with high flow separation. This accounts for the formation of the big lifted longitudinal vortices shown before. There is also a mid-body low pressure zone present in both geometries. In the Ahmed car it is found near the front of the car, immediately after the nose, whereas this zone is spread wider in the Asmo geometry, accounting for the smoother pressure gradients of this geometry.

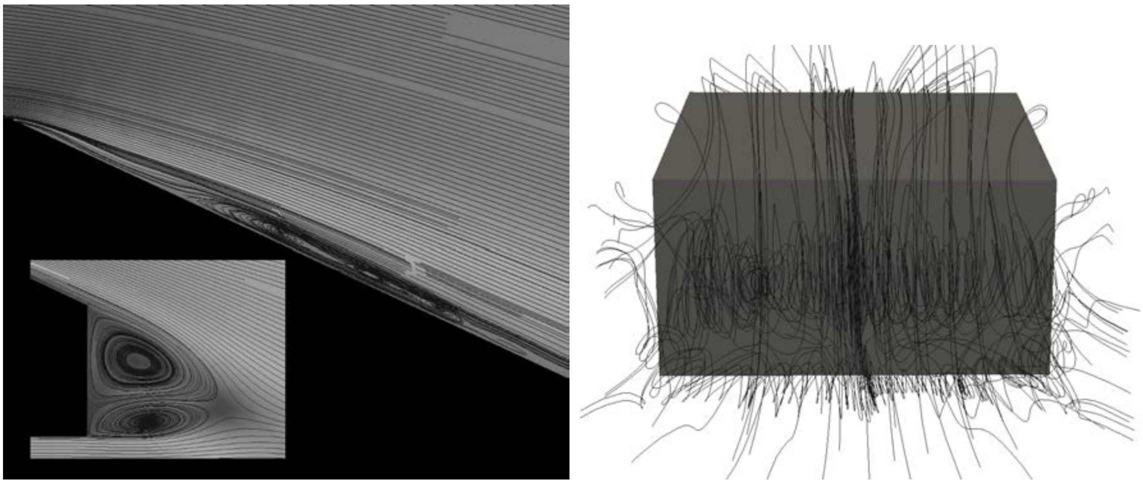

(a) Ahmed car

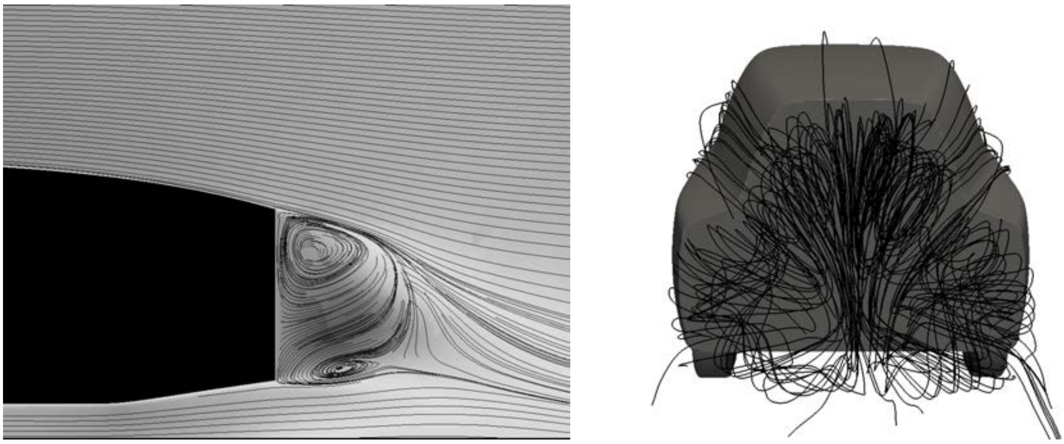

(b) Asmo car

Figure 5.11: Recirculation bubble behind the geometries.

The effects of pressure gradients can be classified in two mayor groups, positive and negative relative to the direction of the flow. These zones can readily be seen in Fig. 5.12.

Instantaneous Flow Structures

Figures 5.13 and 5.14 show the Q iso surfaces in the front of the cars. For comparison sake structures obtained with the same surface mesh but a refined volumetric mesh are shown side by side. The first structure in the front of the Ahmed car is smooth and resembles a laminarized flow. This part of the geometry has a negative pressure gradient (pressure decreases in the direction of the flow); this gradient "pushes" the fluid back, increasing the velocity gradient near the wall, increasing the local wall shear stress. The flow structure in front of the Asmo car is different. After passing the stagnation point (zone with no structure visible), the mild negative pressure gradient along the nose of the car permits the flow to be more stable than that found in the Ahmed car.

As the fluid moves back, it reaches the local pressure minimum and, thus, a zone of positive pressure gradient. Fig. 5.13 shows this point as the transition of the smooth coherent structure to the unstable flow along the top of the car. This zone is characterized by a separation region and a lower wall shear. This is depicted in the figure as a collection of small vortical structures lifting away from the wall. Several authors, such as Minguez et al. [79] and Krajnović and Davidson [57] stated there is a recirculation zone here. Even though the meshes used in the present study are not fine enough for a complete resolution of the flow in this area, evidence (pressure field and coherent

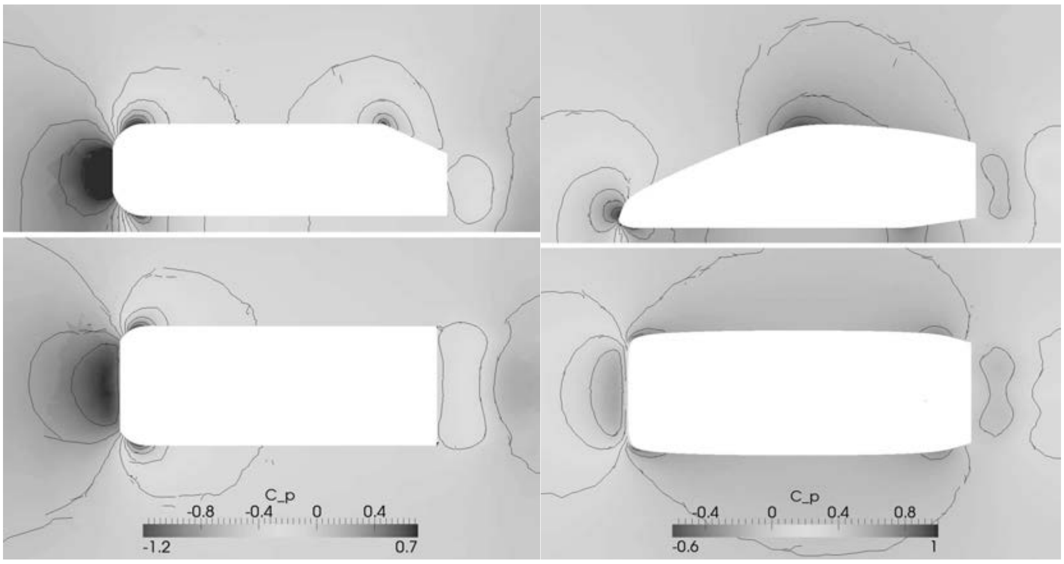

(a) Ahmed car (b) Asmo car

Figure 5.12: Time-averaged non-dimensional pressure contours.

structures) suggests the presence of recirculation in this place. Further back, the pressure gradient becomes small and the coherent structures in the Ahmed car exhibit the turbulent behavior to be expected from the streak instability cycle.

The flow over the Asmo car show very little instabilities. However, evidence of the behavior explained earlier can be found. As the fluid travels through the top of the nose it reaches a local pressure minimum. As the fluid closes on this point the pressure gradient becomes larger and a smoother structure that lightly resembles that of the Ahmed car forms. Upon reaching the low pressure point, the structure breaks down due to the negative pressure gradient. Furthermore, the small vortical structures in the bottom of the car, shown by Fig. 5.14, are vortices shed around the tires. A close inspection of Fig. 5.13 shows a small structure, generated in the lower corner of the car. As was exposed by Krajnović and Davidson [56], this vortical structure is generated by the interaction of the boundary layers of the floor and the underbody of the Ahmed car. The presence of the wheels in the Asmo car prevent this structure from forming.

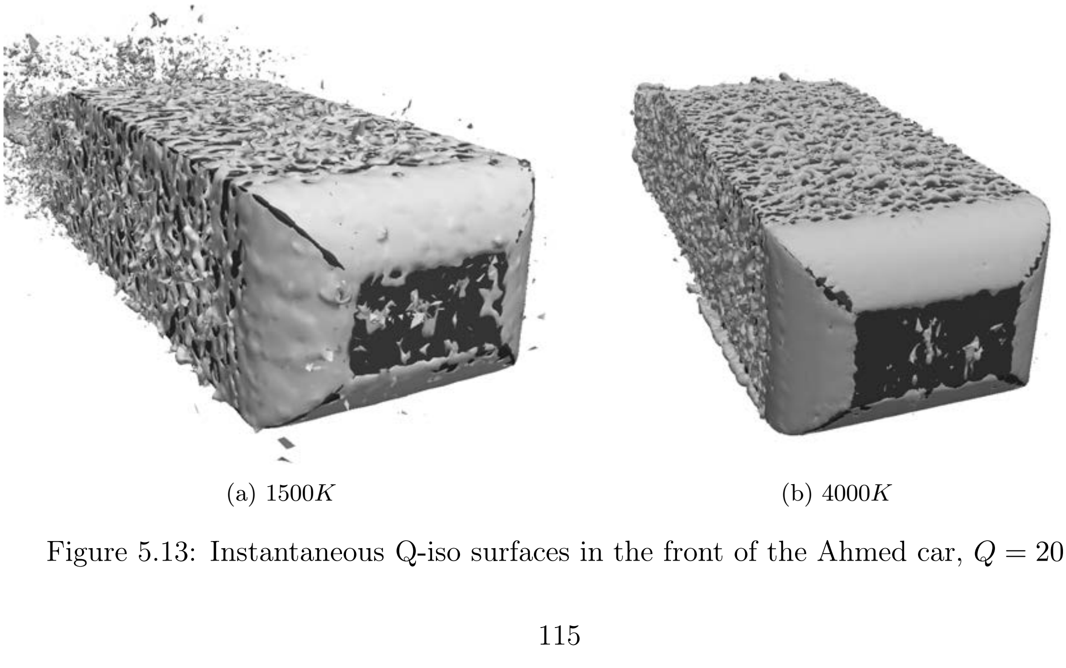

(a) $1500K$ (b) $4000K$

Figure 5.13: Instantaneous Q-iso surfaces in the front of the Ahmed car, $Q = 20$.

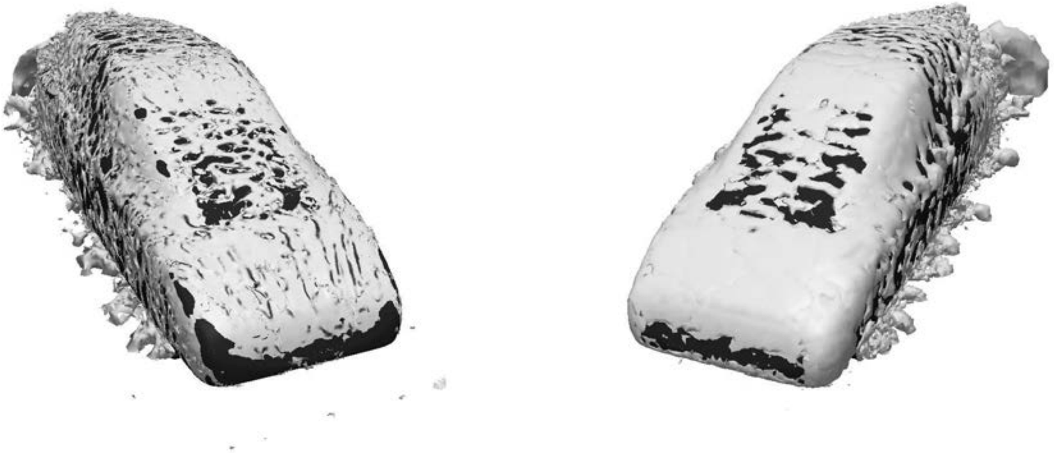

(a) 2800K (b) 5300K

Figure 5.14: Instantaneous Q-iso surfaces in the front of the Asmo car, $Q = 20$.

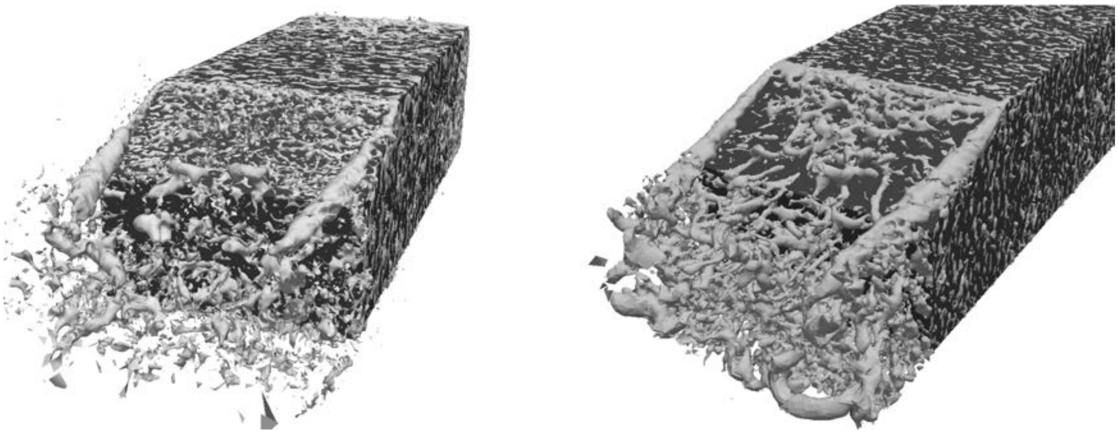

(a) 1500K (b) 4000K

Figure 5.15: Instantaneous Q-iso surfaces in the rear of the Ahmed car, $Q = 200$.

The flow structures in the back of the car are also very different. The slant back is a geometry feature unique to the Ahmed car and it displays very turbulent flow. Fig. 5.15 shows the Q iso surfaces in this region. It shows small vortical structures forming on the surface, right at the edge where the slanted surface starts, as well as several big vortical structures. These structures are the vortices that form the recirculation bubble, the big lifted stream wise vortices (shown earlier) and large horseshoe-like vortices shed from the slant wall.

The small vortical structures are the result of the change in surface direction and the subsequent negative pressure gradient generated. As was explained earlier, this pressure gradient creates flow instabilities, flow detachment, recirculation and flow reattachment. The combination of the flow instabilities and the geometry present add up to vortex shedding in this section.

The turbulent structures in the back of the Asmo car are different in shape and size as those seen in the Ahmed car. Fig. 5.16 shows smaller vortical structures being generated in the rear of the geometry. The vortex shedding phenomenon can be witnessed readily in this geometry; coherent structures detach from the bottom of the car, as well as small vortices detaching from the wheels, the diffuser and the trailing edge of the body. Two large structures, corresponding with the big stream wise vortices aforementioned are also seen. As it is expected in flow over buff

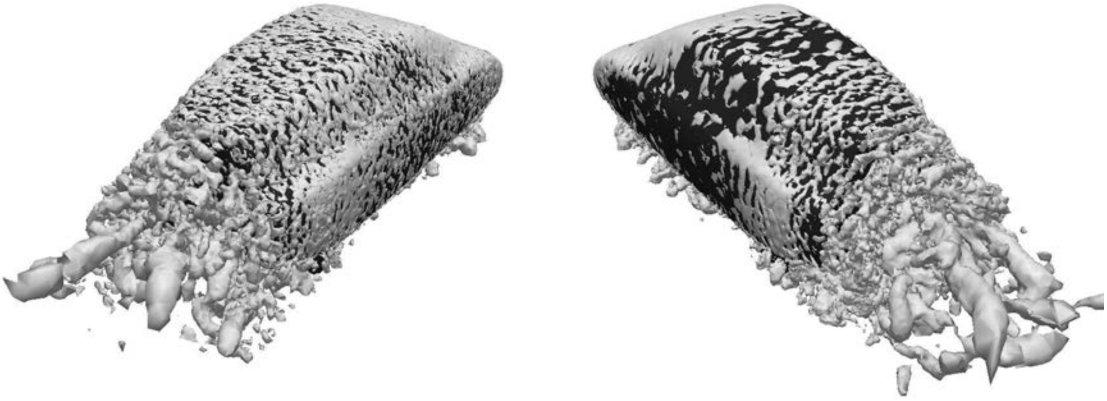

(a) 2800K (b) 5300K

Figure 5.16: Instantaneous iso surfaces in the back of the Asmo car, $Q = 200$.

bodies, both geometries show vortex shedding. However, in the Ahmed car, specially in the slant back, this phenomenon is very strong.

5.4 Conclusions

Challenging large-eddy simulations were carried out in two different geometries, the Asmo car and the Ahmed car; using four different turbulence models, the QR, the VMS, the SIGMA and the WALE. To the authors knowledge, this is the first time the SIGMA, QR and VMS models are used in resolving flow around simplified car models.

When comparing the results obtained in the Ahmed geometry with the experimental results it can be seen that the agreement in the slanted back is acceptable. Considering the coarse meshes used, results in the near wake show fairly good results when compared to the experimental data. The results of the Asmo car are also in quite good agreement with experimental results. Though they are not as accurate as other authors' results with finer meshes, comparisons here presented using such coarse grids are useful to evaluate CLES simulation potential.

Even though the grids used are quite coarse, coherent structures have been well captured. These structures in the flow around the Asmo car are much weaker and exhibit less turbulent behavior than those found around the Ahmed car. The largest structures in the flow, the lifted stream wise longitudinal vortices in the wake, are present in both geometries using the same generation mechanism. However, the geometry features of the Ahmed body allow for the formation of a much stronger vortex.

The recirculation bubble present in both geometries differ both in shape and size. The one present in the Asmo car is smaller, shows a horseshoe shape and is formed by flow coming from the top and the sides of the car. The bubble found in the Ahmed car is formed by two span wise vortices and is created by the flow coming from the top and the bottom of the geometry. The differences in this structure allow for different magnitudes in the pressure fields, being the pressure behind the Ahmed car lower than that found in the Asmo car.

Another difference in pressure is also found in the nose of the car. The low profile nose of the Asmo car results in less stagnation and lower pressures in the front. The Asmo car also exhibits lower pressure gradients around the entire body. This produces a more laminarized flow around the entire geometry, less vortical structures detaching and less vortex shedding in its back.

All the differences in the flow features explained in the previous paragraphs account for the results shown in tables 5.3 5.4, 5.5 and 5.6; the drag coefficient for the Ahmed car is higher than that calculated around the Asmo car. Additionally, the Ahmed car shows a large positive lift coefficient, opposed to the smaller value found for the Asmo car.

It should be pointed out that the LES turbulence models perform quite well in coarse meshes thanks to the conservative formulation used. The SIGMA and VMS models performed very similarly and better than the WALE and QR models in the Ahmed car, where the geometry changes and corners heavily influence the flow. QR and VMS models performed better than WALE and SIGMA models in the Asmo car. However, the VMS model showed better behavior as it deals quite well with flows heavily influenced by the boundary layer and by geometrical features. Overall analysis of the models leads to the conclusion that, from a practical viewpoint, the recommended model to solve cases involving flow past car-like bodies is the VMS model.

Chapter 6

On the IBM approximation for the wheel aerodynamic simulation

Main contents of this chapter have been published in:

Aljure, D. E., Lehmkuhl, O., Favre, F., Martínez, D. and Oliva, A. On the IBM approximation for the wheel aerodynamic simulation *First international conference in numerical and experimental aerodynamics of road vehicles and trains, At Bourdeaux*June 2014.

Abstract

Challenging large eddy simulations (CLES) are performed to the flow around simplified wheels in wheelhouses. Wheel geometry is modeled using immersed boundary methods. Results are compared to previous numerical simulations. Instantaneous flows results and turbulent structures are analyzed to asses the viability of this boundary treatment on the resolution of a rotating wheel.

6.1 Introduction

Aerodynamics of rotating wheels on vehicles is a topic of importance within the automotive industry. Within the last two decades several investigation projects have been carried out to complex flow present in these geometries. Fabianic [25] and Krajnović et. al. [58], amongst others studied a simplified body fitted with one pair of wheels. Régert et al. [109] and Gulyás et al [33] have studied the aerodynamics on the Ahmed car fitted with wheels and wheel-wells. The project carried out by Fabianic consisted in an experimental investigation into the flow around a wheel in a wheel well. Before Fabianic most of the investigation was centered on isolated wheels, whereas his experiments consisted of a simplified body which was fitted with different sized wheel-wells, rotating wheels and a moving ground plane. Their conclusion allowed for a higher understanding of the dynamics involved within the wheel wells and its effect on force coefficients i.e. drag and lift. Régert and Lagos performed computer fluid dynamic (CFD) calculation on a simplified car model (different than that studied by Fabianic [25]. The authors focused on the impact of the distance between wheel and the back of the body on the force coefficients. Régert et al. [109] studied the effect of wheels on the Ahmed Body using RANS simulations. Their results showed an increase in drag and lift coefficients consistent with previous results of force coefficient variations due to wheels and wheelhouses. Krajnović et. al. [58] solved numerically using LES the flow over the geometry first introduced by Fabianic [25]. Pressure coefficient results for the wheel arch and wheel force coefficients reported in this paper show a different trend than the experimental results of Fabianić [25]. The authors blame this difference on a discrepancy between the numerical and the experimental set ups. Gulyás et. al. [33] performed and experimental investigation into the Ahmed car with wheels and wheel wells. Their results consisted on flow visualization on the front wheel.

Immersed boundary method (IBM) approximations were originally developed by Peskin [98] to simulate cardiac mechanisms and blood flow. This method was further developed to solve interface problems with two different materials, the same material at different states and cases where detailed body-fitted mesh generation was impractical and/or complicated, amongst other applications. Mittal and Iaccarino [80] compiled a review on this boundary modeling technique encompassing different numerical methods and cases including flows with immersed solid boundaries. Verzicco et. al. [26] used this boundary condition on non-body conformal grids to simulate several turbulent flow cases accounting for the effect of the presence of a body in the flow by introducing a source term to the governing equations.

The present paper aims at solving the very complex turbulent flow within a wheel well fitted with a simplified rotating wheel using the IBM and challenging large eddy simulations (CLES).

6.2 Definition of the case

The geometries to be considered are the Fabianic body [25] and the 25° slant back Ahmed car fitted with wheel-wells and wheels [109] shown in Figs. 6.1 and 6.2.

Fig. 6.1 shows the dimensions of the Fabianic model and the wind tunnel used for the simu-

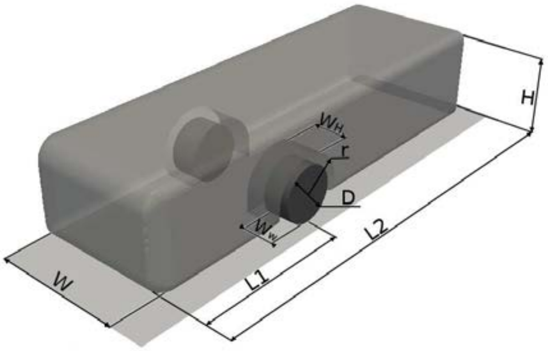

(a) Car

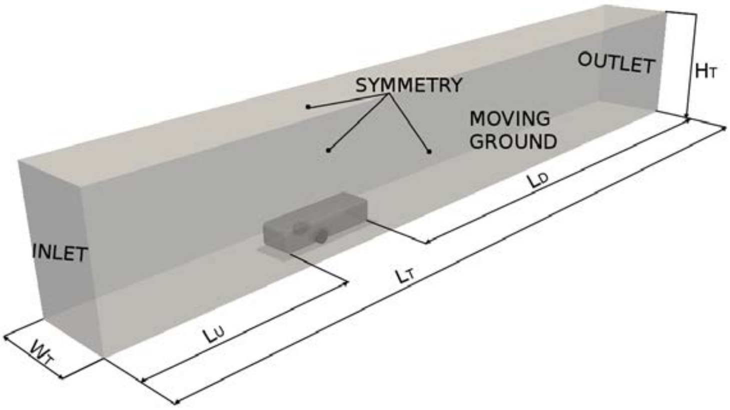

(b) Wind tunnel

Figure 6.1: Fabianic model geometry and computational domain.

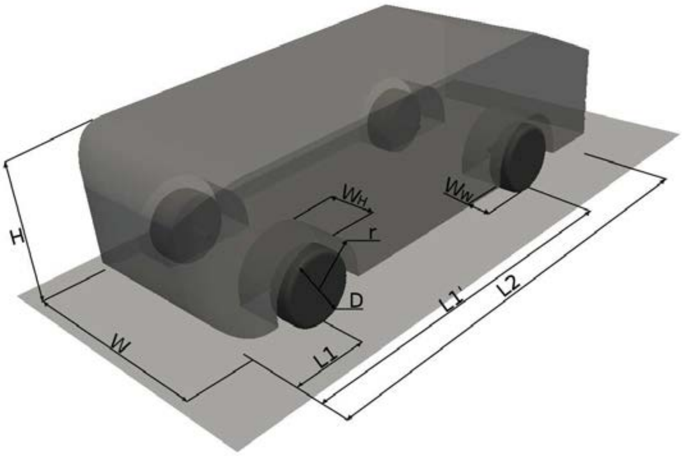

(a) Car

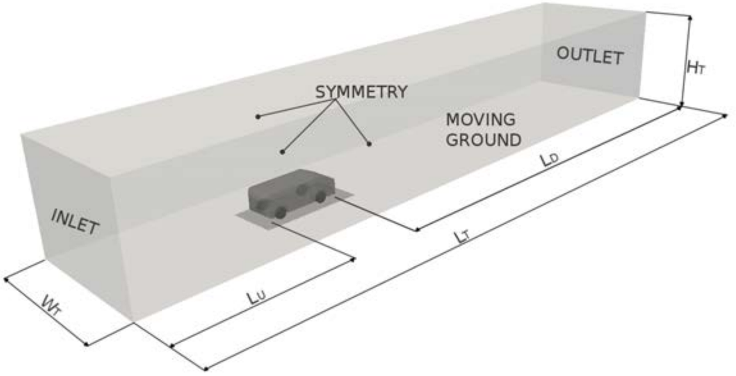

(b) Wind tunnel

Figure 6.2: Ahmed car model geometry and computational domain.

lation. The basic geometry of this model consists in a rectangular box with height (H) and width (W) resulting in an aspect ratio of 1.5 whereas the volume of the wheelhouse is twice the wheel volume. Present dimensions are the same as those used by Krajnović [58], shown in table 6.1. The Ahmed body car is a semi-rectangular vehicle with a rounded front and a slanted back fitted with wheelhouses and wheels. Dimensions for the Ahmed model with wheels and the wind tunnel are shown in Fig. 6.2. Dimensions for the wind tunnel used for this model are the same as for the wind tunnel of Lienhart et. al. [71] and Aljure et. al. [2]. More information on the geometries can be found in [25], [58] (Fabianic body) and [33] (Ahmed body).

6.3 Mathematical and numerical model

In order to study the flow the filtered incompressible Navier-Stokes equations are solved:

$$\frac{\partial \overline{u_i}}{\partial x_i} = 0 \tag{6.1}$$

$$\frac{\partial \overline{u_i}}{\partial t} + \frac{\partial (\overline{u_i u_j})}{\partial x_j} - \nu \frac{\partial^2 \overline{u_i}}{\partial x_j \partial x_j} + \rho^{-1} \frac{\partial \overline{p}}{\partial x_i} - \mathbf{f} = -\frac{\partial \tau_{ij}}{\partial x_j} \tag{6.2}$$

where $\overline{u_i}$ is the three-dimensional filtered velocity vector, $\overline{p}$ is the filtered pressure field, ν stands for the kinematic viscosity and ρ for the density of the fluid. $\mathbf{f}$ is the forcing term corresponding

Table 6.1: Computational domain and geometry dimensions in mm.

(a) Geometry.

	W	H	L1	L2	D	r	W_W	W_H
Fabianic	190.5	127	248.2	591.1	76.6	52.3	36.2	50.5
Ahmed	389	288	216-828	1044	144.167	96	48	96

(b) Wind tunnel.

	W_T	H_T	L_U	L_D	L_T
Fabianic	500	750	1150.4	3019.8	4761.3
Ahmed	1870	1400	2101.4	6048	9194.4

to the IBM (see next section). τ corresponds to the SGS stress tensor:

$$\tau = -2\nu_{SGS}\overline{S} + (\tau : I)I/3 \tag{6.3}$$

where ν_{SGS} is the turbulent or sub grid viscosity and $\overline{S}$ is the filtered rate of strain tensor.

Governing equations are discretized on a collocated unstructured mesh by means of finite volume techniques. A second-order conservative scheme is used for the spatial discretization [141]. Such schemes preserve the symmetry properties of the continuous differential operators and ensure both, stability and conservation of the kinetic-energy balance. The velocity-pressure coupling is solved by means of a fractional-step algorithm, the temporal discretization for the convective, diffusive and derivative parts of equation (6.2) was made using a second order self-adaptive scheme [134] and a back-ward Euler scheme was used for the pressure gradient. For more details about the discretization the reader is referred to [45] and [135]. Turbulence modeling is carried out in the present paper by using the sigma sub grid model [85], shown to perform well where the geometry changes and corners heavily influence the flow [2]. Three dimensional hybrid tetra-prism meshes are build using Ansys IcemCFD software.

6.3.1 Boundary conditions

A constant inlet velocity profile $u_i = (U_{ref}, 0, 0)$ is imposed and simulations run for a $Re = 1.6 \times 10^5$ based on wheel diameter for the Fabianic model and $Re = 2 \times 10^5$ based on model height for the Ahmed car. The wind tunnel outlet is modeled using a pressure based boundary condition. Top, front and back surfaces are modeled with a symmetry condition boundaries and no-slip condition for the car frame. Surface velocity $\boldsymbol{u_s} = \boldsymbol{\omega} \times \mathbf{r}$ is imposed in the wheels via the IBM, where $|\boldsymbol{\omega}| = 2\alpha U_{ref}/D$ is the angular velocity and $\mathbf{r}$ is the vector from the axis of rotation to the surface.

Fluid flow simulations of bluff bodies require meshes that include the whole computational domain and usually fit the body to be subject of study. IBM use non-body conforming grids, avoiding computationally expensive grid generation and grid quality issues. Governing equations are solved on the mesh and a forcing term $\mathbf{f}$ is introduced to model the immersed solid object and its influence on the flow field. As explained before, the fractional-step method is employed to perform the time evolution of the equations. This algorithm calculates a predictor velocity and then corrects it via a Poisson equation. When the predictor velocity is calculated, the source term $\mathbf{f}$ is introduced. As was said earlier, bluff bodies do not align with the meshes causing some cells to fall inside the body. In the present approach three node categories are created, interior, forcing and exterior. Interior and exterior nodes, as their name indicates, are nodes that fall completely inside or outside the object. Forcing nodes are those nodes that have an interior neighbor or are cut by the object's wall. The velocity condition is imposed on interior and forcing nodes modifying the net moment in the cell to specify the adequate velocity value u_i in those nodes. The value of $\mathbf{f}$

is calculated in such a way that the velocity in each node of the grid considers the presence of the object, therefore, **f** has a non-zero value only in the interior and forcing nodes.

$$\mathbf{f} = \frac{V - {u_i}^n}{\Delta t} - RHS \tag{6.4}$$

where V corresponds to the object's velocity (for interior nodes) or a velocity approximation (for forcing nodes), ${u_i}^n$ to the corrected velocity in the previous time-step and RHS corresponds to the predictor velocity calculated under the fractional step algorithm. The velocity approximation on the forcing points is performed using a second-order interpolation scheme [26] based on the distance from the boundary to the node and its neighboring points.

$$V = (a_w u_w + a_1 u_{nb1} + a_2 u_{nb2} + a_3 u_{nb3}) \tag{6.5}$$

there u_w corresponds to the velocity on the wall, u_{nbi} is the velocity of the neighboring points and a_i are the interpolation coefficients. This linear interpolation applied into the predictor velocity introduces error into the projection step of the fractional-step method. To account for this a more detailed calculation of the mass flux in the faces of cells containing forcing points as introduced by Huang and Sung [36], and Kang et. al. [47] is used.

6.3.2 Spatial discretization

Meshes for the present bluff body simulations can be divided into different zones: A fine near wall mesh is necessary to correctly solve the boundary layer and the physical phenomena associated with this zone, the near wake zone must be refined to correctly predict the flow structures trailing the car and finally a detailed mesh must be build where the wheels will lie. With these in mind a prism layer is used near the car wall due to the low non-orthogonal corrections required by this type of elements and the relative simplicity to place these kind of control volumes close to the

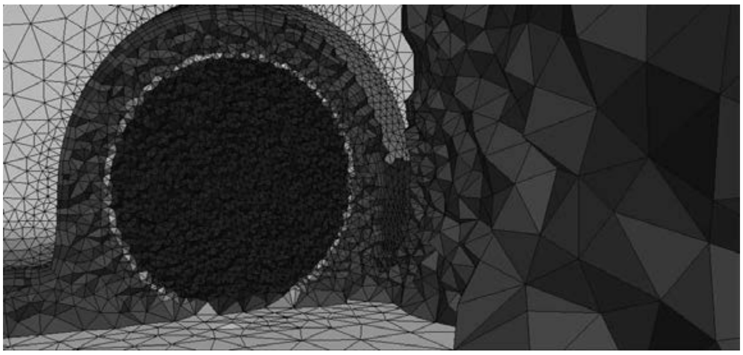

(a) M0

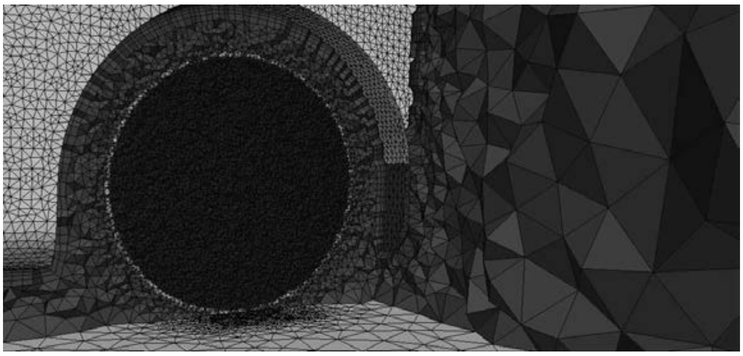

(b) M1

Figure 6.3: IBM approximation - Fabianic model.

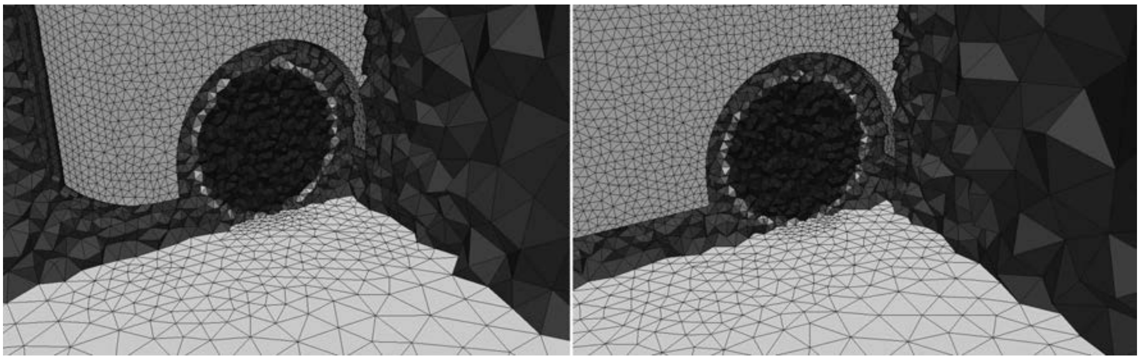
(a) M0

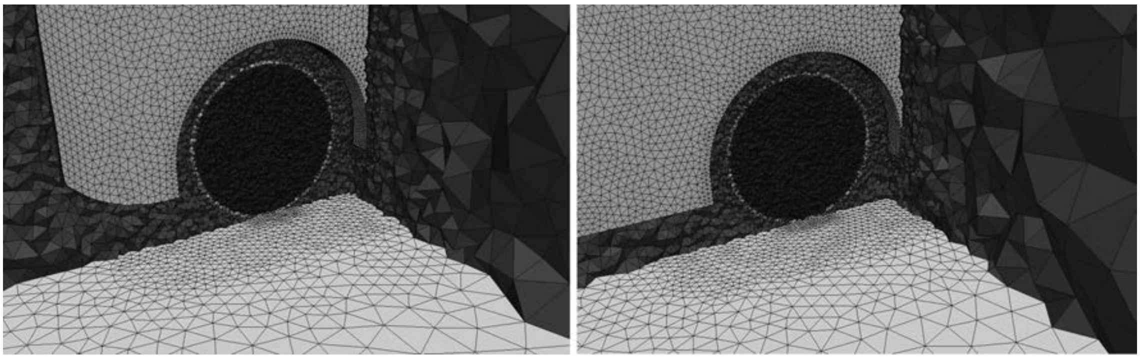
(b) M1

Figure 6.4: IBM approximation - Ahmed model.

surface and mesh concentration is done to correctly model the wheels. The present simulations are focused on the immediate surroundings of the wheels and wheel wells as well as the overall force coefficients. Two meshes are used with each car model, 1.67×10^6 and 4.43×10^6 CV for the Fabianic car and 1.27×10^6 and 3.23×10^6 CV for the Ahmed car. It is important to note that, most of the meshing effort is placed on the wheel areas. Figs. 6.3 and 6.4 shows the IBM approximation of the wheels for the Fabianic and Ahmed models on both meshes used.

6.4 Results and discussion

6.4.1 Fabianic model

Table 6.2 shows results for the drag, wheel drag and lift coefficients obtained from the fine mesh used by Krajnović et. al. [58] and present results for the Fabianic body and the percentage difference between them. Results are in agreement, additionally, as the mesh is refined, results approach those presented by previous authors.

Table 6.2: force coefficients on the Fabianic geometry, comparison to results by Krajnović et. al. [58].

	M0	M1	Krajnović
Drag (%dif)	0.410 (8.75)	0.354 (5.92)	0.3767
Wheel drag (%dif)	0.039 (47.60)	0.020 (24.67)	0.0266
Lift (%dif)	−0.028 (43.97)	−0.047 (4.67)	−0.0493

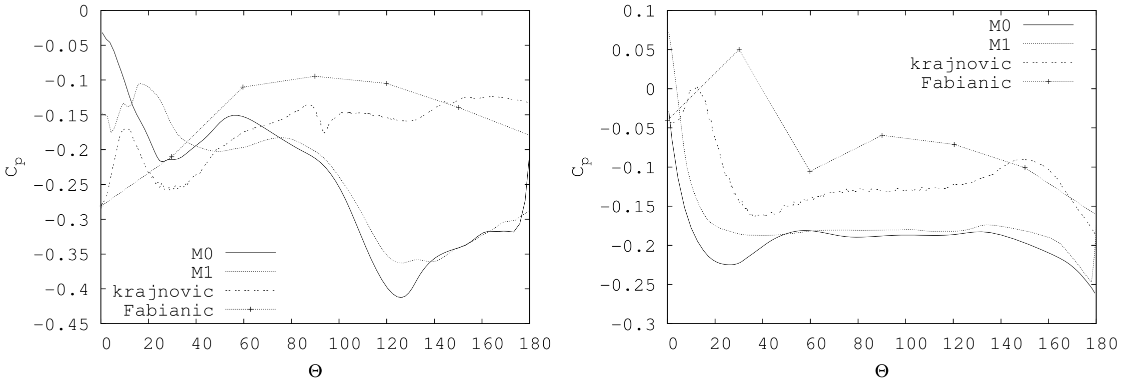

(a) Row 1 (b) Row 2

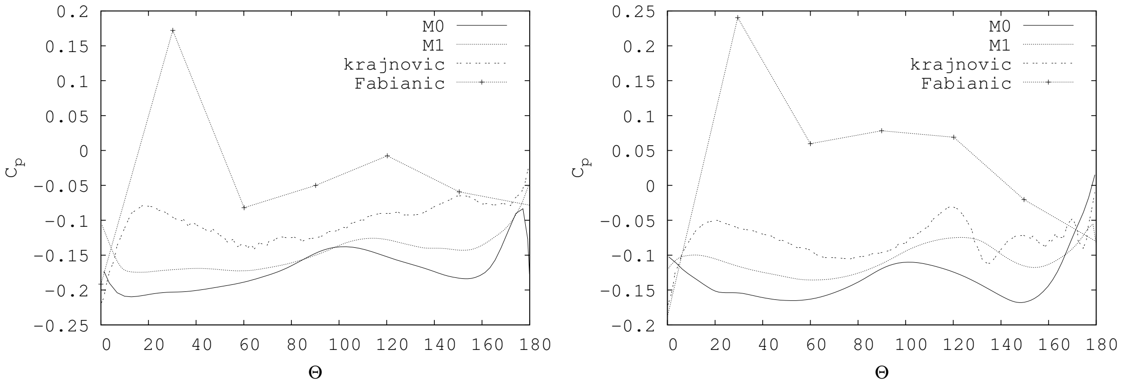

(c) Row 3 (d) Row 4

Figure 6.5: Pressure distribution in the wheelhouse.

Pressure distribution profiles alongside four different arcs within the wheelhouse surface are shown in Fig. 6.5. Row 1 corresponds to the pressure on the outer edge of the body, row 4 corresponds to the inner wall in the wheelhouse. Rows 2 and 3 align with the centerline and inner wall of the wheel respectively.

Results from the present investigation differ to those presented by Fabianic [25] and Krajnović [58]. As indicated by Krajnović, available experimental data for C_P and their results show discrepancies, however, the authors can not point the reason for this further than probable differences in experimental and numerical set ups. Pressure profiles obtained in the present simulations show the same trend in rows 2, 3 and for as those obtained by Krajnović, however they differ in magnitude, having the present results show a lower pressure value, as can be seen in Figs. 6.5b, 6.5c and 6.5d. Results for row 1 largely differ from the results by Krajnović, probably due to insufficient grid resolution. Finally, as seen from the four sub figures results are not in agreement with those obtained by Fabianic. Fig. 6.6 show the $Q = 750$ iso-surfaces found in the present simulations and compares them to the $Q = 1 \times 10^7$ structures presented by Krajnović S. and Basara [58]. It is important to note that results by Krajnović are obtained using finer meshes than those used in the present simulations allowing those results to show a larger number of structures and with greater detail. Present CLES simulations show only the larger structures.

Fig. 6.6a shows the coherent structures viewed from the front of the wheel. Most notorious is the jetting vortex seen on the outside (right side), marked in the image for clarity, which in the present simulations is seen larger than on results by Krajnović. Fig. 6.6b shows the structure seen from the outside of the wheel.

Four major structures can be observed (marked in the figure). Structures 1 and 4 describe

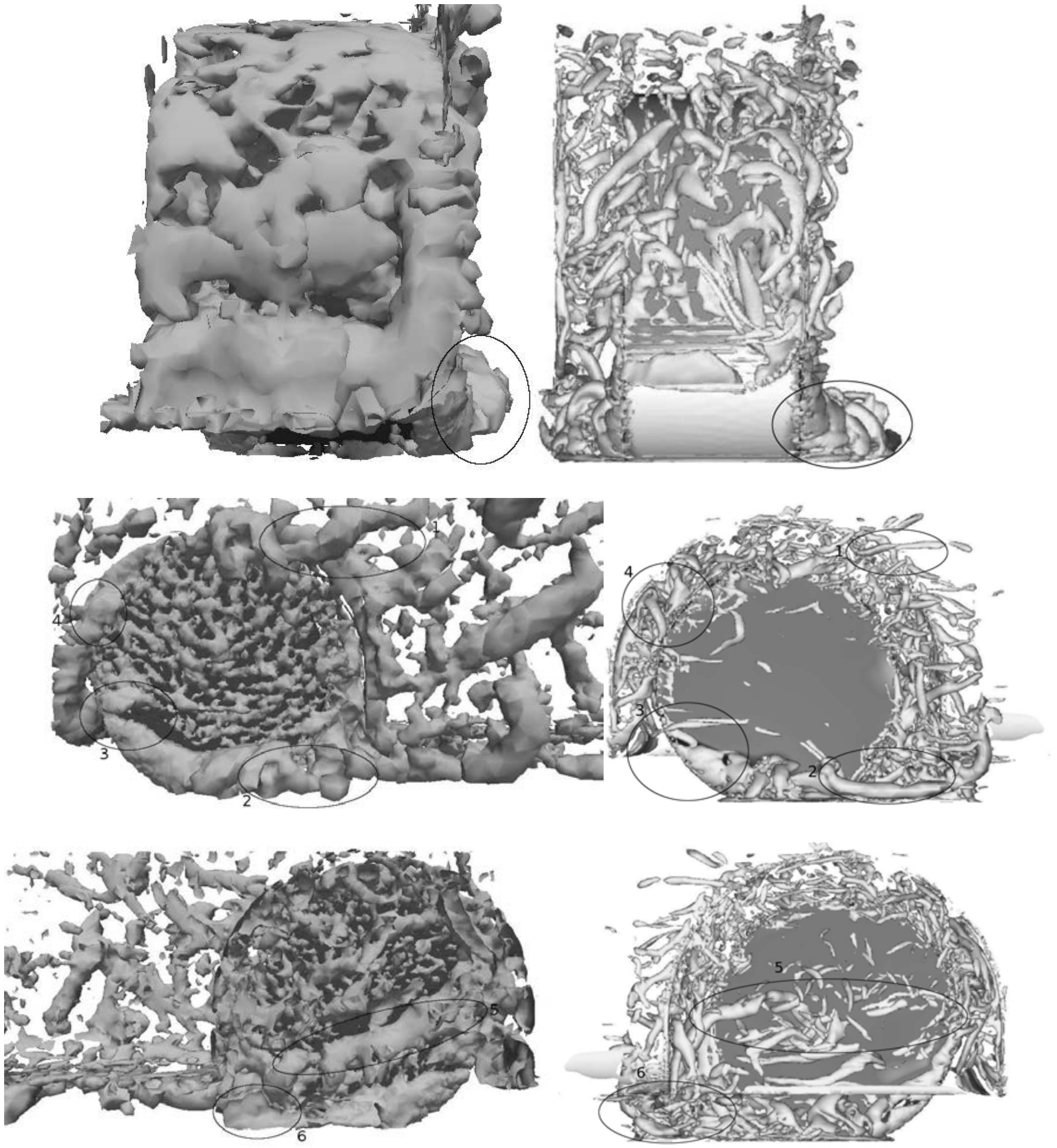

Figure 6.6: (a) Coherent structures on the front of the wheel, (b) coherent structures on the outside of the wheel and (c) coherent structures on the outside of the wheel. Left present results, right Krajnović S. and Basara [58].

vortices spawned from the interaction between the wheel and the wheelhouse, structure 2 is a jetting vortex resulting from the wheel-ground interaction whereas structure 3 is formed by the interaction of the wheel and the incoming flow.

Fig. 6.6c shows the coherent structures on the inside of the wheel. Two major vortical arrangements can be seen (marked on the image). Structure 5 is formed near the middle of the wheel due to the interaction of the rotating surface and the inside wall of the wheelhouse. Structure 6, just as structure 2 is a jetting vortex formed by the wheel-ground interaction. All structures are represented smaller on results by Krajnović than on the present simulations due to grid resolution. Fluid shows an out-ward motion, with the jetting vortices [58] expected on each side of the wheel.

6.4.2 Ahmed model

Table 6.3 shows the force coefficients on the Ahmed car model. Results for the lift coefficient in mesh M0 shows a very large difference when compared to the results by Régert and Lajos,

Table 6.3: force coefficients on the Ahmed geometry.

	M0	M1	Régert and Lajos [109]
Drag(%dif)	0.415 (12.8)	0.367 (0.27)	0.368
Wheel drag(%dif)	0.062 (55.5)	0.031 (22.5)	0.040
Lift(%dif)	0.971 (94.8)	0.530 (6.32)	0.499

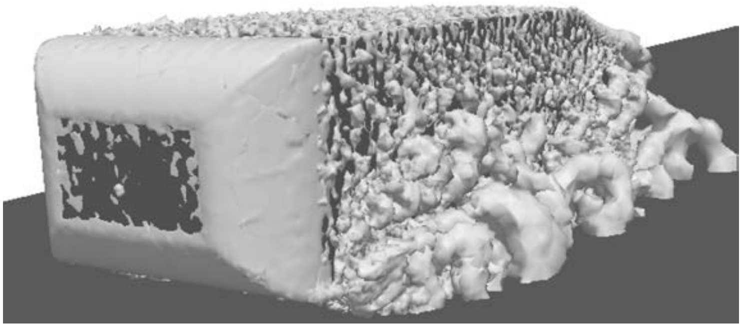

(a) Front

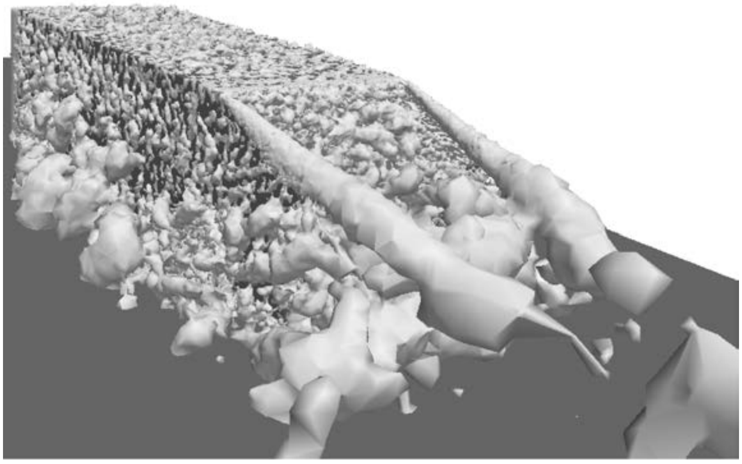

(b) Back

Figure 6.7: $Q = 10$ instantaneous iso-surfaces around the Ahmed body.

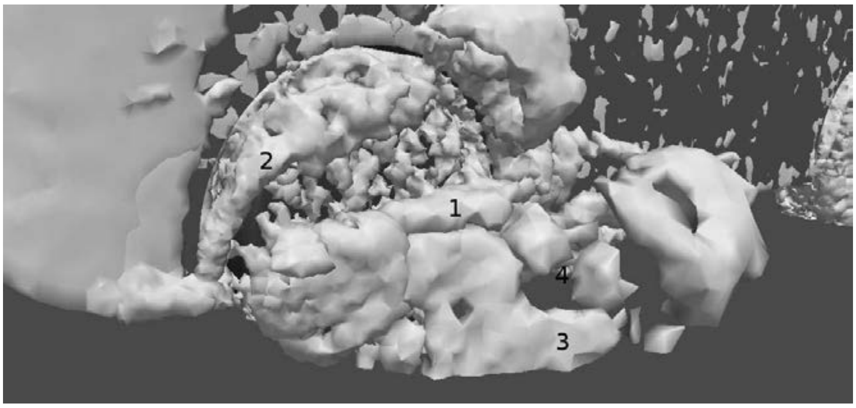

(a) Front

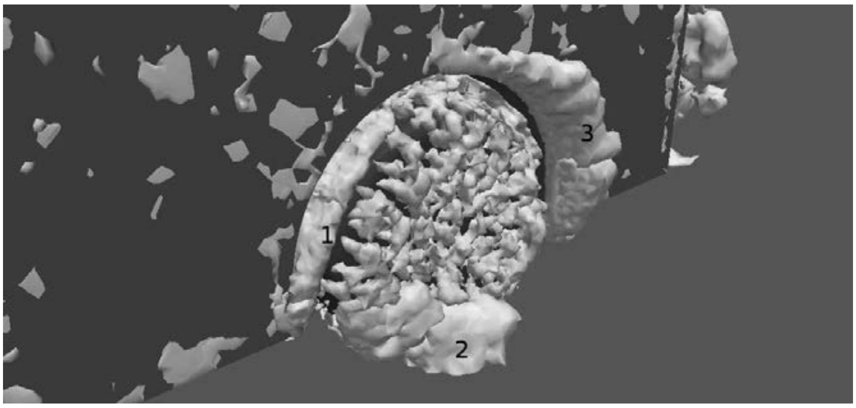

(b) Back

Figure 6.8: $Q = 50$ average iso-surfaces around the Ahmed body.

indicating that it is under-resolved. Results from mesh M1, although with error, are closer to those presented by Régert and Lajos.

Fig. 6.7 shows the $Q = 10$ iso-surfaces around the Ahmed body; vortical structures in this geometry resemble those seen in the wheel-less geometry. Interaction of the wheels with the rest of the body limit the formation of the lower corner vortex, and now visible are the jetting vortices seen in the Fabianic geometry. Additionally, structures stemming from the front wheels are much larger than those from the back wheels. As stated earlier, some structures resemble those seen in the standard Ahmed model such as the big stream wise vortices in the back or the detaching eddies in the slanted surface. The longitudinal vortex that seen along the lower front corner of the car (Aljure et. al. [2], Kranović et al [57]) forms by the interaction of the car and the ground, this structure remains on the flow when using the present geometry [109], however its formation is influenced by the wheel and wheelhouse. Fig. 6.7a shows the outward motion gained by the flow in this part of the geometry where this structure meets the vortices forming around the wheel to create highly turbulent flow alongside the lower side of the car. The fluid around the wheel pushes the vortex outward where it interacts with the wheel flow as can be seen in Fig. 6.8a (structures 1, 3 and 4). Fig. 6.7b shows the structures in the back. Interaction of the rear wheels with the main flow is lower than that seen in the front due to the outward motion the jetting vortices impinges on the flow causing the larger structures to move away from the car, however flow coming from the front wheel has a great influence over the flow on the rear one. It can also be seen from this figure the influence of both, front and rear wheels, on the recirculation bubble and near wake, specially near the rear corners of the car and underside. Finally, the big stream wise vortices and the detaching eddies in the slant back are visible in Fig. 6.7b.

Fig. 6.8 shows the coherent structures around both, front and back, wheels and wheelhouses.

Major vortices seen in Fig. 6.8a are: vortex 1 forming alongside the lower corner of the car, vortex 2 forming along the front edge of the wheelhouse and vortices 3 and 4 forming from the wheel-ground interaction. Fig. 6.8b shows the structures around the back wheel. Major structures seen in Fig. 6.8b are: vortex 1 forming alongside the front corner of the wheelhouse, vortex 2 forming from the wheel-ground interaction and vortex 3 forming in the rear edge of the wheelhouse. Major structures observed in the present results are presented in [109]. It is important to note that structures in the front are larger than in the back due to the influence of the blocking effect exerted by the body: the front wheels have a heavier interaction with the incoming flow than the back wheels do.

It is important to note that the IBM and meshes used in the present investigation do not approximate the wheel as a smooth surface, as observed in Fig. 6.3 and 6.4. This uneven interface introduces small scale vortices into the flow, observed as small grid-oriented vortices in Figs. 6.6 and 6.8.

6.5 Conclusions

Presence of the wheelhouse greatly increase the unsteadiness in the flow and increment the force coefficients. Approximation of the wheel by means of the immersed boundary conditions reduces significantly the mesh requirements and restrictions present, however, surface resolution is sacrificed.

Large scale structures observed are consistent to previous works by other authors, however, the uneven approximation of the wheel surface introduces small scale structures which taint the results. Finer meshes reduce the influence of these flow irregularities.

The combination of CLES and IBM approach serves as an approximation to study the overall behavior of the flow interactions of rotating wheels with the rest of the car geometry correctly predicting force coefficients and large scale structures, however, small length scales are not captured properly.

Chapter 7

Flow over a realistic car model: Wall modeled large eddy simulations assessment and unsteady effects

Main contents of this chapter will be published in:

Aljure, D. E., Calafell, O., Baez, A. and Oliva, A. Flow over a realistic car model: Wall modeled large eddy simulations assessment and unsteady effects. *ERCOFTAC Workshop Direct and Large-Eddy Simulation 11, At Pisa* May 2017.

Abstract

Numerical simulations are carried out on the flow over a realistic generic car geometry, the drivAer-fastback car model. Simulations are performed using a smooth underbody, mirrors, simplified wheels and moving ground. Pure large eddy simulations (LES) and wall-modeled large eddy simulations (WMLES) are used and compared to numerical and experimental results to assess the validity of these approaches when solving complex automotive geometries. Results show that the wall model improves the obtained force coefficients, whereas pressure profiles exhibit mixed results. The wall model used works well in adverse pressure gradients and smooth geometry changes. Results worsen in sections where the flow detaches and experiences large pressure drops. Nonetheless, using the wall model improves the overall flow predictions with a very low computational cost. Flow structures and unsteady effects around the car are also analyzed, obtaining several characteristic frequencies for the different flow structures encountered.

7.1 Introduction

Computational fluid dynamics (CFD) is a very powerful tool for the study of turbulence and turbulent flows, as well as, allowing an in depth study of cases that present massive separations. Recent computational advances have made possible the study of very complex cases by using high performance computing (HPC) and advanced numerical algorithms, such as direct numerical simulations (DNS) and large eddy simulations (LES). Some limitations are found for DNS due to the large range of spatial and temporal scales to be solved. On the other hand, LES are quickly developing to become an important tool in industrial research, however, they still require large amounts of computational resources. In LES, only the smallest (sub-grid) scales of the flow are modeled, while the large scales are explicitly solved. To do so, a sub grid model has to be implemented on the solver [2]. One of the main limitations when using LES is the high computational cost to properly resolve the wall regions, from both a spatial and temporal viewpoint, since these areas enclose a wide range of different scales of motion. The boundary layer has strong interactions with the surrounding flow and heavily influences its evolution even in the far field. Hence, a proper mesh resolution in this area is of vital importance to obtain good results. Since length scales decrease dramatically as the flow approaches the wall, especially at high Reynolds, very small control volumes are required in these regions, increasing the cell count and restricting the time step which makes large-eddy simulation of wall bounded flows at high Reynolds almost unaffordable.

The wall modeled large-eddy simulation (WMLES) aim is to provide a suitable and cost-effective solution for wall bounded flows, resolving the larger eddies of the flow away from the wall and modeling the complex phenomena in the near-wall region. In WMLES, the grid resolution in the wall area is not enough to capture all the flow-related phenomena. Nonetheless, if the grid is large enough, the flow behavior encountered there can be seen as an ensemble average and the treatment of this area can be done by means of statistical tools [101], including the time-averaged Reynolds averaged Navier-Stokes (RANS) formulation. Different strategies have been developed in order to model the boundary layer instead of resolving it explicitly, being the hybrid RANS-LES and wall shear stress models (WSSM) the most relevant. In the first case, the boundary layer region is modeled by means a RANS model while the far field is solved with a LES approach. In the wall shear stress strategy, the whole domain is resolved with a LES model while an accurate wall shear stress, obtained with an external model, is supplied to the LES domain through the solid boundary. A wide variety of WSSM formulations can be found in the literature with different degrees of accuracy and ranges of applicability, namely wall functions (WF), integral boundary layer approaches and zonal or two layer models (TLM). In the simplest wall models (i.e. the wall functions), the wall shear stress is a function of the LES velocity field and it is evaluated through an algebraic expression derived from an a priori known velocity field as in the Werner and Wengle [144] WF, based on the law of the wall. The integral boundary layer models could be considered a more accurate variant of the wall functions in which the governing equations are integrated in the wall normal direction considering non-equilibrium terms such as the advective and the pressure gradient [150]. In the two layer models approach, governing equations are fully or numerically resolved in a fine embedded mesh which extends between the solid wall and a given height lower than the boundary layer thickness. The degree of accuracy is variable depending on the equations solved in the model which may range from a simple diffusive term (i.e. equilibrium model) to the full RANS equations [51, 93]. An extensive review on hybrid RANS-LES approach was published by Spalart [126], while for wall modeling in general and two layer models in particular, detailed information can be found in the reviews of Piomelli [100] and Larsson et al. [61], respectively.

CFD can be used in a variety of industrial related applications. The automotive industry makes great advances every year; engine performance has increased greatly in the past decade, along with weight reduction and safety measures. These advances make aerodynamics more important to ensure high efficiency and vehicle drive stability. Most CFD research on automotive external aerodynamics has been carried out using very simplified models such as the Ahmed or Asmo car models [2]. These simplified bodies give a general idea regarding the fluid flow topology present in cars, however, as their geometries vastly differ from actual car geometries, the results exhibit a high degree of abstraction and do not fully reproduce the real aerodynamic behavior present in automotive geometries. To overcome this deficiency, the drivAer car model was introduced in 2012 [34]. This realistic generic car is based on the geometries of the Audi A4 and the BMW 3 series, and was conceived to investigate the specific flow structures present in current production cars. Heft et al. [34] performed wind tunnel experiments on different configurations of the drivAer model. These configurations are divided by several features: type of back (fastback, estate back and notch back), underbody (detailed and simplified), mirrors (with and without), wheels (with and without) and ground simulation (with and without). The obtained results showed that the influence of the Reynolds number on the drag coefficient lessens with augmenting Reynolds numbers, being almost independent for $Re \geq 4.87 \times 10^6$. Furthermore, pressure profiles over the top, bottom and side of the car were reported in this initial investigation. The comparison between the profiles obtained along the top of the vehicle with and without ground simulation showed nearly no difference, whereas a higher influence was observed on the bottom. Finally, they state the large influence the mirrors exert on the flow over the windshield and side windows, affecting the A-pillar vortex formation. Strangfeld et al. [128] and Wieser et al. [145] performed further experimental observations on the drivAer geometry, including side wind conditions. Their results showed that, for the fastback configurations, independence of the drag coefficient with regards to Reynolds number was achieved at around $Re = 2 \times 10^6$, less than half the value reported by Heft et al. [34]. These experiments were carried out without a moving ground. Moreover, the force measurements were in very good agreement with those performed at TU-Munich by Heft et al. [34]. A decomposed pressure distribution of the drag and lift coefficients helped identify the dominant regions which influence the forces around the car. For the no side-wind case, the areas identified were the upper region of the rear window and the c-pillars. Additionally, from their results a separation bubble was identified in the models rear (at the start of the rear window), showing a symmetric pattern for the Fastback configuration. They also observed considerable fluctuations within the cars wake, which could affect the force measurements. A spectral analysis performed showed several dominant frequencies in the flow, confined in the rear sections of the car and dependent on the measurement location.

Several numerical works have also been carried out with the drivAer model, particularly RANS simulations [5, 31, 32, 43, 99, 123] and hybrid approaches such as detached eddy simulations (DES) [5, 31] or partial averaged Navier-Stokes (PANS) [43]. Other numerical approaches have also been used, such as the lattice Boltzmann method (LBM) [94]. These authors have used meshes ranging from 19×10^6 to 125×10^6 control volumes for Reynolds number $Re = 4.87 \times 10^6$. These authors point out the improvement of results obtained when using unsteady simulations, showing that these algorithms are more suitable to correctly predict forces and correctly capture flow phenomena in automotive external aerodynamics. The flow structure described by the different authors show a very complex wake which exhibits large recirculation regions behind the car [5], counter rotating vortices stemming from the under body [43] and vortices detaching from the A-pillars and the mirrors [32]. It should be noticed that several investigations show that the flow remains attached above the rear window [32, 43], while the observations of Strangfeld et al. [128] and Wieser et al. [145] showed the opposite. In most works a general good agreement of the numerical pressure profiles with those obtained experimentally was reported, however some deviations were found, specially in the vehicle's top. Peters et al. [99] pointed to the presence of the roof stinger in experiments and the differences between the CAD and real geometries as the source for these discrepancies. In addition, force coefficients show some scattering, specially in the lift coefficient. Ashton et al. [5] identified the major source of error at the car's rear section, where separation regions are found and the flow structure is more complex.

Fewer papers have focused on the impact of the rotating wheels and ground simulations on the overall flow configuration over the drivAer car geometry. Guilmineau [32] identified the interactions present between the rotating wheels and the underbody of the car, leading to a reduction in both the drag and lift coefficient (with respect to the same geometry with stationary wheels). This change in force coefficients was also observed experimentally by Heft et al. [34] and numerically by Shinde et al. [123] amongst others. Other observed effects include a change in the vortices stemming from the wheels, particularly those forming around the front wheels. The pressure distribution along the top of the car does not seem to be very affected by the ground simulation, however, significant changes were observed in the pressure profiles around the side and bottom of the car.

One of the main characteristics of external automotive aerodynamics is the wide variety of unsteady effects present in its flow configuration. In this sense, several authors have pointed out the existence of time-periodic phenomena in sedan-type cars. Duell and George [23] and Gilhome [29] both observed characteristic frequencies within the flow around cars and attributed them to large-scale hairpin vortex shedding and shear layer vortex shedding. This phenomena has also been observed by Wieser et al. [145] in his experiments around the drivAer fastback model. In fact, Wieser et al. [145] characterized several frequencies around the drivAer model. Near the model's base region (rear bumper area) a Strouhal number ($St = fH_{ref}/u_{ref}$) of $St \approx 0.07$ was detected (St number normalized with base height). This frequency coincides with the pumping effect described by Duell and George [23]. A second frequency component of $St \approx 1.27$ detected near the base edges is argued to be a shedding frequency. Frequencies of $St = 0.21$ and $St = 4.63$ were also observed around the car's back. Wieser et al. [145] related the former to the characteristic frequencies observed in generic bluff bodies, whereas the higher frequency was associated to the flow detaching from the top of the rear window. A frequency around $St \approx 0.28$, was related to the rear wheel rotation, was also observed behind the vehicle.

Most of the numerical research work performed so far has been carried out using steady state simulations while unsteady simulations have been limited to DES and PANS modeling approximations. In this sense, the present work aims to advance in the understanding of the physics governing the flow over the drivAer geometry, in particular the unsteady effects inherent in automotive aerodynamics. To do so, LES and WMLES simulations will be carried out. Initially, time integration and mesh sensibility analyses will be performed. Afterwards, the WMLES strategy for automotive aerodynamic type flows will be assessed and evaluated by comparing the results obtained from the WMLES with a pure LES solution and performing a sub grid model study using the SIGMA and VMS models, and comparisons to experimental measurements. Finally, an analysis into the unsteady effects and flow structures found around the car will take place.

7.2 Mathematical and Numerical Model

7.2.1 Governing equations

In order to study the flow, the filtered incompressible Navier-Stokes equations are solved numerically:

$$\frac{\partial \overline{u_i}}{\partial x_i} = 0 \tag{7.1}$$

$$\frac{\partial \overline{u_i}}{\partial t} + \frac{\partial (\overline{u_i u_j})}{\partial x_j} - \nu \frac{\partial^2 \overline{u_i}}{\partial x_j \partial x_j} + \rho^{-1} \frac{\partial \overline{p}}{\partial x_i} = -\frac{\partial \tau_{ij}}{\partial x_j} \tag{7.2}$$

where $\overline{u_i}$ stands for the filtered three-dimensional velocity vector, $\overline{p}$ is the filtered pressure scalar field, ν represents the kinematic viscosity and ρ for the density of the fluid. τ corresponds to the sub grid-scale (SGS) stress tensor:

$$\tau = -2\nu_{SGS}\overline{S} + (\tau : I)I/3 \tag{7.3}$$

where ν_{SGS} is the sub grid viscosity, $\overline{S}$ is the filtered rate of strain tensor and I the identity tensor.

To close the formulation a suitable model to evaluate ν_{SGS} is needed. Turbulence modeling is carried out in the present paper by using different SGS models in conjunction with wall models. The models used are: the SIGMA, [85] model and the WALE model within a variational multi scale framework (VMS) [38]. The default filter length chosen is twice the cubic root of the cell volume, $l = 2 \times \sqrt[3]{V}$. A brief description of each model can be found in Aljure et al. [2].

7.2.2 Wall model

A standard algebraic equilibrium wall model was selected [144] to perform an initial assessment of the WMLES strategy applied to automotive aerodynamic studies. This approach has been successfully used in other types of flows such as the flow over the NASA common research model [65] or the flow over buildings [18], amongst others.

Werner and Wengle wall model

The algebraic approximation proposed by Werner and Wengle [144] relies on the assumption that the near-wall velocity profile follows the law-of-the-wall throughout the solid wall region. The algebraic expression is fed with LES velocities corresponding to the first off-wall nodes of the mesh. A linear velocity profile or a logarithmic law are used to determine the wall shear stress depending on whether the off-wall nodes are located in the viscous sublayer or above. Once the wall shear stress is evaluated, it is fed back to the LES computation as an accurate diffusive term for the wall face.

$$u^+ = y^+ \qquad y^+ \leq 11.81 \tag{7.4}$$

$$u^+ = 8.3(y^+)^{1/7} \qquad y^+ > 11.81 \tag{7.5}$$

7.2.3 Numerical method

Using finite volume techniques, the governing equations are discretized on unstructured collocated meshes by means of a second-order conservative scheme [135]. Such schemes preserve the symmetry inherent in the continuous differential operators. As a consequence, the symmetry preserving schemes ensure the conservation of the kinetic energy balance for flows, and therefore stability, at any Reynolds numbers and using coarse grids. The velocity-pressure coupling is solved by using a fractional-step algorithm, the temporal discretization for both the convective and diffusive operators is carried out using a two-step linear explicit scheme [135], whereas an implicit first-order scheme is implemented for the pressure gradient term. The Poisson equation resulting from the enforcement of the mass conservation is solved using a conjugate gradient solver. The present numerical code and discretization approach has shown high accuracy in different cases involving flows with massive separations [2, 3, 66, 67, 113, 114]. Further information regarding the numerical method can be found in Aljure et al. [3], Jofre et al. [45], Trias et al. [135].

All the CFD simulations are performed using the TermoFluids high performance parallel code (www.termofluids.com). The METIS [50] software is used for domain partitioning while core to core communications are performed by means of the Message Passing Interface (MPI) libraries. Moreover, all simulations are computed on the in-house JFF cluster and FinisTerrae II supercomputer at CESGA. Technical information on the JFF cluster and FinisTerrae II supercomputer can be found in www.cttc.upc.edu and www.cesga.es, respectively. Computational time inverted for each simulation is proportional to the number of time-steps solved and their individual cost. For instance, for the largest mesh used, 79×10^6 elements partitioned on 1024 cpus, and the SIGMA model, the required time per iteration is approximately 1.1 s on the FinisTerrae supercomputer. About 8.88×10^5 time steps are performed to achieve the final results, totaling a simulation time of approximately 2.78×10^5 CPU hours.

7.2.4 Case definition

Geometry and Computational Domain

The geometry to be considered is the fastback drivAer car model shown in Fig. 7.1a.

This geometry is placed in a rectangular computational domain modeling a 3/4 open wind tunnel of dimensions $8.8L_{ref} \times 1.75L_{ref} \times 1.3L_{ref}$, where the x-axis corresponds to the stream wise direction, y-axis marks the vertical direction and the z-axis indicates the span wise direction, as shown in Fig. 7.1b. L_{ref} is the longitude of the car ($4.6m$). The front of the car is located at $2.0L_{ref}$ downwind from the inlet boundary. The outlet boundary is at a distance of $5.8L_{ref}$, measured from the rear end of the body.

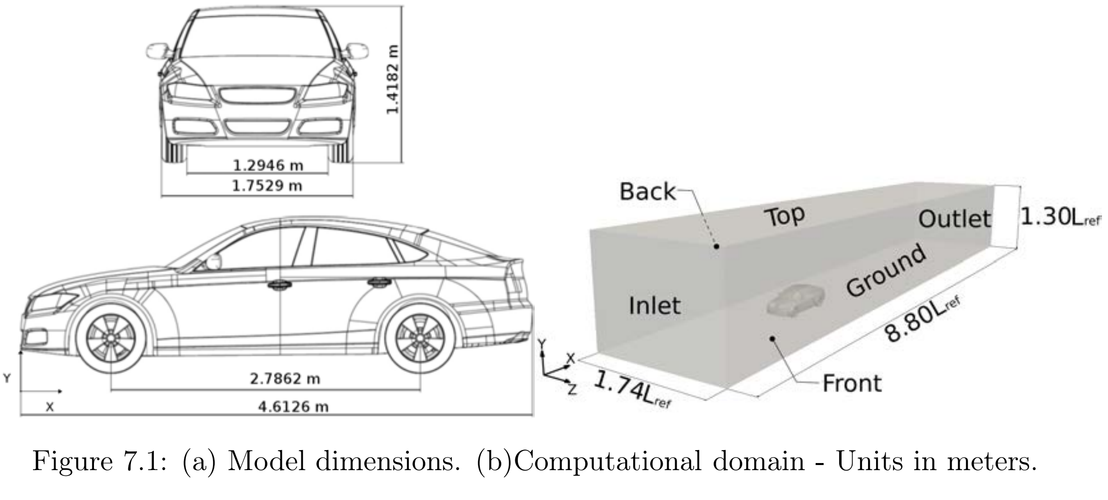

Figure 7.1: (a) Model dimensions. (b)Computational domain - Units in meters.

Boundary Conditions

A constant velocity profile $\mathbf{u} = (u_{ref}, 0, 0)$ is imposed in both the inlet and ground boundaries. The outlet of the domain is modeled using a pressure based boundary condition. As the computational domain is a 3/4 open wind tunnel, symmetry conditions are imposed in the top, front and back boundaries (see Fig. 7.1b). No-slip (or the wall model shear stress) conditions are set for the car surfaces and a surface velocity $\omega \times r$, where ω stands for tangential velocity and r the vector from the axis of rotation to the surface, is set for the wheels assuring the tangential velocity is u_{ref}. The Reynolds number $Re = u_{ref} Lref/\nu$ most used in different works of $Re = 4.87 \times 10^6$, based on car length, has been reduced to $Re = 2.43 \times 10^6$ to decrease the computational effort associated with the solution of the boundary layer. This approach has been successfully used by other authors [56].

7.2.5 Mesh description

Four meshes have been used, containing approximately $900k$ (Mesh 1), $6.5M$ (Mesh 2), $53M$ (Mesh 3) and $79M$ (Mesh 4) control volumes. The meshes are built using prism elements in the near wall area. Furthermore, the near wake zone and the zone trailing the mirrors must be refined to correctly predict the flow structures present in these areas and a refinement area is placed around the rotating wheels to correctly predict the flow resulting from this part. The present simulations are focused on the surroundings of the body and the near wake. Simulations resolving the full wake of the cars require much larger meshes which fall out of the scope of the present study.

Fig. 7.2 shows selected mesh cuts for Mesh 3 ($59M$), used in the present investigation for the WMLES analysis. Fig. 7.2a shows the midplane mesh cut of the car, whereas Figs. 7.2b-c show a stream wise plane cut at the height of the mirrors and rear wheels, respectively.

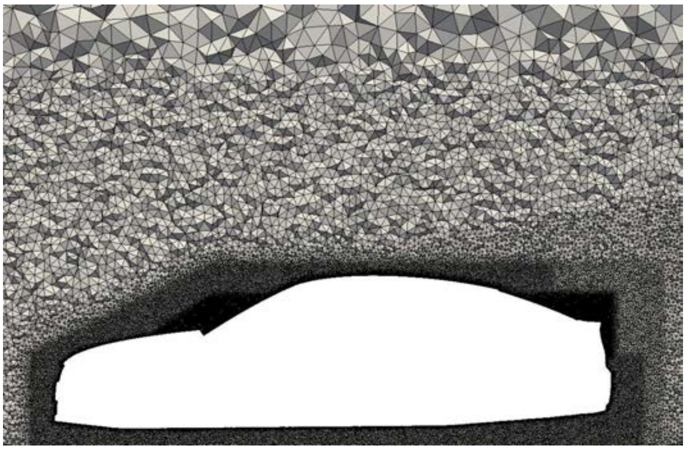

(a) Midplane y=0

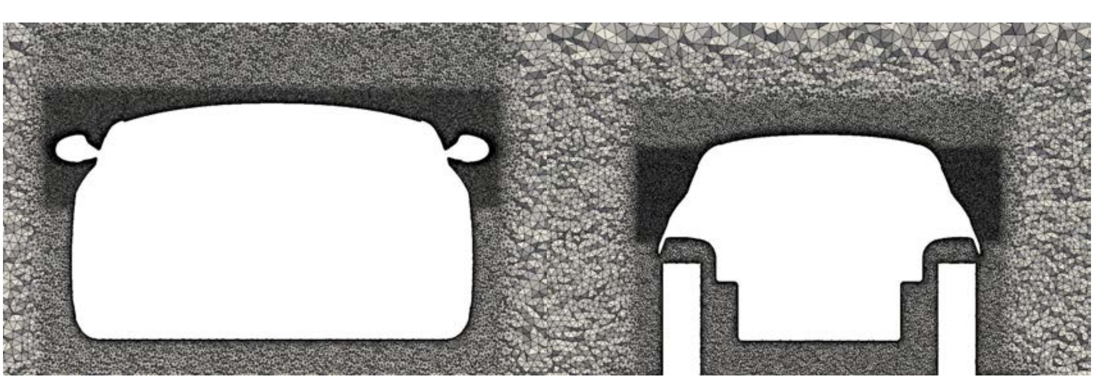

(b) Stream wise x=1.7 (c) Stream wise x=3.5m

Figure 7.2: Visualization of cut planes of the mesh at different positions.

7.2.6 Time integration study

To obtain the numerical results presented in this section, simulations are advanced in time until a statistical stationary flow is reached. Then, in order to ensure converged statistics, instantaneous data is integrated over a sufficiently long-time period. To asses the temporal evolution of the flow, several parameters are studied: Time evolution of the force coefficients (Fig. 7.3) and non-dimensional pressure coefficient ($c_p = (P - P_\infty)/(0.5\rho U_{ref}^2)$ at selected location around the car (Fig. 7.4.

As can be observed from Fig. 7.3, the initial transient behavior is washed out at $TU \approx 2$ ($TU = tu_{ref}/L_{ref}$), then forces stabilize around the values of $C_D = 0.25$ and $C_L = 0.07$ for the drag and lift coefficient, respectively. However, these values are not steady, as its to be expected for turbulent flow. Both, drag and lift coefficient (specially the lift coefficient), show an unsteady behavior. Anyhow, averaged force coefficients show temporal independence in the results.

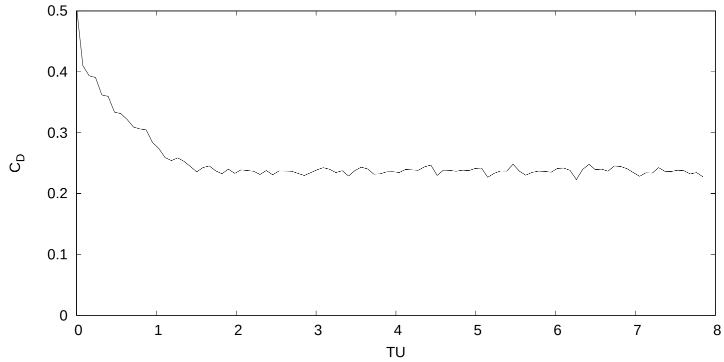

(a) Drag coefficient

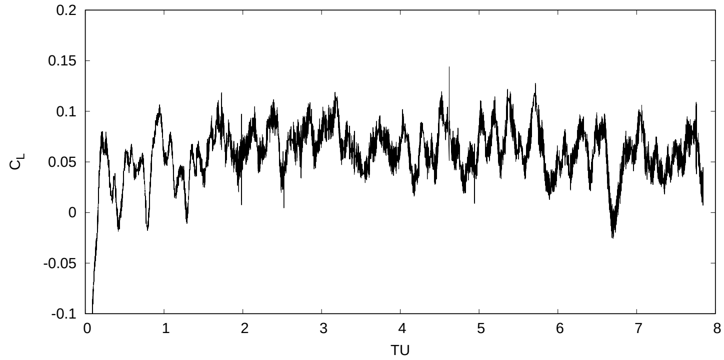

(b) Lift coefficient

Figure 7.3: Force coefficients time evolution for Mesh 4

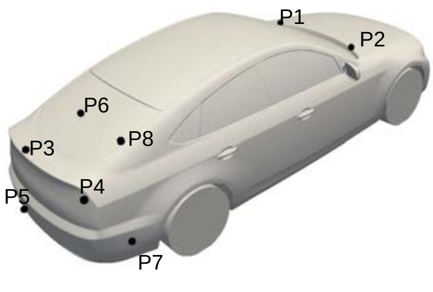

Probe	x/L_{ref}	y/L_{ref}	z/L_{ref}
P1	0.38	0.27	0
P2	0.38	0.27	0.20
P3	0.98	0.24	0
P4	0.98	0.24	0.20
P5	1.01	0.13	0
P6	0.87	0.26	0
P7	0.91	0.11	0.18
P8	0.87	0.26	0.13

Figure 7.4: Numerical probes' location

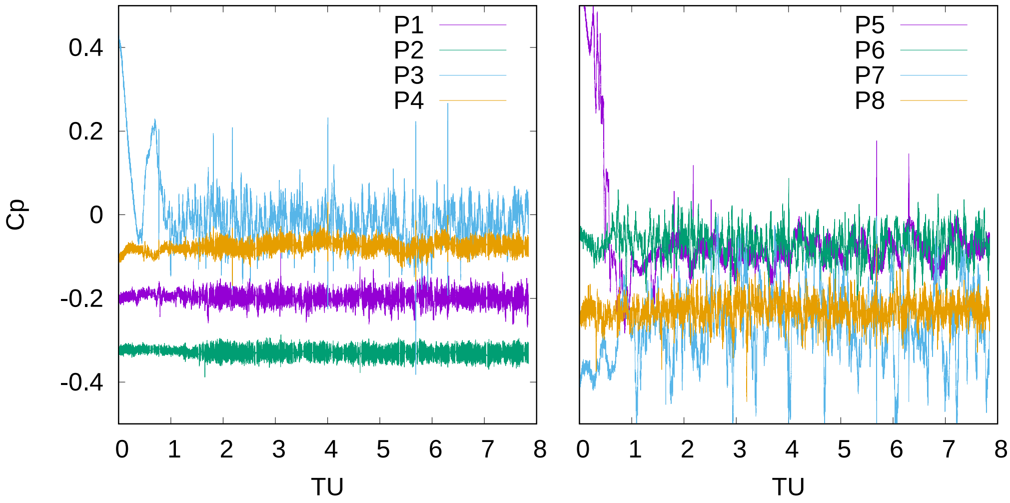

Figure 7.5: Pressure coefficient vs time for the different probes

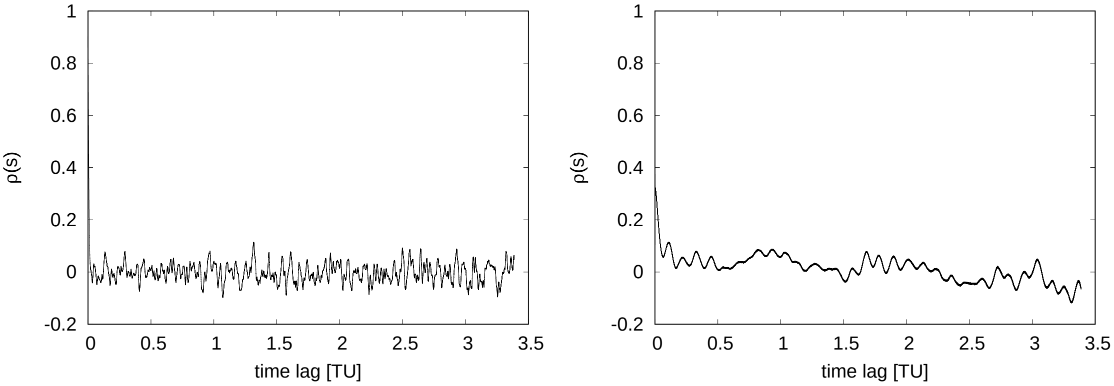

(a) P1

(b) P2

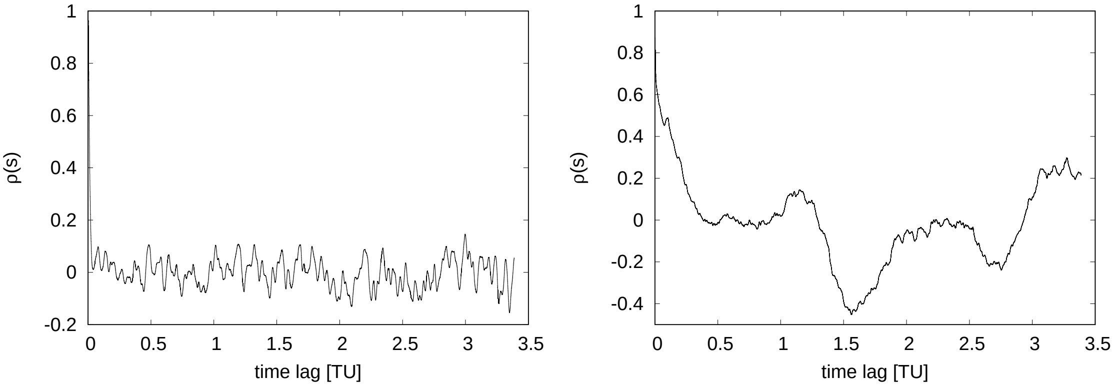

(c) P3

(d) P4

Figure 7.6: Caption on page 139

In order to determine a proper integration time period pressure the pressure coefficient at the different numerical stations is evaluated. Fig. 7.5 shows the time evolution of this magnitude, where large fluctuations are observed at all locations, including what seem to be a oscillatory or

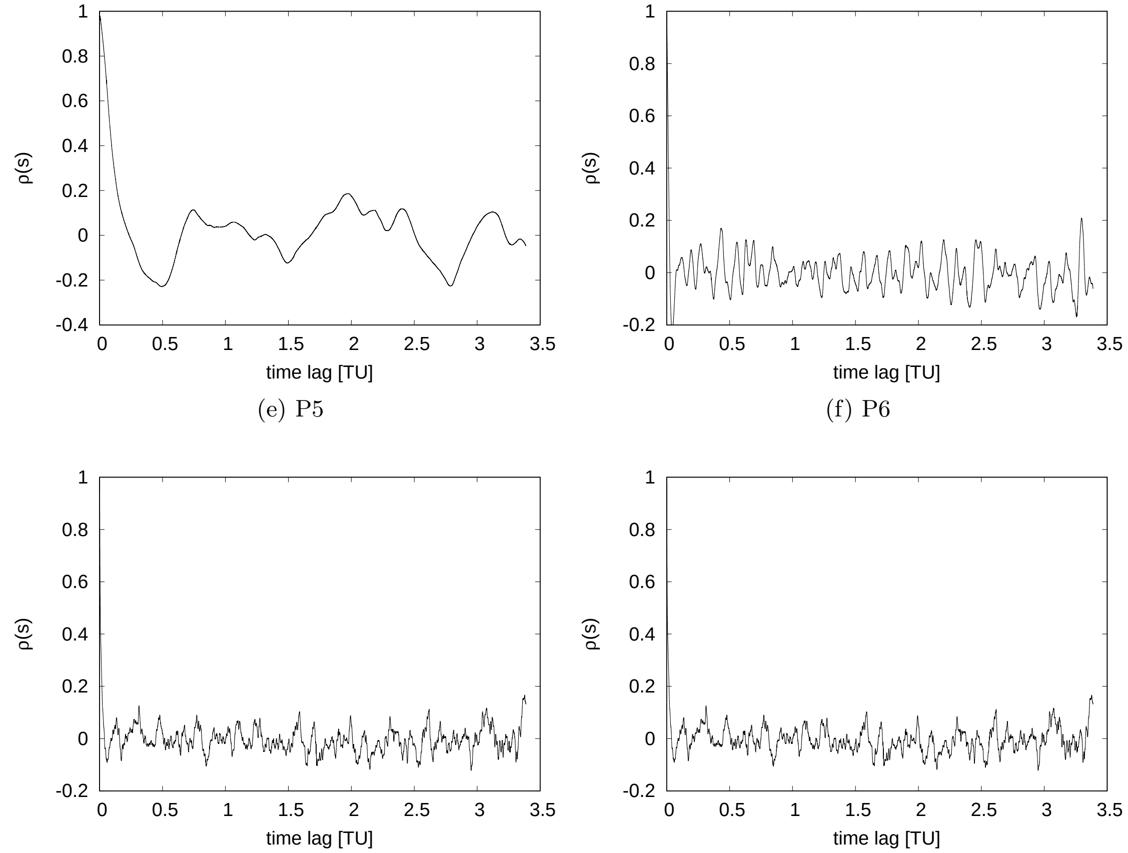

(e) P5

(f) P6

(g) P7

(h) P8

Figure 7.6: Autocorrelation function for the pressure time history at the monitored stations

periodic-like behavior. The autocorrelation function was calculated and plotted for the different stations (see Fig. 7.6) to better understand the unsteady and periodic-like behaviour present. The signal, for all stations, descends rapidly to the 0 value and then oscillates in time. These oscillations reflect a well marked periodic behaviour, however different frequencies are observed amongst the different stations. The largest period observed occurs in stations P4 and P5 (Figs. 7.6d-e), where the period is around $T = 2.6TU$. Instantaneous data is then averaged around $TU = 5.2$ time units in order to capture approximately 2 cycles of the lowest frequency behaviour observed.

7.2.7 Mesh sensitivity study

One of the largest challenges when attempting any LES simulation is the mesh resolution assessment. In the present paper four meshes were constructed, each one relying on information extracted from the previous one. A posteriori analysis of the non-dimensional wall normal distance, in wall units, (y^+) was carried out for each mesh. This distance can be approximated as $y^+ = u_\tau y/\nu$, where u_τ is the friction velocity defined as $u_\tau = \sqrt{|\tau_w|/\rho}$ and τ_w is the wall shear stress, calculated as $\tau_w = \partial u/\partial y$. Average y^+ for the different meshes used are as follows: $y^+ = 272$, $y^+ = 37.2$, $y^+ = 11.8$ and $y^+ = 4.3$ for the meshes 1, 2 ,3 and 4, respectively. Furthermore, Fig. 7.7 shows the y^+ distribution for the first node adjacent to the wall in the four meshes. It should be borne in mind that the approximate locations for the viscous sub layer and the log-law region are defined as $y^+ < 5$ and $y^+ > 10$, respectively. Thus, Mesh 3 presents a surface resolution that captures only the phenomena within the log-layer, whereas the surface resolution for Mesh 4 captures some of the phenomena present in the viscous sub-layer.

In order to assess the influence of mesh resolution within the simulations, force coefficients are

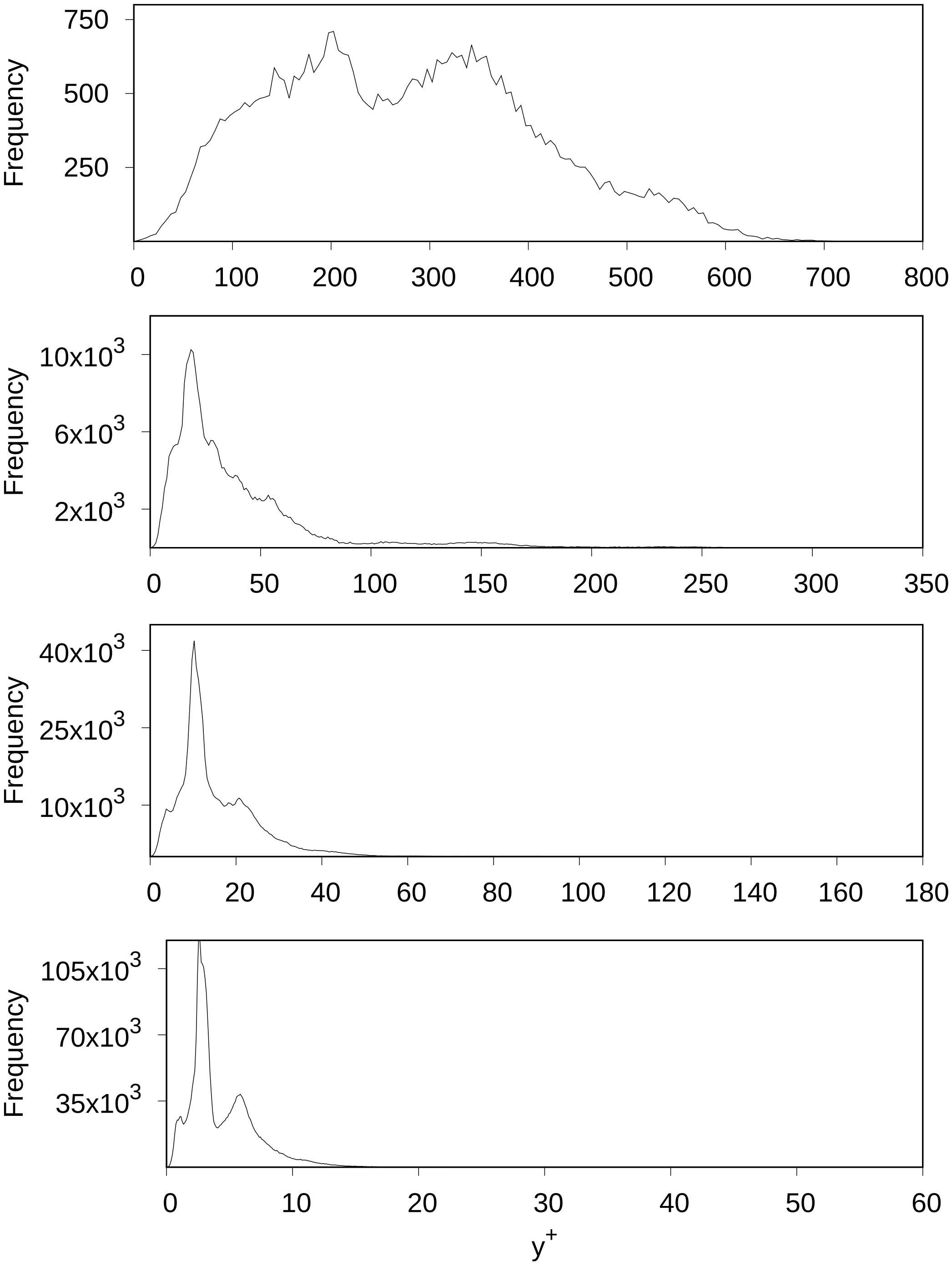

Figure 7.7: y^+ distribution for the different meshes. From top to bottom: Mesh 1, Mesh 2, Mesh 3 and Mesh 4.

compared to literature available results. In this sense, the time-averaged drag (C_D) and lift (C_L) coefficients are summarized in Table 7.1. Also included in the table is the root-mean-square for the lift coefficient C_{LRMS}. Alongside the numerical results, a brief description of the case set-ups used for this analysis is included. For more convenience, a simple system will be used to describe

Case	Mesh	SGS	WM	C_D	C_L	C_{LRMS}
M1_S_NW	1	SIGMA	NO	0.293	0.036	0.023
M2_S_NW	2	SIGMA	NO	0.253	0.057	9.6
M3_S_NW	3	SIGMA	NO	0.246	0.083	0.024
M4_S_NW	4	SIGMA	NO	0.251	0.069	0.021
Exp.[1]				0.243	-0.06	-
EARSM[2]				0.2254	0.0322	-
DES[3]				0.266	0.024	-
$k-\omega$ SST[4]				0.2599	-	-
Exp(no GS)[5]				0.249	0.057	-
DES SST(no GS)[6]				0.2662	0.0235	-
SST-IDDES(no GS)[7]				0.268	0.011	-

Table 7.1: Force coefficients and comparison to selected numerical and experimental results. [1]: Heft et al. [34], [2]: Guilmineau [32], [3] Peters et al. [99], [4]: Shinde et al. [123], [5]: Strangfeld et al. [128], [6]: Guilmineau [31], [7]: Ashton et al. [5]

the different case set-ups. The acronym M3_S_WM describes Mesh 3 (M3) using the SIGMA SGS model (S) and the wall model (WM). The first part of the acronym describes the mesh used (M1:mesh 1, M2: mesh 2, M3: mesh 3 or M4:mesh 4), the second part indicates the SGS model used (S:SIGMA, V:VMS, N: no model) and the final part references to the use of the wall model (WM: wall model used, NW: no wall model used).

In general, force coefficient results present some scattering, i. e., drag coefficient results vary between $C_D = 0.2254$ [32] to $C_D = 0.268$ [5]. Furthermore, the Re number influence on these coefficients should be taken into account. According to the experiments by Heft et al. [34], Re number independence is reached for, $Re = 4.87 \times 10^6$, whereas the experiments carried out by Strangfeld et al. [128] showed independence to be reached for $Re = 2.25 \times 10^6$. Nonetheless, the results obtained fall well within the range they are expected. Moreover, results converge towards the obtained drag coefficient of $C_D = 0.251$ and lift coefficient of $C_L = 0.07$.

A second parameter studied to assess mesh resolution were averaged pressure coefficient profiles.

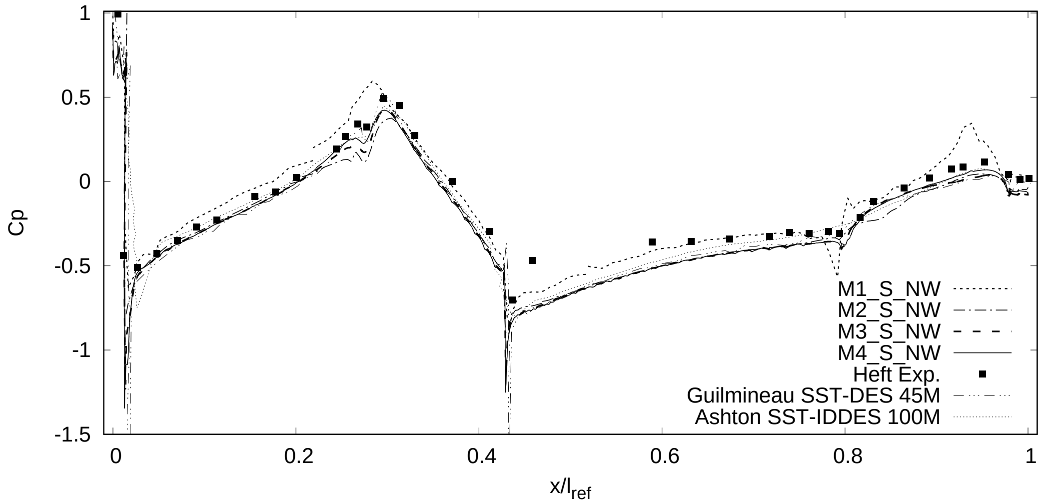

(a) Top

Figure 7.8: Caption on page 142

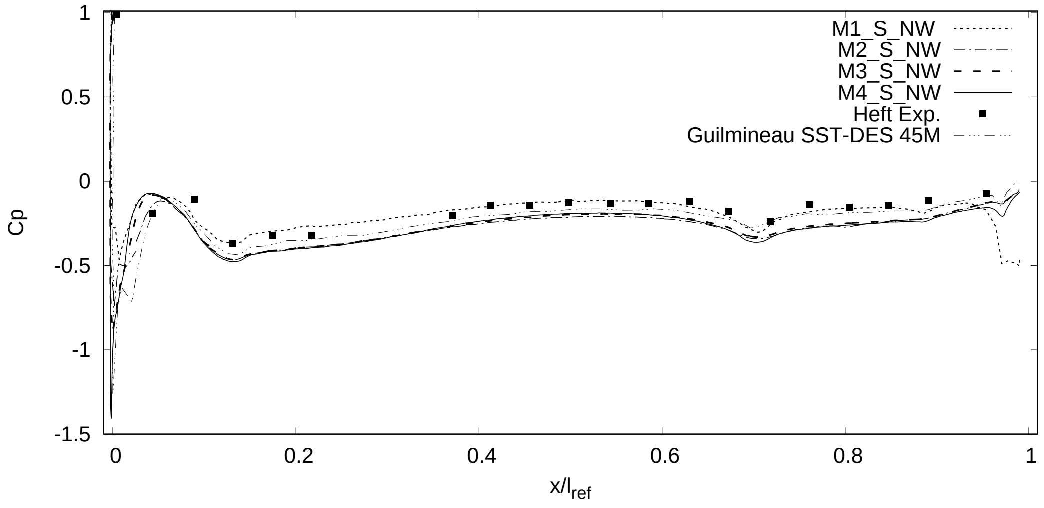

(b) Bottom

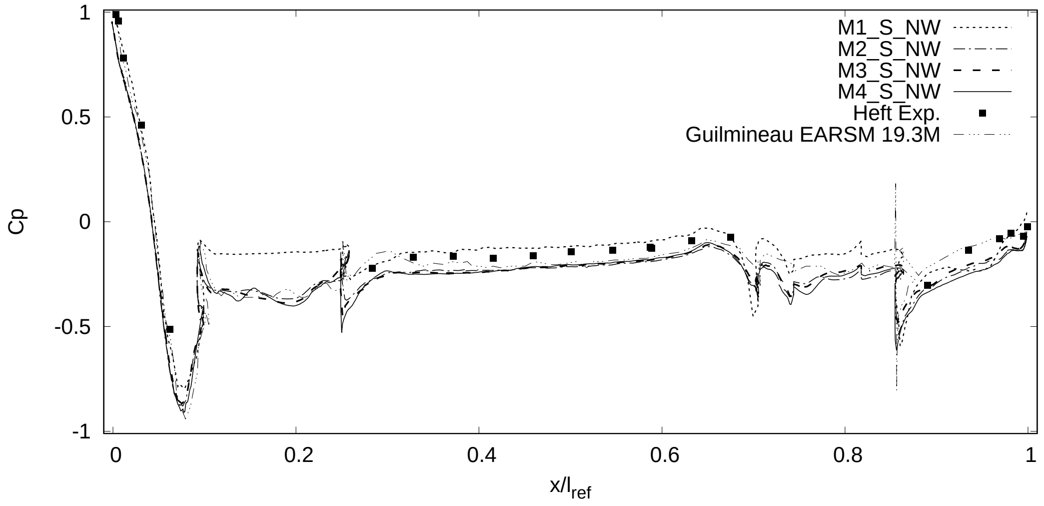

(c) y=0.03L_{ref}

Figure 7.8: Average pressure coefficient profile over (a) the top of the car geometry in the mid plane, (b)the bottom of the car geometry in the mid plane and (c) the side of the car geometry in the horizontal y=0.03L_{ref} plane

Three profiles are plotted in Fig. 7.8: along the top and bottom of the car's mid plane and on the horizontal $y = 0.03L_{ref}$ plane. Similarly as with the force coefficients, these profiles are compared to the pressure measurements reported by [34] and numerical results from [31] and [5]. Small discrepancies are found through the distribution profile, however, the largest is found around $x/L_{ref} = 0.45$. As pointed by Peters et al. [99] and Pasqueali et al. [94], at this location the roof stinger is set up in the wind tunnel experiments, which is not placed in the CFD simulation. In addition, Peters et al. [99] also pointed out that there are some discrepancies between the CAD and the experimental model in the wind shield-roof transition. Results for the three profiles converge to the same curves for the larger meshes, which indicates grid resolution is enough to capture the flow phenomena present around the car.

Observing the force coefficients in Table 7.1, mesh independence of the forces is reached at Mesh 3. Note that for Case 2, although force coefficients are well within the expected values, lift RMS is very high. This indicates the mesh is not fine enough to correctly solve the flow field. Pressure

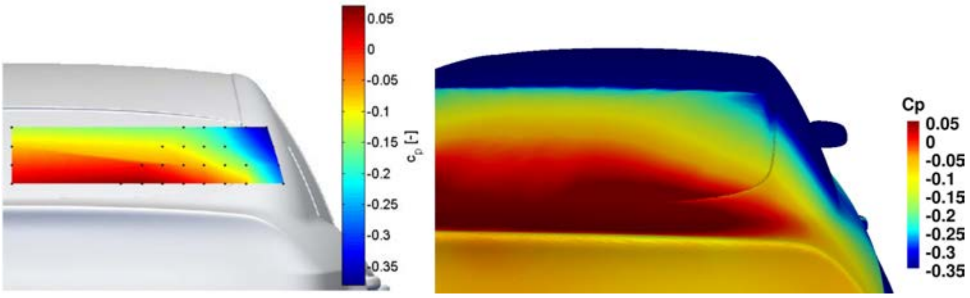

Figure 7.9: Distribution of the pressure coefficient at the rear window. Left: Heft et al. [34], right: present LES

profiles converge towards the results observed in Mesh 4, but the increase in surface resolution from Mesh 3 (693306 faces) to Mesh 4(2779908 faces) helps to better capture the boundary related phenomena.

A final qualitative comparison is carried out for the pressure distribution at the rear window of the car, shown in Fig. 7.9. Average pressure coefficient values from CFD simulations using Mesh 4 are plotted and compared to those reported by Heft et al. [34]. Just as was reported, a large low pressure zone is observed at the C-pillar. This low pressure zone influences the flow around the car and contributes to the formation of a longitudinal vortex named C-pillar vortex. Moreover, the high pressure zone in the back light, which indicates the reattachment of the separation bubble, is also observed.

7.3 RESULTS

7.3.1 WMLES analysis

One of the main objectives of the present paper is to assess the validity of flow solutions using WMLES and different SGS models. The performance of two different models is here analysed. These models are: the SIGMA and VMS, all in conjunction with the wall model presented in section 7.2.4. Additionally, a case was simulated with no SGS modelling, also presented here for comparison.

Table 7.2 shows the different set-ups studied and the resulting time averaged force coefficients. The use of the wall model in mesh three reduces the difference present in the drag coefficient between Mesh 3 and Mesh 4, for both SGS models. The effect on the lift coefficient is more notorious for the SIGMA SGS model, changing from $C_L = 0.083$ to $C_L = 0.056$. The change for the VMS model is much smaller. Nonetheless, there seems to be an improvement in the results

Table 7.2: Force coefficients for the different numerical configurations and experimental results. [1]: Heft et al. [34]

Case	Mesh	SGS	WM	C_D	C_L	C_{LRMS}
M3_S_NW	3	SIGMA	NO	0.246	0.083	0.024
M3_S_WM	3	SIGMA	YES	**0.251**	0.056	0.024
M3_V_NW6	3	VMS	NO	0.250	0.063	0.020
M3_V_WM	3	VMS	YES	**0.251**	0.062	0.023
M3_N_NW	3	NO SGS	NO	0.252	0.064	0.022
M4_S_NW	4	SIGMA	NO	**0.251**	0.069	0.021
M4_V_NW	4	VMS	NO	**0.251**	0.067	0.021
Exp. [1]				0.243	-0.06	-

when using the wall model.

Wall model effect

A more detailed look is taken to examine the effects that the wall model exerts on the flow around the car. Pressure profiles are analysed to asses small scale changes present when using the wall model.

In Fig. 7.10, the pressure profiles in the mid plane along the top of the car are plotted. Cases M3_S_NW and M3_S_WM are compared to the solutions obtained when not using turbulence modelling (case M3_N_NW) and using the finer mesh (case M4_S_NW). When using WM almost no changes are observable for most of the cars length, except for two zones which are affected: the bonnet-wind shield junction (BW-J) and the fastback (FB) (see Figs. 7.10b-c).

Fig. 7.11 shows the averaged streamlines around the car and close ups to the two section of interest identified previously. The BW-J has a small corner that greatly affects the flow configuration. As the flow moves downstream over the bonnet, the gradual pressure increase it experiences is suddenly cut as the junction is reached and flow tends to separate (see section 7.3.4). This

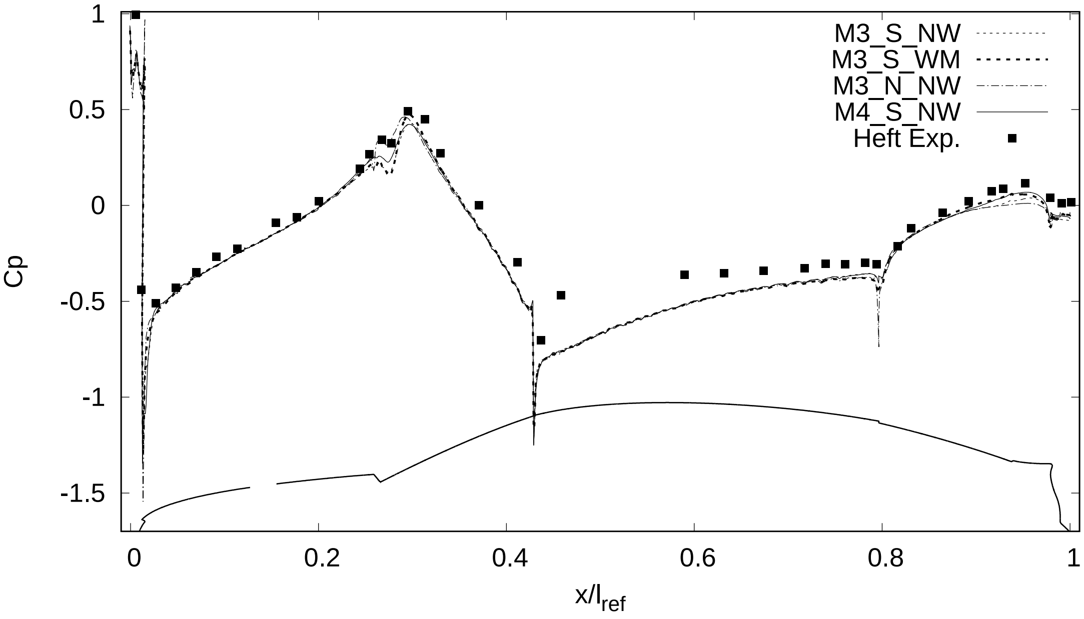

(a) Top

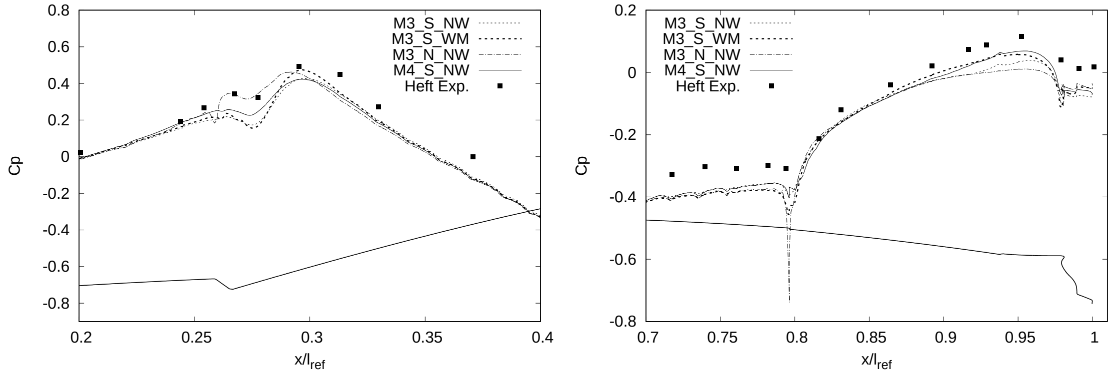

(b) Bonnet-Wind shield

(c) Fastback

Figure 7.10: Averaged pressure coefficient along the top of the car in the mid plane.

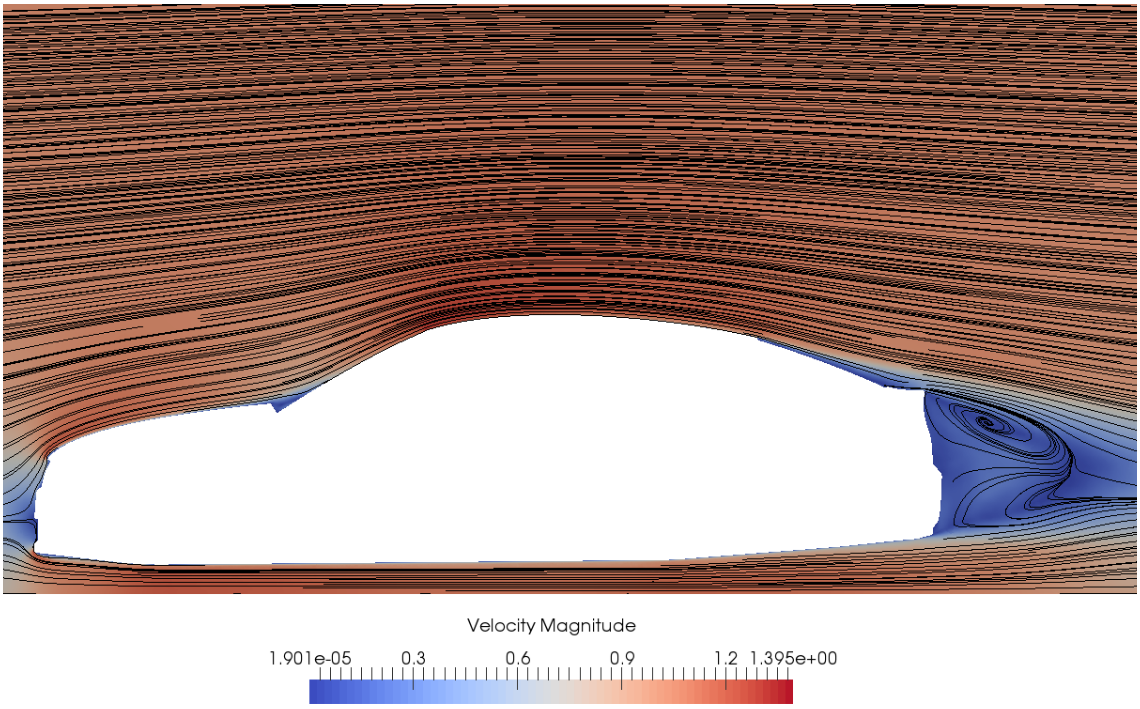

(a) Top

(b) Bonnet-Wind shield junction

(c) Fastback

Figure 7.11: Averaged pressure coefficient along the top of the car in the mid plane.

separation creates a small recirculation zone, shown in Fig. 7.11b. As observed in Fig. 7.10b, the influence of the wall model in this area affects the results negatively. In the front part of the junction, where the flow detaches, the wall model yields slightly closer results to the finer mesh, however, as we move into the junction the pressure decrease predicted by the SIGMA+WM set-up is larger than the SIGMA model alone. Both pressure drops are larger than that predicted by the finer mesh. In the final part of the junction the SIGMA+WM set-up shows a larger pressure recuperation than that showed by the SIGMA model alone. The pressure recuperation resulting from the finer mesh is smaller. Finally, at this area, the results yielded by case M3_N_NW (no turbulence modelling) are quite different than the rest.

Results in the FB area behave differently. Observing Fig. 7.10c, two areas of interest are observed. The first one, around $x/L_{ref} \approx 0.8$, corresponds to a small lip located at the junction between the roof and the FB. In this area, similarly as was observed in the BW-J region, flow detaches, generates a recirculation area and a low pressure zone is created (Fig. 7.11c). Results obtained for case M3_S_WM do not capture well this change in pressure, over predicting the drop. Results for Cases M3_S_NW and M4_S_NW are nearly identical. Again, results from case M3_N_NW are very different than the rest. As the flow moves along the FB a second zone of interest is found. Between $0.75 \leq x/L_{ref} \leq 1$ the pressure results obtained show differences for the different case set ups. Observing Fig. 7.11c, several small recirculation bubbles are observed. The formation of these structures is somewhat different to the separation regions observed for the BW-j

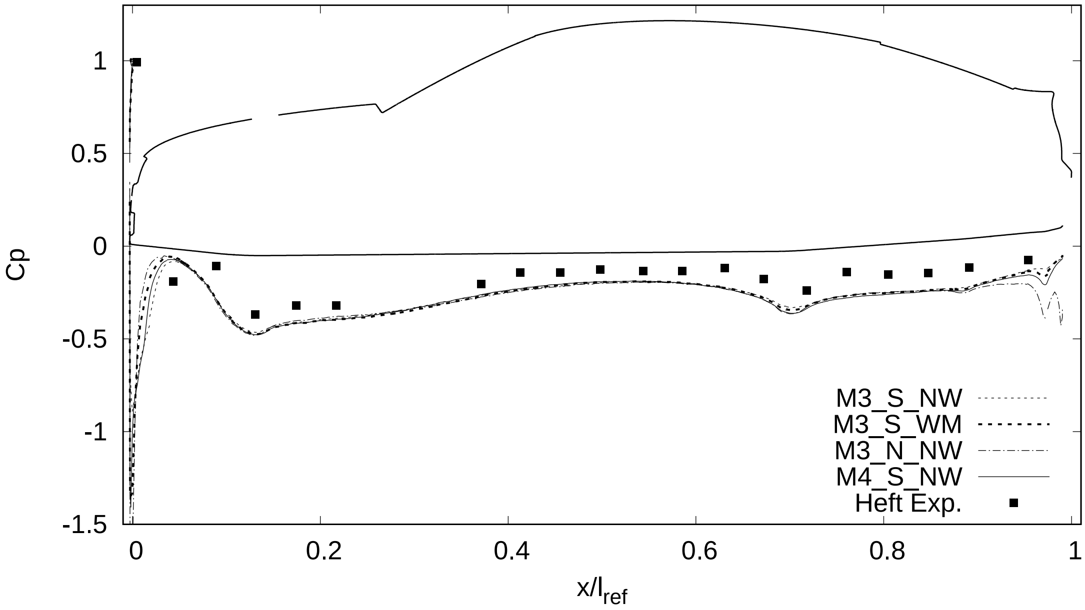

(a) Bottom

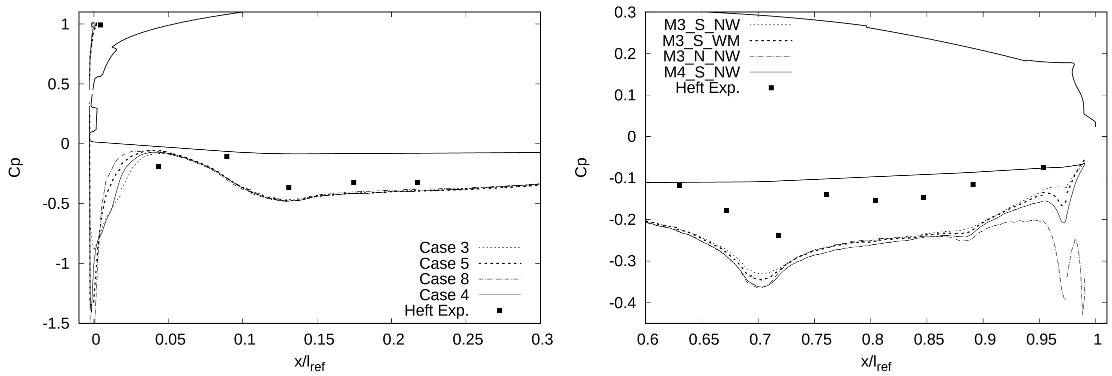

(b) Front

(c) Diffuser

Figure 7.12: Averaged pressure coefficient along the bottom of the car in the mid plane.

or the roof-rear window lip. Flow separation is not induced by a sudden geometrical discontinuity as is the case in the edge in the BW-J or the small lip in the junction between the roof and the rear window. In the FB area a gradual change in the geometry causes the flow to separate and reattach several times. These small separation areas do not induce a large pressure drop. On the contrary, there is a pressure recuperation over this area. For this zone, results from case M3_S_WM are closer to those of case M4_S_NW than the others, indicating a positive effect of using the wall model in this area (Fig. 7.10c).

Fig. 7.12 shows the pressure profiles along the mid plane at the bottom of the car. As has been pointed out by diverse authors [32, 34, amongst others], the pressure coefficient is negative over the whole under body (positive values in the distribution correspond to the small area between the stagnation point and the under body), acting as down force generator. Again, minor differences are observed in these profiles when using the wall model, although two areas stand out: the front of the under body near the wheels (U-F), shown in Fig. 7.12b and the diffuser area (D), in Fig. 7.12c. For the U-f area the pressure prediction for Cases M3_S_NW and M3_S_WM are different, being those from case M3_S_NW a bit closer to case M4_S_NW. Observing Fig 7.11a, this area coincides with the front edge of the under body. Flow separates in this region generating

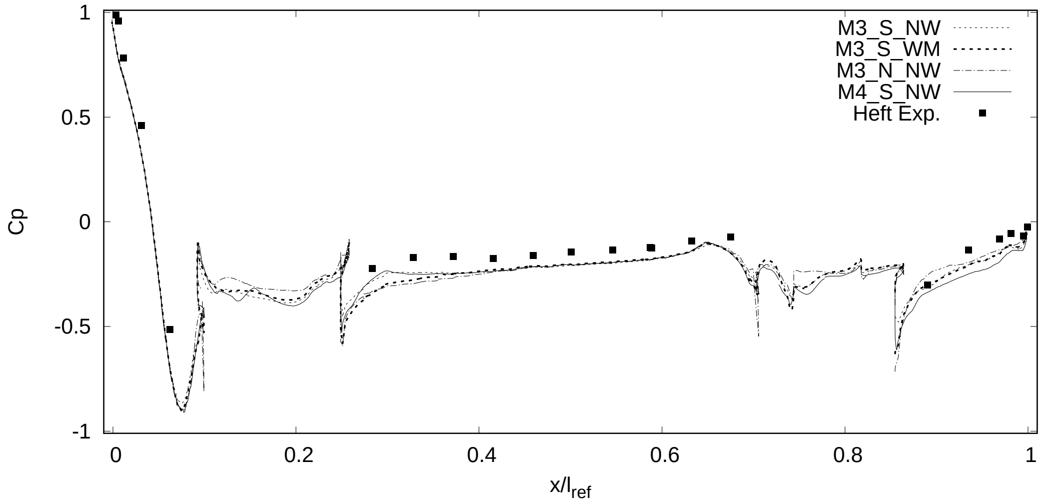

Figure 7.13: Averaged pressure coefficient over the side of the car geometry in the horizontal y=0.03L_{ref} plane

a significant pressure drop, seen in Fig. 7.12b for $x/L_{ref} \approx 0$. The subsequent area is the pressure recovery from this separation region, which is over predicted by the wall model. On the other hand, for area D the wall model (case M3_S_WM) yields closer results to the finer mesh than those obtained for case M3_S_NW, showing a positive effect of the wall model. This area is not subject to flow separation and the diffuser increases the flow area under the car permitting the pressure recovery to be done gradually. A side effect of this pressure recovery is the pressure decrease at its beginning ($x/L_{ref} \approx 0.7$). This pressure decrease is well captured by the wall model, being results from case M3_S_WM closer to case M4_S_NW than those predicted by case M3_S_NW. Similarly as with the pressure profiles over the top, when using no turbulence model results drift away from those obtained by case M4_S_NW. This is specially evident for area D.

The pressure distribution along the side of the car shows a different behaviour (see Fig. 7.13). Flow around this area is heavily influenced by the unsteady effects brought on by the wheel's rotation. Results in the wheel well area, between $0.1 \leq x/L_{ref} \leq 0.25$ for the front and $0.7 \leq x/L_{ref} \leq 0.85$ for the rear, show small changes when using the wall model. Nonetheless, results do not improve when using the wall model. In the areas just after the wheel wells a pressure drop is observed. This pressure drop is generated by the corner present in the car's wheel well. This pressure decrease is well captured by the wall model, however, the pressure recuperation is under predicted at the front and over predicted at the back, when compared to the finer mesh results.

7.3.2 SGS model effect

In order to fully assess the effect the wall model exerts on the flow configuration, results obtained from both SGS models are here compared using both WM and no WM. As has been observed, one of the areas were the wall model works best is in the FB region. In the present section, the pressure profiles along the FB and at the different span wise locations $z/L_{ref} = 0$, $z/L_{ref} = 0.05$, $z/L_{ref} = 0.1$ and $z/L_{ref} = 0.125$ (see Fig. 7.15) are studied and plotted on Fig. 7.14. For comparison sake, the pressure profiles reported by Guilmineau [31] and Strangfeld et al. [128] are plotted as well. It should be noted that the results by Strangfeld et al. [128] are uncorrected and the closed wind tunnel may have had caused an offset in the measurements.

Three regions stand out in Fig. 7.14, the lip in the junction between the roof and the FB ($x/L_{ref} \approx 0.77$), the FB region ($0.8 \leq x/L_{ref} \leq 0.95$ and the rear end of the car ($x/L_{ref} \geq 0.95$). Again, the wall model seems to produce mixed results. It should be noted that there seems to be some influence of the SGS model on the results.

For the span wise locations $z/L_{ref} = 0$ and $z/L_{ref} = 0.05$ (Figs. 7.14a-b), pressure profiles

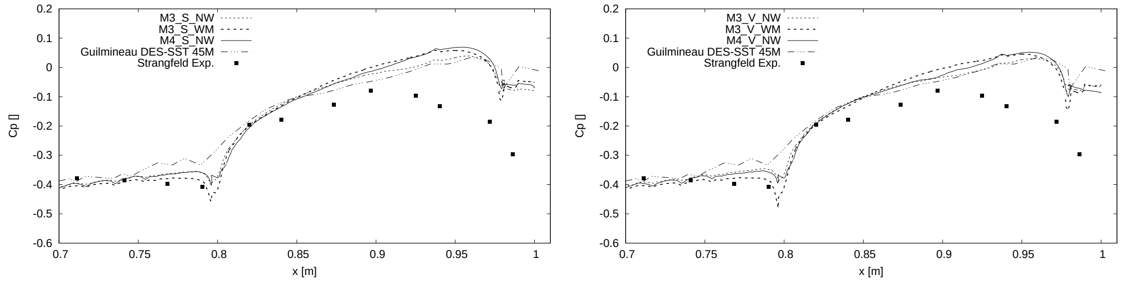

(a) $z/L_{ref} = 0$

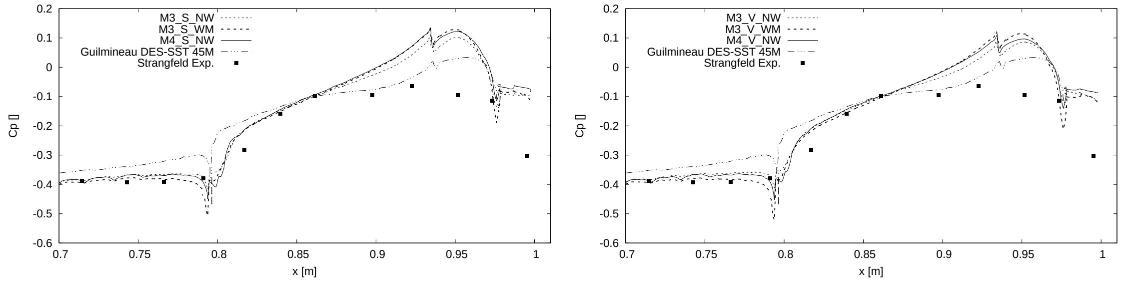

(b) $z/L_{ref} = 0.05$

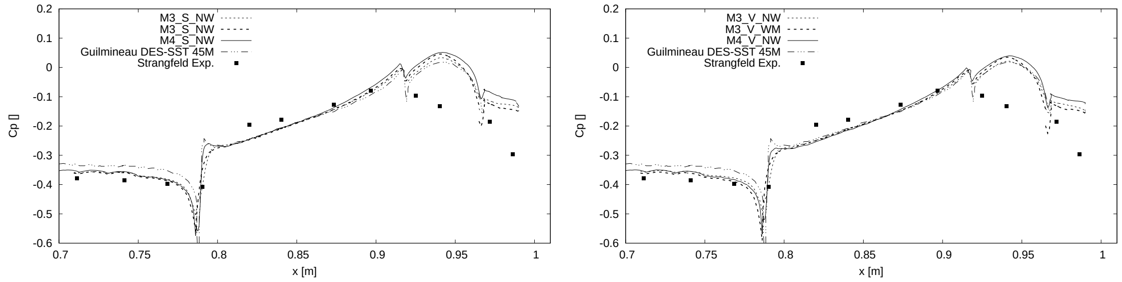

(c) $z/L_{ref} = 0.1$

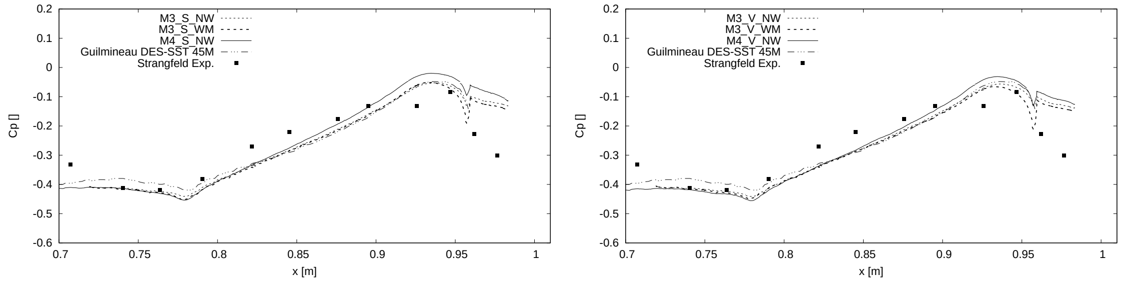

(d) $z/L_{ref} = 0.125$

Figure 7.14: Average pressure coefficient profile over the rear window at different span wise locations and using different SGS models. (a) $z/L_{ref} = 0.00$, (b) $z/L_{ref} = 0.05$, (c) $z/L_{ref} = 0.1$, (d) $z/L_{ref} = 0.125$. Left SIGMA SGS model, right VMS SGS model. Comparison with Guilmineau [31]

Figure 7.15: span wise locations for the pressure profiles at the rear window

over the FB are somewhat different for both models. Results for the lip in the roof-FB junction are almost identical. The wall model has the same negative effect on the solution, over predicting the pressure drop in the separation region. As the flow moves over the FB, the initial pressure recovery from the separation in the roof-rear window transition is slightly faster for the VMS model, however, around $x/L_{ref} \approx 0.9$ results differ. case M4_V_NW shows a smaller pressure value in this area, related with the different recirculation bubbles present along the rear window (see Fig. 7.11c). Nonetheless, the effect from the wall model is similar, having an overall closer prediction to the finer mesh of the pressure recuperation than its non wall model counter part. At the rear section of the FB small differences are observed between the two SGS models. In this area the wall model seems to work better alongside the SIGMA SGS model than it does with the VMS model, when compared to the finer mesh results.

For the span wise location $z/L_{ref} = 0.1$ (Fig. 7.14c), pressure profiles show less discrepancies between the different case set-ups, particularly in the spoiler and FB section. Nonetheless, some improvement is observed in the rear section when using the WM. Again, the wall model seems to improve the overall pressure prediction in this area. Finally, for the outermost location, $z/L_{ref} = 0.125$ (Fig. 7.14d), the results show the WM do not improve substantially the results. At this span wise location, there is no spoiler, but in the same stream wise location the profile crosses over the c-pillar. The wall model seems to improve on the results at the c-pillar for both SGS models. On the contrary, results using the WM are farther away from the finer mesh at the rear of the car.

7.3.3 Time step and CPU time

One of the main concerns when using LES simulations in industry applications is the large computational expense required. As meshes are finer a smaller time step is required in the simulations. In addition, the larger meshes require more time (or CPUs) to solve. Table 7.3 shows the non-dimensional time step, iteration time, number of iterations and total CPU time required for the simulations of cases M3_S_WM and M4_S_NW.

Table 7.3: Average time step dt, iteration time t_{iter}, number of iterations and overall time t_{cpu} required for the different numerical configurations.

Case	dt[TU]	iter	t_{iter}[s]	t_{cpu}[CPU hours]
M3_S_WM	2.03×10^{-5}	3.86×10^{5}	$0.7s$	8.23×10^{4}
M4_S_NW	8.83×10^{-6}	8.88×10^{5}	$1.1s$	2.78×10^{5}

As can be seen in table 7.3, there is a nearly 60% reduction in the time step size when changing from Mesh 3 to Mesh 4 due to the smaller control volumes around the car's surface. This time step decrease causes an increase of 130% in the number of iterations required to simulate the time span required in the present case. Using the WM considerably reduces the computational requirements needed for the present simulations, CPU time is reduced in approximately 70%.

7.3.4 Flow Structures

Flow around the drivAer model is quite complex, where plenty of vortices are formed around the geometry. Unsteady flow is analysed by extracting the coherent structures present around the car. To do this non-dimensional stream wise vorticity $\omega^* = \omega L_{ref}/U_{ref}$ and non-dimensional Q-criterion $Q^* = QL^2_{ref}/U^2_{ref}$ [40] contours are studied and presented in Figs. 7.16 and 7.19. These

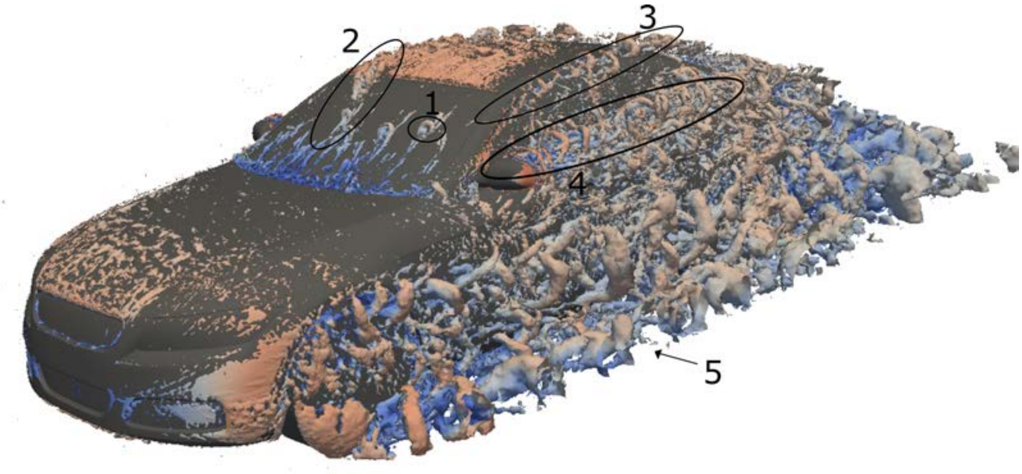

(a) $Q^* = 1$

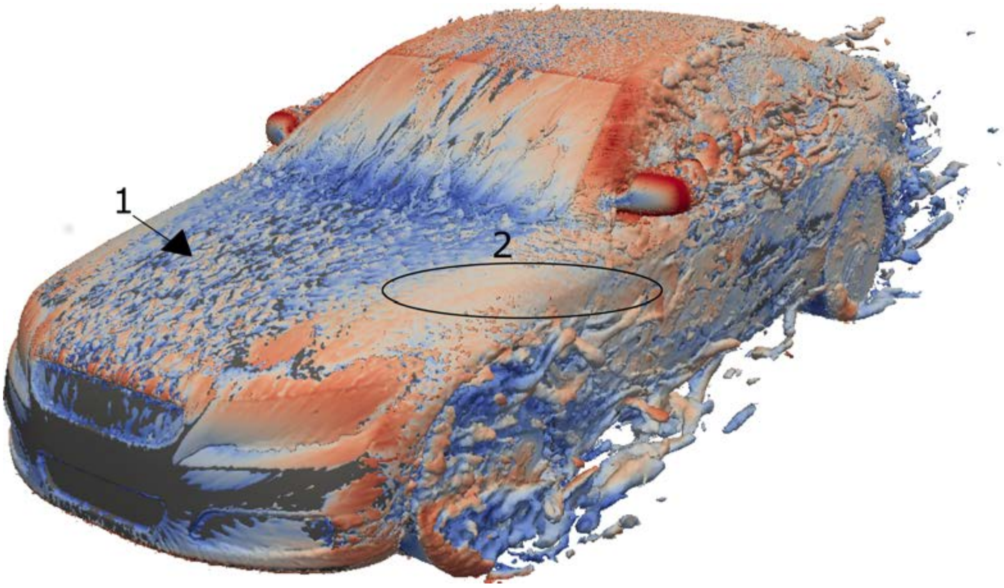

(b) $\omega^* \pm 50$

Figure 7.16: Instantaneous turbulent structures around the car viewed from the front, coloured by velocity magnitude. (a) $Q^* = 1$ iso surfaces. (b) non-dimensional stream wise vorticity $\omega^* \pm 50$.

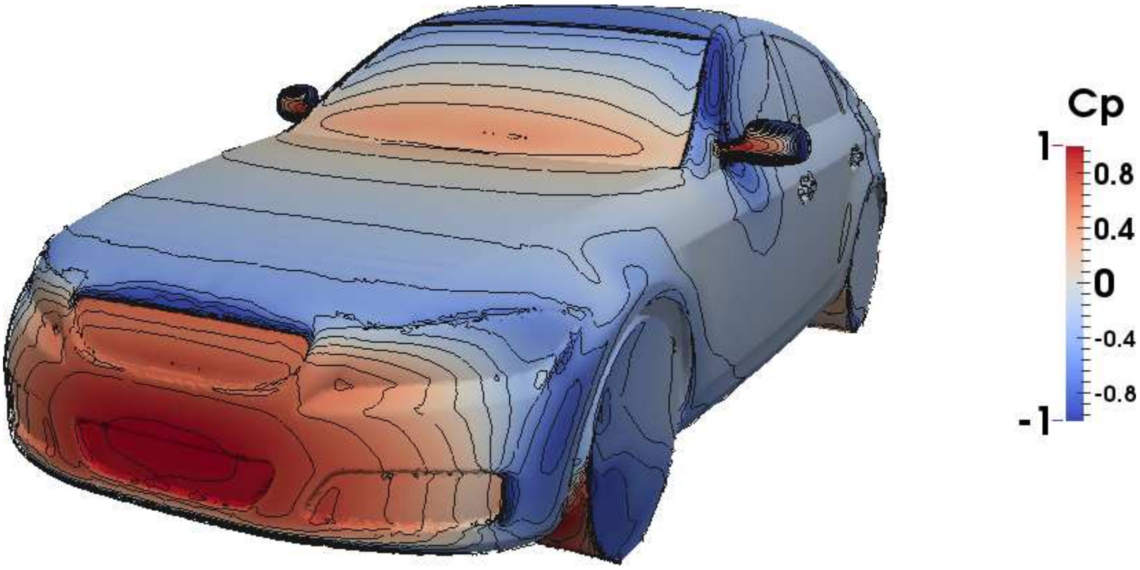

Figure 7.17: Averaged pressure coefficient Cp over the surface of the car.

figures depict the $Q^* = 1$ and $\omega^* \pm 50$ iso contour surfaces viewed from the front and the back of the car, respectively. Additionally, pressure coefficient over the car's surface is also presented in Figs. 7.17 and 7.20. As was pointed out in section 7.3.1, several locations around the car present flow separation and recirculating regions. As these zones are located all over the car, its resulting wake presents a very strong unsteady behaviour.

When observed from the front, several regions stand out (Fig. 7.16). As flow crashes onto the front of the car, it travels through the top part of the bonnet. A stagnation zone is created in the front bumper area and a high pressure bubble encloses most of the car's frontal section (see Fig. 7.17). Flow then travels upwards towards the bonnet and sidewards towards the wheel well area, detaching from the front edge of the bonnet.

In the top of the bonnet, the flow experiences an adverse pressure gradient causing it to decelerate and it presents the streak instability behaviour. This feature consists of small lifted structures from the car's surface, marked as 1 in Fig. 7.16b. As the flow reaches the BW-J, the geometrical discontinuity present there causes the flow to separate again and to generate a recirculation region. As a consequence, the flow detaches from the edge, generating small horseshoe-like vortices that travel up the wind shield (see region 1 in Fig. 7.16a).

In this area a secondary high pressure bubble is created (see Fig. 7.17), indicating the reattachment of the flow to the wind shield surface. The horseshoe-like vortices reach the top edge of the wind shield, detaching again from the car, and creating an additional vortex forming region, marked as region 2 in Fig. 7.16a. This process takes place at different span wise locations feeding instability to the flow downstream.

Along the later of the bonnet the flow behaves differently as it does on the top of the bonnet. As the flow moves over the top corner of the front it detaches, in a similar manner as it does on the centre of the bonnet, however due to the influence of the bonnets side edge, the flow reattaches. Reattachment zones are accompanied by a rise in the surface pressure. The resulting pressure distribution along the surface in the side of the car's nose redirects part of the flow downwards, under the mirror (see region 2 in Fig. 7.16b).

The secondary high pressure zone created in the wind shield pushes the flow outwards, towards the A-pillar. Interactions around this area create vortical structures that move downstream forming the A-pillar vortex (see region 3 in Fig. 7.16a). This structures travel along the top corner of the car and join the flow in the FB region. Furthermore, the mirrors create a large unsteady wake that travels alongside the car and joins the main wake at the rear (see region 4 in Fig. 7.16a). Both these large scale structures are noise sources in external car aerodynamics.

In order to better understand this unsteady phenomena, a fast Fourier transform was performed on the pressure values for the different numerical probes located around the car (Fig. 7.4), yielding

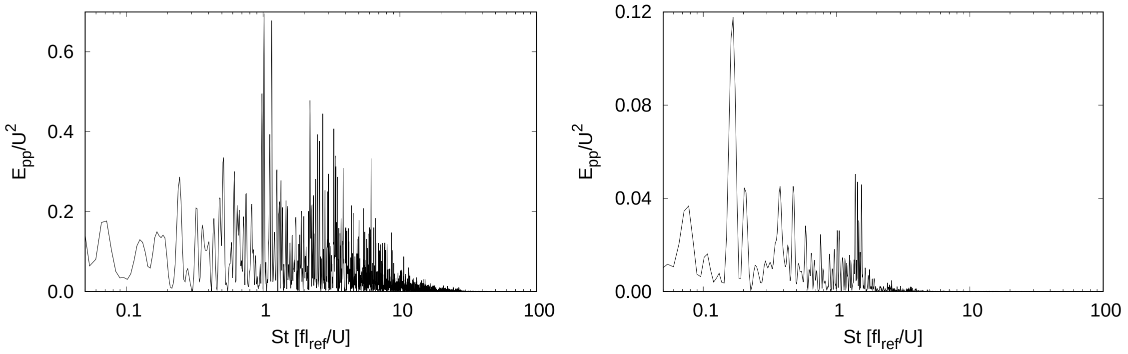

(a) P1

(b) P2

Figure 7.18: Energy spectra for the pressure fluctuations at stations P1 and P2.

the frequency spectra at the specified locations. Frequency is non-dimensionalized with the vehicle's base height ($h_{base} = 0.72m$) and reference velocity $St = fh_{base}/U_{ref}$.

Numerical probe P1 is located on top of the wind shield area, whereas probe P2 is located over the A-pillar.

Fig. 7.18 shows the frequency spectra obtained for probes P1 and P2. A high frequency broad band peak is observed around $St \approx 6.2$ for station P1. The location of this probe suggests this corresponds to the horseshoe-like vortex activity around the wind shield. Additionally, a narrower, more energetic peak is also visible around the non-dimensional frequency $St \approx 1.2$. As Wieser et al. [145] stated, frequencies around this range correspond to shedding phenomena around the car, this energy peak might correspond to the shedding of large scale vortices from the top of the wind shield. A similar peak is observed around $St \approx 1.45$ for station P2, corresponding to the A-pillar vortex shedding. The larger energy peak, observed at station P2 at $St \approx 0.17$ corresponds to the vortices forming at the mirror.

Other structures which are visible from the front correspond to the wheels (region 5 in Fig. 7.16). Both, front and rear wheels, interact heavily with the oncoming flow, creating large scale structures alongside the car. It should be noted that the jetting vortices created by the wheels are the largest structures around the car.

When viewed from behind, the large vortices created by the A-pillar, mirror and wheels are also visible. In fact, these vortices and their interactions with the car downstream, form most of the large trailing vortices that dominate the wake. However, vortices created in the back of the car play also an important role in the wake's formation.

Flow travelling through the car's roof reaches the small lip junction between the roof and the FB. As was observed in section 7.3.1, this region presents flow recirculation and flow detachment forming small scale structures (marked in Fig. 7.19b as region 1). As it can be observed can be observed in Fig. 7.20, the whole FB is subject to an adverse pressure gradient, which contribute to form small longitudinal vortices along the FB (see region 1 in 7.19a). These structures travel downwind and detach from the back of the car (Fig. 7.19). As it was mentioned before, the A-pillar vortices reattach to the car in the FB region, enclosing the flow in this area. Evidence of the reattachment can be seen as two localized high pressure zones in the vehicles rear end, see Fig. 7.20. Finally, the C-pillar vortices are also visible in Fig. 7.19, marked as region 2.

The different numerical probes located at the model's rear section aim to capture the different unsteady phenomena taking place. Fig. 7.21 depicts the frequency spectra obtained for probes P3, P4, P6 and P8. In this area, the high frequency broad band peaks observed at stations P3 and P6 around $St \approx 2.5$ indicate, in a similar way as for P1, the shedding of small scale vortices (Figs. 7.21a,c). A lower frequency peak is also observed for stations P4 and P8 around $St \approx 1$. Again, similarly as with P1 and P2, these peaks correspond to the shedding of large structures around the car. In the case of P8 this frequency corresponds to the large longitudinal vortices that are formed behind the car. Additionally this is the most energetic phenomena observed ($St \approx 1.05$ for Fig.

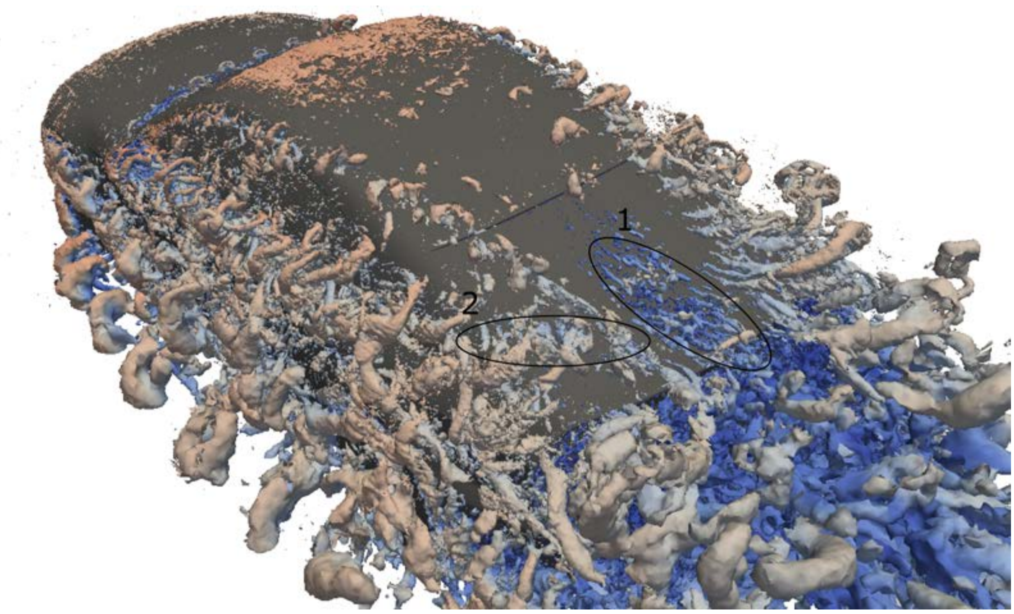

(a) $Q^* = 1$

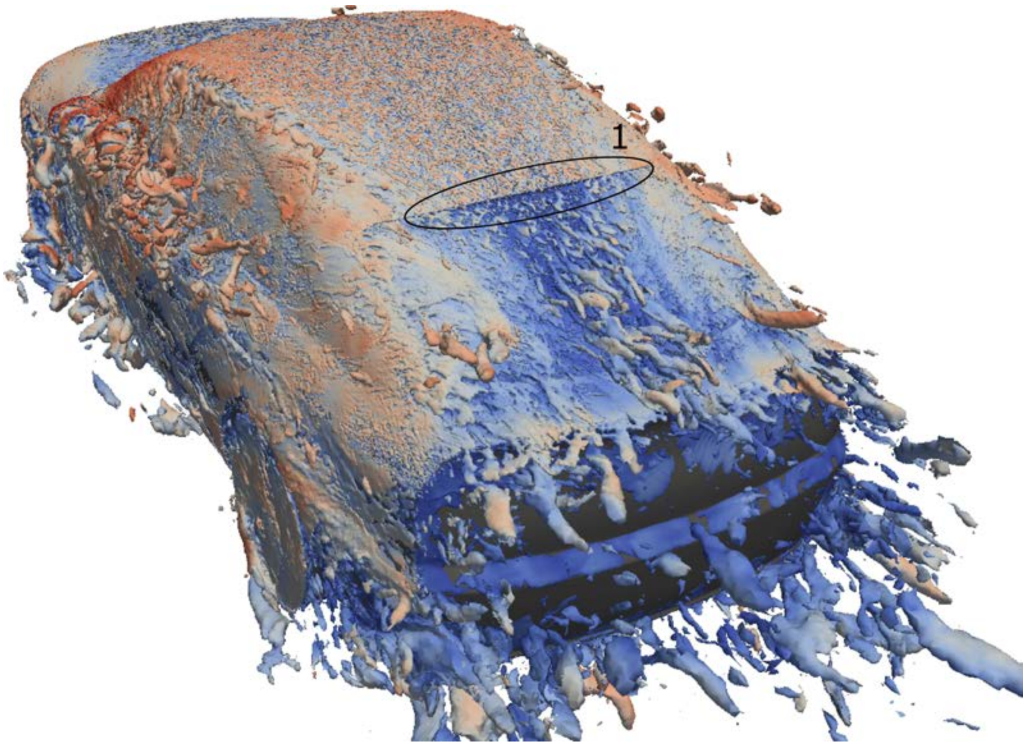

(b) $\omega^* \pm 50$

Figure 7.19: Turbulent structures around the car, viewed from the back, coloured by velocity magnitude. (a) $Q^* = 1$ iso surfaces. (b) non-dimensional stream wise vorticity $\omega^* \pm 50$.

7.21d). The large vortex generated in the mirror is captured by the probe located at station P4. This structure shows a very energetic peak at the frequency $St \approx 0.15$, similar to that observed at station P2 at $St \approx 0.17$.

Figs. 7.22a-b, show the frequency spectra for the numerical probes located at the rear bumper

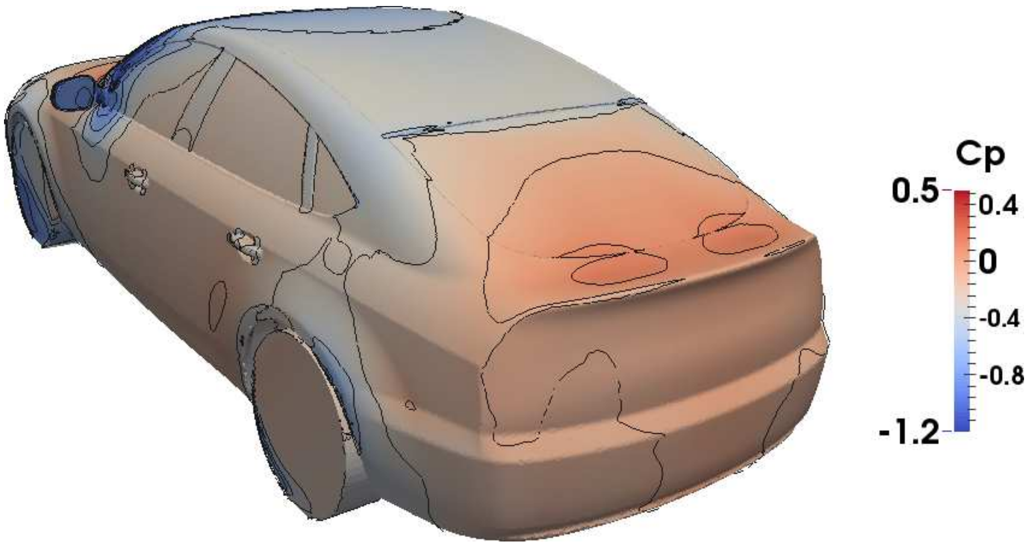

Figure 7.20: Averaged pressure coefficient Cp over the surface of the car.

and wheel wake areas (P5 and P7). As was described by Duell and George [23], there is a pumping effect present in the near wake of car-like geometries. This effect has also been experimentally

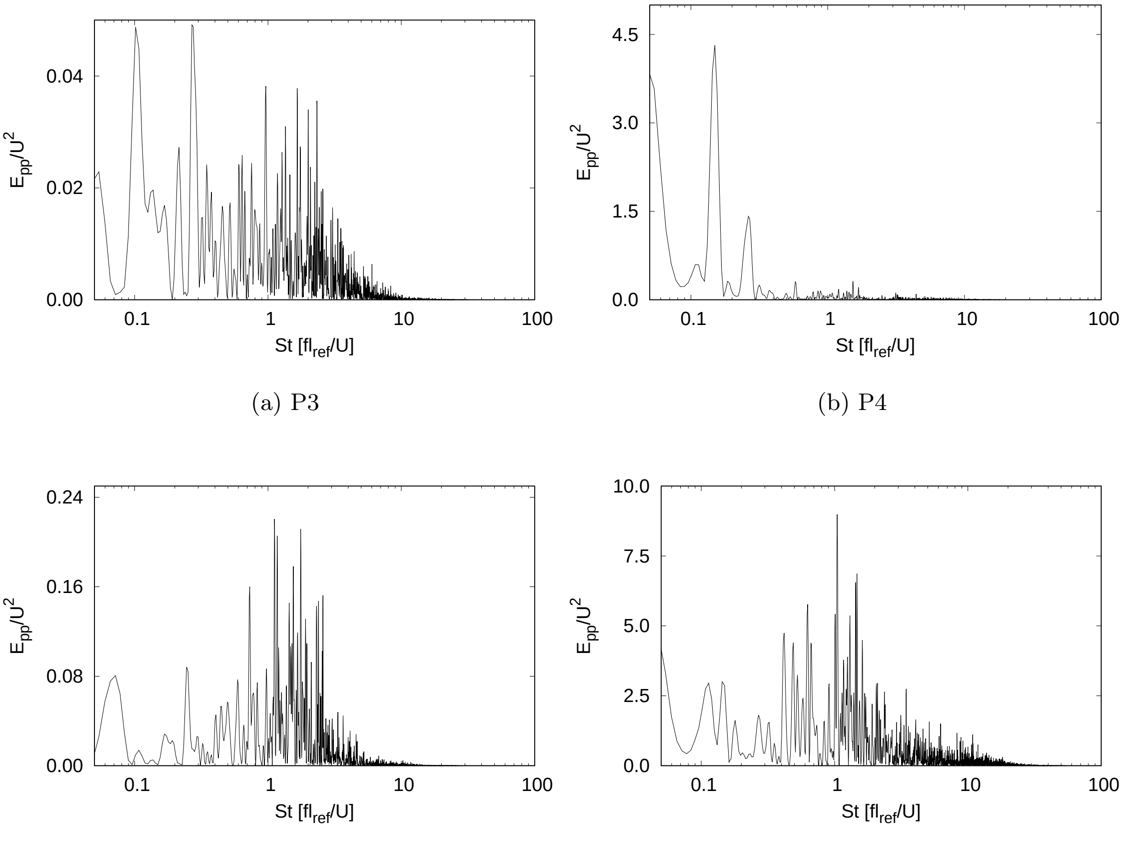

(a) P3

(b) P4

(c) P6

(d) P8

Figure 7.21: Energy spectra for the pressure fluctuations at stations P3, P4, P6 and P8.

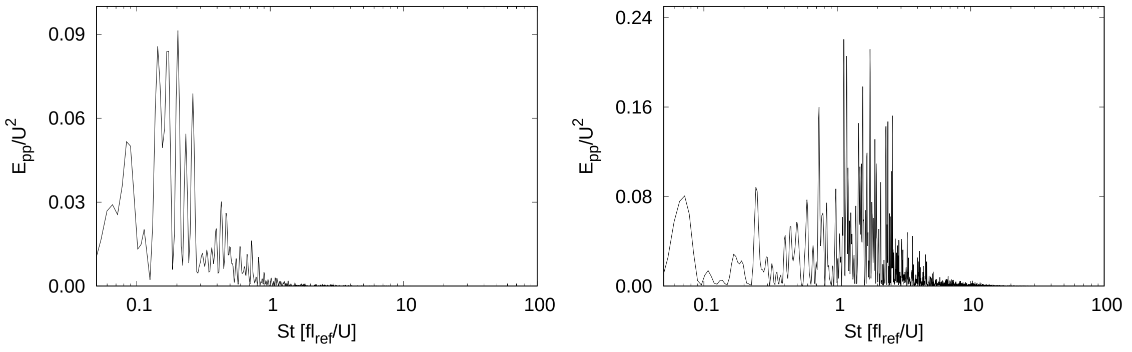

(a) P5

(b) P7

Figure 7.22: Frequency spectra on the drivAer model at the locations specified on Fig. 7.4.

observed by Wieser et al. [145] for the drivAer model. Both, Duell and George [23] and Wieser et al. [145] report a pumping frequency around $St = 0.07$. Station P5 is located in this area (Fig. 7.22a). Energy spectra for the pressure fluctuations in this region show a frequency of $St = 0.08$, indicating this pumping effect seems to be captured in the present simulations, however, the large period of this phenomena requires a longer simulation time to confirm. Finally, A high peak at $St = 0.27$ is seen for station P7 (Fig. 7.22b), located near the rear wheels. This energy peak is induced by the rear wheel rotation, coinciding with the wheels rotating frequency ($St \approx 0.3$).

7.4 CONCLUSIONS

In this work LES and WMLES simulations of the flow around the drivAer car model have been carried out using smooth under body, mirrors, simplified wheels and moving ground. In order to reduce the computational power required to solve the boundary layer-related phenomenology, a reduced reduced Reynolds number has been used. Two values have been reported regarding Reynolds number independence on this geometry. Heft et al. [34] reported results are independent of Reynolds number after $Re = 4.87 \times 10^6$, whereas Strangfeld et al. [128] reported the lower $Re = 2{\times}10^6$ value. Taking this into account, the present simulations were ran using $Re = 2.43{\times}10^6$, and some differences between literature results and present ones is expected. Simulations were ran using 4 meshes, containing $900k$ (Mesh 1), $6.5M$ (Mesh 2), $53M$ (Mesh 3) and $79M$ (Mesh 4) control volumes each. Furthermore, the Werner and Wengle wall model was implemented on Mesh 3, in conjunction with two SGS models: SIGMA and VMS, and results compared to those yielded by the finer mesh.

The very complex flow present around this geometry result in some scattering of the literature available results. Nonetheless, force coefficient and pressure profiles are well within the range of previous authors' results. A Drag coefficient of $C_D = 0.251$ and a lift coefficient of $C_L = 0.07$ are obtained in the present simulations. Although there are discrepancies with the reported results, present simulations are useful to evaluate the WMLES potential.

Force coefficients show improvement when using the WM. Using the SIGMA turbulence model drag coefficient changes from $C_D = 0.246$ without WM to $C_D = 0.251$ using the WM, whereas the change for the lift coefficient is more significant, from $C_L = 0.083$ without WM to 0.056 with WM. This same trend is observed with the VMS model.

Small differences are observed in the pressure profiles, and using the WM gives mixed results. Improvement is observed in zones with adverse pressure gradient and smooth geometrical changes. In the present geometry this zones include the rear window and diffuser areas. Results obtained in zones where the geometry triggers flow separation and recirculation do not show improvement, such as the junction between the bonnet and wind shield or the small lip between the roof and rear window. Results from the two SGS models used (VMS and SIGMA) are compared in several span wise locations in the FB. Both SGS models perform acceptably and show improvement when using the wall model, but the combination of WM and SIGMA SGS model show the best results. Overall analysis of the models leads to the conclusion that, from a practical viewpoint, the WMLES using the Werner and Wengle wall model improves the obtained results with very low computational cost. Additionally, the improvement of the results using the WM allows simulations to be ran in smaller meshes, allowing a larger time step, and thus, a lower number of iterations. In the present case, CPU time required for Mesh 3 with the wall model is around 70% lower than that required for mesh 4.

One of the strongest features LES simulation have is the ability to study flow structures and unsteady effects around the car. This is a very useful tool as it can better predict large scale structures that directly affect aerodynamic behaviour, as well as, unsteady effects which can have an important impact on ride stability and noise generation. Flow around the drivAer geometry is quite complex and a lot of interactions create plenty of vortical structures around the car. The most important structures observed are the mirror induced vortices and those created by the rotating wheels. characteristic frequencies for these phenomena have been measured to be $St \approx 0.15$ for the mirror vortex and $St \approx 0.3$ for the wheel vortices. The shedding of large structures around the car show a non-dimensional frequency of $St \approx 1$. This structures include the A-pillar and C-pillar vortices, vortices detaching of off the wind shield-roof junction. Smaller scale phenomena show a much larger frequency. Small structures detaching of the BW-J area and those forming in the FB area show non-dimensional frequencies around $St \approx 6.2$ and $St \approx 2.5$, respectively. Finally, as has been described in other works, a pumping effect of the wake has been observed in car-like geometries. This frequency has been reported to be around $St \approx 0.07$. A frequency around $St \approx 0.08$ has been captured in the present simulations, however, longer time integration is required to extract conclusions from this phenomenon.

Chapter 8

Conclusions and future work

After a brief introduction in chapter 1, the flow over a circular cylinder at $Re = 5000$ studied via DNS simulations is presented in chapter 2. A spanwise dimention of $2\pi D$ was used to correctly capture the three dimensional phenomena present in this case. This complex behaviour, not observed in lower Reynolds numbers, suggests a fundamental change in the flow configuration. Vortex distortions limited to the vortex formation region have been observed. Evidence that the three-dimensional behavior is the result of the coexistence of two instability mechanisms that resonate is shown.

Chapter 3 studies the changes brought upon the flow when the cylinder is rotating. Similarly as in Chapter 2, DNS simulations were carried out. Vortex shedding was seen to cease for rotation ratios $\alpha > \alpha_{crit} = 2$. For lower α the wake dynamics do not change drastically. However, rotation affects several parameters in the wake. For $\alpha > \alpha_{crit}$ the flow configuration are greatly changes. The vortex formation region dissapears and Taylor-Görtler structures appear. For the larger rotation ratio, $\alpha = 5$, the Taylor-Görtler structures are seen to dettach from the cylinder creating a vortex shedding-like phenomenon. Furthermore, a circumvolving layer is formed around the cylinder, pushing the stagnation point off of the cylinder's surface. Force coefficients also change due to rotation. Drag coefficient decreases for $\alpha \leq 3$ and then increase for $\alpha \geq 3$. Additionally, the Magnus effect creates a lift force that grows with α, surpassing the theoretical limit proposed by Prandtl.

In Chapter 4 a LES study of different valve geometries at an industrial level Re number is carried out. Two geometries and different valve openings are simulated. For this study synthetic turbulence is used at the inlet, allowing the numerical simulations to be one step closer to practical applications. The pressure profile in the valve disc is greatly affected by the change of geometry. Additionally, a significant reduction in the velocity gain within the valve gap is also observed

Following chapters deal with automotive-type simulations. A CLES study on simplified car geometries is carried out in Chapter 5. Though the meshes used are quite coarse, results obtained compare well to other authors' results that used finer meshes. Four turbulence models were used: SIGMA, VMS, WALE and QR models. Coherent structures around the Asmo car are weaker than those observed in the Ahmed car. The latter shows a larger turbulent behaviour resulting in higher drag and lift coefficients. All SGS models used perform well in both geometries. However, the SIGMA and VMS models show better agreement with experimental data than the WALE and QR models.

The effect of rotating wheels is studied in Chapter 6 by means of the immersed boundary method (IMB). Large scale phenomena is captured and overall results are accurate. However, the errors introduced by the IMB taint the results. Wheels and wheelhouses increase the unsteadiness in the flow resulting in an increment of the force coefficients. Using the IMB method reduces mesh requirements, but sacrifices surface resolution.

In the final chapter in the core of this thesis, Chapter 7, a LES and WMLES study is performed on the generic realistic car model DrivAer. Simulations are carried out for the fast back configuration using mirrors, smooth underbody, moving ground and rotating simplified wheels. Some scattering in literature available results was observed. However, the simulations are in agreement with them, resulting useful to evaluate the WMLES potential. Two meshes were used to asses the wall model behavior, observing an overall improvement of the results. A more detailed analysis shows the Werner and Wengle wall model works best flows with no sudden geometry changes such as the rear window of the car of the underbody area. Both SGS models used (SIGMA and VMS) perform well with the meshes used. To asses the influence they pose in the flow solution, results are compared in several span wise locations in the rear window. All in all, the WMLES using the Werner and Wengle wall model improves the obtained results with very low computational cost. It is important to note that there is an important reduction in computational expense when using the WMLES vs a pure LES approach. As the meshes for the WMLES approach requiere less surface resolution, coarser meshes can be used, resulting in larger timesteps and less memory requirements. Additionally, flow structures and unsteady effects were also analyzed. It has been observed that plenty of coherent structures are formed around the car. These include the mirror induced vortices, wheel induced vortices, A-pillar and C-pillar vortices, vortices detaching of off the windshield-roof junction, small structures detaching of the bonnet-windshield junction and small longitudinal vortices that form in the fast back area. Several characteristic frequencies have also been observed regarding the unsteady behaviour of the car.

Future work

Constant growth in computational power have made possible the simulation of more complex problems every year, making it possible to add more detail and solve with greater accuracy these geometries. Some cases to study in the future include: sidewind conditions, detailed wheel simulations by means of sliding meshes and the inclution of detailed underbody and underhood gemoetries.

Bibliography

[1] Ahmed, S. R., Ramm, G., Faltin, G., 1984. Some Salient Features of the Time Averaged Ground Vehicle Wake. SAE paper no 840300.

[2] Aljure, D. E., Lehmkuhl, O., Rodríguez, I., Oliva, A., 2014. Flow and turbulent structures around simplified car models. Comp. Fluids 96, 122–135.

[3] Aljure, D. E., Rodríguez, I., Lehmkuhl, O., D., P.-S. C., Oliva, A., 2015. Influence of rotation on the flow over a cylinder at Re = 5000. Int. J. Heat Fluid Fl. 55, 76–90.

[4] Aronson, D., Brahim, S., Perzon, S., 2000. Multigrid heat transfer calculations using different iterative schemes. SAE Technical Paper 2000-01-0485.

[5] Ashton, N., West, A., Lardeau, S., Revell, A., 2016. Assessment of RANS and DES methods for realistic automotive models. Comput. Fluids 128, 1–15.

[6] Bloor, M. S., 1964. The transition to turbulence in the wake of a circular cylinder. J. Fluid Mech. 19 (2), 290–304.

[7] Borrell, R., Lehmkuhl, O., Trias, F. X., Oliva, A., 2011. Parallel direct Poisson solver for discretisations with one Fourier diagonalisable direction. J. Comput. Phys. 230 (12), 4723–4741.

[8] Böswirth, L., 1982. Theoretical and experimental study on flow in valve channels, parts i and ii. In: Int. Compressor Engineering Conference. pp. 38–53.

[9] Braza, M., Faghani, D., Persillon, H., 2001. Succesive stages and the role of natural vortex dislocations in three-dimensional wake transition. J. Fluid. Mech. 439 (1), 1–41.

[10] Browand, F. K., Troutt, T. R., 1985. The turbulent mixing layer: geometry of large vortices. J. Fluid Mech. 158, 489–509.

[11] Chew, Y. T., Cheng, M., Luo, S. C., 1995. A numerical study of flow past a rotating circular cylinder using a hybrid vortex scheme. J. Fluid Mech. 299, 35–71.

[12] Chong, M. S., Perry, A. E., Cantwell, B. J., 1990. A General Classification of Three-Dimensional Flow Fields. Phys. Fluids 2 (5), 765–777.

[13] Chorin, A., 1968. Numerical solution of the Navier-Stokes equations. Math. Comput. 22 (104), 745–762.

[14] Chou, M.-H., 2000. Numerical study of vortex shedding from a rotating cylinder immersed in a uniform flow field. Int. J. Numer. Meth. Fluids 32, 545–567.

[15] Chyu, C., Lin, J. C., Rockwell, D., 1995. Kármán vortex formation from a cylinder: Role of phase-locked Kelvin-Helmholtz vortices. Phys. Fluids 7 (9), 2288–2290.

[16] Colaciti, A., Valdés, L. M., Aparecido, H., Cabezas-Gomez, L., 2007. Numerical simulation of a radial diffuser turbulent air flow. Appl. Math. Comput. 189, 1497–1504.

[17] Coutanceau, M., Ménard, C., 1985. Influence of rotation on the near-wake development behind and impulsively started circular cylinder. J. Fluid. Mech. 158, 399–446.

[18] Dagnewa, A. K., , Bitsuamlakb, G. T., 2010. LES evaluation of wind pressures on a standard tall building with and without a neighboring building. In: The Fifth International Symposium on Computational Wind Engineering (CWE2010) Chapel Hill, USA.

[19] Damle, R., Rigola, J., Pérez-Segarra, C.-D., Castro, J., Oliva, A., 2011. Object-oriented simulation of reciprocating compressors: numerical verification and experimental comparison. Int J. Refrig. 34 (9), 1989–1998.

[20] di Mare, L., Klein, M., Jones, W. P., Janicka, J., 2006. Synthetic turbulence inflow conditions for lare-eddy simulations. Phys. Fluids. 18, 025107.

[21] Diaz, F., Gavaldà, J., Kawall, J. G., Keffer, J. F., Giralt, F., 1983. Vortex shedding from a spinning cylinder. Phys. of Fluids 26, 3454–3460.

[22] Dong, S., Karniadakis, G. E., Ekmekci, A., Rockwell, D., 2006. A combined direct numerical simulation–particle image velocimetry study of the turbulent near wake. J. Fluid Mech. 569 (9), 185–207.

[23] Duell, E., George, A., 1999. Experimental study of a ground vehivle body unsteady near wake. SAE Technical Paper (1999-01-0812).

[24] Ervin, J. S., Suryanarayana, N. V., Hon Chai, N., 1989. Radial, turbulent flow of a fluid between two coaxial disks. J. Fluid. Eng. 34, 378–383.

[25] Fabianic, J., 1996. An Experimental Investigation of Wheel-Well Flows. SAE Technical Paper (SAE960901).

[26] Fadlun, E., Verzicco, R., Orlandi, P., Mohd-Yusof, J., 2000. Combined Immersed-Boundary Finite-Difference Methods for Three-Dimensional Complex Flow Simulations. J. Comput. Phys. 161, 35–60.

[27] Felten, F. N., Lund, T. S., 2006. Kinetic energy conservation issues associated with the collocated mesh scheme for incompressible flow. J. Comput. Phys. 215, 465–484.

[28] Gerrard, J. H., 1966. The mechanics of the formation region of vortices behind bluff bodies. J. Fluid Mech. 25 (2), 401–413.

[29] Gilhome, B. R., 2002. Unsteady flow structures and forces over/on the rear window and boot lid of sedan automobiles. In: Progress in vehicle aerodynamics III - unsteady flow effects.

[30] Glauert, M. B., 1957. The flow past a rapidly rotating circular cylinder. P. Roy. Soc. Lon. A Mat. 242 (1228), 108–115.

[31] Guilmineau, E., 2014. Numerical simulations of flow around a realistic generic car model. SAE Int. J. Passeng. Cars - Mech. Syst. 7 (2).

[32] Guilmineau, E., 2014. Numerical simulations of ground simulation for a realistic generic car model. In: Proceedings of the ASME 2014 Joint US-European Fluids Engineering Division Summer, Chicago, USA.

[33] Gulyás, A., Bodor, A., Régert, T., Jánosi, I., 2013. PIV Measurement of the Flow Past a Generic Car Body With Wheels at LES Applicable Reynolds Number. Int. J. Heat Fluid Fl.

[34] Heft, A. I., Indinger, T., Asams, N. A., 2012. Introduction of a new realistic generic car model for aerodynamic investigations. SAE Technical Paper (2012-01-0168).

[35] Hinterberger, C., García-Villalba, M., Rodi, W., 2004. Large Eddy Simulation of Flow Around the Ahmed Body. The Aerodynamics of Heavy Vehicles: Trucks, Buses, and Trains. Numer. Heat. Tr. B-Fund., 77–88.

[36] Huang, W.-X., Sung, H. J., 2007. Improvement of mass source/sink for an immersed boundary method. Int. J. Numer. Methods Fluids 53, 1659–1671.

[37] Huang, N. E. andShen, Z., Long, S. R., Wu, M. C., Shih, H. H., Zheng, Q., Yen, N.-C., Tung, C. C., Liu, H. H., 1998. The empirical mode decomposition and the Hilbert spectrum for non-linear and non-stationary time series analysis. Proc. R. Soc. Lond. A 454 (903).

[38] Hughes, T. J. R., Mazzei, L., Jansen, K. E., 2000. Large eddy simulation and the variational multiscale method. Comput Vis. Sci. 3, 47–59.

[39] Hughes T.J.R, Feijóo G.R., M. L., J-B, Q., 1998. The Variational Multiscale Method — A Paradigm for Computational Mechanics. Comput. Method Appl. M. 166, 3–24.

[40] Hunt, J. C. R., Wray, A. A., Moin, P., 1988. Eddies, stream and convergence zones in turbulent flows. In: Proceedings of the Summer Program 1988.

[41] Inoue, Y., Ito, A., Yamashita, S., 2004. UVP measurements of the flow behind a rotating circular cylinder. In: 4th International Symposium on Ultrasonic Doppler Method for Fluid Mechanics and Fluid Engineering, Sapporo, Japan.

[42] Jakirlić, S., Jester-Zücker, R., Tropea, C., 2001. 9th ERCOFTAC/IAHR/COST Workshop on Refined Turbulence Modelling.

[43] Jakirlic, S., Kutej, L., Hanssmann, D., Basara, B., Schütz, T., Tropea, C., 2014. Rear-end shape influence on the aerodynamic properties of a realistic car model: a RANS and hybridLES/RANS study. In: New Results in Numerical and Experimental Fluid Mechanics X, 9th STAB/DGLR Symposium Munich, Germany. pp. 397–407.

[44] Jeong, J., Hussain, F., 1995. On the Identification of a Vortex. J. Fluid Mech. 285, 69–94.

[45] Jofre, L., Lehmkuhl, O., Ventosa, J., Trias, F. X., Oliva, A., 2014. Conservation properties of unstructured finite-volume mesh schemes for the Navier-Stokes equations. Numer. Heat Tr. B-Fund. 64 (1), 53–79.

[46] Jordan, S., Ragab, S. A., 1998. A large-eddy simulation of the near wake of a circular cylinder. J. Fluids Eng. 120 (2), 243–252.

[47] Kang, S., Iaccariono, G., Moin, P., 2009. Accurate immersed-boundary reconstructions for viscous flow simulations. AAIA journal 47 (7).

[48] Kapadia, S., Roy, S., Vallero, M., Wurtzler, K., Forsythe, J., 2004. Detached-Eddy Simulation Over a Reference Ahmed Car Model. In: Direct and Large Eddy Simulations V (ERCOFTAC series). pp. 481–488.

[49] Karabelas, S. J., 2010. Large Eddy Simulation of high-Reynolds number flow past a rotating cylinder. Int. J. Heat Fluid Fl. 31, 518–527.

[50] Karypis, G., Kumar, V., 1998. Multilevel k-way partitioning scheme for irregular graphs. J. Parallel Distr. Com. 48, 96–129.

[51] Kawai, S., Larsson, J., 2013. Dynamic non-equilibrium wall-modeling for large eddy simulation at high Reynolds number. Phys. Fluids 25, 015105.

[52] Kimura, T., Tsutahara, M., 1991. Wake of a rotating circular cylinder. AIAA journal - technical notes 30 (2), 555–556.

[53] Klein, M., Sadiki, A., Janicka, J., 2003. A digital filter based generation of inflow data for spatially develping direct numerical or large eddy simulations. J. Comp. Phys. 186, 652–665.

[54] Kolmogorov, A. N., 1941. The local structure of turbulence in incompressible viscous fluid for very large Reynolds numbers. Dokl. Akad. Nauk SSSR 30 (4).

[55] Kourta, A., Boisson, H. C., Chassaing, P., Ha Minh, H., 1987. Nonlinear interaction and the transition to turbulence in the wake of a circular cylinder. J. Fluid Mech. 181, 141–161.

[56] Krajnović, S., Davidson, L., 2005. Flow Around a Simplified Car: Part1: Large Eddy Simulation. J. Fluid Eng. 127, 907–919.

[57] Krajnović, S., Davidson, L., 2005. Flow Around a Simplified Car: Part2: Understanding the Flow. J. Fluid Eng. 127, 919–928.

[58] Krajnović S., Sarmast, S., Basara, B., 2011. Numerical Investigation of the Flow Around a Simplified Wheel in a Wheelhouse. J. Fluid Eng. 133.

[59] Lam, K., Wang, F., So, R., 2004. Three-dimensional nature of vortices in the near wake of a wavy cylinder. J. Fluid. Struct. 19, 815–833.

[60] Lam, K. M., 2009. Vortex shedding behing a slowly rotating circular cylinder. J. Fluids Struct. 25, 245–262.

[61] Larsson, J., Kawai, S., Bodart, J., Bermejo-Moreno, I., 2016. Large eddy simulation with modeled wall-stress: recent progress and future direcrtions. Mech. Eng. reviews 3 (1).

[62] Lehmkuhl, O., Baez, A., Rodríguez, I., Pérez-Segarra, C. D., 2011. Direct numerical simulation and Large-Eddy simulations of the turbulent flow around a NACA-0012 airfoil. In: Proceedings of the 7th International Conference on Computational Heat and Mass Transfer. pp. 1–8.

[63] Lehmkuhl, O., Borrell, R., Pérez-Segarra, C. D., Oliva, A., Verstappen, R., 2010. LES modeling of the turbulent flow over an Ahmed car. In: ERCOFTAC WORKSHOP Direct and Large-Eddy Simulations 8. pp. 89–94.

[64] Lehmkuhl, O., Borrell, R., Pérez-Segarra, C. D., Soria, M., , Oliva, A., 2007. A new parallel unstructured CFD code for the simulation of turbulent industrial problems on low cost PC cluster. In: Parallel Computational Fluid Dynamics, Ankara, Turkey.

[65] Lehmkuhl, O., Park, G. I., Moin, P., 2016. LES of ow over the NASA common research model with near-wall modeling. In: Proceedings of the summer program 2016, center for turbulence research, Standford. pp. 335–341.

[66] Lehmkuhl, O., Rodríguez, I., Borrell, R., Chiva, J., Oliva, A., 2014. Unsteady forces on a circular cylinder at critical Reynolds numbers. Phys. of Fluids 26, 125110.

[67] Lehmkuhl, O., Rodríguez, I., Borrell, R., Pérez-Segarra, C. D., Oliva, A., 2013. Low-frequency variations in the wake of a circular cylinder at Re = 3900. Phys. of Fluids 25 (8), 085109.

[68] Leonard, A., 1974. Energy cascade in large-eddy simulations of turbulent fluid flows. Adv. Geophys. 18, 237–248.

[69] Leweke, T., Williamson, C. H. K., 1998. Three-dimensional instabilities in wake transition. Eur. J. Mech. B/Fluids 17 (4), 571–586.

[70] Lewis, C., Gharib, M., 1992. An exploration of the wake three dimensionalities caused by a local discontinuity in cylinder diameter. Phys. Fluids 4 (1), 104–117.

[71] Lienhart, H., Stoots, C., Becker, S., 2000. Flow and Turbulence Structures in the Wake of a Simplified Car Model (Ahmed Model). In: DGLR Fach. Symp. der AG STAB, Stuttgart University.

[72] Lin, J.-C., Towfighi, J., Rockwell, D., 1995. Instantaneous structure of the near wake of a circular cylinder: on the effect of Reynolds number. J. Fluid. Struct. 9, 409–418.

[73] Ludwig, G. R., 1964. An experimental investigation of laminar separation from a moving wall. AIAA- Aerospace science meetings (64-6).

[74] Lygren, M., Andersson, H. I., 1999. Turbulent flow between a rotating and a stationary disk. J. Fluid Mech. 426, 297–326.

[75] Ma, X., Karamanos, G. S., Karniadakis, G. E., 2000. Dynamics and low-dimensionality of a turbulent wake. J. Fluid Mech. 410, 29–65.

[76] Mariani, V. C., Prata, A. T., Deschamps, C. J., 2010. Numerical analysis of fluid flow through radial diffusers in the presence of a chamfer in the feeding orifice with a mixed eulerian-lagrangian method. Comput. Fluids 39, 1672–1684.

[77] Matos, F. F. S., Prata, A. T., Deschamps, C. J., 1999. Numerical analysis of the dynamic behavior of plate valves in reciprocating compressors. In: Int. Conference on Compressors and Their Systems. No. C542/031/99.

[78] Matsui, T., 1981. Flow visualization studies of vortices. In: Proc. Indian Acad. Sci. (Engg. Sci.). Vol. 4, 2. pp. 239–257.

[79] Minguez, M., Pasquetti, R., Serre, E., 2008. High Order Large Eddy Simulation of Flow Over the “Ahmed Body” Car Model. Phys. Fluids 20.

[80] Mittal, R., Iaccarino, G., 2005. Immersed boundary methods. Annu. Rev. Fluid Mech. 37, 239–261.

[81] Mittal, S., Kumar, B., 2003. Flow past a rotating cylinder. J. Fluid Mech. 476, 303–334.

[82] Najjar, F. M., Balachandar, S., 1998. Low-frequency unsteadiness in the wake of a normal flat plate. J. Fluid Mech. 370 (101–147).

[83] Nakashima, T., Tsubokura, M., Nouzawa, T., Nakamura, T., Zhang, H., Oshima, N., 2008. Large-Eddy Simulation of Unsteady Vehicle Aerodynamics and Flow Structures. In: BBAA VI International Colloquium on: Bluff Bodies Aerodynamics & Applications.

[84] Nicoud, F., Ducros, F., 1999. Subgrid-scale stress modelling based on the square of the velocity gradient tensor. Flow. Turbul. Combust. 62, 183–200.

[85] Nicoud, F., Toda, H., Cabrit, O., Bose, S., , Lee, J., 2011. Using Singular Values to Build a Subgrid-Scale Model for Large Eddy Simulations. Phys. Fluids 23.

[86] Norberg, C., 1992. An experimental study of the flow around cylinders joined with a step in the diameter. In: 11th Australian Fluid Mechanics Conference, Hobart, Australia.

[87] Norberg, C., 1993. Pressure forces on a circular cylinder in cross flow. In: IUTAM Symposium: Bluff Body Wakes, Dynamics and Instabilities, Göttingen, Germany. Springer-Verlag.

[88] Norberg, C., 1994. An experimental investigation of the flow around a circular cylinder: influence of aspect ratio. J. Fluid. Mech. 258, 287–316.

[89] Norberg, C., 1998. LDV measurements in the near wake of a circular cylinder. In: Advances in Understanding of Bluff Body Wakes and Vortex-Induced Vibration, Washingtong D.C., USA.

[90] Norberg, C., 2001. Flow around a circular cylinder: Aspects of fluctuating lift. J. Fluid. Struct. 15, 459–469.

[91] Padrino, J. C., Joseph, D. D., 2006. Numerical study of the steady-state uniform flow past a rotating cylinder. J. Fluid. Mech. 557, 191–223.

[92] Papangelou, A., 1992. Vortex shedding from slender cones at low reynolds numbers. J. Fluid Mech. 242, 299–321.

[93] Park, G. I., Moin, P., 2014. An improved dynamic non-equilibrium wall-model for large eddy simulation. Phys. Fluids 26, 015108.

[94] Pasqueali, A., Schönherr, M., Geier, M., Krafczyk, M., 2015. Simulation of external aerodynamics of the drivAer model with the LBM on GPGPUs. In: Advances in Parallel Computing, Parallel Computing: On the Road to Exascale. Vol. 27. pp. 391–400.

[95] Pérez-Segarra, C. D., Cadafalch, J., Rigola, J., Oliva, A., 1999. Numerical study of turbulent fluid flow through valves. In: Int. Conf on Compressors and Their Systems. No. C542/021/99.

[96] Persillon, H., Braza, M., 1998. Physical analysis of the transition to turbulence in the wake of a circular cylinder by three-dimensional Navier-Stokes simulation. J. Fluid Mech 365, 23–88.

[97] Perzon, S., Davidson, L., 2000. On Transient Modeling of the Flow Around Vehicles Using the Reynolds Equation. In: ACFD 2000 Beijing, China. pp. 720–727.

[98] Peskin, C. S., 1972. Flow patterns around heart valves: A digital computer method for solving the equations of motion.

[99] Peters, B. C., Uddin, M., Bain, J., Curley, A., Henry, M., 2015. Simulating drivAer with structured finite difference overset grids. SAE Technical Paper (2015-01-1536).

[100] Piomelli, U., 2008. Wall-layer models for large-eddy simulations. Prog. Aerosp. Sci. 44, 437–446.

[101] Piomelli, U., Balaras, E., 2002. Wall-layer models for large-eddy simulations. Annu. Rev. Fluid Mech. 34, 349–374.

[102] Pope, S., 2000. Turbulent flows. Cambridge University Press.

[103] Prandtl, L., 1925. The Magnus effect and windpowered ships. Die Naturwissenchadten 6, 94–108.

[104] Prandtl, L., 1926. Application of the Magnus effect to the wind propulsion of ships. Technical memorandums, NACA 367.

[105] Prasad, A., Williamson, C. H. K., 1996. The instability of the separated shear layer from a bluff body. Phys. Fluids 8 (6), 1347–1349.

[106] Prasad, A., Williamson, C. H. K., 1997. Three dimensional effects in turbulent bluff body wakes. J. Fluid Mech. (343), 235–265.

[107] Rajagopalan, S., Antonia, R. A., 2005. Flow around a circular cylinder–structure of the near wake shear layer. Exp. Fluids 38, 393–402.

[108] Rao, A., Leontini, J., Thompson, M. C., Hourigan, K., 2013. Three-dimensionality in the wake of a rotating cylinder in uniform flow. J. Fluid. Mech. 717, 1–29.

[109] Régert, T., Lajos, T., 2007. The Effect of Wheels on the Aerodynamic Characteristics of and Ahmed Body. In: 3rd European Automotive CFD Conference.

[110] Rigola, J., Lehmkuhl, O., Oliva, A., D., P.-S. C., 2009. Numerical simulation of the fluid flow through valves based on Large Eddy Simulation Models. In: Int. Conf. on Compressors and their Systems, London, England.

[111] Rigola, J., Lehmkuhl, O., Oliva, A., Ventosa, J., D., P.-S. C., 2012. Numerical simulation of the fluid flow through valves based on Low Mach Models. In: Int. Compressor Engineering Conf. at Purdue, USA.

[112] Rigola, J., Lehmkuhl, O., Pérez-Segarra, C. D., Colomer, G., 2009. Turbulent radial outflow between coaxial parallel disks. In: 6th Int. Symp. of Turbulence, heat and Mass Transfer, Rome, Italy.

[113] Rodríguez, I., Borrell, R., Lehmkuhl, O., Pérez-Segarra, C. D., Oliva, A., 2011. Direct numerical simulation of the flow over a sphere at $Re = 3700$. J. Fluid Mech. 25 (25), 263–283.

[114] Rodríguez, I., Lehmkuhl, O., Borrell, R., Oliva, A., 2013. Direct numerical simulation of a NACA0012 in full stall. Int. J. Heat Fluid Fl. 43, 194–203.

[115] Roshko, A., 1954. On the development of turbulent wakes from vortex streets. NACA rep. (1191).

[116] Roshko, A., 1961. Experiments on the flow past a circular cylinder at very high Reynolds number. J. Fluid Mech. 10 (3), 345–356.

[117] Rovaris, J. B., Deschamps, C. J., 2006. Large eddy simulation applied to reciprocating compressors. J. Braz. Soc. Mech. Sci. & Eng. 28 (2), 208–215.

[118] Saad, M., Lee, L., Lee, T., 2007. Shear layers of a circular cylinder with rotary oscillation. Exp. Fluids (43), 569–578.

[119] Satake, S., Kunugi, T., 1998. Direct numerical simulation of an impinging jet into parallel disks. Int. J. Numer. Method H. 8, 768–80.

[120] Schultz, M. P., Flack, K., 2013. Reynolds-number scaling of turbulent channel flow. Comput. Fluids 25, 025104.

[121] Schwerzler, D. D., Hamilton, J. F., 1972. An analytical method for determining effective flow and force areas for refrigeration compressor valving systems. In: Int. Compressor Engineering Conf, Indiana, USA. pp. 30–36.

[122] Serre, E. Minguez, M., Pasquetti, R., Guilmineau, E., Deng, G., Kornhaas, M., Schäfer, M., Fröhlich, J., Hinterberger, C., W., R., 2011. On Simulating the Turbulent Flow Around the Ahmed Body: A French–German Collaborative Evaluation of LES and DES. Comput. Fluids.

[123] Shinde, G., Joshi, A., Nikam, K., 2013. Numerical investigations of the drivAer car model using opensource CFD solver OpenFOAM. In: OSCIC 13, Hamburg, Germany.

[124] Soedel, W., 1992. Mechanics, simulation and design of compressor valves, gas passages and pulsation mufflers. In: Int. Conference on Compressors and Their Systems, Purdue University.

[125] Son, J. S., Hanratty, T. J., 1969. Velocity gradients at the wall for flow around a cylinder at reynolds numbers from 5×10^3 to 10^5. J. Fluid Mech. 35 (2), 353–368.

[126] Spalart, P. R., 2009. Detached-eddy simulation. Annu. Rev. Fluid Mech. 41, 181–202.

[127] Stojkovic, D., Breuer, M., Durst, F., 2002. Effect of high rotation rates on the laminar flow around a circular cylinder. Phys. of Fluids 14 (9), 3160–3178.

[128] Strangfeld, C., Wieser, D., Schmidt, H.-J., Woszidlo, R., Nayeri, C., Paschereit, C., 2013. Experimental study of baseline flow characteristics for the realistic car model drivAer. SAE Technical Paper (2013-01-1251).

[129] Thom, A., 1931. Experiments on the flow past a rotating cylinder. Aeronautical Research Council, Reports and memoranda 1410.

[130] Thom, A., 1934. Effect of discs on the air forces on a rotating cylinder. Aeronautical Research Council, Reports and memoranda 1623.

[131] Thompson, M. C., Hourigan, K., Sheridan, J., 1996. Three-dimensional instabilities in the wake of a circular cylinder. Exp. Thermal and Fluid Science 12, 190–196.

[132] Thompson, M. C., Leweke, T., Williamson, C. H. K., 2001. The physical mechanism of transition in bluff body wakes. J. Fluid. Struct 15, 607–616.

[133] Townsend, A. A., 1976. The Structure of Turbulent Shear Fow. Cambridge University Press.

[134] Trias, F., Lehmkuhl, O., 2011. A self-adaptive strategy for the time integration of Navier-Stokes equations. Numer. Heat Tr. B-Fund. 60 (2), 116–134.

[135] Trias, F. X., Lehmkuhl, O., Oliva, A., Pérez-Segarra, C. D., Verstappen, R. W. C. P., 2014. Symmetry-preserving discretization of Navier-Stokes equations on collocated unstructured grids. J. Comp. Phys. 258, 246–267.

[136] Tsubokura, M., Kobayashi, T., Nakashima, T., Nouzawa, T., Nakamura, T., Zhang, H., Onishi, K., Oshima, N., 2009. Computer Visualization of Unsteady Flow Around Vehicles Using High Performance Computing. Comp. Fluids 38, 981 – 990.

[137] Unal, M. F., Rockwell, D., 1984. The role of the shear layer stability in vortex shedding from cylinders. Phys. Fluids 27 (11).

[138] Unal, M. F., Rockwell, D., 1988. Ovortex formation from a cylinder. part 1. the initial instability. J. Fluid Mech. 90, 491–512.

[139] Verstappen, R., 2011. When does eddy viscosity damp subfilter scales sufficiently? J. Sci. Comput. 49 (1), 94–1110.

[140] Verstappen, R. W. C. P., Veldman, A. E. P., 1997. Direct numerical simulation of turbulence at lower costs. J. Eng. Math. 32, 143–159.

[141] Verstappen, R. W. C. P., Veldman, A. E. P., 2003. Symmetry-preserving discretization of turbulent flow. J. Comp. Phys. 187 (1), 343–368.

[142] Vreman, A. W., 2003. The Filtering Analog of the Variational Multiscale Method in Large-Eddy Simulation. Phys. Fluids 15 (8).

[143] Wark, C. E., Foss, J. F., 1984. Forces caused by the radial out-flow between parallel disks. J. Fluid. Eng. 106, 292–297.

[144] Werner, H., Wengle, H., 1991. Large-eddy simulation of turbulent flow over and around a cube in a plate channel. In: 8th Symposium on Turbulent Shear Flows, Munich, Germany. pp. 155–168.

[145] Wieser, D., Schmidt, H.-J., Müller, S., Strangfeld, C., Nayeri, C., Paschereit, C., 2013. Experimental comparison of the aerodynamic behavior of fastback and notchback drivAer models. SAE Technical Paper (2013-01-1251).

[146] Williamson, C. H. K., 1992. The natural and forced formation of spot-like 'vortex dislocations' in the transition of a wake. J. Fluid Mech. 243, 393–441.

[147] Williamson, C. H. K., 1996. Three dimensional wake transition behind a cylinder. J. Fluid Mech. 328, 345–407.

[148] Williamson, C. H. K., 1996. Vortex dynamics in the cylinder wake. Annu. Rev. Fluid Mech. 28 (1), 447–539.

[149] XFLOW, 2010. Aerodynamic Analysis Involving Moving Parts with Xflow. Tech. rep.

[150] Yang, X., sadique, J., Mittal, R., Meneveau, C., 2015. Integral wall model for large eddy simulations of wall-bounded turbulent flows. Phys. Fluids 27 (2).

[151] Zhang, H.-Q., Fey, U., Noack, B. R., König, M., Eckelmann, H., 1995. On the transition of the cylinder wake. Phys. Fluids 7, 779–794.

Appendix 1: Related projects

The Heat and Mass Transfer Technological Center (CTTC) of the Technical University of Catalonia (UPC) is a research group involved in academic, research and innovation in heat and mass transfer, and fluid dynamics. The investigation center is composed of over 50 professionals working full time in diverse projects. Furthermore, Termo Fluids S.L. is a spin-off from the CTTC, and working in conjunction, has a high capacity of simulating diverse system. The main research activities of the CTTC are focused on basic research on heat and mass transfer phenomena, as well as, fluid dynamics. Some areas the CTTC has experience in are: natural and forced convection, turbulence modeling (RANS, LES and DNS), combustion, two-phase flow, solid-liquid phase change, radiation, porous media, numerical algorithms and solvers, general purpose CFD codes, high performance computing HPC (parallelization) and aerodynamics.

A secondary line involves the application of the technological know-how from the basic studies to the thermal and fluid dynamic optimization of systems and equipment. The present PhD thesis is focused on basic research, however, real life application are of vital importance within the scientific community. In this line, two projects were carried out, in conjunction with the CTTC staff and the formula student team UPC ecoRacing regarding aerodynamic development.

Aerodynamic analysis of the valve of a reciprocating compressor

An analysis of the outlet valve of a reciprocating compressor was carried out. The aim of this study was to identify critical locations interfering with an efficient flow through the valve and compromising the compressor's COP. This study revealed significant obstacles in the flow field that made possible an increase in the efficiency of the compressor. To that end several three dimensional LES simulations were performed on the valve geometry at different opening heights. After studying the valve at different gap openings, two areas were identified as candidates to improve efficiency. To further study this, compressible flow simulations were performed to better understand the flow

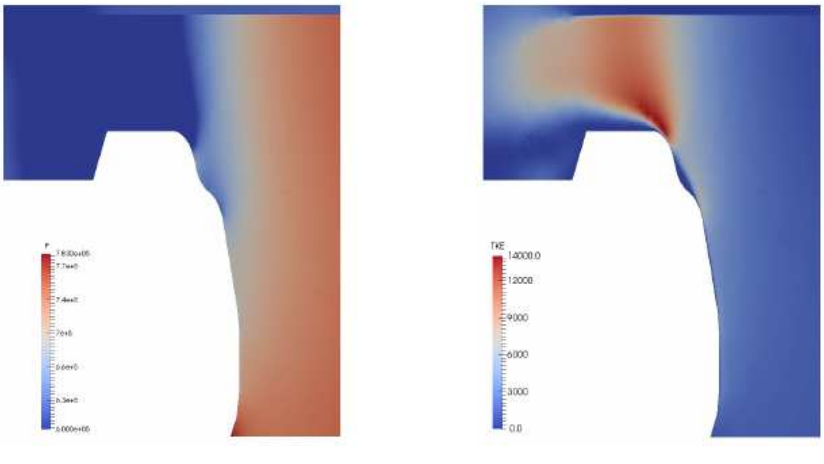

Proposed geometry change for the valve geometry.

behavior. Simulations were carried out for the different gap openings and different geometrical modifications. Finally, after reviewing the results for compressible flow simulations on the valve geometry, several small modifications are proposed to improve its efficiency.

Aerodynamic design and analysis of a formula student car

An analysis of the aerodynamic behavior of a formula student car (the ecoRz from the team UPC ecoRacing) and the posterior design of an aeropackage was carried out. First, isolated elements were analyzed and several iterations performed. Finally, full car simulations were ran, using both RANS and LES methods. The designed aeropackage configuration was built and tested on track during 2016. An evolution of this has been design and set to race on the Formula Student Spain 2017.

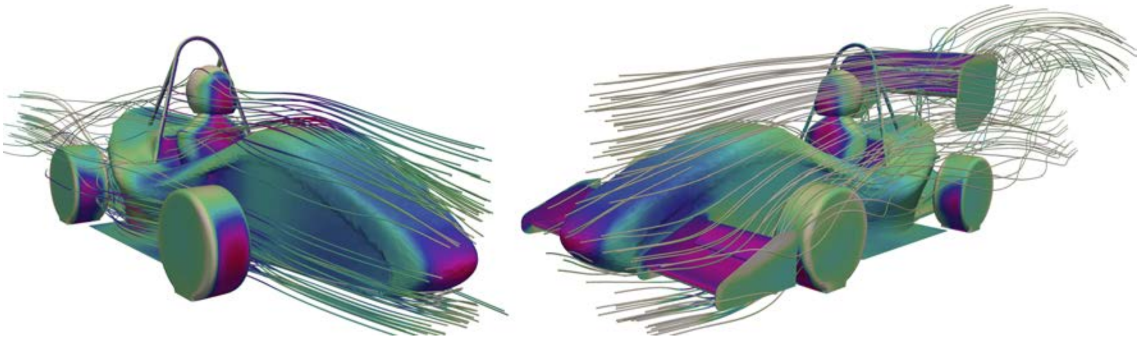

Streamlines over the ecoRz with and without wings.

Appendix 2: List of publications

Aljure, D. E., Calafell, O., Baez, A. and Oliva, A. Flow over a realistic car model: Large eddy simulations and turbulent structures. *ERCOFTAC Workshop Direct and Large-Eddy Simulation 11, At Pisa* May 2017.

Aljure, D. E., Lehmkuhl, O., Rodríguez, I. and Oliva, A. Three dimensionality in the wake of the flow around a circular cylinder at Reynolds number 5000. *Comput. Fluids* 147 2 102-118, 2017.

Aljure, D. E., Rodríguez, I., Lehmkuhl, O., Pérez-Segarra, C.-D. and Oliva, A. Influence of rotation on the flow over a cylinder at Re=5000 *Int. J. Heat Fluid Fl.* 55 79-90, 2015.

Rigola, J., Aljure, D. E., Lehmkuhl, O., Pérez-Segarra, C.-D. and Oliva, A. Numerical analysis of the turbulent fluid flow through valves. Geometrical aspects influence at different positions *IOP Conference Series Materials Science and Engineering*90(1):012026, 2015.

Aljure, D. E., Rodriguez, I., Lehmkuhl, O., Pérez-Segarra, C.-D. and Oliva, A. Influence of rotation on the flow over a cylinder at Re=5000 *10th International ERCOFTAC Symposium on Engineering Turbulence Modelling and Measurements, At Marbella, Spain*, September 2014.

Aljure, D. E., Rodriguez, I., Lehmkuhl, O., Pérez-Segarra, C.-D. and Oliva, A. Aerodynamic fluctuating forces on a rotating cylinder *11th world congress on Computational Mechanics, 6th European conference on computational fluid dynamics., At Barcelona*, July 2014.

Aljure, D. E., Lehmkuhl, O., Favre, F., Martínez, D. and Oliva, A. On the IBM approximation for the wheel aerodynamic simulation *First international conference in numerical and experimental aerodynamics of road vehicles and trains, At Bourdeaux*June 2014.

Aljure, D. E., Lehmkuhl, O., Rodríguez, I., and Oliva, A. Flow and Turbulent Structures Around Simplified Car Models *Comput. Fluids* 96 122-135, 2014.

Aljure, D. E., Rodríguez, I.,Lehmkuhl, O.,Borrel, R. and Oliva, A. Flow and Turbulent Structures Around Simplified Car Models *Conference on Modelling Fluid Flow (CMFF'12) at Budapest*January 2012.